Universidad del País Vasco Euskal Herriko Unibertsitatea

NAZIOARTEKO BIKAINTASUN CAMPUSA
CAMPUS DE EXCELENCIA INTERNACIONAL

université de BORDEAUX

CO-SUPERVISED THESIS PRESENTED TO

OBTAIN THE QUALIFICATION OF

DOCTOR OF

THE UNIVERSITY OF THE

BASQUE COUNTRY AND OF

THE UNIVERSITY OF

BORDEAUX

PhD Thesis by

Francisco Borja Aguirre Yagüe

2021

Sub- and supercritical hydrothermal synthesis of functionalized xonotlite and tobermorite as seed admixtures and their effect on the workability of cement pastes

Under the supervision of
Edurne Erkizia Jauregi and
Cyril Aymonier

Sub- and supercritical hydrothermal synthesis of functionalized xonotlite and tobermorite as seed admixtures and their effect on the workability of cement pastes

PhD Thesis by

Francisco Borja Aguirre Yagüe

2021

Under the supervision of
Edurne Erkizia Jauregi and
Cyril Aymonier

Agradecimientos/ Reconnaissance / Acknowledgement

Aprovecho este pequeño espacio para agradecer a mis directores, la doctora Edurne Erkizia y el doctor Cyril Aymonier, por su dirección y supervisión en estos cuatro años. También aprovecho para a gradecer a la fundación Tecnalia Research & Innovation por la oportunidad que me ofrecieron concediéndome la beca para llevar a cabo este trabajo y por poder además trabajar de algo que de verdad me apasionaba.

Primero, agradezco la acogida que he tenido de mis compañeros en Tecnalia: Jone (y sus grandes historias), Gurutze, Gurtze, Marta, David, Ruben y Alex, Ana, Jontxu, Eunate, Josean, Achu, Aitor, Borja, Iñigo y al resto de personas del edificio 700 en Derio. Lo sé sois muchos y si me dejo a alguien; disculpadme.

Then I would like to thank to my colleagues from ICMCB and specially to my colleagues from office F05. Elen, Brian and Iulia. You were so kind during my stay in Bordeaux and that made me enjoy more my experience in that place. Désolé, mais je n'ai pas appris assez de français pendant mon séjour à Bordeaux. Here I will also include to Laurin. I miss our conversations in the office, it was very nice meeting you and I hope I see you again in Mexico, Spain or even in Austria.

En lo personal, dedico este trabajo a Aroa cuyas vivencias dan para escribir mil tesis doctorales. También hago especial mención al pequeño Gael, que de pequeño tiene poco. Eres todo un grande y un amor de sobrino.

Por supuesto, debo dedicárselo también a Lucia que me lleva animando no solo estos últimos 4 años, si no prácticamente los últimos 12. Solo decir, que has sido fundamental para mí. Una dedicatoria en este manuscrito no es suficiente para agradecerte a ti y a tu familia todo lo que hicisteis.

Por último, pero no menos importante, hago un rinconcito en los agradecimientos a mi colega y amigo Gustavo. Me enseñaste a tomarme la vida con un poco más de calma y seguro que tener que animar a alguien estando también triste no es nada fácil. Por eso te agradezco.

En definitiva, dedico este trabajo tanto a los que ayudaron como a los que no en el desarrollo del mismo, porque ambos me motivaron igualmente a acabarlo.

Table of content

ASTM= American Society for Testing and Materials.

BO= Bridging oxygen.

BPR= Back pressure regulator.

C_2S=Ca_2SiO_4 or belite.

C_3A= $Ca_3Al_2O_6Ca$ or calcium aluminate.

C_3S=Ca_3SiO_5 or alite.

C_4AF= Ca_2AlFeO_5 or tetra calcium ferro aluminate.

C-S-H =Calcium silicate hydrate.

EDS/ EDAX= Energy dispersive X-Ray spectroscopy/ Energy dispersive X-Ray analysis.

FT-IR= Fourier-transform infrared.

HPLC= High performance liquid chromatography.

ICDD= International center for diffraction data.

LS= Lignin sulfonates.

MAS= Magic angle spinning.

MAWL=Maximum allowed water loading.

MCL= Mean chain length.

NBO= Non-bridging oxygen.

OPC= Ordinary Portland cement.

PCE=Polycarboxylate ethers.

PDF=Powder diffraction file.

PEG= Polyethylene glycol.

PMS= Poly melamine sulfonates.

PNS= Poly naphthalene sulfonates.

SBS= Sulfobetaine siloxane.

SCW= Supercritical water.

ESEM= Environmental scanning electron microscopy.

ss-NMR= Solid state nuclear magnetic resonance.

TEM= Transmission electron microscopy.

TGA/DSC= Thermogravimetric analysis/ Differential scanning calorimetry.

XPS= X-Ray photoelectron spectrometry.

XRD= X-Ray diffraction.

XRF= X-Ray fluorescence.

ABSTRACT

There are several factors that influence the choice of construction materials such as mechanical behavior, durability, ease of construction and operational cost. Architects or civil engineers must propose new solutions for the construction and maintenance of more demanding facilities. Moreover, they must guarantee the technical and economic viability of their ideas at the same time. For that reason, the research and development of new construction materials or improvements for the existing ones, are crucial in construction industry.

Cement based materials are a good example of this tendency. Portland cement, although it dates back to mid-eighteenth century, was modified and improved for different applications during all these years from its discovery. Researchers proposed new formulations or additions responding to more demanding needs of cement and concrete from the market. Thus, new products like water reducers, hardening accelerators or retarders appeared to respond these demands.

In recent years nanosilica and other nanoadditions such as certain calcium silicate hydrate nanoparticles have been developed and used to improve mechanical and durability properties in cement and concrete. In the case of calcium silicate hydrates these particles do not react directly with cement but they cause an acceleration of cement hydration. This acceleration is driven by a heterogeneous nucleation mechanism that makes the C-S-H gel, the main product of cement hydration, grow faster. They also receive the name of “seeds”.

However, these materials in suspensions tend to aggregate and absorb mixing water when they are added to cement pastes. The reduction of available water reduces the flowability and hinders the workability of the mixture. Thus, it is necessary to increase the water content in the mixture to recover the initial workability properties. Higher ratios of water over cement powder (w/c), generates more porous structures in hardened pastes with lower mechanical resistance and lower durability. Thus, increasing the content of water causes the opposite effect to the one that it would be obtained adding the nanoparticles.

The most extended method to solve this drawback is the use of superplasticizer admixtures. They allow the reduction of water content in cement mixes maintaining their workability properties. However, several problems have been reported about using these kind of water reducers in the presence of nanoadditions like bleeding or segregation.

The goal of this work is to improve the dispersion of seed particles without having to add more water. This in mind, the thesis focuses on the synthesis and characterization of crystalline calcium silicate hydrate particles with organic functionalities obtained by subcritical hydrothermal reaction and continuous supercritical/hydrothermal reaction in order to obtain particles that can be easily dispersed in cement suspensions.

In this work the synthesis of xonotlite ($Ca_6Si_6O_{17}(OH)_2$) and tobermorite ($Ca_5(OH)_2Si_6O_{16}\cdot 4H_2O$) with polyethylene glycol molecules will be discussed. Moreover, covalent functionalization of xonotlite and tobermorite was also studied by using a siloxane molecule which contain a zwitterionic group. A zwitterion molecule contains a separated positive and negative charge in the same molecule and could stabilize a suspension via electrostatic repulsions. Finally, the addition of these organically functionalized particles to the cement was carried out and their effect in the rheology, hydration reaction and early age mechanical properties were studied.

RESUMEN

Hay varios factores que influyen en la elección de los materiales de construcción, como el comportamiento mecánico, la durabilidad, la facilidad de construcción y el coste de explotación. Los arquitectos o ingenieros civiles deben proponer nuevas soluciones para la construcción y el mantenimiento de las instalaciones más exigentes. Además, deben garantizar la viabilidad técnica y económica de sus ideas al mismo tiempo. Por ello, la investigación y el desarrollo de nuevos materiales de construcción o la mejora de los ya existentes, son cruciales en la industria de la construcción.

Los materiales a base de cemento son un buen ejemplo de esta tendencia. El cemento Portland, aunque su origen se remonta a mediados del siglo XVIII, fue modificado y mejorado para diferentes aplicaciones durante todos estos años desde su descubrimiento. Los investigadores propusieron nuevas formulaciones o adiciones que respondían a las necesidades más exigentes del cemento y el hormigón del mercado. Así, aparecieron nuevos productos como reductores de agua, aceleradores de endurecimiento o retardadores del fraguado para responder a estas demandas.

En los últimos años se han desarrollado y utilizado nanosílice y otras nanoadiciones, como ciertas nanopartículas de silicato cálcico hidratado, para mejorar las propiedades mecánicas y de durabilidad del cemento y el hormigón. En el caso de los silicatos cálcicos hidratados, estas partículas no reaccionan directamente con el cemento, pero provocan una aceleración de la hidratación del cemento. Esta aceleración está impulsada por un mecanismo de nucleación heterogénea que hace que el gel C-S-H, el principal producto de la hidratación del cemento, crezca más rápidamente. estas partículas también reciben el nombre de "semillas de hidratación".

Sin embargo, estos materiales en suspensión tienden a agregarse y a absorber el agua de mezcla cuando se añaden a las pastas de cemento. La reducción del agua disponible reduce la fluidez y dificulta la trabajabilidad de la mezcla. Por ello, es necesario aumentar el contenido de agua en la mezcla para recuperar las propiedades de trabajabilidad iniciales. Una mayor proporción de agua sobre el polvo de cemento (w/c), genera estructuras más porosas en las pastas endurecidas con menor resistencia mecánica y

menor durabilidad. Así, aumentar el contenido de agua provoca el efecto contrario al que se obtendría añadiendo las nanopartículas.

El método más extendido para solucionar este inconveniente es el uso de aditivos superplastificantes. Estos permiten reducir el contenido de agua en las mezclas de cemento manteniendo sus propiedades de trabajabilidad. Sin embargo, se han reportado varios problemas sobre el uso de este tipo de reductores de agua en presencia de nanoadiciones, como el sangrado o la segregación.

El objetivo de este trabajo es mejorar la dispersión de las semillas de hidratación sin tener que añadir más agua. Para ello, la tesis se centra en la síntesis y caracterización de partículas cristalinas de silicato cálcico hidratado con funcionalidades orgánicas obtenidas por reacción hidrotermal subcrítica y reacción supercrítica/hidrotermal continua con el fin de obtener partículas fácilmente dispersables en suspensiones de cemento.

En este trabajo se discutirá la síntesis de xonotlita ($Ca_6Si_6O_{17}(OH)_2$) y tobermorita ($Ca_5(OH)_2Si_6O_{16}$-$4H_2O$) con moléculas de polietilenglicol. Además, se ha estudiado la funcionalización covalente de la xonotlita y la tobermorita utilizando una molécula de siloxano que contiene un grupo zwitteriónico. Una molécula zwitteriónica contiene una carga positiva y negativa separada en la misma molécula y podría estabilizar una suspensión mediante repulsiones electrostáticas. Por último, se llevó a cabo la adición de estas partículas funcionalizadas orgánicamente al cemento y se estudió su efecto en la reología, la reacción de hidratación y las propiedades mecánicas a tiempos cortos de fraguado.

RÉSUMÉ

Plusieurs facteurs influencent le choix des matériaux de construction tels que le comportement mécanique, la durabilité, la facilité de construction et le coût d'exploitation. Les architectes ou les ingénieurs civils doivent proposer de nouvelles solutions pour la construction et l'entretien d'installations plus exigeantes. De plus, ils doivent garantir la viabilité technique et économique de leurs idées en même temps. C'est pourquoi la recherche et le développement de nouveaux matériaux de construction ou l'amélioration des matériaux existants sont essentiels dans le secteur de la construction.

Les matériaux à base de ciment sont un bon exemple de cette tendance. Le ciment Portland, bien qu'il remonte au milieu du XVIIIe siècle, a été modifié et amélioré pour différentes applications pendant toutes ces années depuis sa découverte. Les chercheurs ont proposé de nouvelles formulations ou des ajouts répondant aux besoins plus exigeants du marché en matière de ciment et de béton. Ainsi, de nouveaux produits comme les réducteurs d'eau, les accélérateurs ou les retardateurs de durcissement sont apparus pour répondre à ces demandes.

Ces dernières années, la nanosilice et d'autres nanoadditions telles que certaines nanoparticules d'hydrate de silicate de calcium ont été développées et utilisées pour améliorer les propriétés mécaniques et de durabilité du ciment et du béton. Dans le cas des hydrates de silicate de calcium, ces particules ne réagissent pas directement avec le ciment mais elles provoquent une accélération de l'hydratation du ciment. Cette accélération est due à un mécanisme de nucléation hétérogène qui fait croître plus rapidement le gel C-S-H, le principal produit de l'hydratation du ciment. Ils reçoivent d'ailleurs le nom de "graines".

Cependant, ces matériaux en suspension ont tendance à s'agréger et à absorber l'eau de gâchage lorsqu'ils sont ajoutés aux pâtes de ciment. La réduction de l'eau disponible réduit la fluidité et entrave l'ouvrabilité du mélange. Il est donc nécessaire d'augmenter la teneur en eau du mélange pour retrouver les propriétés initiales d'ouvrabilité. Des rapports plus élevés de l'eau sur la poudre de ciment (w/c), génèrent des structures plus poreuses dans les pâtes durcies avec une résistance mécanique plus faible et une

durabilité plus faible. Ainsi, l'augmentation de la teneur en eau provoque l'effet inverse de celui que l'on obtiendrait en ajoutant les nanoparticules.

La méthode la plus répandue pour résoudre cet inconvénient est l'utilisation d'adjuvants superplastifiants. Ils permettent de réduire la teneur en eau des mélanges de ciment tout en maintenant leurs propriétés d'ouvrabilité. Cependant, plusieurs problèmes ont été signalés concernant l'utilisation de ce type de réducteurs d'eau en présence de nanoadditions, comme le saignement ou la ségrégation.

L'objectif de ce travail est d'améliorer la dispersion des particules de semences sans avoir à ajouter plus d'eau. Dans cette optique, la thèse se concentre sur la synthèse et la caractérisation de particules cristallines d'hydrate de silicate de calcium avec des fonctionnalités organiques obtenues par réaction hydrothermique sous-critique et par réaction supercritique/hydrothermique continue afin d'obtenir des particules pouvant être facilement dispersées dans des suspensions de ciment.

Dans ce travail, la synthèse de xonotlite ($Ca_6Si_6O_{17}(OH)_2$) et de tobermorite ($Ca_5(OH)_2Si_6O_{16}$-$4H_2O$) avec des molécules de polyéthylène glycol sera discutée. De plus, la fonctionnalisation covalente de la xonotlite et de la tobermorite a également été étudiée en utilisant une molécule de siloxane qui contient un groupe zwitterionique. Une molécule zwitterionique contient une charge positive et négative séparée dans la même molécule et pourrait stabiliser une suspension via des répulsions électrostatiques. Enfin, l'ajout de ces particules organiquement fonctionnalisées au ciment a été effectué et leur effet sur la rhéologie, la réaction d'hydratation et les propriétés mécaniques au jeune âge a été étudié.

CHAPTER I: INTRODUCTION

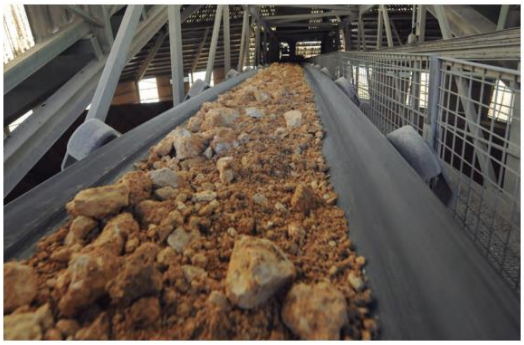

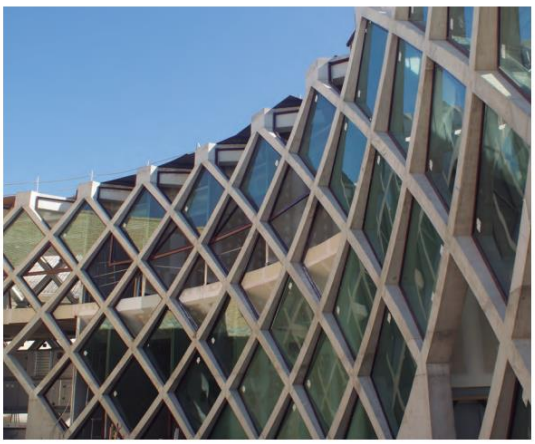

I.1. Introduction to cement industry

Nowadays the word “cement” is used as the general term for Ordinary Portland Cement (OPC). The ASTM standard C 219-94 defines the Portland cement as a hydraulic binder, a binder being a substance capable to harden and bind together coarse to medium grained particles such as, sand, gravel and crushed stone [1].

I.1.1. Portland cement.

Portland cement is considered as an active hydraulic binder which is capable of reacting spontaneously in presence of water and stiffens over time. This mixture of binder and water forms a fluid suspension, that is capable to be mixed, pumped or even introduced in a mold. Then this suspension will react and will form a solid matrix with different fluidity, consistency and mechanical properties (depending on the time passed since it was mixed with water). The time required for cement to resist some pressure without damage is known as setting time and the time required for cement to obtain its full strength is known as curing time.

The development of the actual version of Portland cement started in 1824. Joseph Aspdin patented an invention to produce a hydraulic cement starting from clay and lime precursors. He invented the fabrication of clinker (main component of modern cement) from the vitrification of the raw materials at very high temperature. This process was carried out in a shaft kiln with dry air. This equipment required a lot of energy to reach the necessary temperature for vitrification and the uniformity of properties in clinker product was very low.

It was in 1885 when Frederick Ransome developed the rotatory oven (the actual version of cement kiln) [2]. This new process reduced the cost and time requirements to produce clinker. Moreover, the properties of the clinker obtained where superior to the ones in Aspdin’s invention. After then, several countries worked on changing formulations for new Portland cements. Nevertheless, Ransome’s work in fabrication of clinker boosted the production and use of cement around the world.

Nowadays cement has become the most consumed material in construction applications around the world. Portland cement is the base for fabrication of mortars

(cement and sand mixed with water) and concrete (cement and coarse materials or gravel mixed with water) widely used in construction industry. Its popularity is due to its good mechanical properties, its low price, its resistance to fire and its easy manipulation.

According to the United States Geological Survey (USGS), the production of cement only in United States, the third producer after China or India and the second importer, was equal to 78.9Mt in 2019 (almost 3% higher than in 2018). Even after the pandemic of Covid, and its impact in global economy during 2020, its production was maintained unchanged and the imports of cement in that country increased 28% in respect to 2019 [3].

I.1.2. Composition of cement.

Commercial cement is the product resulting from grinding and mixing the clinker obtained in rotatory kiln furnaces with an addition of a small amount of additive such as calcium sulfate. Clinker in turn, as the mayor constituent in normal Portland cements (more than 90 wt %), is composed by a mix of different phases like calcium silicates, calcium aluminates and calcium ferro aluminates. It typically has a composition around 67wt% of CaO, 2wt% of SiO_2, 5wt% of Al_2O_3 and 6wt% of Fe_2O_3 and other constituents.

The main phase present in clinker is alite or tricalcium silicate Ca_3SiO_5 (C_3S). Alite reacts fast with water and its hydration is responsible of the strength development of cement especially during the first 28 days after being mixed with water. Dicalcium silicate or belite Ca_2SiO_4, in turn, is the second main phase in cement after alite. Its hydration is slow compared to alite and only after curing ages longer than 28 days they have a significant effect in the strength of cement.

Tricalcium aluminate $Ca_3Al_2O_6$ (C_3A) constitutes a lower percent in clinker composition. This phase reacts vigorously with water and causes a rapid setting of cement. This 'flash' or quick set requires a special attention because it drives a rapid development of rigidity and loss of workability in freshly mixed Portland cements. This is the reason why clinker is mixed with controlled amounts of grinded calcium sulfate. Sulfate ions are capable to react with C_3A forming ettringite phase on its surface that inhibits its hydration. Too high contents of calcium sulfate could cause stiffening of cement paste due to its hydration

products (false setting), then the maximum concentration of this additive is always limited around 8%.

Finally, tetracalcium aluminoferrite Ca_2AlFeO_5 (C_4AF) can be observed in clinker composition. It can hydrate fast like C_3A, but the formation of a layer of hydrated iron oxide upon its surface inhibits the hydration of this phase. Other phases of magnesium oxide or alkali oxides (Na_2O and K_2O) can be found in clinker, however the destructive expansion they can cause during its hydration requires a comprehensive control of their content.

I.1.3. Industrial production

Portland cement is produced by heating limestone and clay at 1450°C in a rotatory kiln. Sometimes other calcium sources are employed like aragonite, marl or chalk. In the case of the siliceous raw material, clay is the principal source employed but pit-sand is also used in the process. Moreover, some producer adds aluminum or iron oxides to adjust the formulation of the final clinker [4].

The kiln reactor (Figure 1) is based on a tube with a slope of 3 or 4% from the horizontal that is rotating continuously at 1-4 revolutions per minute. Raw materials enter at the upper end, slide, roll, and flow against a hot gas current produced by a flame located in the lower part of the tube. This area is known as burning zone.

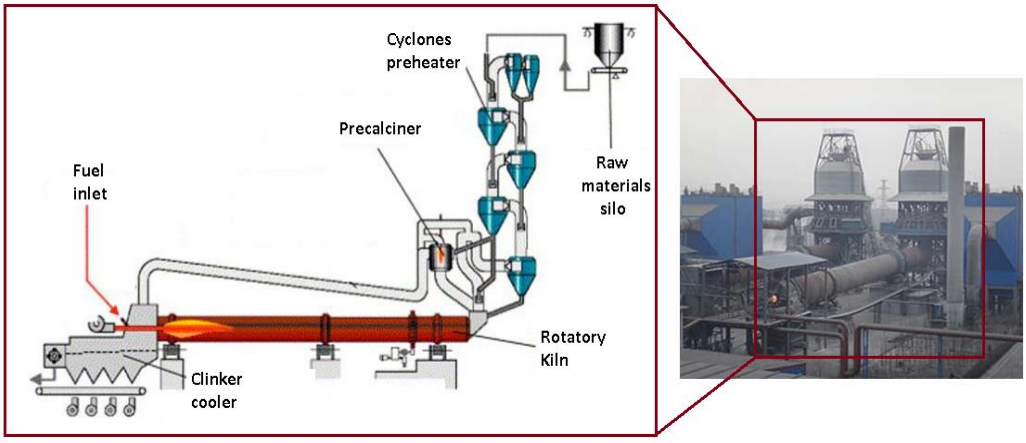

Figure I.1: Simplified scheme of a rotatory kiln in a cement plant. [5]

The first step in the reactor is the drying process of raw materials between 70 and 100°C. During its fall through the precalciner (Figure I.1), the material is heated up to 400°C and

clay decomposition starts transforming into the principal oxides, SiO_2 and Al_2O_3. This process takes place even before the materials are introduced in the rotatory kiln.

In the first part of the kiln tube a temperature between 600 to 1000°C is reached. In this step the belite (dicalcium silicate) formation starts from the reaction between limestone and SiO_2 generated from the decomposition of clay. The excess of calcite is decomposed in CaO and CO_2.

From this point the material arrives to the sintering zone whose temperature is between 1100°C and 1450°C. In this area the material spends around 10 or 15 minutes and the formation of clinker occurs. In this step ferrite and aluminate phases melt and alite phase (tricalcium silicate) is formed from the free lime, silica, and some part of the belite formed previously (1200-1300°C).

Moreover, other polymorphic changes in non-reacted belite and the evaporation of volatiles (mainly alkali metal chlorides) takes place. Finally, at this stage the nodulization process occurs which is the result of the mixture between the liquid phase of ferrites and aluminates and solid particles of alite and belite. Figure I.2 illustrates the consumption and formation of the different phases respect to the range of the temperature in the kiln furnace.

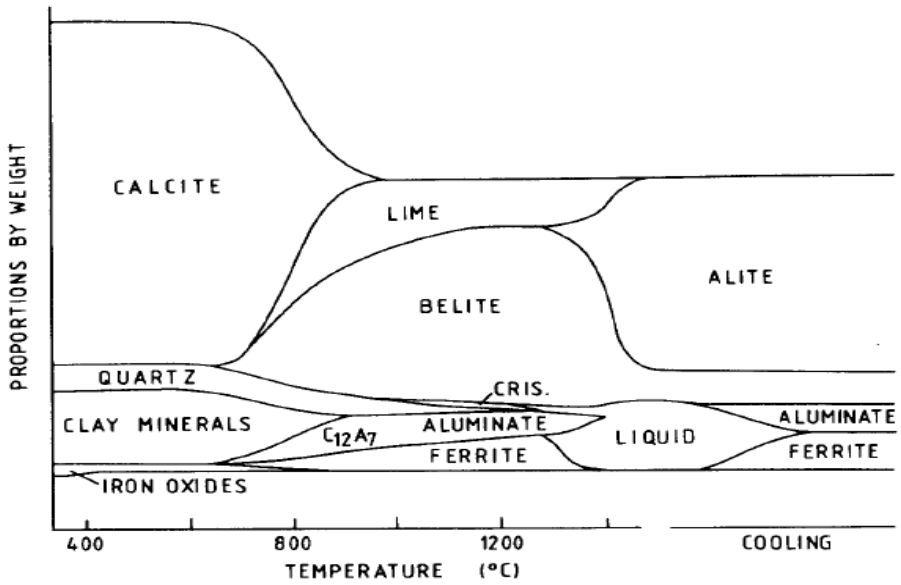

Figure I.2: Phase diagram at different temperature conditions during the production of clinker [1].

Then the hot clinker product is quenched in the final step. The cooling rate is an important parameter that is controlled in cement plants. A fast quenching is always recommended to avoid the formation of large crystals of periclase (MgO). If the quenching is not fast enough, the crystallization and growth of periclase could cause some troubles during grinding or even the hydration of cement. A high content of MgO increase the risk of destructive expansion [6].

Moreover, clinker plants use the recovered heat from clinker in preheater and precalciner systems to heat up the raw materials. The resulted quenched clinker product is composed by alite (50-70wt%), belite (15-30wt%), calcium aluminate (5-10wt%) and calcium ferro aluminate (5-15wt%). This material is then grinded to increase the flowability and reactivity with water. In a typical Portland cement powder, there are between 7 and 9wt% of particles smaller than 2µm and less than 4wt% of particles higher than 90µm [1]. Modern cement is the mixture of grinded Portland clinker and calcium sulfate hydrate (gypsum). The addition of calcium sulfate prevents the flash setting of the cement due to the hydration of aluminates present in the powder. Gypsum is the main additive added to cement, but small quantities of other additives that inhibit aggregation or improve the grindability of clinker [7] can also be found in cement powder.

I.1.4. Cement hydration process.

Hydration process of Portland cement involves several reactions. This process can take month to be completed and even after that time the composition and structure of the reacted product could keep evolving. After 28 days of hydration only a 70% of clinker is reacted and 90% after one year.

As it was mentioned before, cement is basically composed by four phases: alite (C_3S), belite (C_2S), aluminates (C_3A) and ferro aluminates (C_4AF). The presence of a small quantity of calcium sulfate as additive in clinker powder is considered separately but it plays an important role in cement hydration as well. The hydration of cement can be mainly divided in four hydration reactions for C_3S (equation 1.1) , C_2S (equation 1.2), C_3A (equation 1.3) and C_4AF (equation 1.4).

$$2(3CaO \cdot SiO_2) + 6H_2O \rightarrow 3CaO \cdot 2SiO_2 \cdot 3H_2O + 3Ca(OH)_2 \quad (1.1)$$

$$2(2CaO \cdot SiO_2) + 4H_2O \rightarrow 3CaO \cdot 2SiO_2 \cdot 3H_2O + Ca(OH)_2 \quad (1.2)$$

$$3CaO \cdot Al_2O_3 + 3(CaSO_4 \cdot 2H_2O) + 26H_2O \rightarrow 3CaO \cdot Al_2O_3 \cdot 3CaSO_4 \cdot 32H_2O \quad (1.3)$$

$$4CaO \cdot Al_2O_3 \cdot Fe_2O_3 + 2Ca(OH)_2 + 2(CaSO_4 \cdot 2H_2O) + 18H_2O \rightarrow 6CaO \cdot Al_2O_3 \cdot Fe_2O_3 \cdot 2CaSO_4 \cdot 24H_2O \quad (1.4)$$

The two first reactions have the major contribution to the final strength properties of hardened cement. In the case of alite, the hydration reaction is fast compared to belite, so it is the most important constituent for strength development at early hydration stages. Both reactions with water form mainly calcium hydroxide (portlandite), and an amorphous gel phase named calcium silicate hydrate gel (C-S-H gel). This hydration process can be divided in five different steps of dissolution and precipitation to obtain the hydrated product. The different steps of cement hydration can be studied by isothermal calorimetry analysis (Figure I.3) where the heat flow is observed due to the exothermic character of the process. The description of the different stages in hydration is commented below.

- Stage 0: Dissolution of clinker grains in ionic species (Si^{4+}, Ca^{2+} and OH^-) by water solvent. This is a very fast and exothermic reaction. Moreover, dissolution is followed by a rapid deceleration. This deceleration is associated to a critical concentration of silicon ions in which calcium silicate hydrate gel (C-S-H) starts precipitating onto the surface of non-hydrated clinker.

- Stage I: This phase is known as induction step and is associated to a process where the heat generated is very little. This step does not mean that hydration stopped. The hydration is still running but it is not clear at all what is happening during this period. Garnet *et al* [8] proposed a hypothesis about the existence of a preliminary C-S-H layer around non-hydrated cement particles. Bellman *et al.* [9] confirmed by XPS measurements the appearance of a metastable phase created on alite surface. However, no direct evidences were measured by SEM to confirm this hypothesis.

- Stage II: Some authors suggested that C-S-H layer formed during induction could break under osmotic pressure and the nucleation of hydrated products could reach a critical size. In this step a large amount of calcium and hydroxyl ions precipitate as portlandite and this reactivate the dissolution of clinker grains. Precipitation of C-S-H gel restarts, and the heat generated increases again due to the formation of portlandite and the gel.

  This could promote the growing effect of nuclei accelerating the process. The higher is the number of nuclei in this step the faster the hydration reaction evolves. The end of this stage can be observed as a maximum in isothermal calorimetry curve and is considered the end of the setting period where the mix is not fluid anymore and has obtain some resistance to pressure. Moreover, this is the stage where calcium aluminates react with sulfate ions to form ettringite avoiding the flash setting and the early stiffening.

- Stage III: In the following step known as deceleration process, the cement hydration is controlled by the diffusion of Si^{4+} and Ca^{2+} through the porous space in C-S-H product around unreacted clinker grains. During this stage sulfate ions are consumed as well due to the reaction with ettringite phase transformed into monosulfoaluminates. This is observed as a shoulder in isothermal calorimetry curve.

- Stage IV: This is a very slow reaction step due to the bad diffusion of ionic species through the very dense C-S-H product. In this stage the reaction continues only through the inner wall of the C-S-H shell consuming the non-hydrated clinker inside. This step could keep going for years.

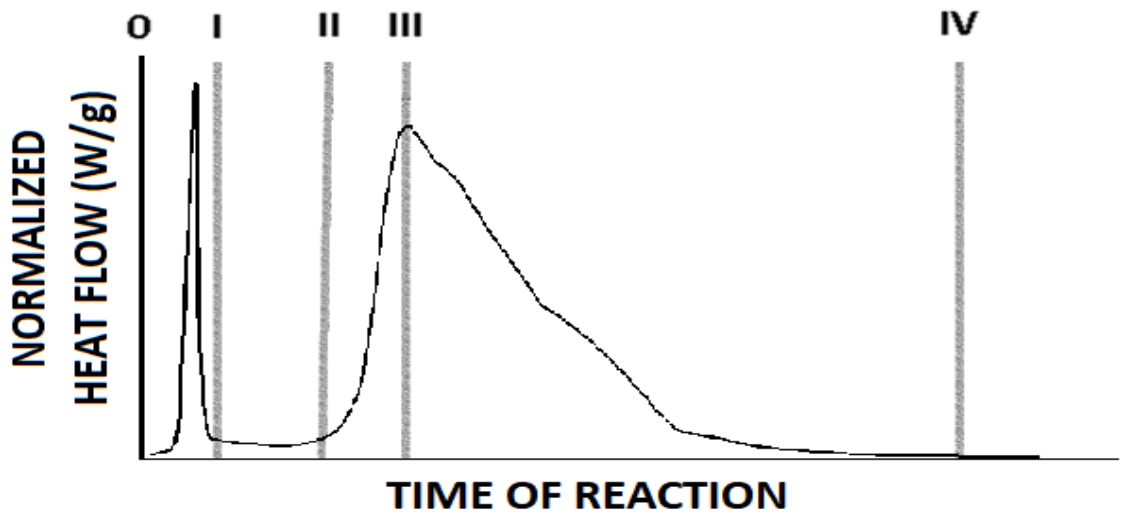

Figure I.3: Isothermal calorimetry curve with characteristic five steps of cement hydration.

I.1.5. Rheology in cement pastes.

Workability in cement and concrete means the facility with which fresh mixed cement and concrete is processed (pumped, mixed, casted, transported…). This property, is related to the quality of cement pastes, directly impacts the strength, appearance, and cost of operation for placement and finishing. Moreover, workability is part of the study of rheology that could be considered as the science that studies the deformation and flow of matter under the influence of stress. This chapter is going to introduce briefly some terms related to rheology that are important to understand the workability of cement.

The best way to describe the workability and rheological behavior of cement paste or any ceramic suspension, is analyzing the laminar shear flow model of the fluid. To do this, the material capable of being deformed, is introduced between two surfaces of area S. One of the surfaces is fixed and the other movable plane is subjected to an external shear force F. Dividing this force by the total area S, it can be calculated the shear stress τ or force per unit area that is responsible of a laminar shear flow as is shown in Figure I.4.

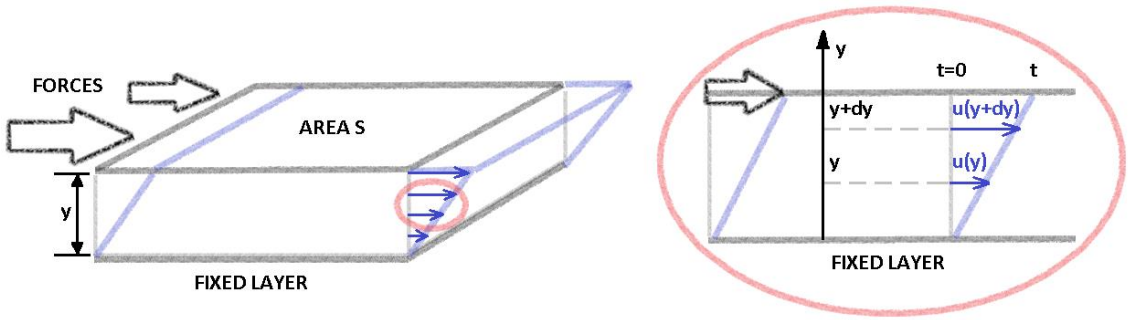

Figure I.4: Schematic illustration of laminar shear flow (left) and detailed image of displacement vectors at different layers of the fluid (right).

The deformation or shear strain is given by equation 2.1.

$$\text{Shear strain: } \gamma(y,t) = \frac{u(y+dy,t)-u(y,t)}{dy} = \frac{du(y,t)}{dy} \qquad (2.1)$$

$$\text{Shear rate: } \gamma' = \frac{d\gamma}{dt} \qquad (2.2)$$

Where u(y,t) and u(y+dy,t) are displacement vectors, at time t, in planes of material located at distances of y and y+dy from the fixed plane. From this shear strain can be calculated the rate of shear strain or "shear rate" that is the derivative of the shear deformation in respect to time (equation 2.2). Cement based materials are subjected to different shear rates depending on which process is applied on it (pumping, casting, mixing…). If a proper study of rheology of a cement paste or concrete mix wanted to be carried out, it is important to establish the range of shear rates in which cement pastes are going to be operated [10].

Then, the rheological behavior depends on an external stress and how the material responds deforming. The different rheological behaviors mentioned in this chapter are illustrated in Figure I.5. The simplest rheological behavior is known as Newtonian. In this case the deformation response to an external stress follows a linear tendency. The value obtained from the shear stress divided by the shear rate is a constant known as apparent viscosity η.

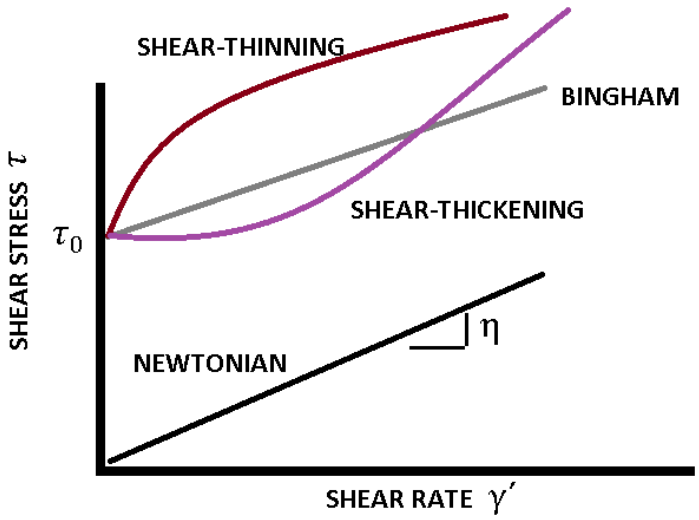

Figure I.5: Illustration of different rheological behaviors for viscous fluids.

Over the years, more realistic models have been developed to describe different viscous fluids such as ceramic suspensions that do not behave as Newtonian ones. Bingham model for example (equation 3), describes a fluid whose viscosity is constant as well, but material does not start to flow until stress applied on it is high enough. This minimum value of stress that is capable to make a material flow is named yield stress (τ_0). As it will be discussed in this chapter, concrete and cement pastes present a yield stress that is the consequence of the attractive interparticle forces between cement particles.

$$\tau = \tau_0 + \eta \cdot \gamma' \qquad (3)$$

More complex models describe materials with a nonlinear relation between stress and shear rate. This means that viscosity is dependent to the shear rate and is not constant as it was described by Newtonian or Bingham type fluids. If apparent viscosity decreases with shear rate a "Shear thinning" behavior is considered. On the other hand, "Shear thickening" fluid presents an increase of apparent viscosity with shear rate (equation 4).

$$\tau = \tau_0 + \eta \cdot (\gamma')^n \quad (4)$$

If n>1 then fluid presents a shear thickening behavior.

If n<1 then fluid presents a shear thinning behavior.

Rheological properties of concrete are affected by cement in its composition, so studying cement matrix properties is a good way to extrapolate results for concrete mixes. Cement paste exhibits a visco-elasto-plastic behavior. This means that below a yield stress value cement does not flow (elastic behavior). Furthermore, when yield stress is overpassed, the material flows and viscosity is dependent to shear rate or the rate of shear strain. In this case cement pastes follow a shear-thinning tendency where apparent viscosity is reduced with shear rate. However, in the most part of the studies the rheological behavior of cement pastes has been studied as a Bingham fluid, with a constant value of viscosity, to simplify the analysis [11].

I.2. Cement admixtures.

Admixtures are considered substances that can be added in small quantities to cement and concrete before or during their mixing with water. They are usually employed in construction to modify the mixing, transporting, placing, or curing properties of mixes during concrete operations.

There are several examples of admixtures prepared to enhance the performance of cement and concrete. These materials can be divided in groups depending on their effect on mixtures. The most used admixtures in construction industry are the following:

- Plasticizers or water reducers,
- Retarder admixtures,
- Accelerating admixtures.

I.2.1. Plasticizers and superplasticizers.

Water and more important its content in cement pastes, expressed as the water over cement weight ratio (w/c) has a significant effect in properties of fresh and hardened cement mixes. Water behaves as a good solvent capable to create a high concentrated medium of ion species from clinker grains. Furthermore, it is responsible of generating cohesive forces between cement particles that significantly reduce the apparition of bleeding or segregation during the initial wetting of cement powder. This effect is crucial to give to the paste its workability properties. Adjusting the water content in cement pastes is the simplest way to tune its rheological properties.

Moreover, water acts as a reactant in hydration and setting of cement and its relative content in respect to cement powder is crucial to guarantee a good performance and durability of concrete elements. A very low content of water makes that non-reacted water cannot reach non-hydrated material. The lower w/c ratio the harder is for water to penetrate the non-hydrated particles. This stops the hydration and setting of cement and gives low mechanical properties.

On the other hand, a cement pastes with w/c ratio higher than 0.42 could hydrate completely cement particles but the excess of non-reacted water remains in the material and could cause a negative effect in the final mechanical properties of hardened material. This is due to water evaporation that generates undesired porosity reducing the compressive strength of the material. So, a good adjustment of water in cement formulation is not trivial and it requires a special attention.

During the last decades have been developed different polymeric solutions that allow working with lower water contents without losing mechanical or rheological properties. Plasticizers and superplasticizers are considered as polymeric dispersant that allows the reduction of water in formulations maintaining the right workability. Explained in rheological terms, they can maintain yield stress increasing solid contents or reducing water in the mixture. Moreover, they can be used to eliminate the excess of non-reacted water (capillary water) in hardened cement increasing its durability [54,63].

Different types of plasticizers and superplasticizers can be found in the construction field. The most employed are the following:

- Lignosulfonates (LS) obtained as byproducts in the paper industry. Capable of reducing the required water in cement formulation, they are used since 1930s. However, they are found to retard the setting time. Even if they are affordable and give good rheological properties, they are not recommended for cold weather applications. The chemical structure is shown in Figure I.6.

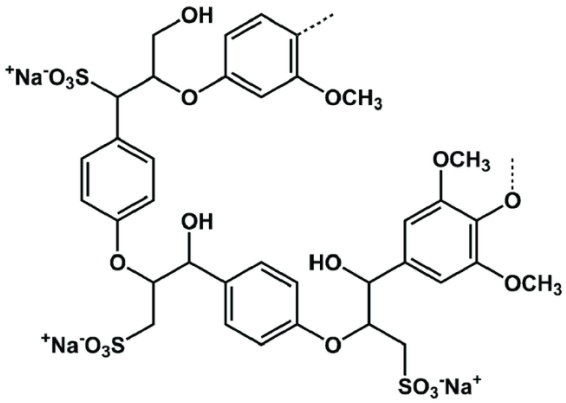

Figure I.6: Structure of lignosulfonate plasticizer polymer.

- Polynaphthalene sulfonates condensates (PNS). These polymers are the result of polycondensation of naphthalene monomers with a sulfonate group attached (Figure I.7). They have higher dispersing properties than LS, however, they are not compatible with all types of cement. They are very sensitive to the content of gypsum in cement because gypsum can reduce the adsorption of these polymers onto cement particles.

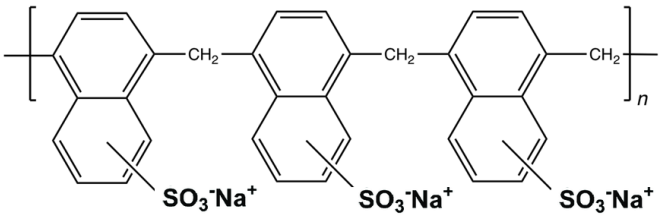

Figure I.7: Structure of polynaphthalene sulfonate plasticizer polymer.

- Polymelamine sulfonates (PMS) obtained as product from condensation of melamine with formaldehyde and Sulfite (Figure I.8). They are preferably used in precast industry because they do not retard the setting as PNS does.

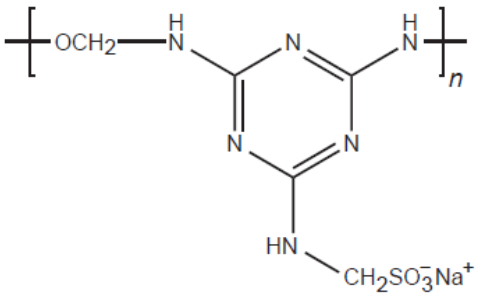

Figure I.8: Structure of polymelamine sulfonates polymer.

- Polyethylene oxide phosphonate. The phosphonate group in its structure is capable to be adsorbed easily on cement particles compared to sulphonate groups. They reduce considerably the viscosity due to steric hindrance driven by the polyethylene oxide chain (Figure I.9). However, they significantly retard the hydration of alite (C_3S). They are marginally used for hot weather applications.

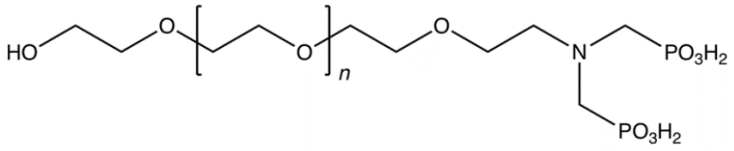

Figure I.9: Structure of polyethylene oxide phosphonate plasticizer molecule.

- Polycarboxylic ethers (PCE) are hyperbranched polymers that present an anionic backbone composed by carboxylic groups and a lot of nonionic polyethylene glycol polymer chains. Its comb shape (Figure I.10) reduces drastically the required water content in the mix formulation maintaining a good rheological properties and workability. The use of this kind of superplasticizers have become crucial to the production of self-consolidating concretes with very low yield stress values.

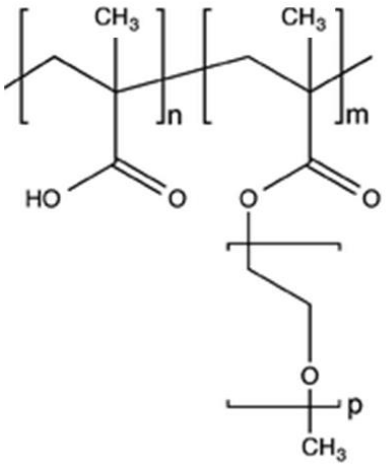

Figure I.10: Structure of poly carboxylic ether superplasticizer polymer.

In all cases these polymeric molecules are adsorbed onto cement particles reducing or eliminating the attractive interparticle forces and reducing the yield stress and viscosity. In one hand, PNS, PMS and LS behave as strong polyelectrolytes with a strong charge

located at the exterior layer when they are adsorbed onto the particles. The charge is located far from the particle surface and this increases repulsive forces.

This effect is based on a high polymer concentration on surface which generates an osmotic pressure that introduces water from the bulk of the solution separating particles from each other. It is also known as electrosteric repulsion effect. The charge contribution of these kinds of polymers can be observed as a negative increase in z-potential measurements.

On the other hand, PCE polymers prevent contact between particles through a steric hindrance effect. The most part of the charge in this polymer is in carboxylic groups near to particle surface. Their effect is more related to the physical separation due to the large volume of the lateral polymeric chains in its structure. This separation by steric hindrance reduces significantly attractive interactions of Van der Waals [61].

I.2.2. Retarder admixtures.

These admixtures slow down the rate of hydration for cement. They are employed for high temperature applications to avoid a quick set of cement mixes that could create imperfections in the material. There are several examples or cement retarders like gypsum, starch, cellulose, or even common sugar. The complexation of calcium ions or the adsorption onto non-hydrated particles, portlandite precipitates or C-S-H products could extend the induction time in cement hydration and retarding the setting and hardening.

I.2.3. Conventional accelerating admixtures.

Substances as calcium chloride or calcium formate are cheap additives that were found to accelerate the cement hydration and thus reduce the induction period. Measurements of soft X-ray transmission microscopy were carried out by Juenger *et al.* [12] to study the effect of adding $CaCl_2$ in C-S-H gel. They proposed the formation of a more permeable structure of C-S-H gel taking place due to the presence of more calcium ions in the medium. Plusquellec and Nonat [13] confirmed these results and proved that increasing calcium concentration drives a modification on surface properties and permeability of hydration product. This higher permeability is responsible of a faster

growth for C-S-H gel. Recent studies proposed the supersaturation of calcium silicate hydrate gel induced by the increased concentration of calcium ions in the medium. This could influence nucleation and growth of hydration product [89].

I.2.4. Other accelerating admixtures. Pozzolanic ashes or natural pozzolans.

Long time ago it was proven that some natural materials harden under water in presence of lime. These mortars were first produced with materials extracted by Romans from the city of Pozzuoli near to Naples and Mount Vesuvius. The earth in this area, rich in volcanic ashes (pozzolana or pozzolanic ashes), gave the name of pozzolans to a wide family of materials like obsidian or diatomaceous earth, capable to react with lime [14].

Natural pozzolans react with lime because they content a percentage of vitreous silica (or mixes of amorphous silica and alumina) in its composition that came from the rapid cooling down of volcanic ashes. This amorphous material is the origin of its high reactivity. The presence of unsaturated ions and its higher specific surface make them more reactive than other more ordered structures. At the end the reaction between pozzolans and lime gives a secondary C-S-H product that reduces cavities in cement and increases its durability. Moreover, their reactivity is so high that the average time of hydration for conventional Portland cement is reduced.

It is important to remark that the finer these admixtures are, the higher reactivity they can achieve. For that reason, several studies have tested nanosilica particles as accelerating admixtures as well [15]. These particles are also capable to react with calcium dissolved in cement suspension and form hydrated products.

However, reducing too much their size involves a huge reduction in workability of its cement pastes. This makes necessary a modification in cement formulations increasing the amount of required water or using other admixtures capable to adjust the rheology (superplasticizers) [16].

I.2.5. Other accelerating admixtures. Calcium silicate hydrates. Seeding effect.

Pozzolans and other nano structured materials can accelerate the hydration of cement through the reaction of these materials with calcium ions dissolved in suspension. However, there are other particles that increase the deposition of ion species around the interface between liquid medium and particle surfaces (heterogeneous nucleation). Thus, particles of calcium silicate hydrates accelerate the growth of hydrated product without reacting directly. This effect is known as seeding effect [17].

Figure I.11 illustrates the effect of adding calcium silicate hydrate particles as nucleation points in cement suspension. The addition of these particles increases the available surface where ion species can deposit and rearrange to precipitate as C-S-H gel. Increasing this surface means that there are more reactive points in solution and the distance between the bulk solution and the deposition surface is reduced as well. Then the time needed for these species to reach the saturation state and precipitate is reduced.

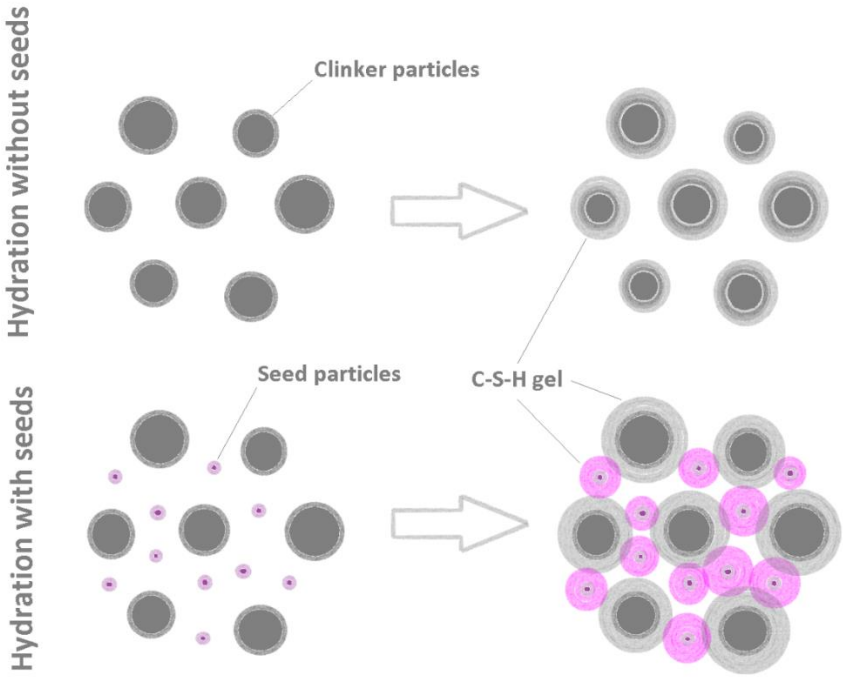

Figure I.11: Illustration of the effect of seed particles in cement hydration.

Thomas *et al.* [18] studied the addition of amorphous C-S-H particles to C_3S. In that work it was observed that these particles increased the rate of hydration of C_3S. On the other hand, they studied an increase of precipitation of hydrates in the capillary pores. They

could also confirm this through the observation of SEM images taken for hydrated pastes with the additions. So, addition of seed particles drives to the filling of the space between particles with hydration products. This increases the compressive strength values of cement pastes in early ages and improves the durability of hardened mixes [19].

Previous works have talked about the use of crystalline phases of calcium silicate hydrates as accelerator agents in cement hydration [90]. Then some crystalline calcium silicate hydrate phases such as xonotlite and tobermorite has been shown to act as seeds as well [20].

I.2.5.1. Xonotlite.

Xonotlite with the chemical formula $Ca_6Si_6O_{17}(OH)_2$ is a natural mineral discovered for the first time in Tetela de Xonotla, Mexico, in 1886. This crystalline phase of calcium silicate hydrate is formed under hydrothermal conditions in high alkaline media. Nowadays, there are different sites where this mineral has been located like Veneto in Italy, Northern Cape in South Africa, or Boulder Shire in Australia. It was also localized in North of America, Japan and New Zealand mixed with other phases like wollastonite ($CaSiO_3$) or tobermorite ($Ca_5Si_6O_{16}(OH)_2 \cdot 5H_2O$). Sometimes it can present traces of Mg, Na, Fe and Mn.

This material has been widely used as insulating material for high temperature applications in industry [21]. Furthermore, there are some applications for this material as flame retardant, dyeing agent in paint industry, or drip suppressant. Some studies have even explored its use as reinforcing material in cement for construction applications [22].

Xonotlite is considered as an inosilicate mineral composed by a double silicate chain. Xonotlite structure was described as a sandwich like arrangement with a double silicate chain alternated by calcium oxide layer. It presents a monoclinic crystalline system described by L. Black [23] for synthetic samples prepared by hydrothermal synthesis maintaining a Ca/Si molar ratio equals to 1.0. Moreover, xonotlite presents different polytypes depending on how calcium octahedral is attached to the silicate chain respect to the position of the consecutive double silicate chains [24].

Commonly in all xonotlite polytypes, there is a polyhedral chain of calcium in octahedral coordination per two calcium chains in sevenfold coordination with oxygen. Octahedral and sevenfold coordinated calcium ions are sharing an edge to form chains along the b axis (see Figure I.12). These chains are bound sharing an edge as well and forming a layer of calcium oxide parallel to the plane (001).

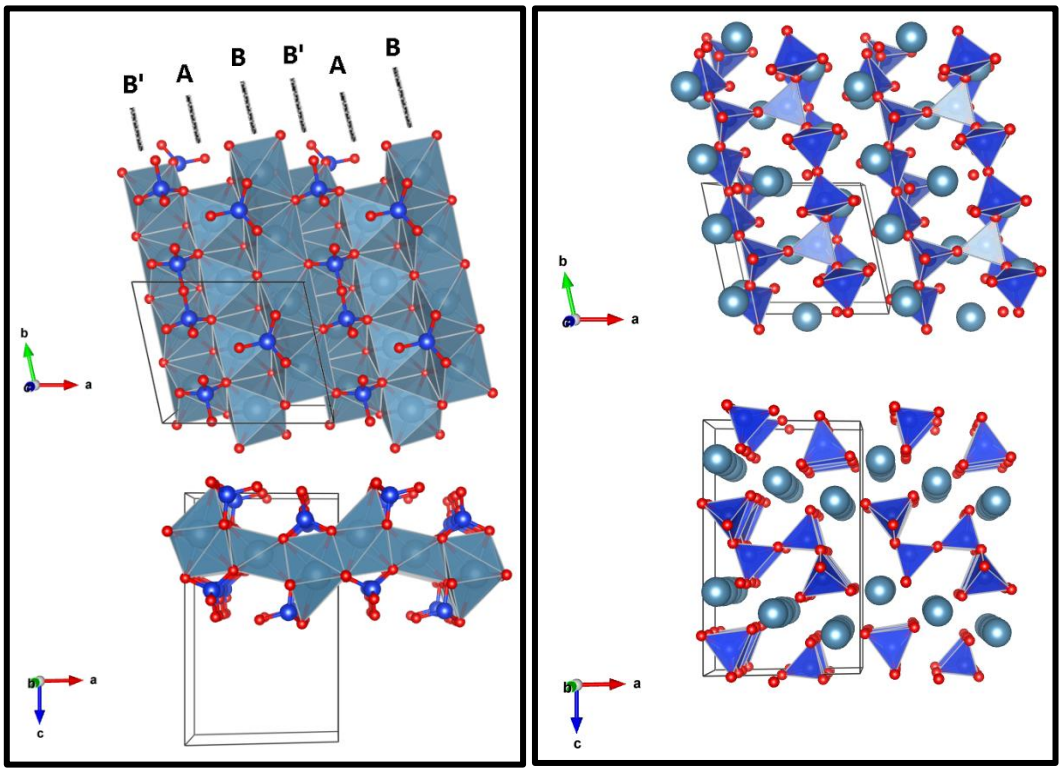

Figure I.12: Illustration of crystalline structure of xonotlite. Detailed arrangement of calcium oxide layers (Left) and silicate chains (right). Note: small blue spheres are silicon atoms, big blue spheres are calcium atoms and red spheres are sharing oxygen atoms. A is octahedral coordinated chain of calcium oxide, B and B' are sevenfold coordinated chains of calcium oxide,

Each silicate chain in xonotlite has a periodicity of three silicate tetrahedra (SiO_4^{4-}). Two of them are paired and they alternate with other third tetrahedron bound to the single silicate tetrahedron from the second silicate chain. This conformation is named "Dreier doppelkette". Moreover, these double silicate chains share oxygen atoms from calcium octahedra to complete the xonotlite structure.

I.2.5.2. Tobermorite.

Found for the first time in Tobermory, Scottland, in 1880, tobermorite is a rare mineral that crystallizes in hyper-alkaline hydrothermal conditions [25]. It is usually found mixed with zeolites, calcite or portlandite in basaltic rocks and skarn resulted from metasomatism (hydrothermal recrystallization of different minerals in nature).

Tobermorite can be classified in three main structures depending on the hydration degree of its structure. The amount of water determines the distance between one calcium oxide layer and the following layer next to it. This distance is associated to the crystallographic plane (002) also known as basal distance. Following this criterion, in nature there are three different phases associated to tobermorite: 14Å-tobermorite, 11Å-tobermorite and 9Å-tobermorite where 14Å, 11Å and 9Å are the basal distances of the different polymorphs.

The polymorphs with lower basal distance can be obtained from the dehydration of other polymorphs. For example, 11Å-tobermorite can be obtained from dehydration of 14Å-tobermorite under 80-100°C. In the case of 9Å-tobermorite, this phase is obtained from dehydration at 300°C of 11Å-tobermorite. In this work, organic modified particles of 11Å-tobermorite where synthesized and characterized. This section will briefly talk about the structure of 11Å-tobermorite and its transformation into 9Å-tobermorite.

Merlino *et al.* [27] described the structure of 11Å-tobermorite samples obtained from Wessel South Africa. According to that work, 11Å-tobermorite is composed of layers of sevenfold coordinated calcium polyhedral parallel to the direction (001) and infinite silicate tetrahedral chains of wollastonite-type that run along b axis. Silicate chains form “Dreier-doppel kette” silicate chains like in xonotlite, but the way these silicate tetrahedra are oriented differently and the space generated between calcium oxide layers is larger (Figure I.13).

There are still some difficulties to describe with precision the crystallographic structure of 11Å-tobermorite. First, this is due to the poor crystallinity of samples found in nature, and then, the existence of two similar polymorphs of 11Å-tobermorite. These two polymorphs were named as normal and anomalous, and the only way to distinguish

them is by their thermal behavior at 300°C. Normal 11Å-tobermorite dehydrates to form 9Å-tobermorite and anomalous polymorph remains without dehydration.

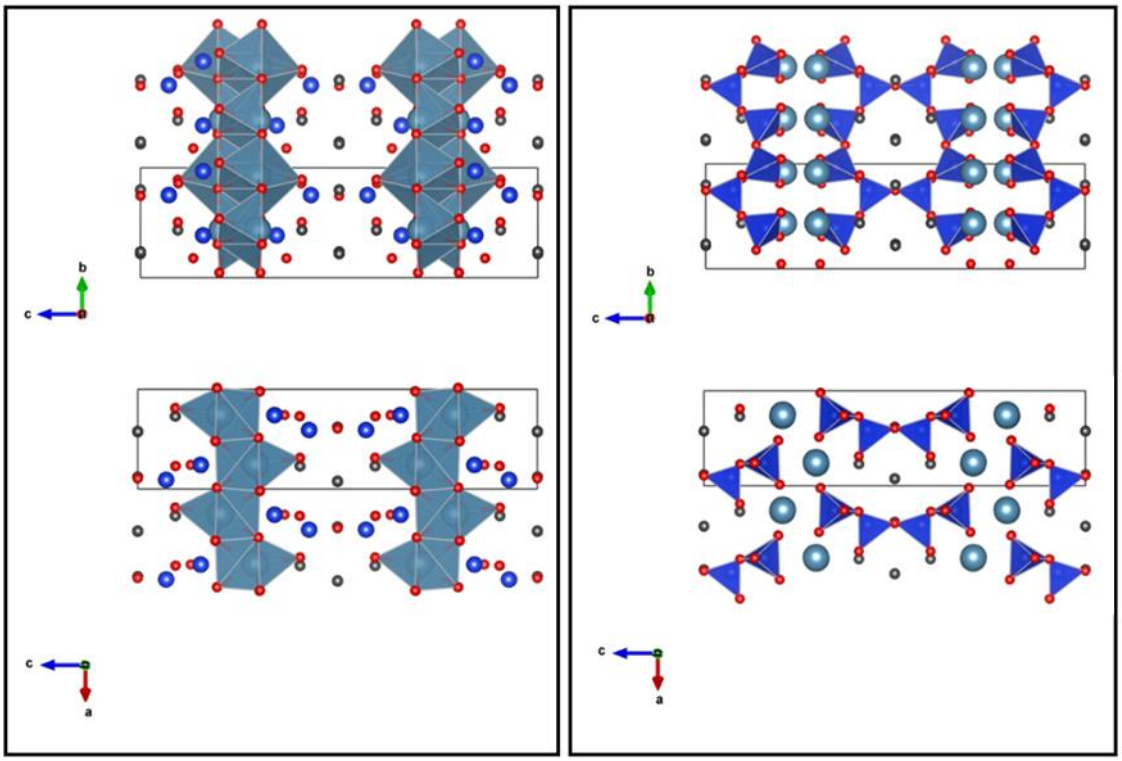

Figure I.13: Crystalline structure of 11 Å-tobermorite. Detailed illustration of calcium oxide layers arrangement (left) and silicate chains arrangement (right). Note: small blue spheres are silicon atoms, big blue spheres are calcium atoms and red spheres are sharing oxygen atoms.

The dehydration mechanism of 11Å-tobermorite to 9Å-tobermorite is not well described yet. However, Merlino *et al.* proposed for anomalous polymorph the existence of calcium atoms located in cavities between calcium oxide layers and silicate chains, that are strongly bonded to water molecules and could be the responsible of this thermal stability [28, 29]. It was determined that 4 molecules of 5 in 11Å-tobermorite disappeared during its dehydration at 300°C, leaving silanol groups in the structure of 9Å-tobermorite. Moreover, double chains collapse and become single chains. Calcium layers remains parallel to direction (001) but channels created between calcium layers and silicate chains are reduced in respect to 11Å-tobermorite.

Tobermorite structure allows the partial substitution of silicon by aluminum atoms. Some authors established the maximum amount of aluminum attached to the silicate chain in 15% (expressed as Al/(Si+Al) molar ratio) [25, 20, 31]. Above this molar percentage, hydrogarnet appears as secondary phase product [32].

Some researches tried to find in which position the aluminum (or aluminate tetrahedra) substituted silicon atoms in tobermorite [33, 34]. According to these authors, substitutions of aluminum in non-paired positions along the silicate chain are more favorable. Moreover, there are two possible substitutions for silicon by aluminum. Aluminum in branching position if it is bound to the consecutive silicate chain (branching also named non bridging) or if it is not bound to the consecutive chain due to the presence of a vacancy in that chain (bridging). Both situations are illustrated in Figure I.14.

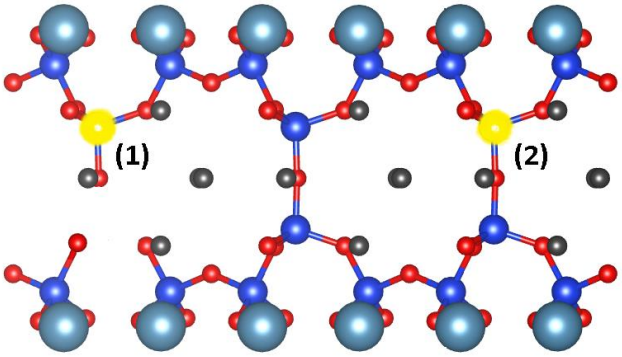

Figure I.14: Illustration of aluminum substitutions in bridging positions (1) and branching positions (2) along silicate chain in aluminum substituted tobermorite.

I.2.6. Mineral admixtures and its effect in rheology of fresh cement pastes.

It is important to describe the forces that act in the system and define the fluidity of a solid suspension like cement paste for understanding the effect of admixtures in cement workability. First, cement particles or any ceramic suspension in water experiments a hydrodynamic force that arises from fluid movement itself. Then it can be described a Brownian motion that is driven by thermal motion forces and inertial forces that could be significant at high shear rates. Gravitational forces, on the other hand, are responsible of bleeding and segregation of solid and water phases in mixes.

Finally, the different attraction and repulsion interactions between cement particles can modify the fluidity of the paste significantly. Particles in water suspensions can experiment fluctuations of polarization at particle surface that induce a response in other particles close to the first ones. At the end, this effect comes from solid surfaces in water charged due to the dissociation of surface groups and/or specific adsorption of ion species present in solution. These interactions tend to be attractive and are named dispersion forces or Vander Waals forces.

Goüy and Chapman [57] proposed a model to describe the distribution of ions in a charged interface. These "double layer" model interpreted two zones: Stern or inner layer composed of very condensed charges and diffuse or outer layer where charges are more dispersed. Z-potential technique is capable to measure approximately the surface charge associated to the potential in diffuse layer [58].

In this model when two charged surfaces approach (Figure I.15), the electrical double layers overlap generating an excess of ions in that area. If the concentration of ions is low enough far from these two charged particles an osmotic pressure is generated, and this makes that ion species dilute with water from the bulk of the liquid. This is the origin of repulsive forces or electrostatic repulsions responsible to maintain stability in colloidal suspensions.

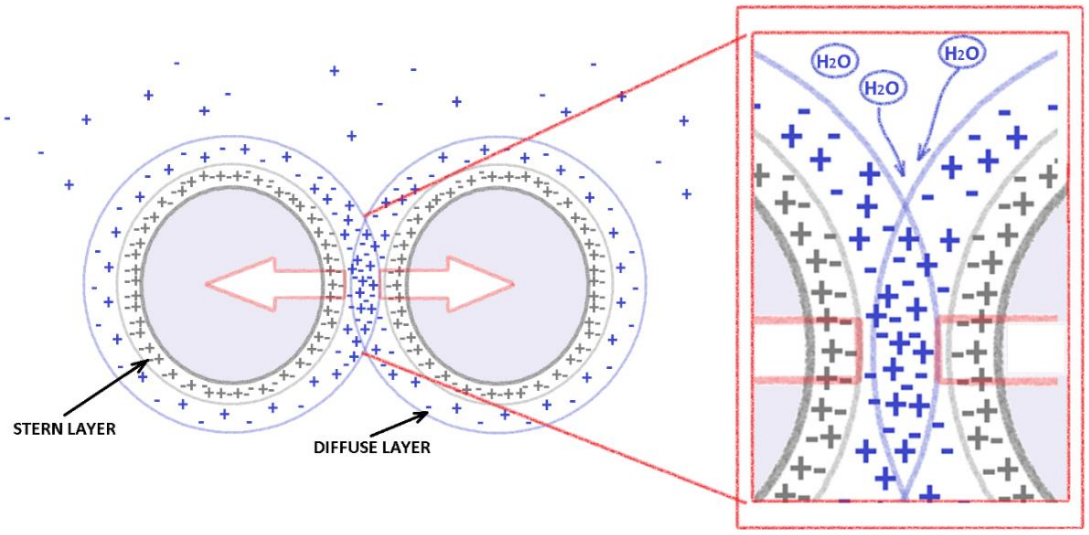

Figure I.15: Illustration of electrostatic repulsion between two particles in Goüy and Champman double layer model.

However, in the case of cement there is a high concentration of ion species. This high concentration means a high ionic strength of this medium that reduces the Debye length, that is considered the thickness of the diffuse layer in which repulsive potential is significant. Then a high ionic strength reduces the range electrostatic repulsion and makes Van der Waals interactions predominant.

Derjaguin, Verwey, Landau and Overbeck developed a theory, DLVO theory, that explains the stability of aqueous suspensions as a balance of forces expressed as electrostatic potentials. They considered Van der Waals attractive forces and electrostatic repulsive forces as additive and independent terms. This theory considers three situations depending on the ionic strength or ions concentration in solution. These situations are shown in Figure I.16.

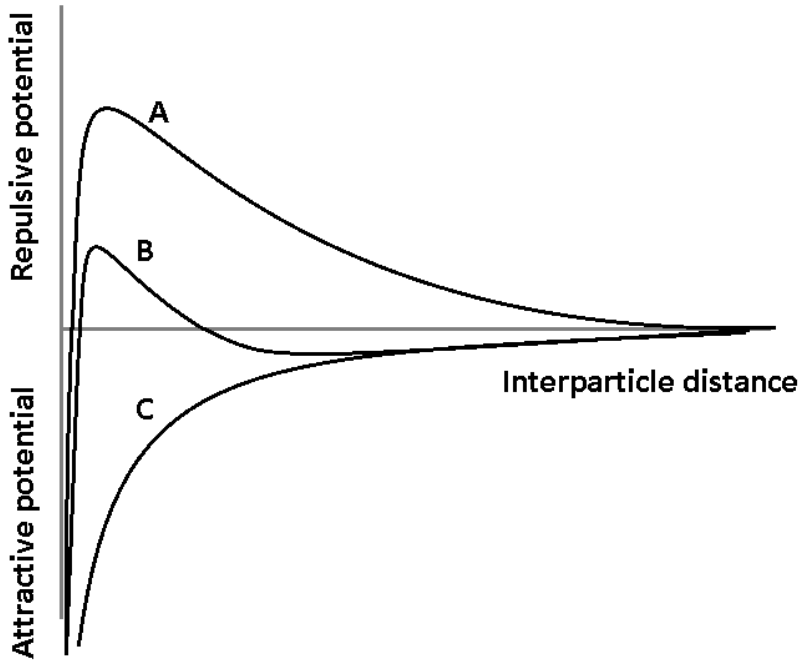

Figure I.16: Illustration of different interparticle interactions depending on ionic strength of the suspension medium. A) Low ionic strength and high energy barrier. Repulsive interactions domain. B) Moderate ionic strength and low energy barrier. At short distances Van der Waals interactions are significant. C) Very high ionic strength. Attraction forces domain.

First, at low ionic strength, electrostatic repulsions are large and are more significant than Van der Waals forces. This means that it exists an energetical barrier capable to avoid aggregation between particles. When the ionic strength is increased, the

electrostatic repulsion effect is decreased, and Van der Waals attraction becomes significant. This is interpreted in DLVO theory as a reduction of the energy barrier that is necessary to avoid aggregation. On the other hand, at high ionic strength, the energy barrier disappears, and particles get closer and aggregate at the end.

Rheological properties, like yield stress, of cement pastes has a huge dependency on this balance between attractive and repulsive interparticle forces. In the case that attractive forces dominate over repulsive forces, particles tend to aggregate causing an important increase of yield stress and viscosity. If the repulsive interactions dominate over attractive forces, then the dispersion becomes more stable and increases its fluidity.

It has been demonstrated in previous studies that addition of mineral additives (fly ash, silica fume…) have an effect in rheological behavior of cement pastes [58]. Variables like particle size distribution, specific gravity, morphology or the interparticle forces can modify rheology in different ways.

Rheology in ceramic suspensions is strongly dependent to the volume of particles in the system. Krieger and Dougherty [60] proposed a model in 1959 that correlated this solid concentration and apparent viscosity of the suspension (equation 5). Following that expression, the viscosity of the system increases as the volume fraction of particles in suspension increases.

$$\mu(\varphi) = \mu_0(1 - \frac{\varphi}{\varphi_m})^{-\eta\varphi_m} \qquad (5)$$

Where,

μ_0 is the apparent viscosity of a fluid,

φ and φ_m are solid concentrations in volume (or volume fraction) of solid and maximum concentration allowed, respectively,

η is the intrinsic viscosity (function of shape of particles in suspension).

Flatt and Bowen [61] found a correlation between the yield stress and volume fraction as well. As it can be observed from equation 6 the higher is the solid concentration (expressed as volume fraction), the higher is the energy needed to break the particles network and make the suspension flow (higher yield stress).

$$\tau_0 = m \cdot \frac{A_0 \cdot a^*}{d^2 \cdot h^2} \cdot \frac{\varphi^2(\varphi - \varphi_{PERC})}{\varphi_m(\varphi_m - \varphi)} \qquad (6)$$

Where:

A_0 is the Hamaker constant (that indicates how strong are Vander Waals interactions),

a* is the curvature of contact area between particles,

d is average diameter of particles,

h is interparticles distance,

φ is the fraction volume of solids,

φ_m is the fraction volume at maximum compacity,

$\varphi_{PERC}$is the percolation threshold (minimal volume fraction to achieve a connected grid of particle clusters in suspension).

It considered several parameters related to compacity (volume fraction of solids in suspension ϕ), particles size distribution (average particle diameter d, curvature of particle surface a*) and interparticle distance h. This last parameter correlates the effect of PCE superplasticizers and the yield stress reduction due to the decrease of attractive forces of Van der Waals.

This model also shows that the smaller is the average size of the particles, the higher yield stress is obtained. Then, the addition of small particles or even nanometric sized particles could have a very negative effect on the cement paste rheology. This effect has been observed in previous studies about the use of nanoadditions in cement and concrete [62, 63].

I.3. Synthesis of calcium silicate hydrate compounds.

As it was introduced in pozzolans section, amorphous or vitreous materials based on silicon are very reactive to calcium ions in presence of water. They react very fast even at ambient conditions and a precipitation reaction takes place to form a C-S-H gel. However, there are other precipitation routes to obtain amorphous C-S-H. For example, the use of silicate salts and calcium salts precipitated in water under ambient conditions is reported to obtain C-S-H gels [35].

On the other hand, the polycondensation of metal alkoxides hydrolyzed with water (sol-gel route). TEOS (tetraethoxysilane) can be used as silicon precursor and then calcium ethylates are added to intercalate calcium ions in the aqueous medium. The properties of the product obtained are tuned by pH modifications. A gel product is obtained at pH below 7 but a colloidal sol of these materials can be obtained using a basic pH [36].

However, other routes are employed if the crystallinity or morphology of seed additions are needed to be controlled. These techniques are based on solubilization and recrystallization of SiO_2 and CaO species in water under high temperature and pressure conditions (hydrothermal synthesis). The main goal of using these alternative routes is obtaining reduced size particles with controlled crystallinity and morphology. Precipitation and sol-gel routes have proven the effect of surfactants and ultrasound treatments [37, 38] to modify the morphology and size of C-S-H products, but these strategies are less cost effective than the use of hydrothermal synthesis techniques.

I.3.1. Synthesis of xonotlite and tobermorite by hydrothermal routes.

Hydrothermal synthesis was firstly thought to reproduce the extreme pressure and temperature conditions that can be found in natural geothermal reactions [39]. This technology can be used to synthesize materials that are not possible to obtain at milder conditions or it would take too much time.

Hydrothermal process is only one of the different solvothermal routes used for the obtention of inorganic crystals. There are different organic solvents employed for synthesis of particles in solvothermal conditions (methanol, ethanol, or toluene for example are widely used). However, hydrothermal route that uses water as reaction medium has become the most sustainable and secure option in respect to the other organic solvents employed. Water is non-flammable, non-toxic, abundant and easy to manage l

The first application for hydrothermal route was the obtention of large single quartz materials [40]. After this discovery, hydrothermal route was used to obtain many different minerals with high purity in a short period of time. Due to this reason,

hydrothermal route has been studied for the synthesis of crystalline phases in the ternary system $CaO\text{-}SiO_2\text{-}H_2O$.

The synthesis of crystalline phases of calcium silicate hydrates takes place in a sealed autoclave. After heating the vessel, a saturated steam atmosphere appears, and high temperature and pressure conditions allows the precipitation of crystalline phases.

The $CaO - SiO_2 – H_2O$ system have tens of different phases that are very difficult to obtain with high purity and crystallinity. Temperature conditions, concentration of precursor solutions and the reaction time can be tuned to modify size, morphology, and crystallinity of the final product. Hong *et al.* [41] developed a phase diagram (Figure I.17) for crystalline phases of calcium silicate hydrates prepared by hydrothermal synthesis. This simplified diagram represents the stability of different crystalline phases at different temperatures and Ca/Si molar ratios.

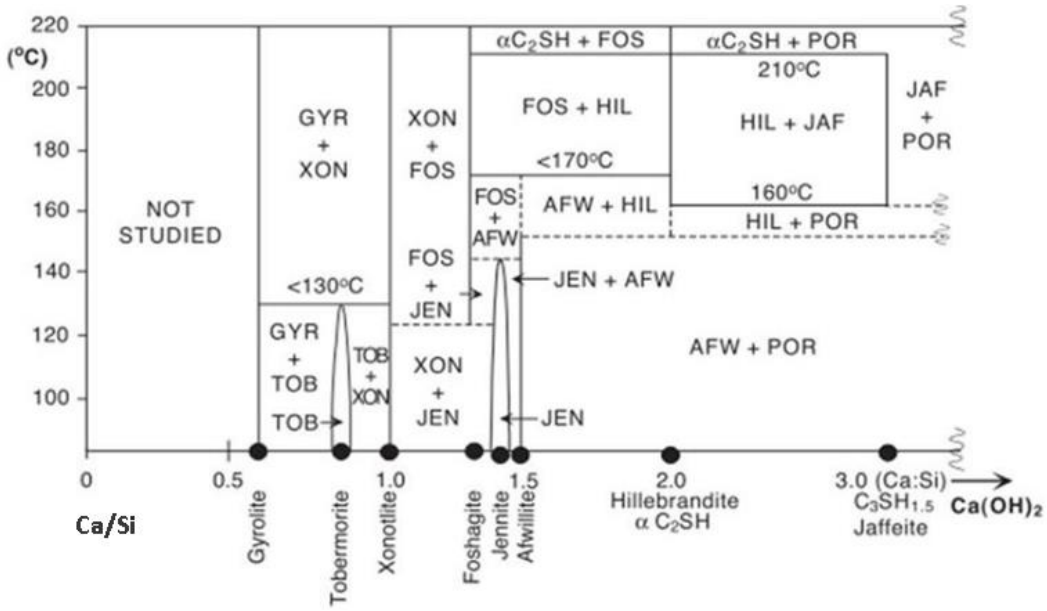

Figure I.17: Phase diagram of calcium silicate hydrates depending on Ca/Si molar ratio and temperature conditions during its synthesis. Figure obtained from experimental results in laboratory by S.Y. Hong [41].

According to the diagram developed by Hong, xonotlite is a very stable phase synthesized maintaining a Ca/Si molar ratio of 1.0. In the case of tobermorite pure tobermorite can be obtained with a molar ratio limited to 0.83 and a maximum

temperature of 130°C. Above this limit tobermorite would recrystallize and form mixtures with xonotlite.

There are a lot of publications about the thermal stability of tobermorite and its transformation into xonotlite [42, 43]. Heller and Taylor [44] found that the minimum temperature to obtain pure xonotlite from SiO_2 and CaO precursors under hydrothermal conditions is 160°C. Moreover, according to their results they considered that the minimum Ca/Si molar ratio should be 1.0.

Flint *et al.* [45] reported for the first time the synthesis of 11Å-tobermorite with a Ca/(Si+Al) molar ratio of 0.8 at 150°C. Harker et al. [46] estimated the stability of tobermorite around 170°C and Speaksman et al. observed that above 140°C xonotlite starts forming from tobermorite using a Ca/Si molar ratio near to 1.0 [47].

In 1957 Kalousek *et al.* [32] demonstrated the stabilization of 11Å-tobermorite by the addition of aluminum. In this study it was used 170°C, 0.45% of aluminum and a Ca/(Si+Al) ratio of 1.0. On the other hand, Mitsuda *et al.* [31] carried out similar experiments where two different Ca/(Si+Al) ratios were studied, 1.0 and 0.8. For each ratio, the content of aluminum was varied from 0% to 15%. This studied demonstrated that 0.8 ratio is more favorable to produce pure tobermorite and higher temperature was confirmed to promote a faster crystallization.

I.3.2. Supercritical Water route (SCW).

Water confined in a closed system with a given volume is always found in a liquid-vapor equilibrium defined by pressure and temperature conditions. As the temperature and pressure of water is increased high enough (374°C of temperature and 22.1 MPa of pressure), the liquid and vapor phases in equilibrium coalesce into a single phase. As it can be seen in pressure-volume diagram of water (figure I.18) there is a temperature where the liquid and vapor equilibrium disappear. Above this point, named the critical point, water appears in single phase that it is defined as a supercritical fluid.

Furthermore, the properties of water in this phase are very different to the properties of liquid or gas phases. In fact, supercritical water shows a lower density than normal water (about 1/3 of density for water below supercritical point) and lower viscosity

(about 1 or 2 orders of magnitude compared to normal water). Moreover, the dielectric constant is lower as well and the ion product is decreased between 10- and 100-times respect to subcritical water. In one hand, the decrease of density and viscosity causes an increase of diffusion coefficient related to the facility of chemical species to diffuse through the medium. Then the change in ion product causes changes in solubility. In supercritical conditions organic compounds and gases become soluble in water medium and inorganic compounds become non-soluble.

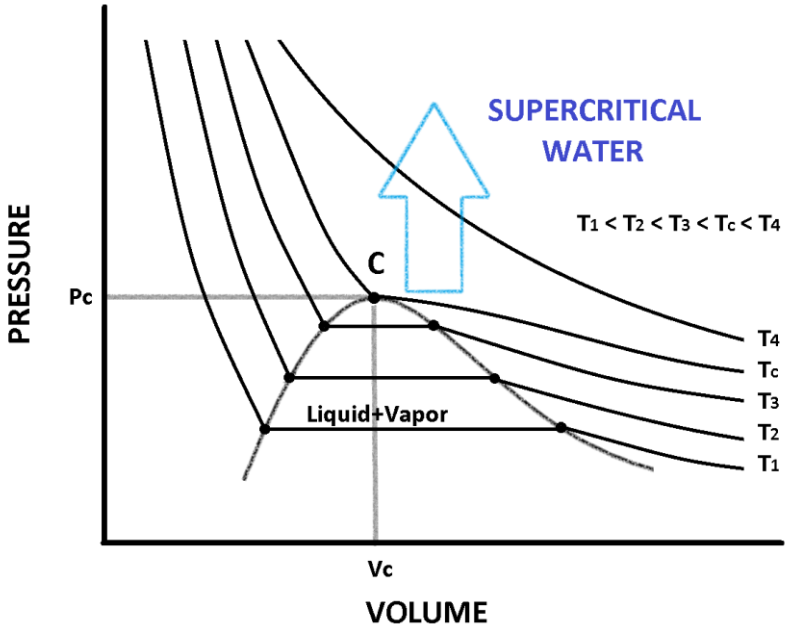

Figure I.18: Pressure- Volume diagram of water. Note: C points indicates the critical point of water.

The synthesis of metal oxides nanoparticles through supercritical water routes is well reported in literature [48, 49, 50]. This kind of hydrothermal synthesis is based on the unique properties for water above the critical point.

As it was mentioned, around the critical point water experiments large variations in density and viscosity, but also in dielectric constant (ε) and ion product (K_W) of water. Dielectric constant is very important in the determination of equilibrium constant for ions solubilization. Sue *et al.* [51] proposed a model to estimate the equilibrium constant for solubilization of inorganic species in supercritical water. This model correlates the equilibrium constant and the dielectric constant using the equation 7.

$$\ln\ \mathrm{K(T,\rho))} = \ln \mathrm{K}(T_o, \rho_0) + \frac{\Delta H}{R}\left(\frac{1}{T} - \frac{1}{T_0}\right) - \frac{\omega_j}{RT}\left(\frac{1}{\varepsilon(\mathrm{T},\rho)} - \frac{1}{\varepsilon_0(T_o,\rho_0)}\right) \quad (7)$$

Where:

K is the equilibrium constant for solubilization of aqueous inorganic species,

T, ρ and ε are temperature, density, and dielectric constant at experiment conditions,

T_0, ρ_0 and ε_0 are temperature, density, and dielectric constant at 1bar and 25˚C,

R is the gas constant,

ΔH is the enthalpy change at reference state (1bar and 25˚C),

ω_j is the Born coefficient determined experimentally.

It can be observed that the last term of this equation, associated to a Born-type equation [52], is dependent to dielectric constant of the water medium. On the other hand, as can be seen, in Figure I.19 there is a huge dependency between the dielectric constant of water and the temperature and pressure conditions. When critical point is reached, ε experiments a large reduction. Then, at supercritical conditions, the last term associated to Born-type equation becomes significant and reduces the equilibrium constant. This is translated to a loss of solubility of ions in SCW.

Then, SCW becomes a non-polar medium (the dissociation constant of water is also reduced drastically) and the metal salt solution reaches an extremely high degree of saturation that makes metal ions precipitates.

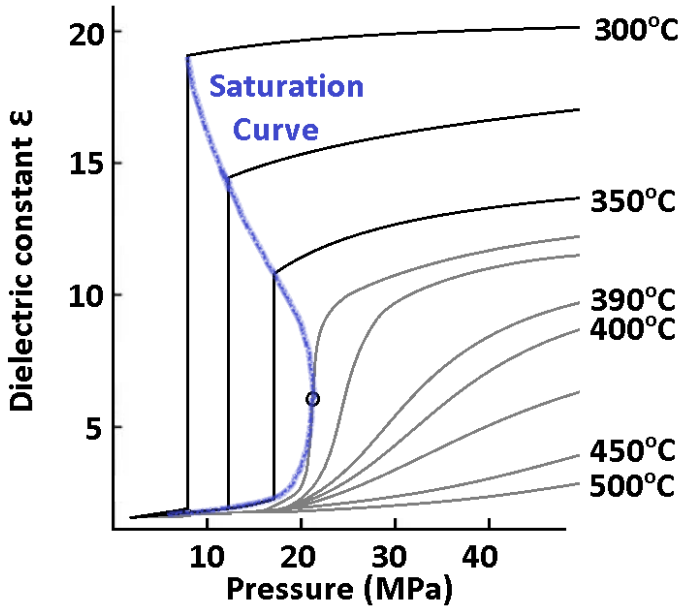

Figure I.19: Temperature and pressure dependency of dielectric constant parameter of water.

On the other hand, supercritical routes in water are considered instantaneous reaction favored by high temperature conditions and peculiar mass transfer properties of supercritical water. Recently, A. Yoko *et al.* [53] evaluated the kinetics of NiO precipitation from a nitrate salt in water around the critical point. This reaction was adjusted to a first order kinetics where the slope calculated from -ln(1-χ) (where χ is the conversion of nickel salt into nickel oxide) divided by the residence time, was considered the apparent rate constant (K_{app}) for the formation of NiO product. This parameter depends on two terms (equation 8), one associated to the chemical reaction control (net reaction rate constant or K_{net}) and another associated to the mass transfer control (mixing rate constant or K_{mix}).

$$\frac{1}{K_{app}} = \frac{1}{K_{net}} + \frac{1}{K_{mix}} \qquad (8)$$

This last term has a strong dependency with Reynolds number (relation between inertial forces of a fluid being pumped and viscous forces) that can be calculated from equation 9. Above the critical point, water experiments a drastically reduction of viscosity that is translated into an increase of the Reynolds number. This also means that the mass transfer coefficient in supercritical water is favored significantly and apparent rate

constant is controlled mainly by the chemical reaction. So, there is no kinetic limitations, associated to mass transfer phenomena, for precipitation.

$$Re = \frac{\rho \cdot u \cdot D}{\eta} \qquad (9)$$

Where:

ρ is the density of the fluid,

u is the linear flow velocity of the fluid,

D is characteristic dimension of the system like the diameter of a pipe where the system flows,

η is the dynamic viscosity of the fluid.

These two effects of supersaturation and chemical reaction control are the key of the specific features of supercritical hydrothermal synthesis. In one hand, kinetics is so fast, and solubilities of salt precursors and intermediates are low enough that an instantaneous nucleation process takes place and consumes the most part of reactants. Unlike subcritical hydrothermal routes, the precipitates do not grow more, and ultra-fine particles are obtained. This is the reason why supercritical water is a widely used route to obtain nanosized materials with a narrow size distribution. Moreover, this technology was proved to be flexible enough to modify properties like particle crystallinity or morphology as well through changes in pressure and temperature conditions or adding oxidating or reductive agents [54].

M. Diez-Garcia *et al.* proved for the first time the use of supercritical water route for obtention of nanosized xonotlite [55] and tobermorite [56] particles. They proved the formation of these crystalline phases using a very short residence time in a continuous tubular reactor. They also demonstrated the advantages of this technique to obtain highly pure and narrow size distribution nanoparticles of calcium silicate hydrates. Moreover, in the case of tobermorite, they found changes in morphology in respect to the same material prepared at subcritical conditions. Samples prepared under supercritical conditions are fibrillar compared to plates shaped particles obtained by subcritical water routes.

I.4. Functionalization of mineral admixtures.

This work is based on the acceleration of the nucleation process during early hydration steps adding crystalline CSH particles (xonotlite and tobermorite phases) to cement paste. These particles will act as heterogeneous nucleation points (seeds) where the C-S-H gel is able to grow easier [65]. Raising the number of nucleation points along the bulk, the overall hydration rate will be accelerated.

However, as it was mentioned in previous sections, there are rheological issues associated to the addition of these structures. Then, this work focused on the surface functionalization as the main strategy for reducing or eliminating the rheological problems associated to particles additions. This strategy was based on using steric hindrance or electrostatic repulsion effects to stabilize CSH particles in fresh cement mix.

I.4.1. Functionalization with polyethylene glycol.

Polyethylene glycol (PEG) or also known as polyethylene oxide is a polyether polymer (Figure I.20) resulted from polymerization of ethylene oxide monomer. PEG is widely used in different applications for food industry [66]. Moreover, PEG is used as solvent in numerous organic reaction [67] and is even employed for biotechnological or pharmaceutical applications like vaccines [68].

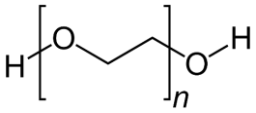

Figure I.20: Chemical structure of polyethylene glycol polymer.

There are several examples of the use of PEG in composites with inorganic particles and nanoparticles. Previous studies validated the use of PEG/SiO_2 or PEG/SiO_2-Al_2O_3 particles as phase change composite materials (PCM) for energy storage applications [69, 70]. Some papers talk about the use of PEG/CSH composites prepared at hydrothermal conditions for PCM applications as well [71]. Moreover, mixes of PEG and amorphous CSH was prepared for studying the effect of these polymer on particles porosity. These composites found great interest for wastewater treatment [72].

For cement and concrete applications have also been published different papers talking about the characterization of CSH/polymer composites [73, 74, 75]. Beaudoin *et al.* [76, 77, 78] studied the use of PEG polymers (PEG with MW from 300 to 1000) as modifier agents of CSH particles prepared by precipitation routes at room temperature. They defend a correlation between the use of PEG and increases of durability of Portland cement-based materials. Later, other publications have tried to characterize further this interaction between PEG and CSH [79].

As it was mentioned in previous section, PEG is widely used for its surfactant properties as part of lateral chains in PCE superplasticizers [80]. BASF chemical company registered a patent based on the use of amorphous C-S-H gel seeds with PCE functionalities prepared by precipitation routes at room temperature as well [81]. Some authors even used PEG as non-adsorbed polymer to improve the effectiveness of some PCEs superplasticizers [82]. However, the negative effect on the rate of cement hydration, limited the use of PEG for applications in construction.

This work proposed the controlled use of PEG in crystalline CSH particles. The main idea is stabilizing the seed addition to guarantee a good dispersibility of these particles in cement matrix. This approach is based on the steric hindrance capable to reduce considerably the attraction forces of Vander Waals. Moreover, the addition of PEG onto inorganic surface was thought to be in one step during particles precipitation via hydrothermal conditions. This is a simple, fast and cheap method to obtain composite particles with desired crystallinity and morphology.

I.4.2. Functionalization with zwitterionic molecules.

This family of molecules have the presence of negative and positive charges at the same time and separated by few atoms in its structure, that means that they contain a strong dipole in a small space inside its structure.

There are several examples even in biology where it can be found natural zwitterions. Phospholipids, that are part of cell membranes for example, have a zwitterion group located in its polar head. These groups located in amphiphilic macromolecules are

capable to inhibit the non-specific interactions between membrane cells and proteins or even other cells membranes.

For this reason, several studies have been carried out recently to use this chemistry to avoid non-specific interactions of proteins [83] or fouling effect for membrane applications [84]. Recent studies have proved good result in stabilization of silica nanoparticles modified with zwitterionic groups [85, 86]. This functionalization is capable to enhance the repulsive charge interactions between particles avoiding aggregation [87].

Few works were published about the application of zwitterionic molecules in cement or concrete based materials. These studies focused on application of zwitterionic groups in the structure of new promising PCE superplasticizers. These new formulations showed good results for cement that included high contents of clay as montmorillonite metakaolin [88].

This thesis also undertook the use of zwitterionic sulfobetaine siloxane (SBS), as stabilizing element bound covalently to CSH seeds. Its structure is shown in Figure I.21. As it was proposed for PEG modified particles, particles functionalized with SBS were prepared in one step synthesis. Then it was tested their effect on rheology and cement hydrations

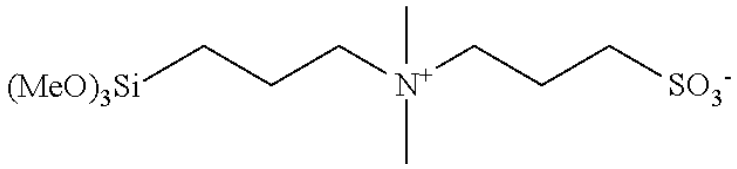

Figure I.21: Structure of sulfobetaine siloxane molecule.

I.5. Main objectives and outline of the thesis.

Different applications for cement and concrete demand a fast setting and hardening of prepared mixtures. Concrete precasting plants, for example, need to attain relatively high compressive strength after few hours in order to meet construction demands. Steam or radiant heat curing is the most extended procedure to reduce the production time (quick turnaround of formwork and reduction of storage space). However, heat

curing increases the cost of the final product and reduces its durability due to the appearance of microcracking. So, the existence of alternative ways to accelerate the setting and hardening and reduce the process cost at the same time has become a priority for this industry.

Nanoadditions, as nanosilica, or seeds of calcium silicate hydrates, where found as good accelerating materials capable to attain good compressive strength values at early setting stages of fresh cement and concrete mixtures. Though, their impact on rheology and workability involves additional expenses associated to new formulations and the use of plasticizers or water reducers. Moreover, these nanometric structures reduce the effect of plasticizers and in some cases could cause segregation issues. So, there is an interest on developing new admixtures capable to accelerate the setting and hardening of cement or concrete and improve their mechanical properties or durability, maintaining the workability of the suspension at the same time.

This thesis looks for the study of the synthesis and characterization of crystalline phases of calcium silicate hydrates particles (xonotlite and tobermorite) functionalized with organic molecules to improve (or at least not worsen) the rheology of cement pastes. This work explores the superficial modification of these particles to reduce their agglomeration when they are introduced as accelerating materials in cement matrix.

Therefore, this work proposed two different ideas for the stabilization of calcium silicate hydrates particles. The use of polyethylene glycol polymers and sulfobetaine siloxane molecule are commented for stabilization of particles by steric hindrance and electrostatic repulsion, respectively. Moreover, two different hydrothermal synthesis routes (subcritical and supercritical) were employed for the preparation of these products. In chapter 2, the materials, synthesis conditions used, and the characterization techniques employed for the obtention of modified xonotlite and tobermorite products are described.

Chapter 3 and chapter 4 are focused on the characterization of structure and morphology of xonotlite and tobermorite products, respectively, synthesized in presence of polyethylene glycol (PEG) and sulfobetaine siloxane (SBS) by subcritical hydrothermal conditions in a batch reactor. Then effect of PEG in structure of

precipitated particles is commented as well. Moreover, this part of the thesis describes the effect of these products in cement hydration and the rheology with cement pastes. By comparison, chapter 5 explore the synthesis of xonotlite and tobermorite with PEG polymers under supercritical hydrothermal conditions using a continuous setup.

Finally, in chapter 6, general conclusions are summarized according to the results obtained in previous chapters. Furthermore, perspectives of these new accelerating admixtures in cement industry are commented.

I.6. References.

[1] H. F. W. Taylor, *Cement Chemistry 2nd Edition*, Thomas Telford, **1997**. ISBN: 9780727739452.

[2] F. M. Lea and P. C. Hewlett, *Lea's Chemistry of Cement and Concrete 4th Edition*, Arnold, **1998**. ISBN: 9780750662567.

[3] Cement statistics and information from U.S. geological survey (USGS). https://www.usgs.gov/centers/nmic/cement-statistics-and-information.

[4] S. Yang, S. Wang, C. Gong, L. Lu, X. Cheng, Cem. *Mater. Construcc*. 65,31(**2015**).

[5] M. Sadeghian and A. Fatehi, *J. Process. Control., 21, 2,* (**2011**), pp. 302-308.

[6] M. Nokken, *Aci. Mater. J., 107, 1,* (**2010**), pp. 80-84.

[7] C. J. Engelsen, *Quality Improvers in Cement Making – State of the Art*, (**2008**).

[8] E.M. Gartner and H.M. Jenning, *J. Am. Ceram. Soc. 70, 10* (**1987**), pp. 743-749.

[9] F. Bellman et al., Cem. Concr. Res. *43, 9,* (**2012**), pp. 1189-1198.

[10] N. Roussel. Understanding the Rheology of Concrete. Chapter 7: Superplasticizers and the rheology of concrete. (**2012**). Woodhead Publishing. ISBN: 978-0-85709-028-7.

[11] W. R. Schowalter *and* G. Christensen, *J.Rheol. 42, 865* (**1998**).

[12] M.C.G Juenger, P.J.M. Monteiro, E.M. Gartner, G.P. Denbeaux, *Cem. Concr. Res. 35* (**2005**) pp. 19–25.

[13] G. Plusquellec and A. Nonat, Cem. Concr. Res. 90 (**2016**) pp. 89–96.

[14] P.C. Aïtcin and R.J. Flatt. Science and Technology of Concrete Admixtures. (**2016**). Woodhead Publishing. ISBN: 978-0-08-100693-1.

[15] L.P. Singh, S.R. Karade, S.K. Bhattacharyya, M.M. Yousuf, S. Ahalawat, *Constr. and Build. Mater. 47 (**2013**) pp. 1069-1077.*

[16] M. Berra, F. Carassiti, T. Mangialardi, A.E. Paolini,M. Sebastiani, *Constr. Build. Mater. 35* (**2012**) pp. 666-675.

[17] F. Wang, X. Kong, L. Jiang, D. Wang, *Constr. Build. Mater. 249* (**2020**) 118734.

[18] J. J. Thomas, H.M. Jennings, J.J. Chen, *J. Phys. Chem. C., 113,* (**2009**), pp. 4327-4334.

[19] G. Land and D. Stephan, *Cem. Concr. Compos. 87*, (**2018**), pp. 73-78.

[20] M. Diez **2017**. *"Synthesis by supercritical fluids methods of advanced additions for cementitious materials"* Universidad del País Vasco/Université de Bordeaux. Repositorio institucional ADDA EHU Biblioteka UPV/EHU.

[21] G. Wei, X. Zhang, F. Yu, *Int. J. Thermophys ., 28,* (**2007**) ,pp. 1718–1729.

[22] N.M.P Low and J.J. Beaudoin, *Cem. Concr. Res.,23,5,* (**1993**), pp. 1016-1028.

[23] L. Black, K. Garbev, A. Stumm, Adv. Appl. Ceram., 108,3 (**2013**), pp. 137-144.

[24] C. Hejny and T. Armbruster, *Z. Kristallogr. 216* (**2001**) pp. 396-408.

[25] S. Shaw, S. M. Clark, C. M. B. Henderson, *Chem. Geol. (***2000)**, *167*, pp. 129-140.

[26] I. G. Richardson, *Cem. Concr. Res.* **2004**, *34*, 1733–1777.

[27] S. Merlino and E. Bonaccorsi, T. Armbruster, *Eur. J. Mineral. (***2001)**, *13*, pp. 577-590.

[28] S. Merlino and E. Bonaccorsi, T. Armbruster, *Am. Mineral. (***1999)**, *84*, pp. 1613-1621.

[29] S. Merlino and E. Bonaccorsi, T. Armbruster, *Eur. J. Mineral. (***2000)**, *12*, pp. 411-429.

[30] M. Sakiyama and T. Mitsuda, *Cem. Concr. Res. (***1977)**, *7*, 681–685.

[31] T. Mitsuda and H. F. W. Taylor, *Cem. Concr. Res. (***1975**), *5*, 203–210.

[32] G. L. Kalousek, *J. Am. Ceram. Soc.* **1957**, *40*, 74–80.

[33] H. Manzano, J.S. Dolado, A. Ayuela, *J. Phys. Chem. B***,** *113, (***2009**) *pp.* 2832–2839.

[34] W. Liao, W. Li, Z. Fang, C. Lu, Z. Xu, *Materials*, *12*(22), 3765 (**2019).**

[35] H. Matsuyama and J. F. Young, *Adv.Cem. Res.,12, 1,* (**2000**), pp.29-33.

[36] D. Stephan and P. Wilhelm, *Z. Anorg. Allg. Chem., 630,* (**2004**), pp. 1477-1483.

[37] M. Mehrali, S.F.S. Shirazi, S. Baradaran, M. Mehrali, H.S.C. Metselaar, N.A. Bin Kadri, N.A.A. Osman, *Ultrasonics Sonochemistry, 21, 2,* (**2014**) pp. 735-42.

[38] M. Zhang and J. Chang, *Ultrasonics Sonochemistry, 17, 5,* (**2010**), pp. 789-792.

[39] K. Byrappa and M. Yoshimura, *Handbook of Hydrothermal Technology*, (**2001**). ISBN: 978-0-8155-1445-9.

[40] R. Roy and O.F. Tuttle, *Phys. Chem. Earth, 1,* (**1956**), pp. 138–180.

[41] S. Y. Hong and F. P. Glasser, *Cem. Concr. Res. (***2004)**, *34*, pp. 1529–1534.

[42] E. Bonaccorsi and S. Merlino, *Rev. Miner. Geochem. (***2005)**, *57*, pp. 241–290.

[43] S. Diamond, *J. Am. Ceram. Soc. (***1964**), *47*, 593–594.

[44] L. Heller and H. F. W. Taylor, *J. Chem. Soc. (***1951**), pp. 2397–2401.

[45] P. E. Flint, H.F. McMurdie, L.S. Wells, *J. Res. Natl. Bur. Standards., 21 (***1938**).

[46] I. Harker, *J. Am. Ceram. Soc. 47,* (**1964**).

[47] K. Speakman, *Miner. Mag. J. Miner. Soc., 36 , 284,* (**1968**).

[48] M. Claverie, M. Diez-Garcia, F. Martin, C. Aymonier, *Chem. Eur. J., 25, 23*, (**2019**), pp. 5814-5823.

[49] C. Aymonier, G. Phillipot, A. Erriguible, S. Marre, J. Supercritical fluids, 134, (**2018**), pp. 184-196.

[50] T. Adschiri, K. Kanazawa, K. Arai*, J.Am. Ceram. Sor., 75,4,* (**1992**), 1019-1022.

[51] K. Sue, T. Adschiri, K. Arai, *Ind. Eng. Chem. Res., 41,* (**2002**), pp. 3298-3306.

[52] E. S. Amis and J. F. Hinton, Solvent effects on chemical phenomena; Academic Press: New York, (**1973**) ISBN: 9780120573011.

[53] A. Yoko, Y. Tanaka, G. Seong, D. Hojo, J. *Phys. Chem. C, 124,* (**2020**), pp. 4772−4780.

[54] T. Adschiri*, K. Kanazawa, K. Arai, J. Am. Ceram. Soc. 75,* (**1992**.), pp. 2615–2620.

[55] M. Diez-Garcia, J.J. Gaitero, J.I. Santos, J.S. Dolado *J., C. Aymonier, Flow. Chem.* 8, (**2018**), pp. 89–95.

[56] M. Diez-Garcia*, J.J. Gaitero, J.S.Dolado, C. Aymonier, Angew. Chem.* (**2017**), 129, pp. 1–6.

[57] R.J. Flatt, Cem. Concr. Res.*,3,* (**2004**) pp. 399-408.

[58] P. Attard, D. Antelmi, I. Larson, *Langmuir,16,* (**2000**), pp. 1542-1552.

[59] J.I. Tobón, O. Mendoza, O.J. Restrepo, M.V. Borrachero, J.J. Paya, *Materiales de Construcción, 70, 340, e231* (**2020**).

[60] I.M. Krieger and T.J. Dougherty, *Journal of Rheology 3, 137* (**1959**).

[61] R.J. Flatt and P. Bowen, *J. Am. Ceram. Soc.* 89, 4, pp. 1244-1256.

[62] E. García-Taengua, *Composites Part B: Engineering, 81, (***2015***), pp. 120–129.*

[63] L. Senff, D. Hotza, S. Lucas, V.M. Ferreira, *Mater. Sci. Eng. A* 532 (**2012**) pp. 354-361.

[64] P. Samui. New Materials in Civil Engineering. Chapter 8: The superplasticizer effect on the rheological and mechanical properties of self-compacting concrete. (**2020**) Butterworth-Heinermann. ISBN: 978-0-12-818961-0.

[65] R. Alizadeh, *J.Mater.Chem.,*19, (**2009**), pp. 7937–7946.

[66] F.E. Bailey and J.V. Koleske, Chapter: "Polyoxyalkylenes". Ullmann's Encyclopedia of Industrial Chemistry. Weinheim: Wiley-VCH (**2000**).

[67] J. Chen, S.K. Spear, J.G. Huddleston, R.D. Rogers, *Green Chem. 7,2* (**2005**), pp. 64-82.

[68] P. Giavina and B.J. Kalil, *World Allergy Organization Journal 14:100532* (**2021**).

[69] L. He, J. Li, C. Zhou, H. Zhu, X. Cao, B. Tang, *Solar Energy 103* (**2014**) pp. 448–455.

[70] B. Tang, C. Wu, M. Qiu, X. Zhang, S. Zhang, *Mater. Chem. Phys. 144* (**2014**) pp. 162-167.

[71] T. Qian, J. Li, X. Min, Y. Deng, W. Guan, H. Ma, *Energy 82* (**2015**) pp. 333-340.

[72] W. Guan, F. Ji, D. Fang, Y. Cheng, Z. Fang, Q. Chen, P. Yan, *Cer. Int. 40* (**2014**), pp. 4415–4420.

[73] H. Matsuyama and J.F. Young, *Chem. Mater. 11(1):16* (**1999**).

[74] R. Morlat, G. Orange, Y. Bomal, P. Gordard, J. Mater. Sci. 42(13):4858 (**2007**).

[75] Dario M, Molera M, Allard B, J. Radioanal. Nucl. Chem. 270(3):495 (**2006**).

[76] J.J. Beaudoin, L. Raki, R. Alizadeh, *Cem. Concr. Comp. 31* (**2009**) pp. 585–590.

[77] N.M.P Low and J.J. Beaudoin, *Cem. Concr. Res.,23,5,* (**1993**), pp. 1016-1028

[78] J. J. Beaudoin, H. Dramé, L. Raki, R. Alizadeh*Mater. Struct. 42* (**2009**), pp. 1003-1014.

[79] Y. Zhou, C.A. Orozco, E.Duque-Redondo, H. Manzano, G. Geng, P. Feng, P. J.M. Monteiro, C. Miao, Cem. Concr. Res. *115 (***2019***)* pp.20-30.

[80] E. Janowska-Renkas, *Procedia Engineering 108* (**2015**) pp. 575-583.

[81] Roland Reichenbach-Klinke and Luc Nicoleau., Patent US20110263749A1 (2011)

[82] A. Lange and J. Plank, Cem. Concr. Res. *79* (**2016**) pp. 131-136.

[83] S. Chen, J. Zheng, L. Li, S. Jiang, *J. Am. Chem. Soc. 127,41,* (**2005**), pp. 14473–14478.

[84] A. Venault and Y. Chung, *Langmuir, 35, 5*, (**2019**) pp. 1714–1726

[85] Z.G. Estephan, J.A. Jaber, J.B. Schlenoff, *Langmuir, 26, 22* (**2010**), pp. 16884–16889.

[86] B.R. Knowles, D. Yang, P. Wagner, S. Maclaughlin, M.J Higgins, P.J. Molino, *Langmuir, 35, 5*(**2019**) pp. 1335-1345.

[87] A.J. Worthen, V. Tran, K.A. Cornell, T.M. Truskett, *Soft Mater.*, 12, (**2016**) pp. 2025-2039.

[88] J. Ren, S. Luo, S. Shi, H. Tan, X. Wang, M. Liu, X. Li, *Clay Minerals,* 1-9. (**2021**).

[89] T. Vehmas, A. Kronlöf, A. Cwirzen, *Mag. Concr. Res., 70, 16,* (**2018**), pp. 856-863.

[90] E. John, J.D. Epping, D. Stephan, *Constr. Build. Mater., 228* (**2019**) 116723.

CHAPTER II. EXPERIMENTAL SECTION

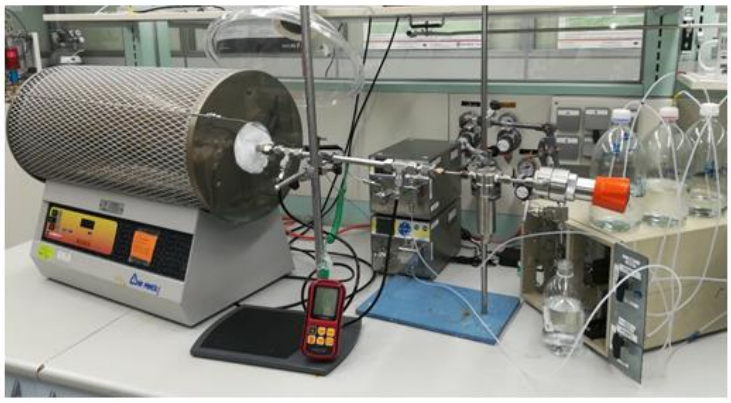

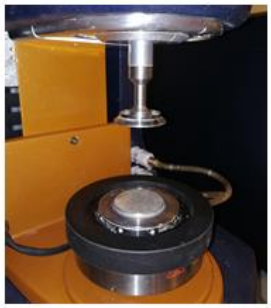

II.1. Materials.

All chemicals employed in this work, except the sulfobetaine siloxane molecule, were obtained from commercial sources and used without further purification. For the synthesis in subcritical conditions calcium oxide as well as amorphous silica and alumina were used. Calcium oxide was obtained from calcination of $CaCO_3$ anhydrous (>99% purity, from Sigma Aldrich (MERCK)) for at least 5 hours at 1000°C. Colloidal amorphous nanosilica in water dispersion stabilized by Na_2O (45%w/w Levasil from AkzoNobel company) and $Al_2O_3 \cdot H_2O$ (Nyacol Al20SD 96% w/w from Nyacol TECHNOLOGIES INC.) were employed as Si and Al precursors, respectively.

In the case of synthesis in continuous reactor soluble salts were employed for Ca, Si and Al precursors. The salts employed were Ca $(NO_3)_2 \cdot 4H_2O$ (>99%purity), $Na_2SiO_3 \cdot 9H_2O$ (>98% purity) and Al $(NO_3)_3 \cdot 9H_2O$ (>98% purity). All these reactants were purchased from Sigma Aldrich (MERCK). Polyethylene glycol (PEG) compounds of different molecular weights (M_W =600, 1500, 4000 g/mol) were purchased from Scharlau Chemicals.

For the synthesis of sulfobetaine siloxane, 1,3-propanesultone (98% purity) and (N,N-dimethylaminopropyl)trimethoxy silane (96% purity) purchased from Sigma Aldrich were used as starting materials. Freshly distilled acetone under argon dried over $MgSO_4$ was used as reaction solvent.

MiliQ purity water was used as solvent in the synthesis reactions. Moreover, the water employed for hydrothermal routes was first boiled to remove any dissolved CO_2 to avoid formation of calcium carbonate.

II.2. Hydrothermal synthesis under subcritical conditions.

II.2.1. Batch reactor setup.

All the synthesis reactions were carried out in a closed batch reactor at 215°C and 250°C depending on the synthesis and at their autogenous pressure. The reactor used is a commercial setup from Parr Instruments Co. and it is based on a stainless-steel vessel which can be set up to high temperature and pressure conditions below supercritical point (Figure 22).

Figure II.1: Parr instruments' subcritical batch reactor.

The total volume of the reactor is 600mL, hermetically closed that contains the synthesis precursors and products during the reaction. Hydrothermal conditions in the system are maintained using an external electrical resistance heater. The internal temperature is registered by a Type J thermocouple, the pressure can be monitored in an analog manometer installed and the stirring rate is also monitored during the experiment.

Moreover, the reactor includes a coiled tube for the refrigeration. This cooling coil is connected to an external chiller that cools and recirculates cold water to control the inner temperature more precisely. A PID feedback controller regulates and adjusts this heating/cooling system during the reaction.

The batch reactor setup employed in this work is composed of:

- 600mL vessel (452HC3 566289 HASTC 111811-year 2012). Its working range is between -10°C and 500°C. It could endure 138bar as maximum pressure.
- Stirring system with magnetic suspension (joints made of neodymium magnets) A1120HC6 HASTC M34391. This magnetic stirrer is cooled by water avoiding demagnetization of neodymium during the reaction,
- "Parr 4848 Reactor Controller". PID feedback control and software "Parr controller Communication Utility",
- Type J thermocouple sensor,

- Industrial Analog manometer “Span Liquid filled SC-2 gauge”,
- Water chiller system “MTA’s TAE EVO”.

Before starting the experiments, the manufacturer instructions were followed to select the maximum filling volume allowed inside the vessel. This maximum volume would prevent any overpressure during the experiment. The mathematical formula that describes the Maximum Allowable Water Loading (MAWL) is gathered in equation 10.

$$MAWL = \frac{SF \cdot (VV)}{(VM)} \qquad (10)$$

Where:

- SF= Security Factor,
- VV= Volume Vessel,
- VM=Volume Multiplier at maximum temperature,
- Applying a security factor of 0.75, the volume of the reaction vessel (600mL) and a volumetric expansion factor of water or Volume Multiplier at 250°C [10], the reactor should not be filled more than 360mL. In this case, a 300mL total volume has been prepared to carry out the reactions.

II.2.2. Subcritical synthesis of pristine xonotlite (X_Pristine).

The first experiments carried out intended to reproduce the synthesis of different Calcium Silicate Hydrates polymorphs using subcritical hydrothermal conditions. The state of art of synthesis associated to different C-S-H polymorphs is well described in literature [1, 2, 3]. Among the different C-S-H phases, xonotlite is the most common and easiest crystalline structure to be synthesized hydrothermally using a calcium/ silicon ratio of 1.0 [4, 5, 6].

Xonotlite was synthesized following the synthetic route developed by M. Diez-Garcia *et al*. [7]. In a typical synthesis, 4g of Levasil (45%w/w of SiO_2, 0.03mole of SiO_2) and 1.68g of CaO (0.03moles) are introduced in the reactor with 300mL of boiled miliQ water.

The concentration of sodium in the reactor medium was controlled for this synthesis. A sodium content above 10%w/w of Na_2O in the mixture could produce secondary reactions that give Pectolite as undesired byproduct [8, 9]. Regarding the calcium oxide precursor, since it was obtained from $CaCO_3$, it was necessary to ensure a good decarbonation by calcination and the immediate use of the calcined product to avoid reabsorption of CO_2.

The reactor was closed and heated up to 250°C. The autogenous pressure generated was 38bar and the system was quenched after 4 hours of reaction at 250°C. The solid was collected and washed twice with acetone. Then it was dried at 80°C for 4 hours minimum. The stirring rate was fixed to 260RPM. The total amount of product obtained was 3.48g.

II.2.3. Subcritical synthesis of pristine tobermorite (T_Pristine).

Tobermorite is not as easy to synthesize in laboratory as other calcium silicates hydrates like xonotlite. Tobermorite is a phase obtained in a narrow temperature range and a very specific Ca/Si ratio. The time required to synthesize is too long and some stabilization elements must be added to shorten the time of reaction and guarantee the purity of the final product. Nevertheless, some authors have been able to obtain tobermorite in a short period of time by subcritical and supercritical techniques [12, 13].

Tobermorite was synthesized following a procedure employed by M. Diez-Garcia for the obtention of aluminum substituted tobermorite [7]. In this case a ratio of Ca/(Si+Al) 0f 0.83 was used. In a typical synthesis 1.64g of Levasil (45%w/w, 0.0123mole of SiO_2), 0.67g of CaO (0.0119mole of CaO) and 0.113g of Al_2O_3 (0.001mole) were introduced in reactor with 300mL of boiled miliQ water. In this case the closed reactor was heated up to 215°C. The autogenous pressure generated was 18bar and the system, was quenched after 4 hours. Solids collected were washed twice with acetone and dried at 80°C for 4 hours minimum. The total amount of product obtained was 1.62g.

II.2.4. Subcritical synthesis of polyethylene glycol modified xonotlite and tobermorite.

Xonotlite and tobermorite modified/functionalized samples were obtained under the same conditions employed for the pristine ones but adding polyethylene glycol polymer

dissolved in the water medium. In all modified samples, polyethylene glycol was added, with a Ca/PEG molar ratio of 1.5, to the water medium and then the reaction was carried out in the sealed reactor.

This thesis focused on three different polyethylene glycols with different molecular weights (Mw 600, 1500 and 4000g/mole) purchased to Scharlau Chemicals. In the case of xonotlite 12g (0.02 moles) of PEG MW 600g/mole, 30g (0.02 moles) of PEG Mw 1500g/mole and 80g (0.02 moles) of PEG Mw 4000g/mole were introduced with CaO and SiO_2 precursors to obtain modified/functionalized xonotlite samples. On the other hand, for modified/functionalized tobermorite samples, 5.9g (0.0098 moles) of PEG Mw 600g/mole, 12g (0.008 moles) of PEG Mw 1500g/mole and 32g (0.008 moles) of PEG Mw 4000g/mole were introduced in the reactor vessel during the synthesis. After the reaction step every sample was filtered and washed with acetone twice.

After drying at 80°C for 4 hours 4.28g of xonotlite with PEG MW600g/mole (X_P600), 5.53g of xonotlite with PEG MW1500g/mole (X_P1500) and 9.2g of xonotlite with PEG MW4000g/mole (X_P4000) were gathered. On the other hand, after 4 hours of synthesis 1.8g of tobermorite with PEG MW600g/mole (T_P600), 1.98g of tobermorite with PEG MW1500g/mole (T_P1500) and 2.54g of tobermorite with PEG MW4000g/mole (T_P4000) were obtained.

II.2.5. Synthesis of sulfobetaine siloxane reactant.

The synthesis followed in this thesis to obtain sulfobetaine siloxane (SBS) is the same one employed in reference14. In a typical reaction, 4.54g (0.037moles) of 1,3-propanesultone and 37mL of anhydrous acetone were introduced in a 100mL 2-neck round-bottom flask. This flask was closed by septum, purged with Argon for other 25min and stirred at 1000RPM with a magnetic stirrer.

Then 8.25mL of (*N*, *N*-Dimethylaminopropyl) trimethoxy silane (0.037moles) were added dropwise using a 10mL syringe. After 30min of reaction the transparent solution becomes white. The reaction is stirred for 6h at room temperature before the product is filtered, washed by distilled acetone, and dried at 60°C overnight under vacuum. The SBS chemical structure and its formation reaction is showed in figure II.2. Finally, the

recovered dry powder, which is very hygroscopic, is stored in a desiccator under vacuum until it is used.

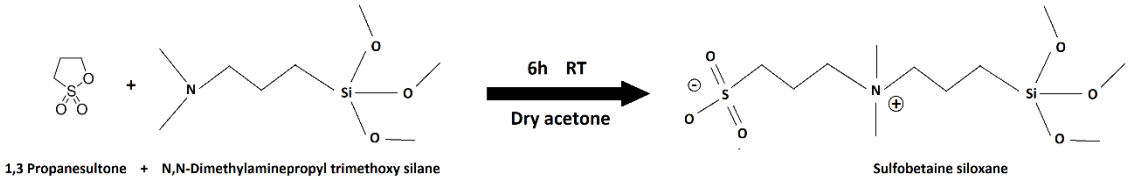

Figure II.2: Synthesis reaction and chemical formula of sulfobetaine siloxane.

II.2.6. Subcritical synthesis of covalent functionalization of xonotlite and tobermorite.

With the aim of synthesizing xonotlite and tobermorite functionalized with sulfobetaine siloxane 1/4 substitution in moles of the SiO_2 precursor was done maintaining a total ratio of Ca/Si of 1.0 in the case of xonotlite and Ca/(Si+Al) of 0.83 in the case of tobermorite. Furthermore, two reaction times were studied for both xonotlite and tobermorite functionalization, 4h and 8h. Below, a general description of the reactions carried out for SBS functionalization of xonotlite and tobermorite are given. Xonotlite modification/functionalization with SBS (X_SBS_4h and X_SBS_8h): In a typical synthesis, 3.2g of Levasil (45%w/w of SiO_2, 0.024mole of SiO_2), 1.97g of SBS (0.006mole) and 1.68g of CaO (0.03mole) are introduced in the reactor with 300mL of boiled miliQ water. The reactor was closed and heated up to 250°C. The autogenous pressure generated was 38bar and the system was quenched after 4 hours (X_SBS_4h) or 8 hours (X_SBS_8h) of reaction at 250°C. In both cases the solids were collected and washed twice with acetone. Then they were dried at 80°C for 4 hours minimum. In the case of the reaction at 4 hours 4.5g of product was obtained and in the 8 hour reaction 3.7g of product was obtained.

Tobermorite modification/functionalization with SBS (T_SBS_4h and T_SBS_8h): In a typical synthesis 1.31g of Levasil (45%w/w, 0.0098moles of SiO_2), 0.81g of SBS (0.0024moles), 0.67g of CaO (0.0119moles) and 0.113g of Al_2O_3 (0.001moles moles) were introduce in reactor with 300mL of boiled miliQ water. The closed reactor was heated up to 215°C. The autogenous pressure generated was 18bar and the system, was quenched after 4 hours (T_SBS_4h) and 8 hours (T_SBS_8h). Solids collected were

washed twice with acetone and dried at 80°C for 4 hours minimum. The total amount of product obtained at 4 and 8 hours was 1.25g and 1.68g respectively.

II.3. Hydrothermal synthesis under supercritical conditions.

II.3.1. Continuous reactor setup.

The continuous supercritical reactor employed in this work is a home-made setup built in ICMCB facilities (Figure II.3). It allows multiple configurations and can be better adapted to different requirements due to its flexibility. Figure II.4 shows the scheme of the first proposed design. It consisted of two "Jasco" PU2080 HPLC pumps (number 2 in Figure II.4) that introduce the solutions of the starting material into the reactor. Two 3-ways valves were installed before each pump to change the feed from precursor solution to distillated water during the experiments. Moreover, in order to avoid any carbonation, argon was bubbled through the reactant solutions during the experiment (number 1 in Figure II.4).

Figure II.3: Photography of the continuous reactor setup from group 7 "Supercritical Fluids" at ICMCB.

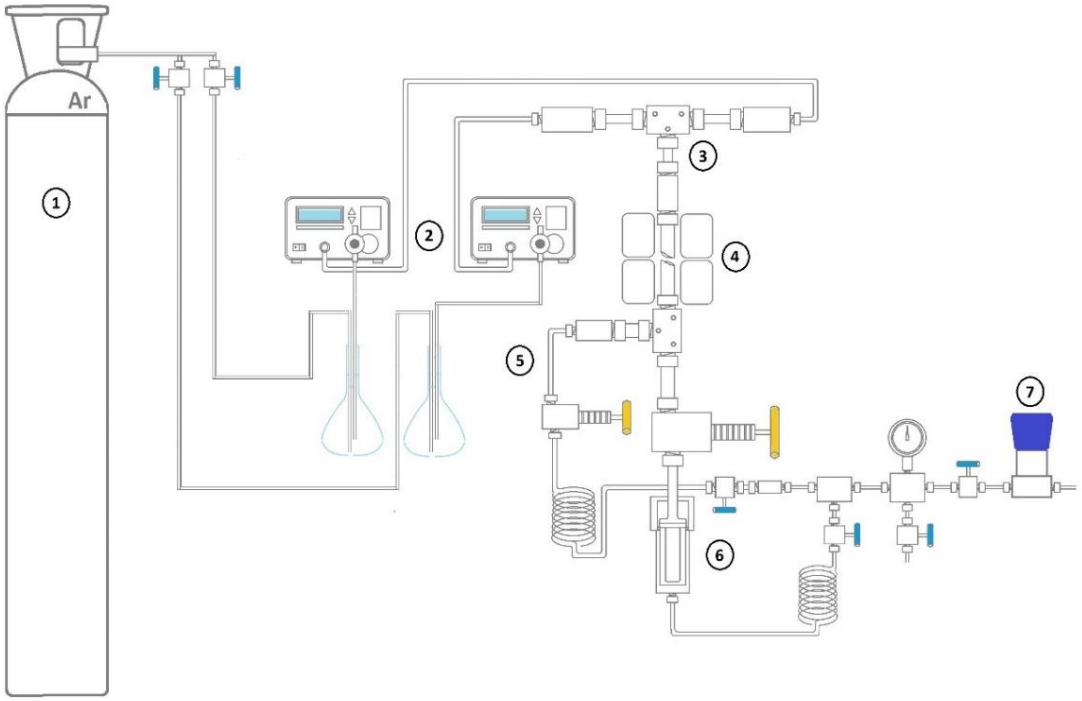

Figure II.4: Scheme of the continuous reactor. First assembly design. 1) Argon bottle, 2) HPLC pumps, 3) Mixing point of the two starting material solutions, 4) Electrical ceramic heaters, 5) Bypass line, 6) Filter line, 7) Back pressure regulator.

The reactor is composed by a vertical pipe with an outside diameter (OD) of 9/16" made of 316L stainless steel. The tube is heated by two electrical heaters to get the desired reaction temperature. The pressure inside the system is generated and maintained by the two HPLC pumps that push the solutions through a restriction located at the end of the system. Both solutions meet and are mixed at the beginning of the reactor which is at the right temperature and pressure. The reaction solution stays in the reactor the adequate reaction time which is controlled by the flow rates and the volume of the reactor. Once the reaction solution gets out of the reactor it goes through a filter which collects the synthesized product and then the solution comes out of the system through the back-pressure regulator.

The restriction at the end of the setup (number 7 in Figure II.4) is produced by a "TESCOM" back pressure regulator (BPR). In fact, BPR can regulate the size of this restriction to adjust the upstream pressure. This BPR can operate at maximum conditions of 414bar and 74°C.

Between the reactor pipe and the BPR, there is a stainless-steel filter where the product is collected. This element is followed by a coiled tube and both, filter and tube, are

submerged in an ice-water bath. Thus, the filtered powder and the remaining liquid are cooled down. Ice-water bath intends to stop the reaction and avoid gasification of water after depressurization. Moreover, cooling down the solution prevents the BPR from breaking.

The main parameter that must be considered to design a continuous reactor is the residence time. This is the effective time that reactants spent inside the reactor at the desired pressure and temperature conditions. The residence time determines the conversion of reactants, crystallinity and particle size of the final product. This time is defined by the total flow rate and the internal volume of the pipe, and it can be calculated from equation 11. This expression includes a correction that considers variations in density of the fluid due to the supercritical conditions.

$$R_t = \frac{V}{Q} \cdot \frac{\rho_{(P_{SC},T_{SC})}}{\rho_{(P_0,T_0)}} \qquad (11)$$

Where,

V is the internal volume of heated reactor tubing,

Q is total flow rate generated by HPLC pumps (Q_1 and Q_2),

$\rho(P_{SC}, T_{SC})$ density of water at chosen supercritical conditions,

$\rho(P_0, T_0)$ density of water at standard conditions (1 atm and 20°C).

In order to know the actual temperature inside the reactor tube, a calibration was performed before carrying out the reactions. Two long thermocouples, named T_1 and T_2 were employed to measure the temperature at the both ends, R1 (top) and R2 (bottom), of the ceramic heaters. A detailed scheme of the location of the thermocouples during the calibration and the downstream fitting configuration built to carry out the temperature calibration is shown in Figure II.5.

It was observed that the first heater is capable of obtaining the desired temperature and the bottom one maintains the conditions until the end of the effective length. Table II.1 and equation 12 are the results of calibration in our system.

Table II.1:Temperature calibration of the continuous reactor

Set point: T1= T2= 400°C			
Q_1= Q_2 (mL/min)	R1 (°C)	R2 (°C)	Preheating (°C)
1.0	332	400	-
1.5	338	398	-
2.0	343	395	-
2.5	346	395	-
2.8	348	395	-
3.0	354	395	-
3.3	358	395	-
4.0	373	395	-
5.0	389	395	-
6.0	405	395	-
7.0	391	394	100
7.5	395	394	100
8.0	400	395	100

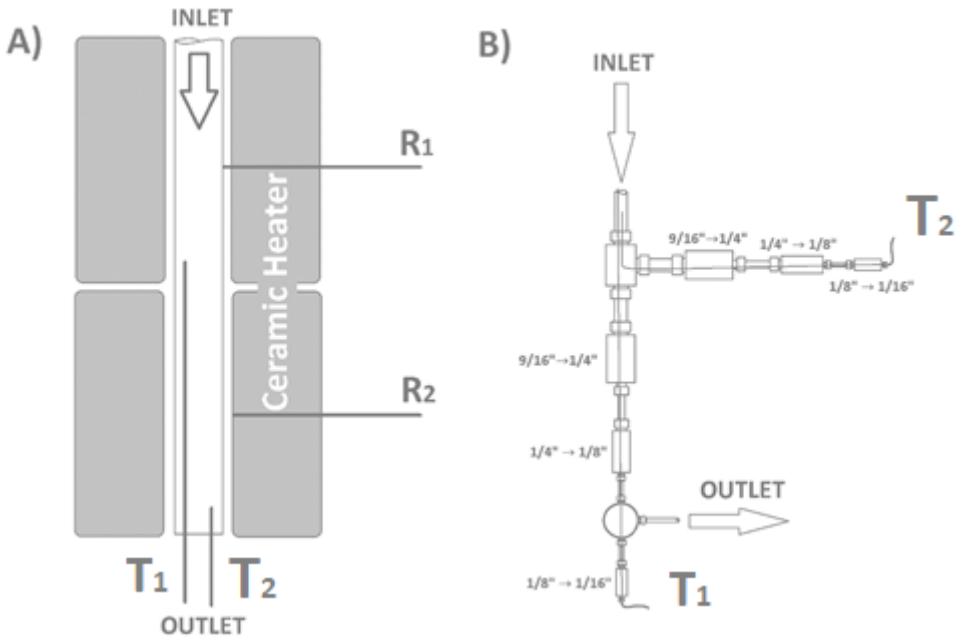

Figure II.5: Detailed location of thermocouples during calibration (A) and detailed scheme of calibration setup assembly (B).

$$R_1 = 1.2329 \cdot T_1^2 + 6.377T_1 + 324.19 \qquad (12)$$

Following equation 12, it is possible to calculate the temperature setpoint in the top heater depending on the total flow rate employed during the synthesis. At high flow rates, it was necessary to install a preheater (Figure II.6) in the calcium precursor line that could heat up the calcium solution up to 100°C. This way the ceramic heater was able to heat up the solution inside the reactor pipe to reach 400˚C of temperature.

Figure II.6: Detail of preheater installed in calcium line

Thus, the desired temperature of 400°C at different flow rates and residence times was guaranteed.

II.3.2. Modification on the design of the reactor. Second setup.

The original design had a bypass line (number 5 in Figure II.4) included in the reactor. The objective of the bypass line was to allow the recovery of the product from the filter without having to stop the reaction allowing the reaction solution bypass the filter (number 6 in Figure II.4).

After some experiments different problems were found using this setup. First, the valves installed in the bypass and filter lines caused restrictions that created clogging in the reactor tube (Figure II.7). Due to this clogging the pressure in the system increased and it was so high that the experiment had to be stopped. In the end, almost no or very low quantity of material was recovered from the filter.

Figure II.7: Material deposit stuck in needle valve mechanism.

On the other hand, if we try to recover the material gathered by the filter and operate through the narrower bypass pipe, part of precipitated product could clog the system in this line as well, even if we have started pumping water. If we want to prevent this, we should flow distillated water for a while before closing the filter line and opening the

bypass. Nevertheless, we could increment the possibilities of clogging along the filter line as well.

Then, if we want to operate a continuous reactor for this application, the reactor setup must be simplified, eliminating the possible restrictions and direction changes due to the fittings employed. The design is crucial if we want to scale up this technology and minimize material deposits or clogging.

Moreover, we have observed that, the clogged material can get out the system during the experiment but after a longer period than expected. This can be observed during synthesis that pressure system increases and decreases very fast. So, the residence time of this material inside the reactor changes drastically. It must be considered that clogging phenomena have an effect even in the size and crystallinity of our product. A wise reactor design can increase the operation time and even the quality of our product controlling better the residence time.

The new reactor design employed is shown in Figure II.8 and tried to minimize all the problems found with the first design. In the new design, the bypass and the intermediate valves were taken off completely. All the experiments carried out using this setup enable to recover a higher quantity of synthesized material in the filter.

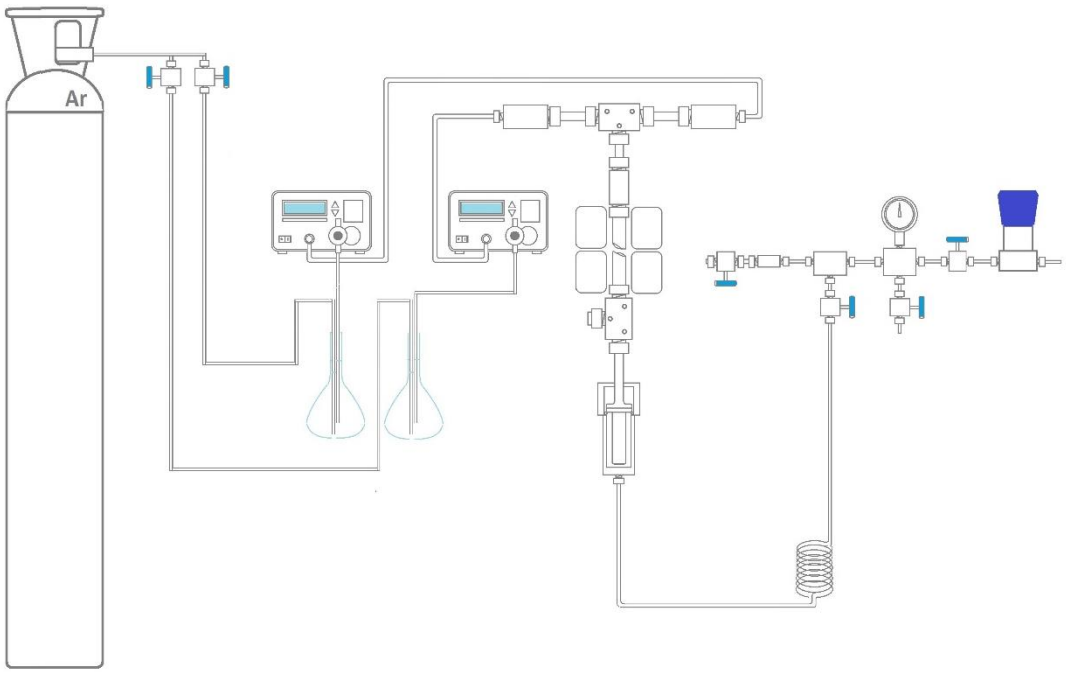

Figure II.8: Scheme of the continuous reactor after the changes. Second setup.

II.3.3. Pristine xonotlite synthesis in supercritical conditions.

$Na_2SiO_3 \cdot 9H_2O$ as silicon precursor and $Ca(NO_3)_2 \cdot 4H_2O$ as calcium precursor were used in these experiments. The quantities employed for solution preparation are shown in Table II.2. The Ca/Si molar ratio was fixed to 1.0 in every experiment. In samples prepared in the presence of polyethylene glycol, the molar ratio Ca/PEG was fixed to 1.5 the same as in the samples prepared in batch subcritical reactor. In every experiment the polyethylene glycol was dissolved in the sodium silicate solution and introduced at the same time.

Table II.2: Preparation summary of Si and Ca precursor solutions for synthesis in the continuous reactor.

Sample	$[Na_2SiO_3 \cdot 9H_2O]$ M	$[Ca(NO_3)_2 \cdot 4H_2O]$ M	MW PEG (g/mol)	g PEG/ L water
X_Pristine_SC	0.05	0.05	-	-
X_P600_SC	0.05M	0.05	600	20.15
X_P1500_SC	0.05M	0.05M	1500	50.35
X_P 4000_SC	0.05M	0.05M	4000	134.35

In the beginning, the synthesis was carried out using the same residence time used by Diez-García *et al.* in the small-scale reactor [15], but after the results obtained, a correction in residence time was carried out to optimize the purity of the product in this setup. Table II.3 summarizes all the synthesis conditions carried out for this study.

Table II.3: Summary of different flow rates and residence times used in this study for the synthesis of xonotlite.

Temperature (°C)	Pressure (bar)	Pumps flow rate Q1=Q2 (mL/min)	Residence time (s)
400	235	3.3	20
400	235	4.3	13
365	235	9.9	22
350	235	9.9	25
325	235	9.9	27

II.3.4. Tobermorite synthesis in supercritical conditions.

The final reactor setup for the xonotlite synthesis was also used for the synthesis of tobermorite. However, problems arise with this design, which will be later described, when it was used to synthesize tobermorite with the different PEGs. Because of this the setup was redesign again. In general terms, the reactor was redesigned in order to carry out the tobermorite-PEG synthesis in two steps. In the first step the tobermorite would be synthesized followed by the addition of PEG to the reaction solution. The main change introduced was a third inlet inserted after the reactor tube. Moreover, the bottom heater R2 was switched off during the reaction in order to prevent the degradation of the PEG. Figure II.9 shows the tobermorite-PEG setup.

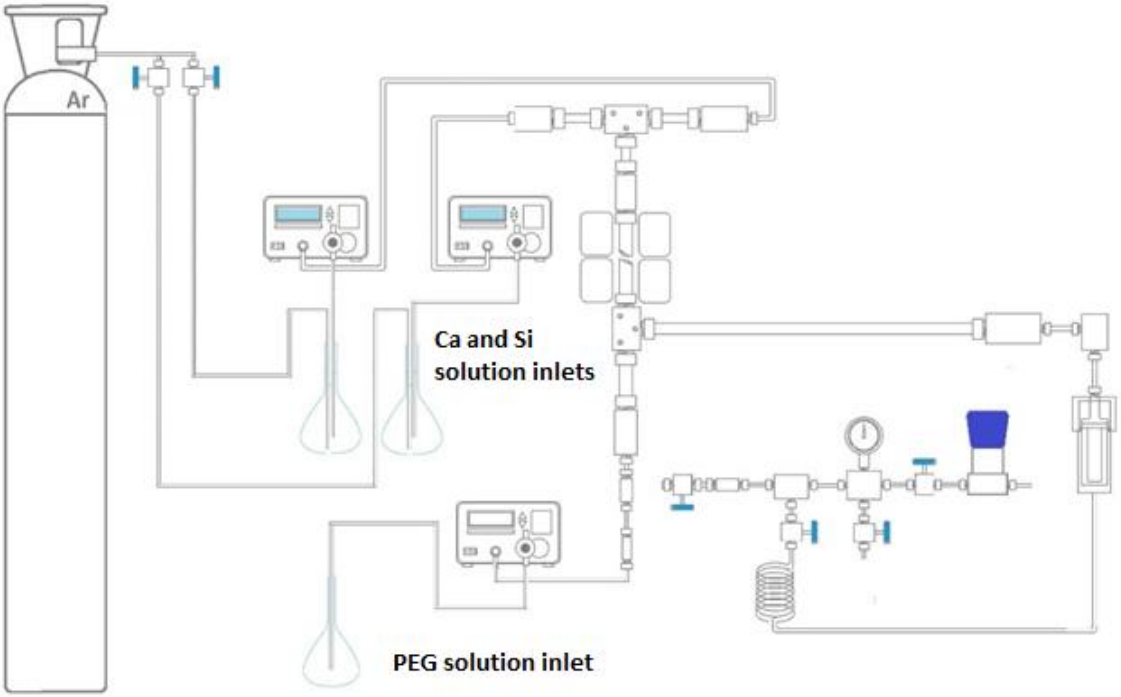

Figure II.9: Scheme of continuous reactor in two steps for tobermorite synthesis. Third setup.

The solution precursors employed in this experiments were $Na_2SiO_3 \cdot 9H_2O$ as silicon precursor, $Ca(NO_3)_2 \cdot 4H_20$ as calcium precursor and $Al(NO_3)_3 \cdot 9H_2O$ as aluminum precursor. Aluminum salt was employed as stabilization element as in subcritical batch reactions. The Ca/(Si+Al) ratio was fixed to 0.83 and the aluminum content (Al/Si+Al) was fixed to 15% as maximum content found in literature for this kind of structures. Furthermore, the reaction carried out with polyethylene glycol maintained the ratio Ca/PEG equal to 1.5. Solution concentrations and experiment conditions are shown in Table II.4.

Table II.4: Summary of synthesis conditions employed for tobermorite.

[Ca]	Al/(Si+Al)	Ca/(Si+Al)	T (°C)	P (bar)	Q1=Q2 (mL/min)	Residence time (s)
0.01M	0.15	0.83	400	235	4.5	7
0.01M	0.15	0.83	400	235	6.5	5

II.4. Preparation of cement pastes.

Prepared samples were added to cement powder in 1% w/w (weight of particles per weight of cement) and the solids were premixed for 1 min at 300 RPM. Then water (water/cement weight ratio equal to 0.4) was added, and the mixture was mechanically stirred for 1.5min at 750 RPM, the stirring was stopped for 1min and then it was stirred again for 1.5min at 750 RPM.

Once the paste was well mixed, part of the paste was used to study its rheological properties, part was employed to study the hydration by calorimetry, and the rest was cast into six 6x1x1cm^3 molds (Figure II.10 B) which were stored for 8 and 24 hours in a humidity chamber (temperature of 20°C and 96% of humidity). After that time the specimens were demolded, and flexural and compression tests were carried out. The equipment employed to mix the cement pastes was a Heidolph RZR 2102 Control mixer and an IBERTEST compacting machine was used to compact the paste.

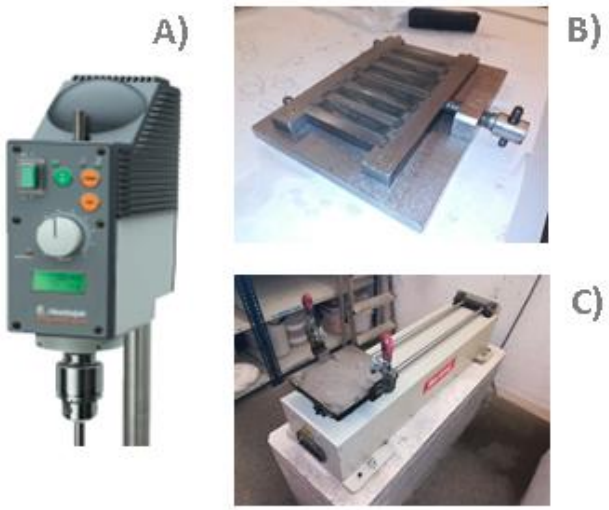

Figure II.10: Equipment employed to mix the cement pastes. Mixer (A),6 6x1x1 cm^3 mold (B) and compacting machine (C)

II.5. Characterization methods.

This work has focused not only in synthesis of different seed admixtures by different synthesis routes. This worked has focused on structural, elemental and morphological analysis of the obtained products. Moreover, several methods have been used to characterize the rheological and mechanical behavior of these admixtures in fresh and cured cement pastes, respectively. This section will describe the different characterization methods and assays employed.

II.5.1. X-ray diffraction measurements.

An X-ray diffractometer (XRD) "Phillips PANalytical X'Pert powder PW 1820" was employed to characterize the crystalline phases present in synthesized samples. Most samples were measured in a 27cm back-loading sample holders. In some cases, when the amount of sample obtained is not enough to fill the sample holder, a silicon holder was employed to carry out the measurement. The measuring conditions used are associated to programs "rutina_ASTM" and "rutina corta" and are shown in Table II.5. All the collected spectra were analyzed using "PANalytical HighScore Plus 4.8" software.

Table II.5: Measurement settings for X-Ray diffractometer.

	CuKα1 (1.5406A)
Initial angle [°2θ]	2.01
Final angle [°2θ]	74.99
Voltage and intensity settings	40kV, 40mA
Divergence slit type	Fixed
Divergence slit size [°]	1
"Rutina ASTM" program	
Angle step [°2θ]	0.02
Measuring lapse per step [s]	2
"Rutina corta" program	
Angle step [°2θ]	0.02
Measuring lapse per step [s]	1

II.5.2. Nuclear Magnetic Resonance (NMR)

Nuclear Magnetic Resonance can measure samples in solution and solid state. Both methods are excellent ways to determine the exactly chemical group positions and composition in our samples. This technique is based on the effect of a radiofrequency wave pulse on a sample under a constant applied magnetic field.

If we disturb this magnetic moment using an electromagnetic pulse orientated in a different angle from the applied magnetic field, we can measure a precessing

magnetization (resonance) produced in the sample. This pulsed wave, which has a specific frequency, can resonate with a specific element nucleus. An element can interact with this wave in different ways depending on the neighbors they have surrounding them.

In a conventional NMR spectrum, we measure the chemical shift parameter. This value corresponds to the difference between the resonance frequency of a nucleus and a reference frequency. That difference is always the same and is associated to the chemical environment where a specific atom is surrounded by specific neighbors. The intensities of each peak in the spectrum is related to the population of each type of chemical site.

The transductor in the equipment is based on an external coil, free of influence of the radiofrequency field, that experiments an electrical current induced from the precessing magnetization of the nucleus spins. This electrical signal can be represented in a FID (Free Induced Decay) curve.

A real FID graphic in time domain is too complicated to extract the frequency of the different resonances present in the sample. So, the best way to proceed is introducing the time dependent signal to a computer. Using a Fourier transformation, we can convert the signal from the time domain to the frequency domain.

Due to the nature of the samples prepared during this thesis, measurements were carried out in solid state NMR (ss-NMR). Solid state-NMR was also used because it could help us to distinguish structural changes in crystalline phases. However Solid-State NMR has some disadvantages due to solids which behave different in NMR experiments.

The ss-NMR spectra present a signal broadening due to the orientation-dependent interactions on nuclear spins. In one hand this broadening effect can be narrowed experimentally but on the other hand in some cases this can provide some useful chemical information.

There are three different broadening interactions: Anisotropic Chemical Shielding (Diamagnetic and Paramagnetic), Dipole-Dipole Coupling and Quadrupole Coupling. High-resolution NMR uses different special equipment to provide the same info

available for high resolution NMR (Magic-Angle spinning, Cross Polarization or special 2D experiments for example).

In polycrystalline samples, small crystals have several orientations respecting to static applied magnetic field. Depending on the nucleus and the chemical environment we obtain dispersed peaks. This is due to the shielding effect produce by electrons and its anisotropic distribution around the nucleus. This effect is called Chemical Shift Anisotropy (CSA) and is proportional to the applied magnetic field.

Magic-Angle Spinning (MAS) is used to eliminate the broadening resulted from the Anisotropic Chemical Shielding. It consists on the rapid isotropic motion of the sample to sharpen the NMR lines. As the angular dependency of Chemical Shift Anisotropy follows the equation 13.

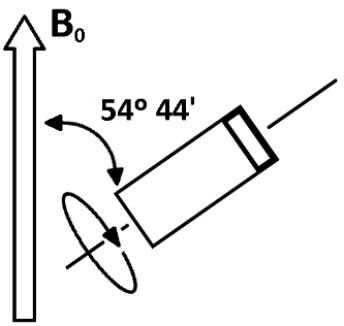

Figure II.12: Scheme of bearing probe orientation in respect to external magnetic field.

$$3\,cos^2\theta - 1 \qquad (13)$$

We can find that this formula is equal to 0 when the incident angles is 54° 44'. So, if the sample is put spinning on a rotor and with a 54,7° of inclination respect the magnetic field (magic angle) is possible to reduce these broadening effects (Figure II.12). This technique is also able to reduce Dipolar- Dipolar interactions but in some cases like ^{13}C NMR is not possible to make spin samples fast enough to eliminate Dipolar Broadening for some organic compounds.

The NMR spectra carried out in this study were recorded on a "Bruker Ultrashield 9.4 T" (AVANCE III 400) operated at 400MHz and equipped with a MAS-DVT probe. The data were collected and processed by solid state NMR department of SGIKER-UPV/EHU general services.

Three different MAS NMR were carried out based on ^{29}Si isotope, ^{13}C isotope and ^{1}H isotope. In the case of aluminum substituted tobermorite samples ^{27}Al NMR was carried out as well. In Table II.6 is gathered all the measurement conditions employed to obtain ss-NMR spectra in this work.

Table II.6: Measurement parameters followed for ss-NMR characterization.

Isotope analysis	Bearing probe (mm)	Spinning rate (kHz)	Pulse length (µs)	Pulse frequency (MHz)	Recycling delay (s)
^{29}Si	4	10	4	79.5	50
^{13}C	4	10	3.5	100.6	5
^{27}Al	4	10	0.45	104.3	0.5
^{1}H	4	10	3.85	400.2	1

II.5.3. X-ray Photoelectron Spectroscopy (XPS).

First known as Electron Spectroscopy for Chemical Analysis (ESCA), X-ray photoelectron spectroscopy (XPS) was introduced by Kai Siegbahn in mid-1960's. It consists on a surface quantitative technique. XPS can give information regarding the elemental analysis of a compound, the chemical state of the atoms and their electronic state inside a compound.

In other words, XPS is employed for determining chemical composition on sample's surface and structural analysis for inorganic, metal, semi-conductive and polymer compounds. Its use has grown very fast in the recent decades and now a lot of scientific literature and databases with reference spectra exist.

The way it works is based on the photoelectric effect explained by Albert Einstein in 1905 (Figure II.13). During the measurement, the sample is placed in an ultra-high vacuum (<10^{-9}mbar) chamber and it is irradiated by a monoenergetic (X-rays filtered by a monochromator) soft X-ray photon source. The most common used X-ray sources are Mg Kα (1253,6eV) and Al Kα (1486,6eV).

When the sample is exposed to the X-rays, a photon with a certain energy can eject electrons from the atomic electronic shell. Carrying out the measurements in ultra-high vacuum avoids interferences from gas molecules inside the measurement chamber.

The equipment measures the kinetic energy of the emitted electrons ($E_{Kinetic}$) as well as the number of electrons ejected. Through the kinetic energy of the expelled electron

and the X-ray photons energy (E_{photon}), it is possible to determine the binding energy ($E_{binding}$) associated to the electron ejected from the atom using the equation 14.

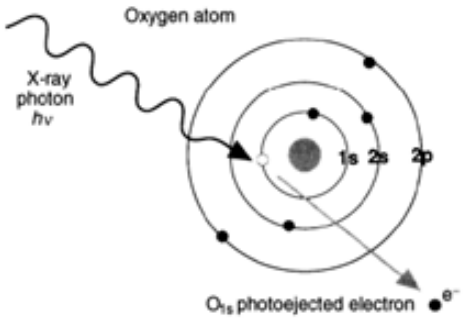

Figure II.13: Interaction photon-electron in photoelectric phenomena. Illustration about electron-photon interaction in orbital 1s.

$$E_{binding} = E_{photon} - (E_{Kinetic} + \phi_s) \qquad (14)$$

Where,

$\phi_s$is the spectrometer work function.

The penetration depth of the X-rays into the samples is between 1 and 10 microns. However, the electron penetration is much lower. Sampling depth is referred to the depth from which the 95% of photoelectrons are scattered when they reach the surface. This depth is around three times the wavelength of the incident photons source (for AlK_αν=1-3.5nm). Therefore, only electrons expelled from a depth of tens of Angstroms can leave the sample without energy loss and give a good XPS signal. Those electrons ejected from a deeper stratus suffer an inelastic energy loss that increases the background at higher binding energy from the main photoelectron signals.

Moreover, there are two photoionization phenomena associated to XPS. Photoelectron is the main signal but also Auger Electron (Figure II.14) can be produced after the photoelectron has left the element. In this case other electron has been expelled due to the rearrangement of electrons in the ionized atom shell.

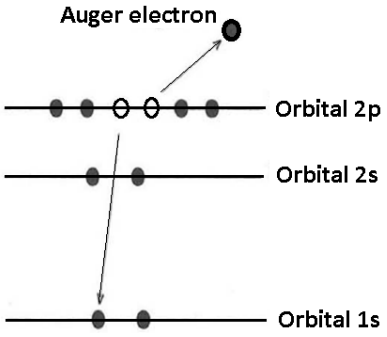

Figure II.14: Energy bands illustration about Auger Electron generation.

In a XPS spectrum the number of electrons detected versus the electron binding energy in a fixed small energy interval is plotted. There are also other peaks in a XPS spectrum that are not the main contributions and they have to be considered to carry out a good line identification. These lines are X-ray satellites, X-ray Ghost lines, shake up lines, multiple splitting lines, valence lines and energy loss lines.

This technique is not only capable of identifying elements and quantify them inside the sample. It can measure changes in binding energies of a core electron within an element due to a change in chemical bonding of that element with other neighbors inside the structure. So, changes in chemical environment or interactions present in the structure for a specific element can be observed by XPS.

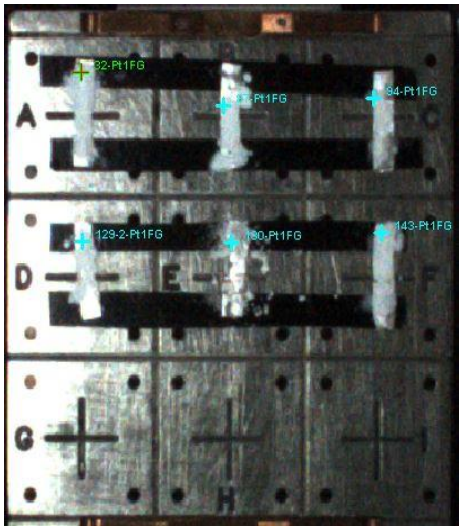

Figure II.15: Image of prepared samples inside vacuum chamber in XPS equipment.

The XPS experiments, were carried out in ThermoFisher Scientific K-ALPHA equipment located in PLateforme Aquitaine de CAractérisation des MATériaux (PLACAMAT) by Christine Labrugère. Each sample was measured as received and the powder was mounted, dusting and pressing, onto an indium plate as it can be seen in Figure II.15. The analysis was undertaken using a AlKα (hυ=1486,6eV) X-ray source and a 400-micrometer spot size. A pressure of 10^{-7} Pa was reached in the chamber when transferring the samples. As we are working with insulating samples, these tend to charge, and a flood gun is used to eliminate this effect.

The full spectra (0-1100eV) were obtained with a constant pass energy of 200eV. After an initial overall spectrum, more precise spectra were recorded with a 40eV pass energy for the important elemental lines (i.e. Si2p, Ca2p, Al2p, O1s, Na1s and C1s).

An ionized argon sputter-etching treatment was done to the sample. This ion etching is commonly used to obtain information on elemental composition as a function of the etched depth. Sputter rates can be calibrated and translate the sputtering time in depth

information. By doing this, surface contaminants can be removed and, the elemental composition profile of our samples can be described.

Furthermore, high resolution spectra were quantified and fitted using the ADVANTAGE software provided by ThermoFisherScientific.

II.5.4. Scanning Electron microscopy (SEM).

Scanning electron microscopy images were obtained with a "FEI Quanta 200 ESEM" microscope. This equipment is an Environmental Scanning Electron Microscope that works with high and low vacuum and allows to analyze samples without metallizing them. Images of samples can be taken using a secondary electron detector or a back-scattering detector.

Furthermore, this equipment includes a Fluorescence Dispersive Energy Spectrophotometer (EDAX) to analyze different heavy elements in the samples. We set high vacuum conditions and a work distance of 10mm during the measurements. To carry out the elemental analysis, the electron emission source was set up with a voltage of 30kV (emission intensity of 102µA).

II.5.5. Low-Resolution Transmission Electron Microscopy (LR-TEM).

A "JEOL JEM-2200FS/CR" equipment located in BIOGUNE Research Centre was used. It is equipped with a "GATAN CCD UltraScan 4000 SP (4008x4008pixels)" camera. The electron source is a ZrO/W filament that works with a maximum voltage of 200kV. This allows a limit resolution of 0.14nm.

The samples were prepared by ultrasound in a diluted water suspension (100 mg/L). A drop of this suspension was deposited on a copper grid and let it dry for 1h at room temperature. Previously these grids are treated with plasma treatment to enhance the contact of the drop to the substrate where is deposited.

II.5.6. High Resolution Transmission electron microscopy (HR-TEM).

High-resolution C_s-corrected TEM imaging was used for the observation of particles at high magnifications. This part of the study was outsourced to CIC-nanoGUNE in San Sebastian. The equipment used was a TITAN 60-300 (ThermoFisher, ex FEI) HR-TEM. It is equipped with a high-brightness Schottky field effect gun (*XFEG*) with a monochromator and operates with an acceleration voltage of 300kV.

Samples were prepared by dispersing the particles by ultrasound in acetone (>99.8% purity) (100 mg of sample/Liter of acetone). and placing a drop of the suspension on a substrate and letting it dry.

II.5.7. Infrared spectroscopy (FT-IR).

Conventional Transmission Infrared spectra of the samples were measured at room temperature using a Perkin-Elmer Spectrum 100FTIR. It was operated over the range 400-4000cm^{-1}. Samples were prepared by dilution of the sample powder in a dry solution with KBr (around 2% w/w).

II.5.8. Elemental analysis by X-Ray Fluorescence (XRF).

In this work, a "Thermo Scientific" ARL PERFORM'X 4200 equipment was used for the characterization of the elemental analysis of several of the samples. This equipment uses 4200W solid-state X-ray generator working at 70kV or 140mA maximum.

II.5.9. Thermogravimetric Analysis and Differential Scanning Calorimetry.

TGA-DSC measurements were carried out at Malaga University. A "TGA/DSC 1 METTLER TOLEDO" was employed. This equipment is composed of a horizontal oven "HT1600", that can work between room temperature and 1600°C, and an ultra-highly sensitive "MX5" weight scale with a "HSS6" Pt-Rh DSC sensor. The weight scale is refrigerated by water at 22°C and protected with a N_2 gas stream at 20ml/min.

TGA-DSC analysis were carried out in 70µL of alumina pots in which 5mg of sample were introduce. The measurements started at 30°C and ended at 900°C (heating rate 10°C/min). The atmosphere employed was air with a flow rate of 50mL/min.

II.5.10. Z-Potential measurements.

A "Zetasizer nano z" is an instrument capable of measuring two properties of particles in suspensions: particle size and Zeta potential. This study has focused on its used to determine the colloidal stability of samples in water, by measuring their Z-potential.

The equipment can determine the size of particles suspended by measuring their Brownian motion using Dynamic Light Scattering (DLS). In order to measure the Zeta potential, the equipment combines two different techniques, the electrophoresis technique, and laser doppler velocimetry. To do this the instrument has a 532nm 'green' laser equipped, that measures how fast a particle moves in a liquid when an electric field is applied.

The velocity of the particle and the electrical field applied are data that analyzed together with density and dielectric constant properties of the particles, provided by the user, gives the zeta potential as result.

To carry out these experiments, suspensions of two different concentrations in water were prepared for each kind of sample. First, 25mg and 50mg of solid were added to 10mL of miliQ water. Then each preparation was treated with ultrasound for 10min before measuring. Three measurements were carried out for each sample and the stabilization time employed in each measurement was 5min per condition to guarantee a representative average value of z-potential.

II.5.11. Isothermal Calorimetry.

The Calorimetry measurements to study the effect of the additions in cement hydration, were performed on a "TA Instruments' TAM air isothermal calorimeter". It is composed of eight channels that can work at the same time measuring the heat generated during cement hydration. This equipment can regulate and stabilize the temperature inside the system (Set point of 25±0.02°C).

6g of cement paste with the addition were introduced in 20mL polystyrene flask and put inside the calorimeter channels. The equipment needs one flask with the sample and another with 6g of water. The water flask is a reference to measure the heat flow generated.

II.5.12. Rheological analysis.

A "TA Instrument Discovery HR1 Hybrid" rheometer was employed. This equipment can measure the rheological behavior of different cement pastes.

A 40mm parallel plate geometry has been employed to do the rheological test. The flow sweeps employed in these tests were logarithmic, increasing shear rate from 0.01 s^{-1} to 100.0 s^{-1} and then decreasing from 100.0 s^{-1} to 0.01 s^{-1}. 20 points per decade were measured and no soak time (time needed to homogenize temperature) was applied during the experiments. The temperature conditions during the measurements are controlled by a Peltier plate cooled by a "Thermo Cube" water chiller. The experiments were carried out at 20°C.

II.5.13. Flexural and compression tests.

Mechanical tests were carried out to the cement specimens with the different calcium silicate hydrate additions at 8 and 24h. Ibertest ELIB-10-W universal machine was used with two different accessories to carry out flexural and compression tests. The specimens tested were prism shaped samples of 6x1x1 cm.

The specimens were tested first at bending. Then the resultant pieces were tested at compression. All the cement pastes probes have a water cement ratio of 0.4 and contain a 1% weight of nano additions. Table II.7 shows the test conditions used for cement specimens.

Table II.7: Electromechanical test machine settings

	Test specimens after 8 h		Test prisms after 24 h	
	flexural settings	compression settings	Flexural settings	compression settings
Dimensions (mm)	60x10x10	60x10x10	60x10x10	60x10x10
Movement rate (mm/min)	30	30	30	30
Loading rate (mm/min)	1	5	10	10
Initial preload (N)	1	10	5	10

II.6. References.

[1] Gartner, E.M., Jennings, H.M., *J. Am. Ceram. Soc. 70*, (**1987**), pp. 743–749.

[2] R. Gabrovsek, B. Kurbus, D. Mueller, W. Weiker, *Cem. Concr. Res.23*, (**1993**), pp. 321–328.

[3] T. Mitsuda and H.F.W. Taylor, *Cem. Concr. Res. 5*, (**1975**) 203–210.

[4] W. Tan, G. Zhu, Y. Liu, Z. Zhang, L. Liu, *Cem. Concr. Res. (***2015**), *72*, pp. 69–75.

[5] L. Black, K. Garbev, A. Stumm, *Adv. Appl. Ceram.* 108, 3 (**2009**).

[6] X. Li and J. Chang, *J. Mater. Sci. 41*, (**2006**), pp. 4944–4947.

[7] M. Diez-Garcia **2017**. *"Synthesis by supercritical fluids methods of advanced additions for cementitious materials"* Universidad del País Vasco/Université de Bordeaux. Repositorio institucional ADDA EHU Biblioteka UPV/EHU.

[8] E. B. Nelson and G. L. Kalousek, *Cem. Concr. Res. 7, 6,* (**1977**), pp. 687-694.

[9] K. Baltakys and R. Siauciunas, *Materials Science-Poland, Vol. 25, No. 1*, (**2007**)**.**

[10] F. Liu, X. D. Wang, J. X. Cao, *International Journal of Minerals*, *Metallurgy and Materials, 20*, *1*, (**2013**), pp. 88-88.

[11] Stirrer reactor manual "Parr Instruments" 230M Safety in the Operation of Reactors & Pressure Vessels. https://www.parrinst.com/support/downloads/manuals/

[12] X. Huang, D. Jiang, S. Tan, *Mater. Res. Bull.*, *37*, (**2002**)**,** pp. 1885–1892.

[13] M. Diez-Garcia*, J. J. Gaitero, J. S.Dolado, C. Aymonier, Angew. Chem.* (**2017**), 129, pp. 1–6.

[14] Z. G. Estephan, P. S. Schelenoff, J. B. Schlenoff, *Langmuir, 26(22),* (**2010**), pp. 16884–16889.

[15] M. Diez-Garcia, J. J. Gaitero, J. I. Santos, J. S. Dolado, C. Aymonier, *J. Flow. Chem.* 8, (**2018**), pp. 89–95.

CHAPTER III. SYNTHESIS OF XONOTLITE MODIFIED WITH ORGANIC COMPOUNDS IN BATCH REACTOR.

III.1. Pristine xonotlite synthesized in subcritical conditions.

The experiments carried out at 250°C and 38bar to synthesize pristine xonotlite looked for reproducing previous experiments and establishing the optimal conditions for the next experiments that involved organic modifications. This part of the chapter is focused on the characterization of pure phases. It will allow establishing a reference sample and will help to study the effects of organic modifiers on crystalline structures.

III.1.1. Structural analysis of pristine xonotlite.

Unlike previous works [2-7], the synthesis of xonotlite carried out in this study was prepared in only 4h following the synthetic route developed by M. Diez-Garcia [8]. The yield of the reaction ranged between 98 and 100%. Only 4 hours were necessary to obtain a product whose XRD diffractogram showed to be crystalline xonotlite.

Figure III.1 shows the XRD pattern of the obtained product. Most of the peaks could be assigned to xonotlite phase (ICDD data base, PDF 00-023-0125) [1] concluding that the main phase obtained was crystalline xonotlite.

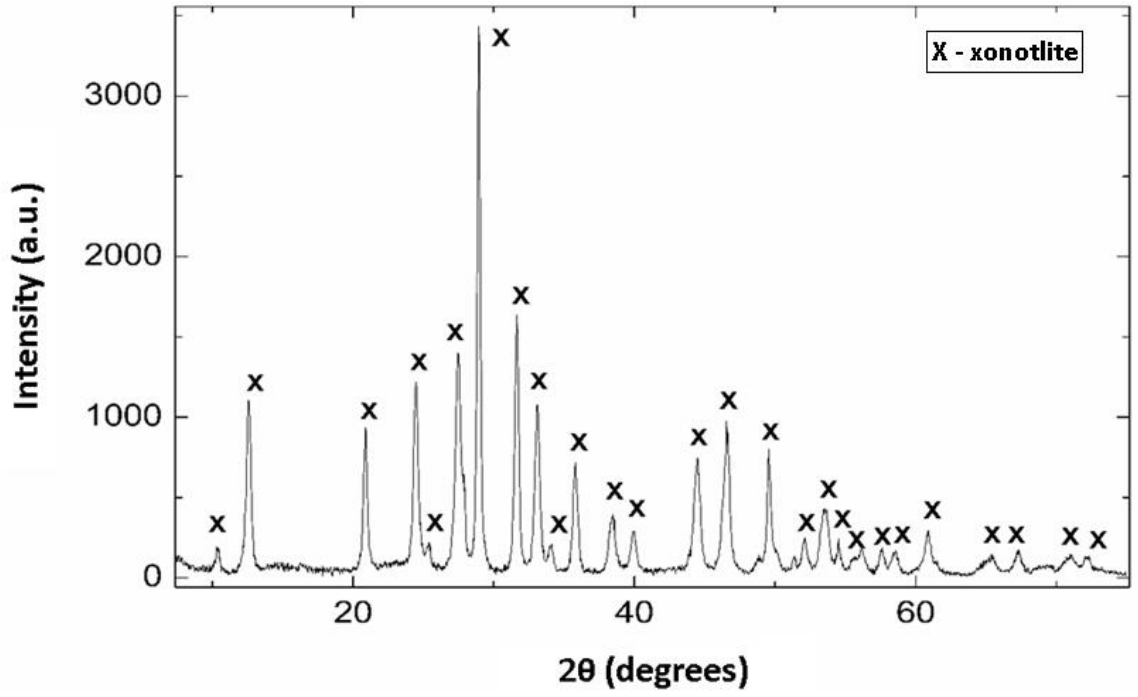

Figure iII.1: XRD pattern of crystalline xonotlite obtained at 250°C 38 bar for 4 hours.

It is important to mention the presence of a peak at 4.21Å (2θ=52.13°) is associated to the plane (400) that is characteristic of xonotlite. Contributions like (200) or (320), associated to xonotlite peaks at 8.5Å (2θ=25.38°) and 3.08Å (2θ=49.95°) respectively, were also found in the XRD pattern. No significant shifts from XRD contributions of natural or synthetic xonotlite were measured.

In preliminary results, few impurities were observed. The main byproduct found was Calcite ($CaCO_3$) in small traces. It is worth to highlight that Calcium Silicate hydrates, even crystalline phases like xonotlite, are very susceptible to absorb CO_2 if there are some residual humidity on its surface under air atmosphere [10, 11]. This can be avoided working at inert atmosphere, because during its manipulation or characterization this carbonation effect can happen residually. Nevertheless, the carbonation was eliminated for the successive experiments as can be seen in results showed in Figure III.1.

The elemental analysis of the product was carried out by EDS which showed that the sample synthesized contain a Ca/Si ratio close to 1 (Ca/Si=1.04) which is the ratio of the ideal structure of xonotlite. In order to evaluate the suitability of the EDS as a characterization method for elemental analysis of the Ca/Si ratio the sample was also characterized by FRX. The FRX analysis gave a Ca/Si ratio of 1.00 (see Table III.1 for the different values of each element obtained by EDS and FRX) which is very similar to the value given by the EDS. This indicates that EDS is suitable to measure the Ca/Si ratio of the synthesized samples.

Table III.1: Comparative values of elemental analysis between XRF and EDS measurements for xonotlite pristine.

Element	Atomic % by XRF	Atomic % by EDS	Correction factor
Calcium	19.97	19.36	1.03
Silicon	19.93	18.64	1.07
Oxygen	60.1	62.00	0.97
Ca/Si	0.998	1.038	0.97

Infra-red spectroscopy was employed to complement the structural information given by X-ray diffraction. Figure III.2 shows the infrared spectrum of the synthesized pristine xonotlite. Typical bands of calcium silicate hydrates are observed in the IR spectrum. The

narrow absorption band at 3612 cm^{-1} can be assigned to the stretching vibration mode of Ca-OH groups. This band is characteristic of xonotlite. Large bands at around 1082cm^{-1}, 975cm^{-1} and 903cm^{-1} are associated to asymmetric stretching vibrations of Si-O bonds. Furthermore, there is also an intense band at 1200cm^{-1} which is also related to stretching vibrational mode of Si-O bond and it is a characteristic band of xonotlite. According to the study of Yu *et al.* [12] who compared the IR bands with the ^{29}Si NMR signals, the band at 1200 cm^{-1} is due to the vibration of Si-O bonds in branching positions and the bands at 1082cm^{-1}, 975cm^{-1} and 903cm^{-1} can be assigned to the Si-O bonds in pairing position [13]. Other intense contribution can be found between 457cm^{-1} and 671cm^{-1}. They can be associated to the bending vibrational mode of O-Si-O and Si-O-Si [5].

Moreover, there are also other contribution around 820cm^{-1} which could correspond to silicate tetrahedra located at the end of silicate chains or located next to a silicon vacancy or imperfections [12]. However, this region overlaps with other bands associated to carbonated species and thus the assignment of those bands is not certain.

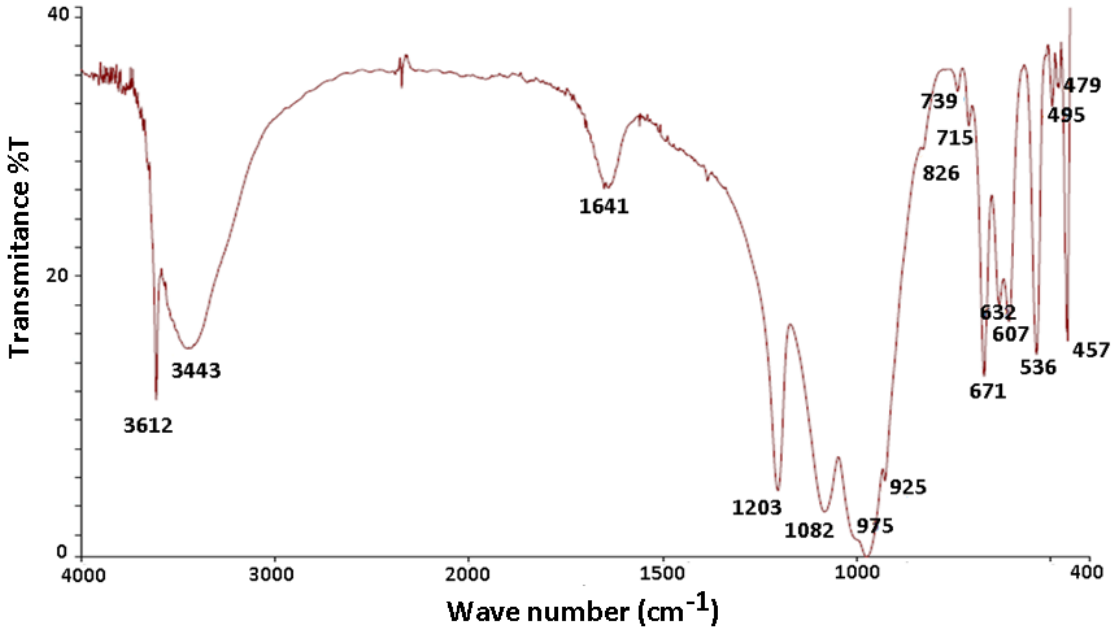

Figure III.2: FT-IR spectrum of pristine xonotlite synthesized at 250°C 38bars for 4 hours.

There is a large band around 3400cm^{-1} which can be assigned to the stretching mode of hydroxyl groups from silanol (Si-OH) or/and water molecules suggesting that there might be silanol groups in the structure. Theoretically, the ideal structure of xonotlite does not contain silanol groups although many synthetic ones do [13].

Furthermore, a shoulder around 1414-1481 cm^{-1} was observed which is typical of C-O stretching vibrational modes in carbonate anions [13, 14]. Although a quantitative analysis was not carried out by FT-IR, the conclusion was that the product obtained is crystalline xonotlite; carbonate contribution is not significant and can be assumed to be negligible.

^{29}Si and ^{1}H ss-NMR experiments have been also carried out in this work to analyze further the structure of xonotlite. ^{29}Si NMR spectrum (Figure III.3) presents two main peaks for xonotlite, -87ppm (Q^2) and -98ppm (Q^3). Q^2 and Q^3 are associated to silicon atoms in tetrahedral coordination that are bound to two or three other silicate tetrahedra through oxygen atoms respectively.

According to the literature, Q^2 and Q^3 contributions are also named pairing (or bridging) and branching silicate tetrahedra respectively [15-17]. Furthermore, the Q^2 peak shows a splitting suggesting that there are two signals. According to the reference [18] this is due to two different chemical environments around the silicon atoms in bridging position with different bonding lengths and angles inside the structure.

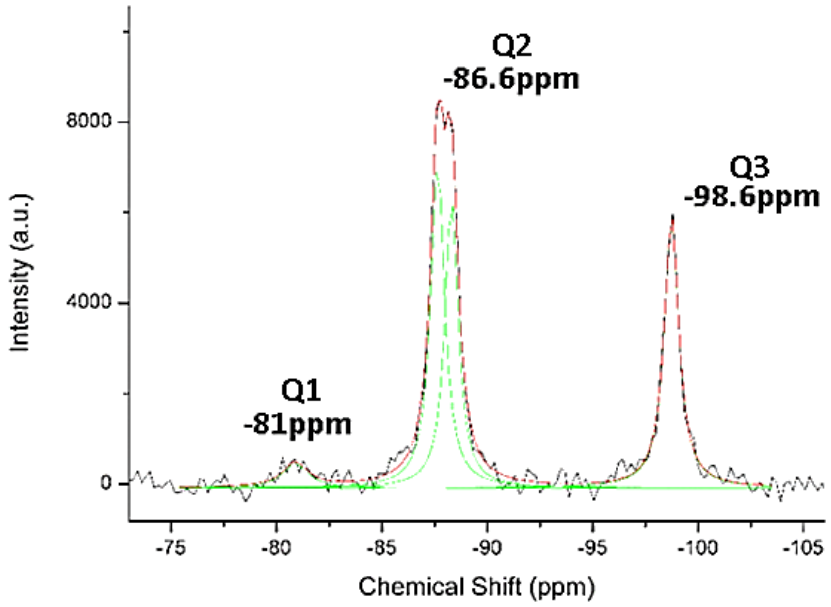

Figure III.3: Experimental (black curve) and deconvoluted (red curve) ^{29}Si solid state nuclear magnetic resonance of pristine xonotlite. The green curves are the individual peaks used for the deconvolution of the signals.

Furthermore, a small peak at -81 ppm which can be assigned to Q^1 is also observed. It is typically found in xonotlite synthesized by hydrothermal routes. This peak is related to silicates which are bound to only one other silicate tetrahedra. They are found at the end of the chains and at imperfection sites in the xonotlite crystal. The lowest Q^1 contributions are present in xonotlite, the less imperfections are in its structure [15].

More information like polymerization degree of silicate chains or deviations from theoretical structure in xonotlite can be extracted from NMR spectra deconvolution. To do so the signals of the spectrum were deconvoluted fitting them to pseudo-Vogt curves as shown in Figure III.3 (green curves) and their areas were calculated (Table III.2). In one hand, we calculated the Q^2/Q^3 ratio from the areas obtained in Pseudo-Voigt deconvoluted curves. The silicate chains in xonotlite grow along the b- axis (the same direction of the length of these fibers) following a Dreierketten arrangement [8]. As it was mentioned in chapter 1, Q^2/Q^3 ratio in the ideal structure should be 2.0 according to the ideal structure of xonotlite (see section 1.2.5.1). The result for pristine xonotlite in this study was 2.1, near to the value for perfect quasi infinite chain of silicate in the ideal xonotlite.

Table III.2: Areas calculated from deconvolution of 29Si ss-NMR of pristine xonotlite sample.

Chemical shifts of the fitted peaks in the deconvoluted ^{29}Si ss-NMR spectrum	Deconvoluted area	Relative intensities of peaks (%)
-98.7ppm (Q^3)	7898	30.7
-88.3ppm (Q^2)	7632	29.6
-87.6ppm ($Q^{2'}$)	8963	34,8
-80.9ppm(Q^1)	1253	4.9

From deconvoluted areas of the ^{29}Si NMR signals it is also possible to calculate the mean chain length parameter (MCL). This value is obtained from Q^1 population ratio (equation 15) and it gives indirectly information about the average length of silicate chains in xonotlite [19, 20]. The MCL value for pristine xonotlite obtained in this study was 41. This is higher than other values reported in the literature, around 15 for C-S-H with a

Ca/Si molar ratio near to 1.0 [40]. The higher this parameter is, the more crystalline the structure of xonotlite is considered.

$$\mathbf{MCL} = \frac{\mathbf{2}}{\frac{\mathbf{Q^1}}{(\mathbf{Q^1}+\mathbf{Q^2}+\mathbf{Q^3})}} \qquad (15)$$

^{1}H ss-NMR of t pristine xonotlite was also carried out (Figure III.4). In the spectrum a signal at 2.05ppm with two shoulders at 1.77ppm and 1.12ppm can be seen. Furthermore, two broad peaks at 3.48ppm and 4.8ppm can also be observed. Noma *et al.* [18] characterized natural and synthetic xonotlite by ^{1}H MAS NMR. Based on this study the signal at 2.05ppm is can be assigned to the protons of the -OH groups bound to calcium and the signal at 1.77ppm is associated to protons attached to silanol groups (Si-OH). However, the authors of ref [18] did not observe a peak at 1.12ppm which is observed in the actual work. Protsak *et al.* [21] in their study of the surface structure of hydrophobized fumed silica nanoparticles by ^{1}H NMR obtained a signal at 1.1ppm which they assigned it to the proton of isolated silanol groups, indicating the difference in chemical shift found comparing it to the chemical shift around 1.8 ppm usually found for silica [21]. Taking this into account, the signal at 1.12 ppm of pristine xonotlite could be also assigned to the protons of silanol groups but with a slightly different chemical environment to the silanol protons of 1.77ppm.

Furthermore, the two wider and less intense signals at 4.8ppm and 3.45ppm can be associated to adsorbed water on xonotlite [21]. The existence of these contributions confirms the previous results of FT-IR (hydroxyl groups stretching mode around 3400cm^{-1} and water bending mode at 1600cm^{-1}) which already suggested that there are silanol groups and adsorbed water in the structure. Moreover, the presence of silanol groups in ^{1}H NMR confirms the presence of vacancies in the silicate chain already indicated by the observed Q^1 signal in ^{29}Si NMR.

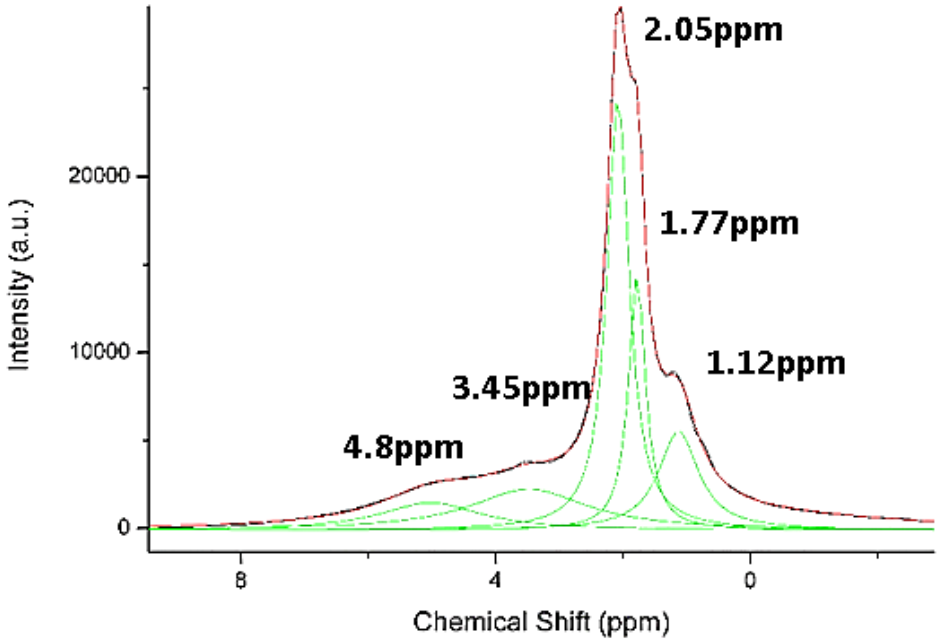

Figure III.4: Experimental (black curve) and deconvoluted (red curve) ^{1}H solid state nuclear magnetic resonance of pristine xonotlite. The green curves are the individual peaks used for the deconvolution of the signals.

Pristine xonotlite has been characterized by XPS as well with the purpose of describing/understanding further its structure. The XPS technique can provide useful information about the composition and chemical environment of surface elements.

However, it is important to mention that there are some problems associated to the insulating nature of silicates in this kind of samples that worsen the resolution of this technique. Moreover, the small shifts in binding energy observed for signals in samples of calcium silicate hydrates, makes more difficult to carry out its analysis.

In order to obtain the elemental analysis on surface by XPS, samples were treated with Ar ions (sputtering). This etching process allows to remove residual carbon (adventitious carbon) or other contaminants adsorbed on the surface layer. This way it is possible to obtain a composition profile of the different elements present in the sample at different etching times (Figure III.5 B). As it can be observed in the plot (Figure III.5 B), pristine xonotlite showed a similar composition of calcium and silicon atoms on its surface that confirms the expected Ca/Si ratio of 1.0.

High resolution experiments with lower pass energies were carried out to obtain information about the interactions between the different elements (Ca, Si, O and C) with their chemical environment. Furthermore, this measurement is obtained without sputtering treatment to avoid any modification or change in our samples. High resolution spectra obtained for xonotlite samples can be observed in Figure III.6.

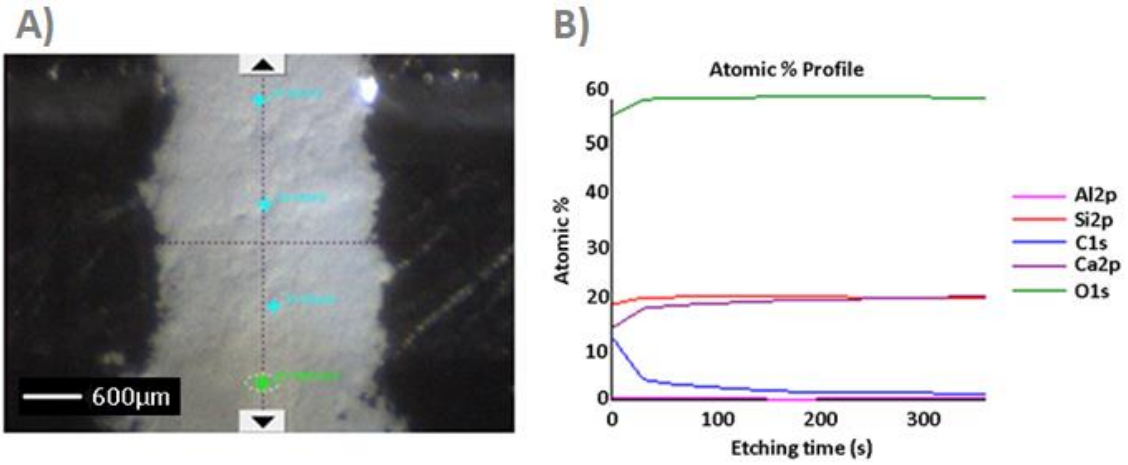

Figure III.5: Photography of the sample in XPS vacuum chamber A), sputtering composition profile of xonotlite sample B).

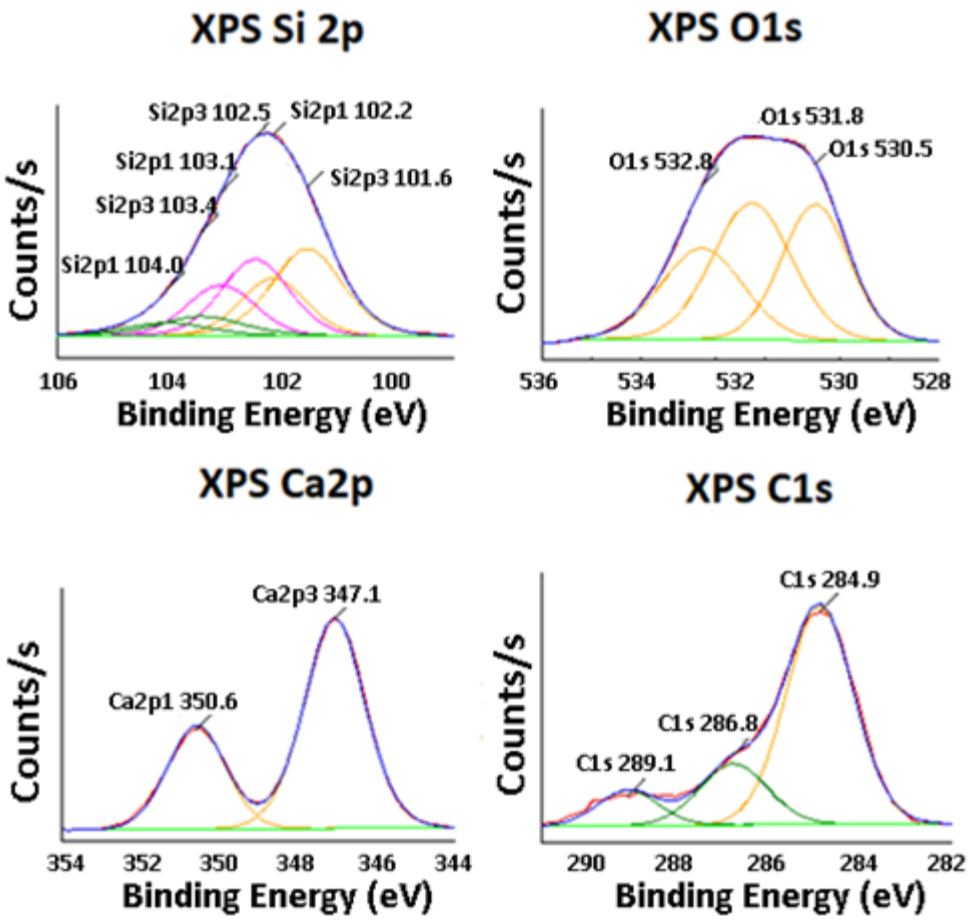

Figure III.6: Si2p, O1s, Ca2p and C1s XPS deconvoluted curve spectra of pristine xonotlite. Experimental (blue curve) and background (green curve).

Si2p band was selected to analyze instead of Si2s due to its sharper and more intense shape. In this case the obtained band for Si2p contributions was deconvoluted into 3 doublets (the doublets in each peak are associated to orbitals 2p 3/2 and 2p 1/2). This study focuses only in the binding energies for 2p 3/2 orbitals which are the ones showing the lowest binding energy in each doublet. One peak was observed at 101.5eV, another at 102.5eV and the last one at 103.4eV.

According to Putnis *et al.* [22] silicon atoms that are bound to other silicon atoms by oxygens (Si-O-Si), also named bridging oxygens, present longer bonding lengths, and higher binding energies than silicon atoms bound by a non-bridging oxygen to calcium atoms (Si-O-Ca) [23]. Following this interpretation, we associated the peak at 102.5eV to Si-O-Si bonding in silicate chains.

The other two peaks at 101.5eV and 103.4eV could be related to non-bridging oxygen positions like Si-O-Ca and Si-O-H (with a lower population in the structure), respectively. The contribution at 103.4eV associated to Si-O-H bonding also confirms the presence of silanol groups on xonotlite surface and it confirms the previous results obtained by infrared spectrum and ^{1}H ss-NMR.

In the case of O1s peak, the signal was deconvoluted into three main contributions at 530.5eV, 531.7eV and 532.7eV. The two first contributions are associated to non-bridging (NBO) and bridging oxygens (BO), respectively [24] and the last one could be associated to molecular water in xonotlite pristine. The association for bridging and non-bridging is explained due to the higher electronegativity of silicon in respect to calcium. Higher electronegativity decreases, atomic shielding experimented by bridging oxygens and this is associated to a higher binding energy [24].

Two signals, each fitted by one peak in the deconvolution process, of calcium element were obtained, one for Ca2p3 and another for Ca2p1 orbitals. According to literature Ca2p3 is more intense and sensitive to binding energy shifts. XPS analysis of Ca2p3 electrons in calcium gave a binding energy of 347.07eV, a reasonable value if it is compared to literature [24]. Ca2p3 for calcite contribution (around 347.2eV) is difficult to be distinguished from xonotlite Ca2p3 curves because is overlapped in that region.

In the C1s spectrum three signals can be observed which were deconvoluted by fitting each signal corresponding to 284.8eV, 286.5eV and 289eV. The first two contributions are not related to the sample and only can be interpretated as the presence of adventitious carbon on surface due to the exposure of xonotlite to moist air. However, the contributions at 289eV could be related to superficial carbonated groups.

III.1.2. Morphological analysis of pristine xonotlite.

Pristine xonotlite was characterized by scanning electron microscopy (Figure III.7 A) and transmission electron microscopy (Figure III.7 B). The morphology of the sample is needle or fiber-like as expected [25]. The images show that the fibers are agglomerated forming highly porous aggregates. The length of the needles is around 1µm and 3µm and the width around 80nm.

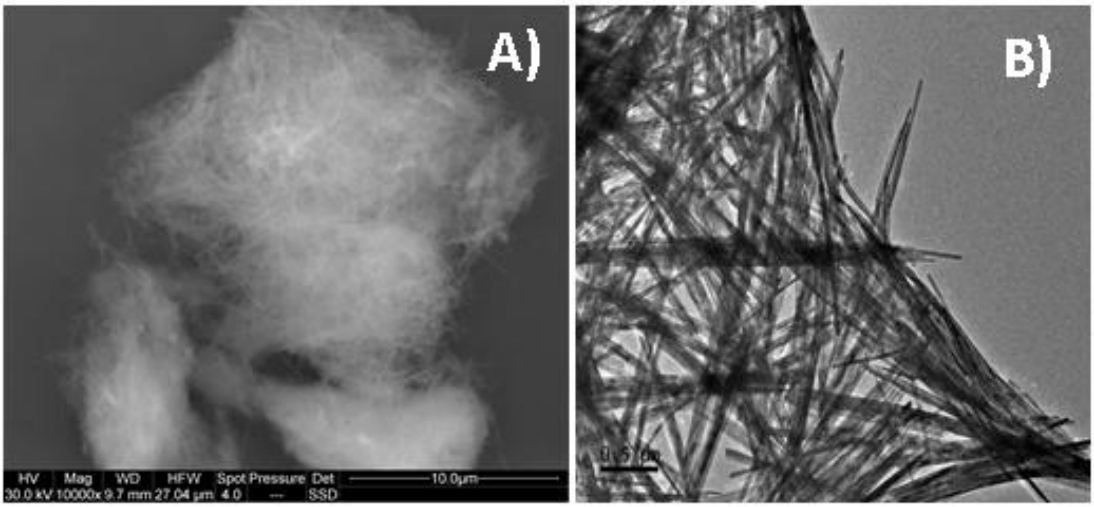

Figure III.7: SEM (A) and TEM (B) images of aggregated xonotlite fibers.

It is worth highlighting that pristine xonotlite did not easily dispersed in water, even using an ultrasound probe. The images showed that the fibers were not well dispersed and that it formed tangled larger structures (Figure III.7 A). It was concluded that this kind of crystals prepared in stirred batch reactor tends to aggregate forming spherical-like larger microparticles [9] due to its acicular shape.

HR-TEM characterization was also carried out to analyze the crystallinity of pristine xonotlite (Figure III.8). In the image a magnified fiber is shown. In the fiber different planes along its length can be observed. A value of 8.59Å was obtained for lattice distance between these planes oriented in the (200) direction. There are no significant differences between the measured value and the distance of 8.6Å reported in literature for a well crystallized xonotlite phase [25].

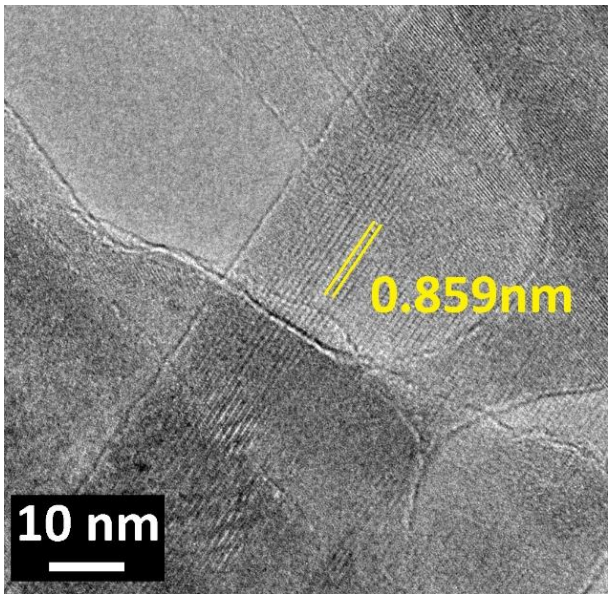

Figure III.8: Magnified HR-TEM image of pristine xonotlite particle.

From these results it can be concluded that the temperature and pressure conditions employed were enough to obtain a crystalline sample of xonotlite. These conditions will be used for samples modified with polyethylene glycol as well. Moreover, the structural parameters of a pristine xonotlite samples were well described to be compared to modified ones.

III.2. Xonotlite modified with polyethylene glycols. Synthesis under subcritical conditions.

This section is focused on the different effect observed in structure of xonotlite samples prepared in presence of polyethylene glycol polymers. These effects will be well characterized in order to make a comprehensive characterization of the product formed and analyze their behavior in cement pastes.

III.2.1. Structural analysis of modified xonotlite with PEG.

All the samples were characterized by XRD (Figure III.9). For xonotlite pristine and PEG MW600 modified xonotlite (X_P600), every diffraction peak was fitted to crystallized xonotlite (PDF 00-023-0125) [1]. The xonotlite samples modified with PEG MW1500 (X_P1500) and PEG MW 4000 (X_P4000) on the other hand, present two new intense

contributions around 19° and 23° associated to the presence of high molecular weight polyethylene glycol in the solid (PDF 00-049-2095) [30].

No significant changes in basal peak position or other peaks of the xonotlite were observed. This suggests that the PEG molecules did not enter inside the crystal, between silicate chains and CaO layers. Several studies can be found in the literature where the researchers have tried to intercalate PEG molecules within the CaO silicate layers in CSH gels, but no evidence of insertion of these organic molecules were found [29-31].

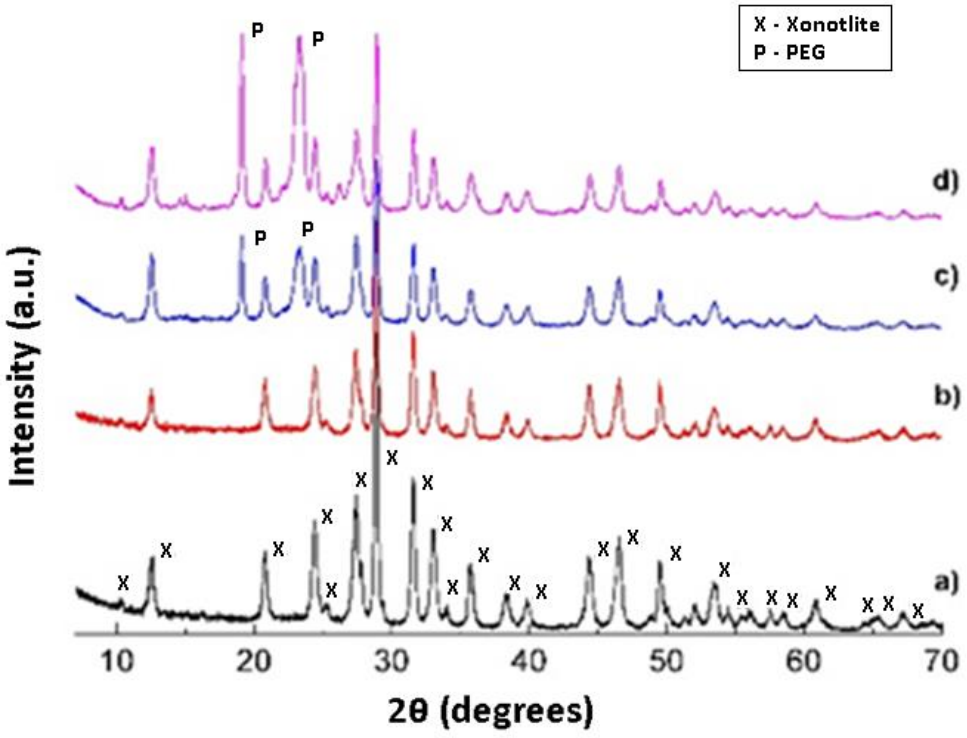

Figure III.9: XRD spectra of X_Pristine (a), X_P600 (b), X_P1500 (c) and X_P4000 (d).

In every FT-IR spectrum (Figure III.10) carried out for modified xonotlites the typical signals found in pristine xonotlite (3613cm^{-1}, 3400cm^{-1}, 1200cm^{-1}, 1083cm^{-1} and 975cm^{-1}) can be observed. It is also found a little signal around 815 cm^{-1} that corresponds to ending silicate tetrahedra in silicate chains. Signals with wavenumbers around 1400-1500 cm^{-1} typical of C-O stretching vibrational modes in carbonated species are even depreciable in modified ones [5, 13, 14]. So, there is no significant carbonation effect in the product as it was observed in XRD analysis. Furthermore, signal associated to water bending around 1600cm^{-1} and hydroxyls stretching at 3400cm^{-1} are also present for modified xonotlites.

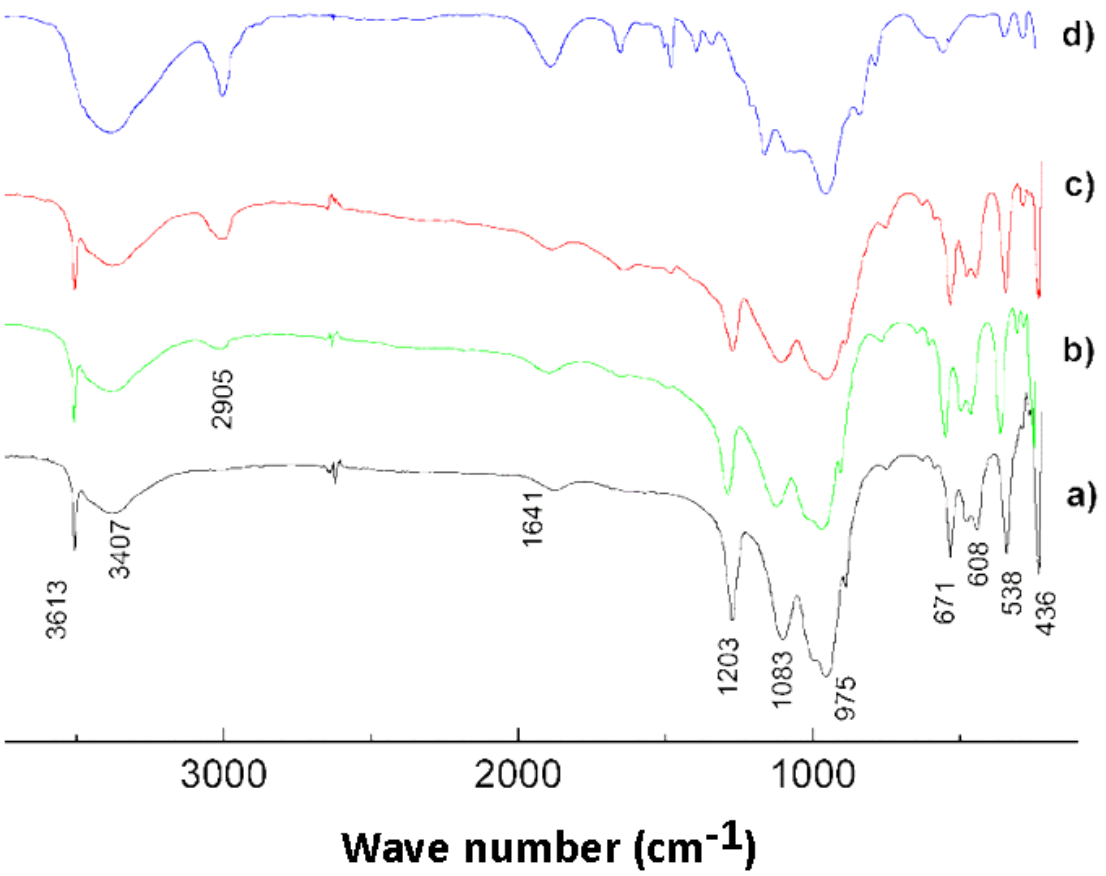

Figure III.10: FT-IR spectra of pristine xonotlite(a), X_P600 (b), X_P1500(c) and X_P4000 (d).

In all PEG modified samples, an absorption band at 2900 cm^{-1} associated to C-H stretching vibration of alkyl groups can be seen [32-34]. Moreover, it can be observed that this contribution increases when the molecular weight of the PEG added increases. The samples were characterized by TGA and the content of the organic compound in the samples was calculated to be 16%, 31.1% and 64,8% for samples X_P600, X-P1500 and X_P4000 respectively (see Table III.11). Taking this into account the increase in the signal around 2900cm^{-1} measured by FT-IR could be explained by the higher content of PEG in samples with higher molecular weight polymers.

^{29}Si, ^{13}C and ^{1}H ss-NMR experiments have been carried out in this work to analyze further the structure of the products. ^{29}Si NMR spectra plotted in Figure III.11 for all obtained samples show the three peaks found in pristine xonotlite. Q^2 (-87ppm) and Q^3 (-98ppm) signals appear which are due to silicon atoms in SiO_4^{4-} in bridging and branching positions in the silicate chain respectively [15, 16, 18]. In every modified sample

(X_P600, X_P1500 and X_P4000), Q^1 contribution is also found. This peak is due to the presence of silicate tetrahedra bound only to another silicate tetrahedra by an oxygen atom. As mentioned earlier, this peak is associated to silicate tetrahedra at the end of the silicate chains and imperfections due to the presence of vacancies along the silicate chain in the crystal.

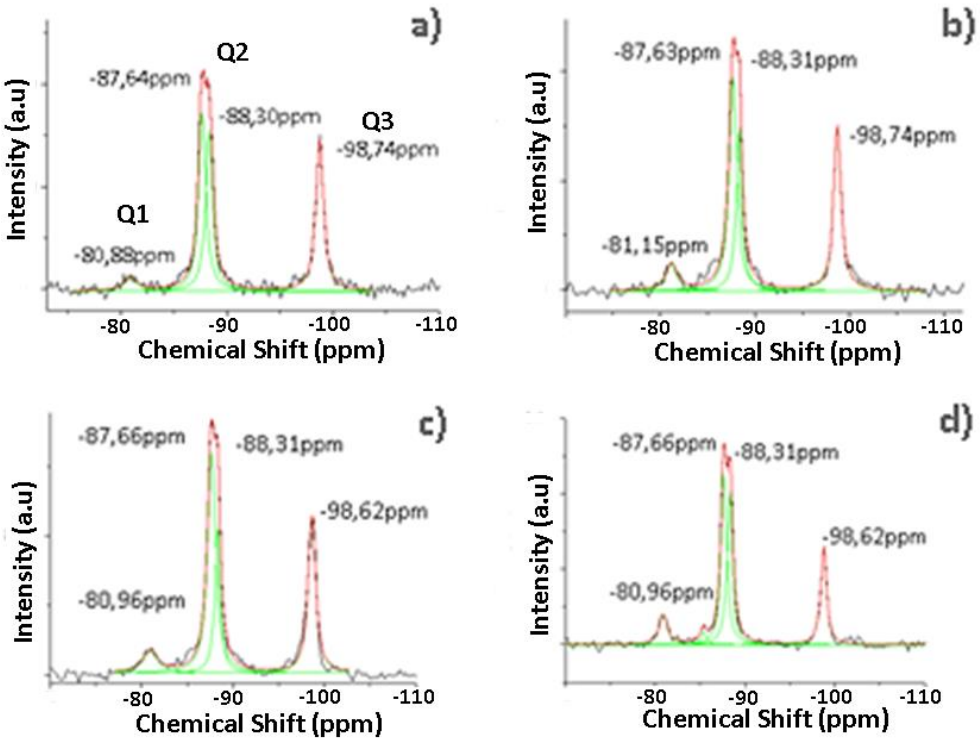

Figure III.11: ^{29}Si NMR of unmodified xonotlite (a) and PEG MW 600 (b), PEG MW 1500 (c) and PEG MW 4000 (d) functionalized xonotlite samples.

In order to study the effect of functionalizing with different molecular weights of PEG on the structure of xonotlite, a deconvolution analysis of the ^{29}Si NMR signals was carried out using a pseudo-Voigt profile. Then, the ratio Q^2/Q^3 and the populations of Q^3 and Q^1 were calculated (Table III.3). Furthermore, the mean chain length of the silicate chain was also calculated from Q^1 population following equation 15.

When PEG is added to the system or the molecular weight of the PEG employed is increased the Q^2/Q^3 ratio increases. In this study Q^2/Q^3 ratio increases from 2.1 in the case of xonotlite pristine to 2.17 for xonotlite prepared with PEG MW1500 (X_P1500) and 3.14 for xonotlite with PEG MW4000 (X_P4000).

Furthermore, according to the obtained results, the Q^1 contribution increases and MCL value decreases when the molecular weight of the PEG employed is increased. All these results indicate that the silicate chains of xonotlite are getting shorter when adding PEG and that xonotlite is losing crystallinity when the weight of PEG is increased in the reactor medium and confirms other results observed in literature [31, 35].

Table III.3: ^{29}Si ss-NMR Q^3 and Q^1 population Q^2/Q^3 ratio and mean chain length of prepared xonotlite samples.

SAMPLE	Q^2/Q^3	$Q^3/(Q^1+Q^2+Q^3)$	$Q^1/(Q^1+Q^2+Q^3)$	MCL
X_PRISTINE	2.10	0.307	0.049	40.81
X_P600	2.13	0.296	0.071	28.18
X_P1500	2.17	0.288	0.088	22.22
X_P4000	3.14	0.218	0.097	20.61

^{13}C ss-NMR spectra (Figure III.12) show three signals in all xonotlite samples functionalized with PEG. One signal is at 72.75ppm, another at 70.47ppm and the third at 61.15ppm. The most intense signal at 70.47ppm is due to intermediate carbons in polyethylene glycol chain and the peak at 72.75ppm is due to terminal carbons next to hydroxyl ending groups. The contribution at 61.15ppm could be associated to carbon next to the terminal carbon of the polymer chain (see Figure III.12 D).

Every signal has been compared to ^{13}C ss-NMR of the PEG employed in the synthesis and the same peaks can be observed. However, no significant shifts or new peaks were found in ^{13}C spectra of the modified xonotlite samples. This could indirectly indicate that there is no covalent or strong bonding between PEG and xonotlite surface.

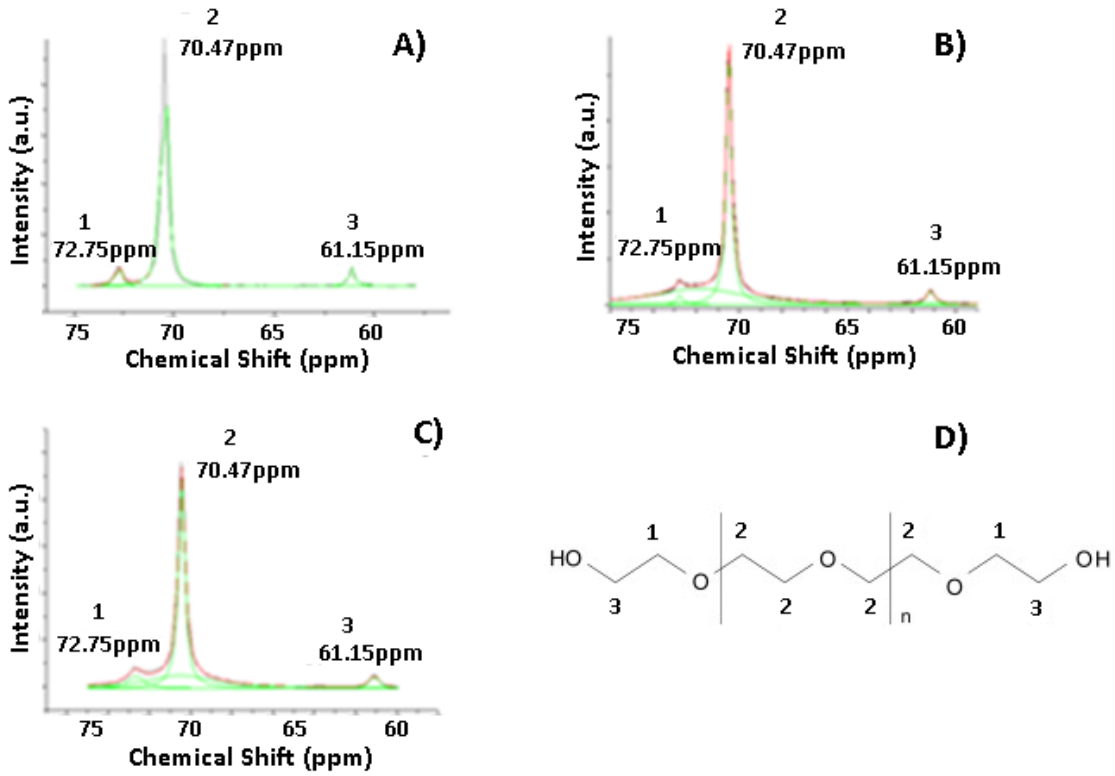

Figure III.12: ^{13}C ss-NMR of X_P600 (A), X_P1500 (B) and X_P4000 (C). Chemical structure of PEG molecule and atom assignation to ^{13}C NMR (D).

The different compounds were also characterized by ^{1}H ss-NMR (Figure III.13). The spectra of all the samples show one peak at 1.77ppm chemical shift related to protons in silanol groups, 2.05ppm peak of Ca-OH groups and a very intense peak around 3.53ppm related to the protons in alkyl ether groups of the polyethylene glycol [16]. This peak is very large, overlaps partially with the rest of the contributions and increases as the molecular weight of PEG increase. In all cases the peak around 1.12ppm can also be observed. According to literature [21] this peak could be associated to isolated silanol. No shift of the signals was observed, comparing to the pristine xonotlite signals, in either of the ^{1}H ss-NMR spectra of the compounds with PEGs which suggests that there is not a strong interaction between the protons of the PEGs and hydroxyl groups of xonotlite. One aspect to highlight is the increase of water contribution in samples with higher molecular weight polyethylene glycol. This could be related to the hygroscopic character of this polymer that could favor the presence of moisture in samples.

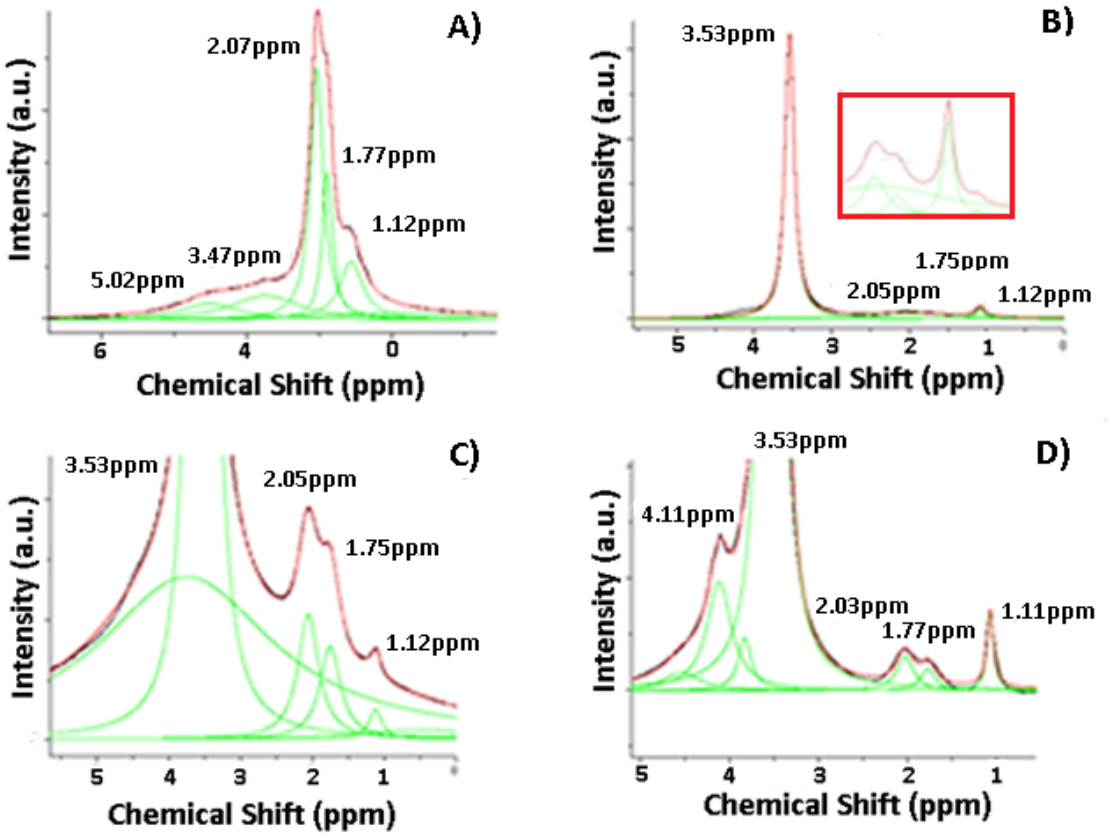

Figure III.13: 1H NMR of pristine xonotlite samples (A) and X_P600 (B), X_P1500 (C) and X_P4000 (D).

To further analyze the structure of the functionalized products and learn about the interaction between the PEG molecules and the xonotlite structure, samples were characterized by X-Ray photoelectron spectroscopy (XPS). This technique is able to provide useful information about the elemental composition and the interaction between different chemical elements by different kinds of bonding in a single phase.

Argon sputtering of the surface of the xonotlites with PEGs and the elemental analysis at different etching times was also carried (Figure III.14). This etching is usually done to eliminate any organic pollutant that might be adsorbed on the surface and could mask the measurement. After 300 seconds of sputtering, almost the total residual carbon located on the surface of pristine xonotlite was eliminated (Figure III.14 A).

However, in the profiles observed in PEG modified samples, a higher content of carbon is observed and even after 600 seconds of etching a content of carbon remains, especially in the compounds with higher molecular weight PEGs, although it reduces as the etching time increases. From this analysis it could be concluded that the most of

carbon in the modified samples is located at the surface and this agrees with the results obtained with XRD where no increase in basal distance was observed.

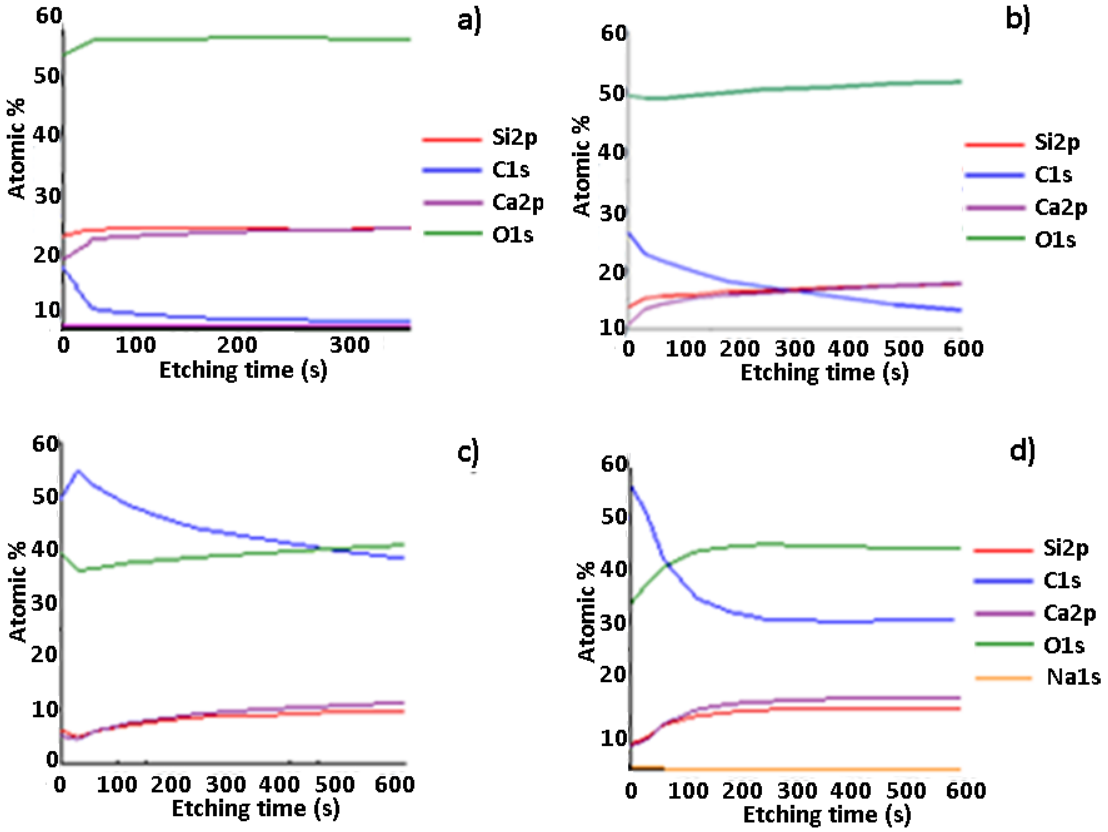

Figure III.14: Elemental analysis at different etching times (i.e. C1s, O1s, Si2p, Ca2p, Al2p) by XPS for xonotlite pristine (a), X_P600 (b), X_P1500 (c) and X_P4000 (d).

In this work we have also focused on high resolution spectra of Si2p 3/2, Ca2p 3/2, O1s and C1s signals in non-sputtered samples. The main goal of using XPS is analyzing further the presence and effect of PEG in the xonotlite structure. Thus, we would be able to describe better the interaction of inorganic and organic components.

Si2p 3/2 band was selected instead of Si2s due to its sharper and more intense shape. After the deconvolution the Si2p 3/2 band in each of the compounds analyzed the band was fitted with 3 main doublets (composed by two signals associated to the orbital 2p

1/2 and 2p 3/2. One peak was fitted at 101.5eV, another at 102.5eV and the last one at 103.5eV. The deconvoluted curves have been plotted in Figure III.15.

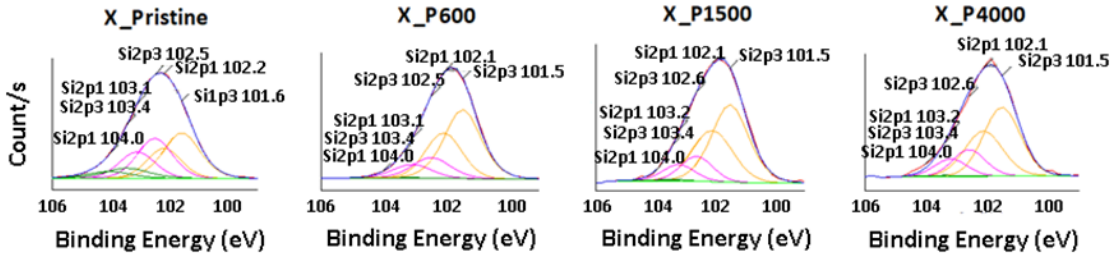

Figure III.15: Deconvoluted curves from XPS data analysis of Si2p contributions in pristine xonotlite (X_Pristine), X_P600, X_P1500 and X_P4000.

Taking into account the structure of xonotlite it is expected that the silicon atoms bound to OH groups to be the least numerous ones comparing to the silicon atoms bound to bridging oxygens (Si-O-Si) and also to calcium atoms. Because of that the peak at 103.5eV has been assigned to the Si-OH binding energy. Regarding the other two peaks, and as it was mentioned earlier in the text, bridging silicates or silicon atoms bound to a bridging oxygen which is bound to another silicon along the silicate chains, present longer bonding lengths, and higher binding energies [28] than other silicon-oxygen bonding (oxygen bound to calcium). This in mind, we associated the peak at 102.5eV to Si-O-Si bonding (oxygen in bridging position) in silicate chain as we did for pristine xonotlite. The other peak at 101.5eV has been assigned to the silicon-oxygen bond in Si-O-Ca position.

No significant shifts of Si2p3/2 were detected when unmodified and modified samples with PEG are compared. This suggests no significant interaction between silicate chains and the polymer. However, in Figure III.15 it can be observed that the population of silicon atoms bound to bridging oxygens (pink curves in Figure III.15) is reduced respect to silicon atoms bound to non-bridging oxygen atoms (orange curves in Figure III.15) for samples modified with PEG. This could confirm that there are more vacancies along silicate chain which is getting shorter due to the presence of polymer during the synthesis.

In Figure III.16 the binding energies of the O1s orbital of the different compounds are shown. The shape of the band changes from one compound to the other one but they all have been fitted to three peaks. The binding energies of the peaks are very similar in all the compounds which are 530.5eV, 531.7eV and 532.7eV. The two first contributions are associated to non-bridging (NBO) and bridging oxygens (BO) respectively according to the assignment done by Black *et al.* [24].

The last contribution at 533eV could be assigned to two chemical groups. On one hand this energy binding can be associated to molecular water. This could be the case in pristine xonotlite. On the other hand, this energy binding has also been measured in other compounds modified with PEG and has been assigned to the oxygens bound to the carbon (C-O-C) in the ethylene glycol groups of PEG [27]. Nevertheless, it is interesting to mention that an increase in the intensity of this peak is observed when the molecular weight of PEG is increased which suggests that this signal is due to at least, in part to the polyethylene glycol groups.

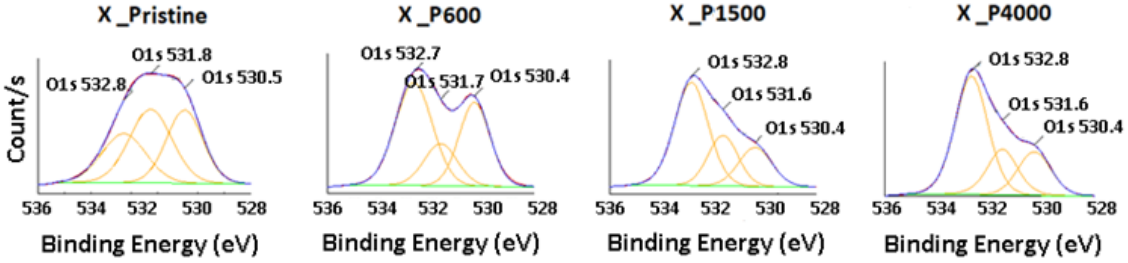

Figure III.16: Deconvoluted curves from XPS data analysis of O1s contributions in X_Pristine, X_P600, X_P1500 and X_P4000.

Table III.4 shows the NBO/BO ratios of the silicate oxygen atoms calculated from O1s deconvoluted curves. The tendency is not clear, but an increase of non-bridging oxygens between modified and unmodified samples can be distinguished. Since every Q^3 silicon in double silicate chain is attached to one non-bridging oxygen per 3 bridging oxygens [51], the increase of NBO/BO could suggest the loss of silicate tetrahedra in Q^3 positions. Similar result was concluded from the analysis of the ^{29}Si ss-NMR signals explained earlier.

There are authors in literature that reported a dependence between silicate chain length and binding energies of O1s signals in XPS [36, 37]. However, in this study no significant change in binding energies for oxygen due to the presence of polymer was found.

Table III.4: Non-bridging over bridging oxygen ratios analyzed by high-resolution XPS.

Samples	NBO/BO
X_Pristine	0.85
X_P600	**1.86**
X_P1500	**0.86**
X_P4000	**1.02**

The energy bindings found for the calcium ion is shown in Figure III.17. Two main signals were detected, one around 350eV (Ca2p1) and the other around 347eV (Ca2p3/2). Although the same two signals were measured for pristine xonotlite and xonotlite with PEGs, there is a significant decrease of binding energy for Ca2p 3/2 signal in the functionalized xonotlites. As can be seen in Table III.5, an energy reduction of 0.3eV (measurement error is 0.1eV) was found overall in the Ca2p 3/2 signal in the functionalized xonotlite compounds compare to the pristine xonotlite.

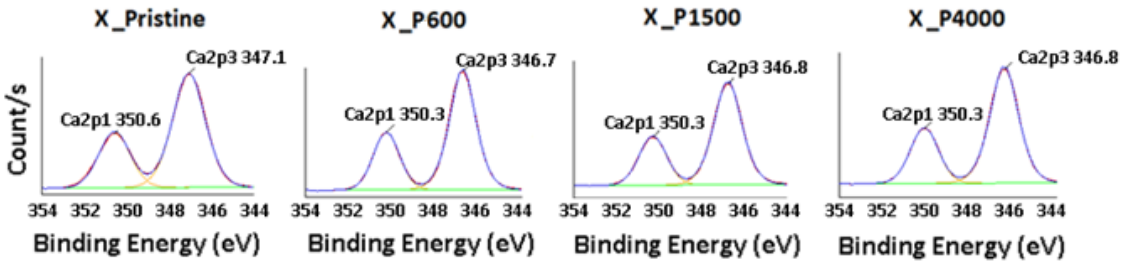

Figure III.17: Deconvoluted curves from XPS data analysis of Ca2p contribution in (from left to right) X_Pristine, X_P600, X_P1500 and X_P4000.

Table III.5: Ca2p3 peak position in high resolution XPS.

Samples	Ca2p3/2 Binding energy (eV)
X_Pristine	347.07
X_P600	**346.73**
X_P1500	**346.77**
X_P4000	**346.78**

If it is considered that a change in the calcium chemical environment, like an increase in coordination number or any additional interaction, could change the length and strength of calcium bonding and this could cause a shift in Ca2p 3/2 signal, then we could assume that the presence of PEG is capable to affect in some way the Ca-O interaction in calcium oxide layers. This difference could be explained as the coordination of lone pair electrons of the oxygen from the ethylene glycol groups to calcium.

The last signal analyzed was the C1s contribution (Figure III.18). The curve was deconvoluted and fitted to three peaks. One peak is around 284.8eV and is associated to carbon-carbon bonding (carbon-hydrogen contribution overlaps in this region), other peak at 286.5eV associated to carbon-oxygen bonding and one last peak around 289eV that is present in every sample and is associated to carbonate group (CO_3^{2-}) from carbonation.

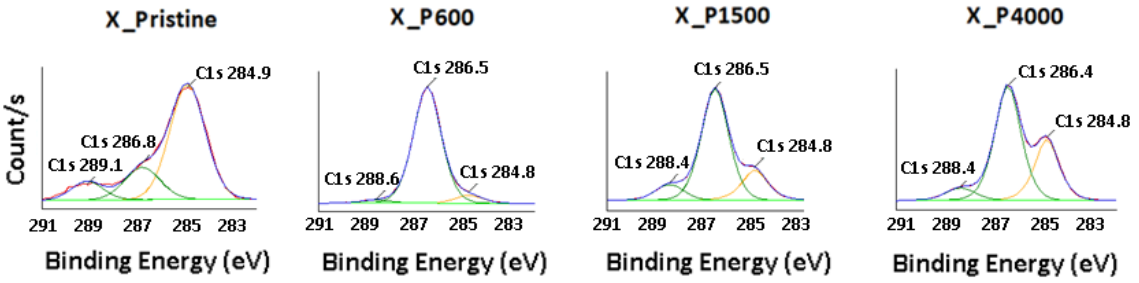

Figure III.18: Deconvoluted curves from XPS data analysis of Si2p contributions. Curves from left to right: X_Pristine, X_P600, X_P1500 and X_P4000.

Table III.6 shows the deconvoluted areas and the ratio obtained from carbon-carbon and carbon-oxygen interactions in samples modified with PEG. From these results it is observed that the higher molecular weight of the polymer used the higher the area of

both peaks and the higher also is the ratio between them (C1s 284.8/ C1s 286.5). This is associated to the higher presence of C-H groups when the molecular weight of PEG is increased as it could be expected. However, no significant influence of the xonotlite on the C1s binding energy was observed suggesting as expected, that there is not much interaction between the C-C/C-H backbone and xonotlite.

Table III.6: Binding energies, deconvoluted areas for PEG modified xonotlites.

Sample	Binding Energy (eV)	Chemical bonding Assignment	Area (CPS·eV)	Area C1s (C-C)/ Area C1s (C-O)
X_P600	284.75	C-C	4310.89	**0.06**
	286.48	C-O	65353.87	
X_P1500	284.82	C-C	20405.84	**0.27**
	286.49	C-O	76325.91	
X_P4000	284.83	C-C	42834.30	**0.50**
	286.43	C-O	84796.68	

III.2.2. Elemental analysis of modified xonotlite with PEG.

From the results obtained for pristine xonotlite pristine it was concluded that elemental analysis carried out by EDS can give an accurate value of Ca/Si molar ratios. Taking this into account this technique has been used to analyze the Ca/Si ratio for xonotlite samples modified with PEG as well. Table III.7 shows all the Ca/Si molar ratios obtained from EDS analysis. Carbon composition has been excluded to calculate molar ratios.

Table III.7: Summary of results from EDS elemental analysis in unmodified and modified xonotlite samples.

Element	X_Pristine	X_P600	X_P1500	X_P4000
Calcium	19.36	18.45	15.82	7.28
Silicon	18.64	18.21	17.31	8.37
Oxygen	62.00	63.31	66.87	84.35
Ca/Si	**1.04**	**1.01**	**0.91**	**0.87**

From these results can be concluded that there is a decrease of Ca/Si when the molecular weight of PEG employed increases. One interpretation for this result is that glycol groups in PEG are capable to coordinate calcium ions in reaction suspension causing vacancies in different areas of calcium oxide layers. This capacity of polyethylene glycol to coordinate calcium was reported previously in the literature [38].

Furthermore, this coordination of PEG to Ca could inhibit interaction between silicate tetrahedra and calcium from CaO causing silicate tetrahedra vacancies in silicate chains (confirmed previously by ^{29}Si- ss NMR). Moreover, this loss of calcium that causes vacancies in silicate chain which could be related to disappearance of one non-bridging oxygen per two bridging oxygens. Thus, it could be justified the increase of NBO/BO ratios found by XPS as well.

III.2.3. Morphological analysis of modified xonotlite with PEG.

The different compounds were characterized by transmission electron microscopy (Figure III.19). Modified samples as well as the unmodified ones present needle or fiber like morphologies and no significant morphology changes due to the presence of PEG can be observed.

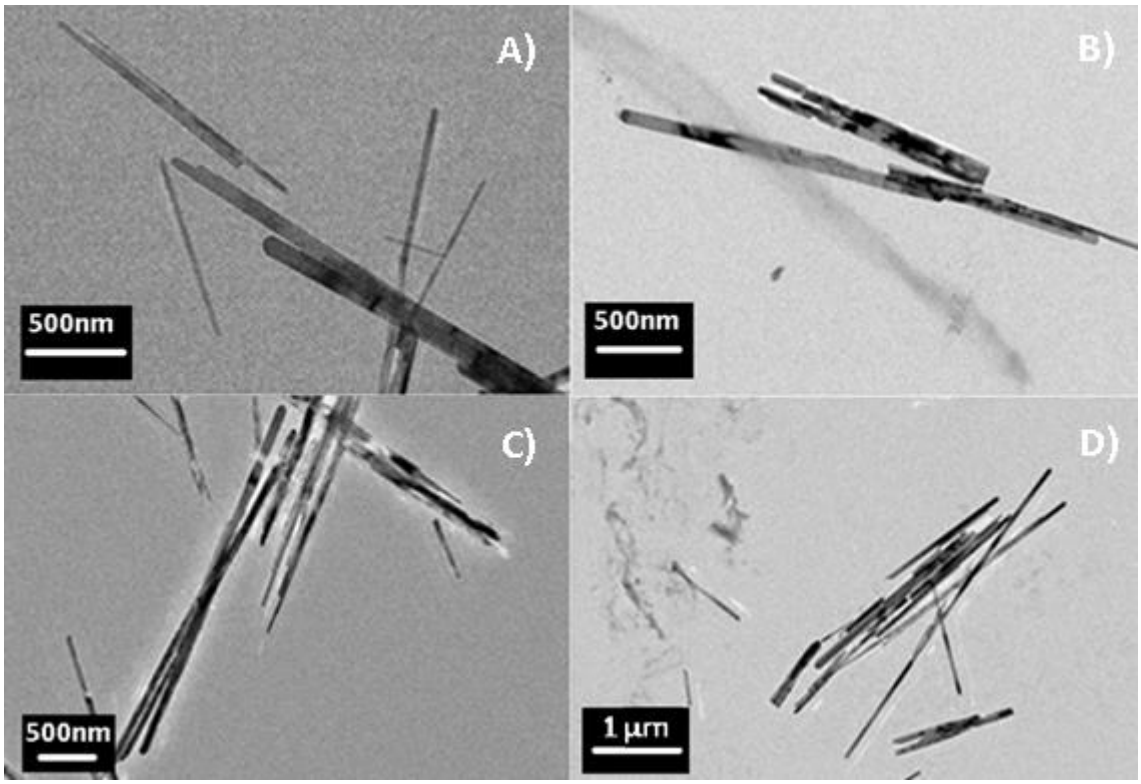

Figure III.19: LR-TEM images of X_Pristine fibers (A), X_P600 (B), X_P1500 (C) X_P4000 (D).

A total of 150 fibers for each compound sample has been analyzed using Fiji, an ImageJ distribution software, to carry out 3 length and 3 width measurements per fiber. After the measurements, a normal distribution of the collected data was plotted (Figure III.20) to analyze the size distribution of the different products.

According to the results obtained there is a width increase of the particles modified with PEG compared to the pristine xonotlite. The pristine xonotlite has a mean width of 50nm, the X_P600 of 80nm, the X_P1500 of 60nm and lastly the X_P4000 of 90nm. The largest mean width is shown by the X_P4000 compound. The width distribution also gets wider if PEG is added to the reaction.

Regarding the length of the PEG does not seem to have much effect on the length of the fibers (mean length was found around 1.5µm for pristine xonotlite, X_P600 and X_P1500). Only in the case of X_P4000 an increase in the mean length can be observed with a mean length above 2µm.

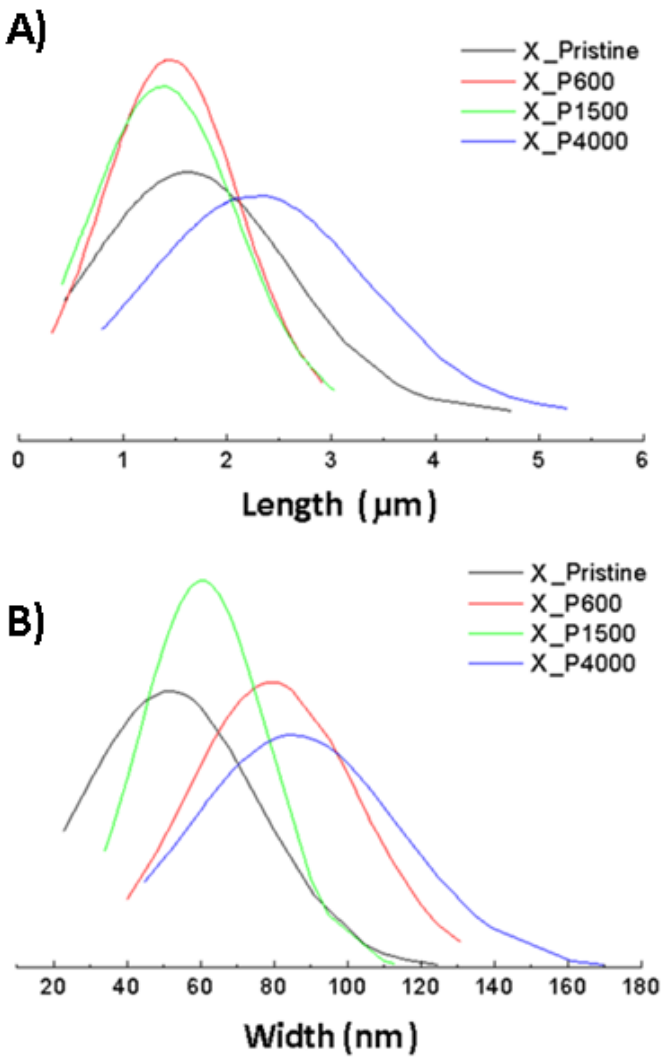

Figure III.20: Normal distribution of xonotlite fibers length (A) and width (B).

High resolution images were also taken for each synthesized material. From these images, lattice distance along fiber crystals were measured and they are shown in table III.8. These results showed no difference in lattice distance associated to (200) (distance between the CaO layers) along the length of the fibers. This is further evidence showing that the PEG molecules are not intercalated between silicate chains and CaO layers in the xonotlite structure.

Table III.8: Lattice distance of modified xonotlite samples synthesized under subcritical conditions.

Sample	Mean Lattice Distance (nm)
X_Pristine	0.859
X_P600	0.859
X_P1500	0.857
X_P4000	0.869

According to the results mentioned in this section it can be concluded several things. First, the presence of PEG during precipitation of xonotlite in batch hydrothermall reactor shortens the length of the silicate chains, according to ss-NMR. The higher molecular weight of PEG is employed, the shorter is this length. Moreover, the presence of PEG did not change the basal distance of the crystal or the mean lattice distance between calcium oxide layers. So, it could be considered that the polymer is not located between silicate chains or calcium oxide layers but PEG could be located on surface. The interaction of PEG and xonotlite is weak and associated to the interaction with calcium according to the XPS measurements.

III.3. Xonotlite samples modified by sulfobetaine siloxane.

Besides the modification of particles with PEG, in this work the covalent functionalization of xonotlite by organic moieties has also been studied. In this study sulfobetaine siloxane molecule (SBS) (Figure III.21) was employed with the idea of binding the zwitterion covalently to the silicate chain of xonotlite through the siloxane group by condensation reaction with the silica in an alkaline medium (produced by the addition of CaO). The SBS structure is based on a dipolar group, a molecule with a cation and an anion located very close to each other (zwitterion group). The main goal of using this kind of molecule was to utilize the charge of the zwitterion dipole to avoid aggregation between particles through electrostatic repulsion.

1/4 in moles of the SiO_2 reactant (Levasil) was substituted by sulfobetaine siloxane maintaining a total Ca/Si ratio of 1 for the synthesis of xonotlite and a total Ca/(Si+Al) ratio of 0.83 for the case of tobermorite. The rest of the reaction conditions (temperature, reaction time etc.) used were maintained the same as in the $CaO+SiO_2$

hydrothermal synthesis. The SBS molecule was synthesized in the lab following the synthesis described in chapter II, right before using it in the hydrothermal reaction.

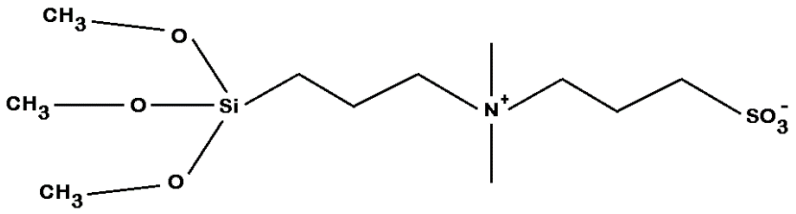

Figure III.21: Chemical structure of SBS.

FT-IR and ^{13}C ss-NMR were used to characterize if the molecule was synthesized correctly. Figure III.22 shows FTIR spectrum obtained from non-hydrolyzed SBS molecule. The presence of absorption bands at 1040 cm^{-1} and 1200cm^{-1} can be seen in the spectrum, which are associated to stretching vibrational mode of sulfonate group in SBS [1] indicating the formation of the molecule.

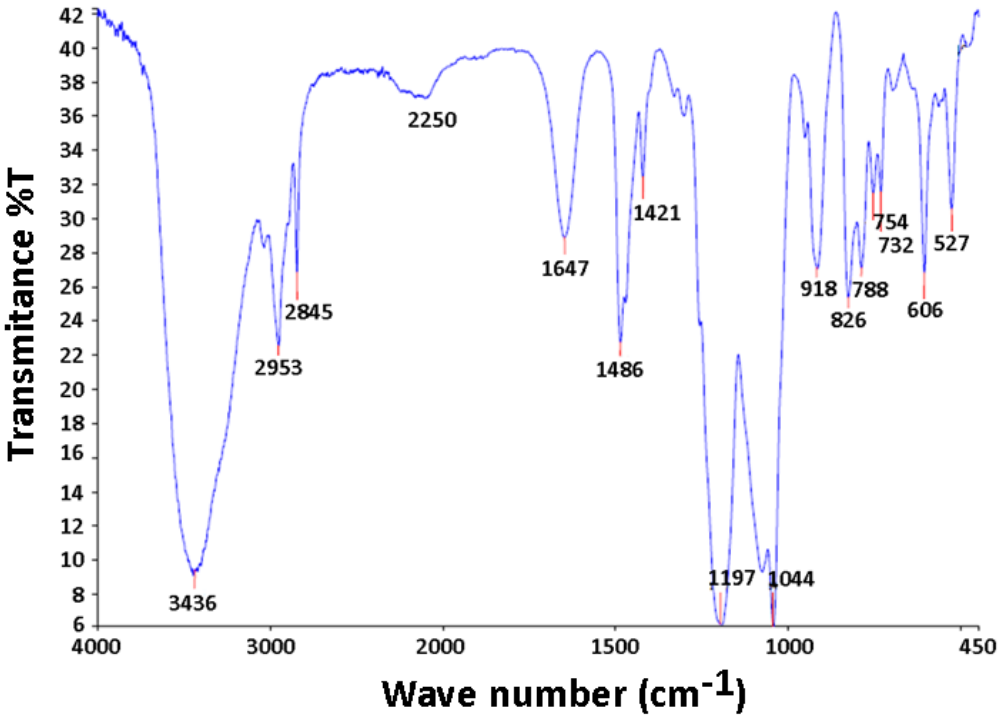

Figure III.22: FT-IR spectrum of non-hydrolyzed sulfobetaine siloxane (SBS).

Moreover, a band around 1420cm^{-1} and at 1490cm^{-1} corresponding to Si-O- and -CH_2 scissoring vibrational modes, respectively, are also observed. Stretching vibrations

mode for -CH_2 groups are also measured around 2900cm^{-1} [1]. There are also two bands at 1647cm^{-1} and 3437cm^{-1} which can be assigned to bending and stretching modes of water respectively. This water comes from air humidity since the SBS is a very hygroscopic molecule.

In addition, the SBS molecule was also characterized by ^{13}C NMR. Figure III.23 shows the results obtained from solid and liquid ^{13}C NMR. Every contribution in NMR spectra was compared to NMR measurements carried out in liquid phase in literature [42, 50] and assigned to contributions of non-hydrolyzed SBS molecule. This reasserts the results obtained in FTIR and confirms that sulfobetaine siloxane has been prepared correctly.

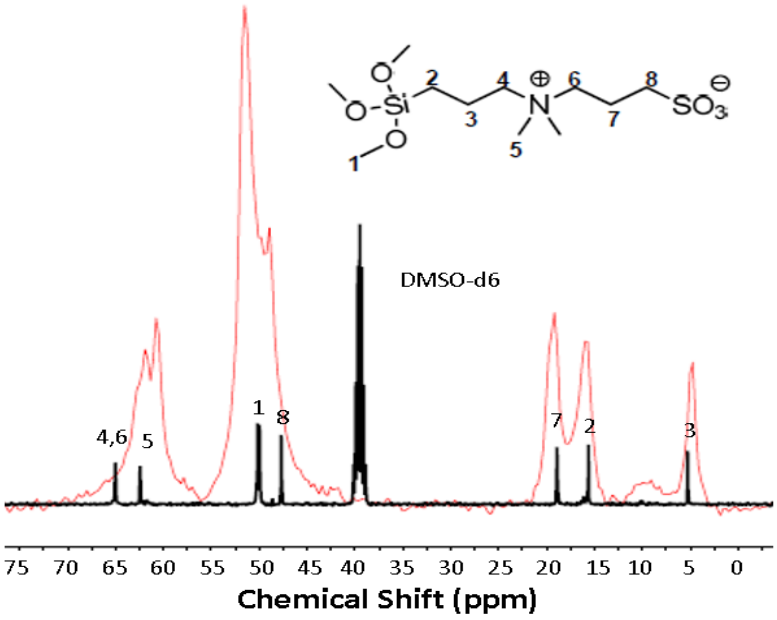

Figure III.23: ^{13}C NMR of sulfobetaine siloxane (SBS). Black spectrum corresponds to liquid NMR and red spectrum corresponds to solid state NMR.

Concluding this section, TGA/DSC measurements were also carried out. This allowed comparing thermal stability of prepared reactant to literature and on the other hand it is important to estimate the range of temperature where this molecule is stable. As it can be observed in Figure III.24, a significant loss of weight happens above 250°C. This loss is reported in literature as degradation of zwitterion group in SBS [43]. Therefore, it can be concluded that SBS is a good candidate to be employed as silicon source for hydrothermal synthesis of tobermorite (synthesized at 215°C) or even for xonotlite phase synthesized at 250°C.

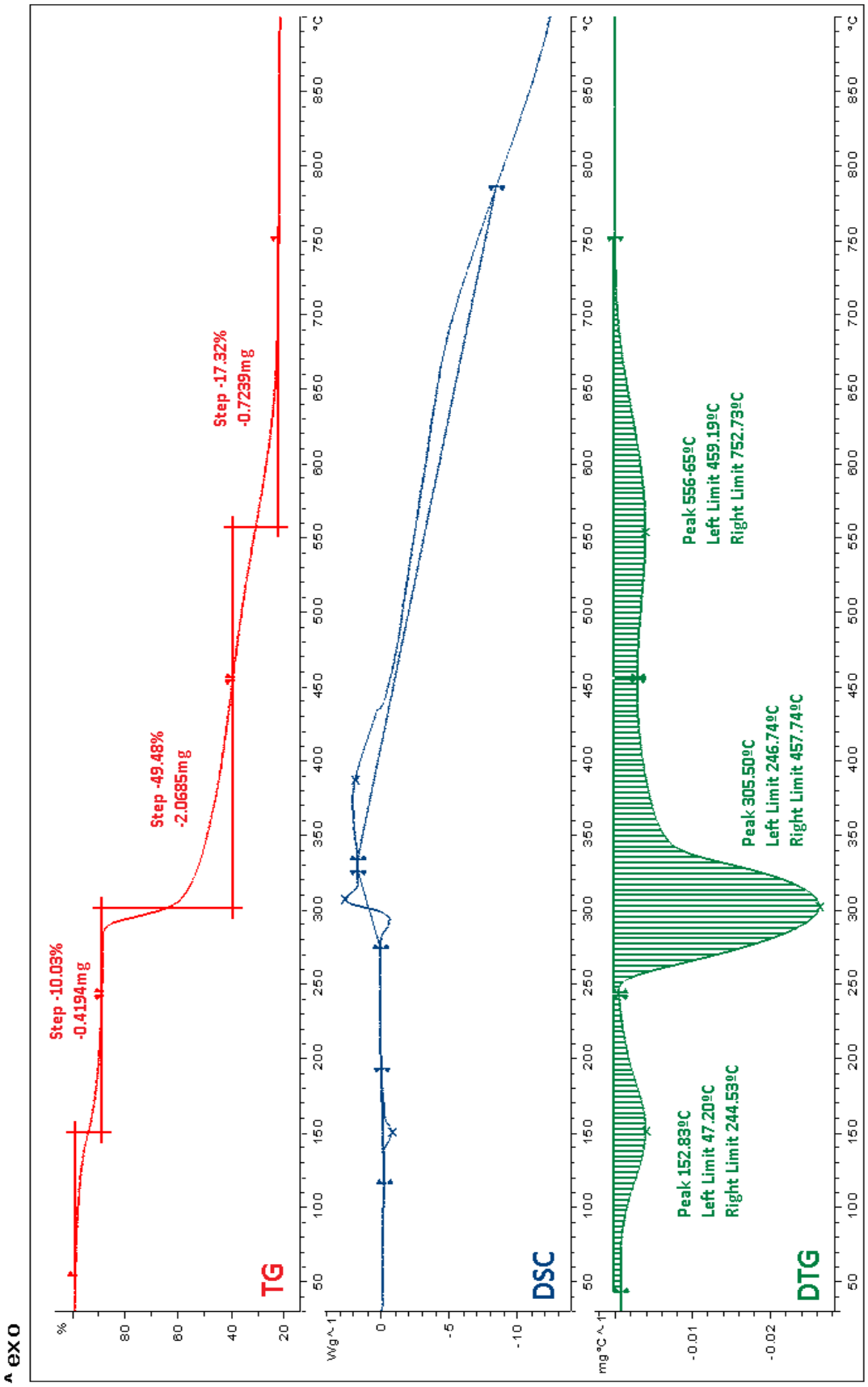

Figure III.24: Thermogravimetry (red curve), differential scanning calorimetry (blue curve) and differential thermogravimetry (green curve) of non-hydrolyzed SBS.

III.3.1 Structural analysis of xonotlite like samples modified with SBS.

In Figure III.5 is shown the XRD diffractogram of the sample synthesized during 4h for an SBS/SiO_2 molar ratio equal to 1/4. As it can be observed the XRD diffractogram is not very crystalline and few diffractions could be associated to xonotlite according to data base (PDF 00-023-0125). There are two diffractions, at 30.24° and 42.30° which could be tentatively assigned to a SiO_2 phase (coesite) although the peaks are not very crystalline. Therefore, impurities of SiO_2 were found as byproduct.

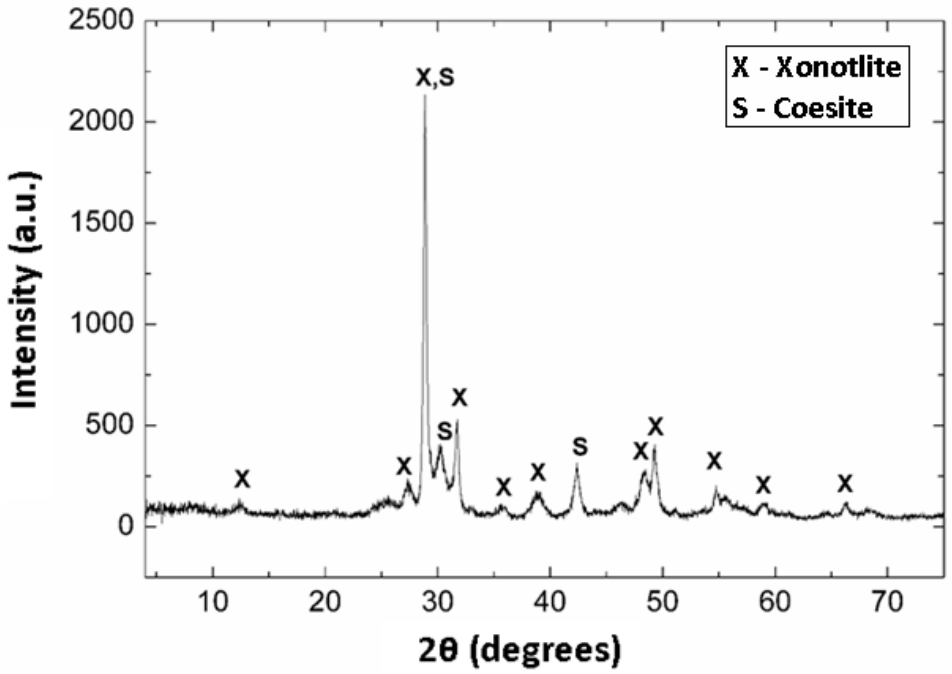

Figure III.25: XRD curve of SBS functionalized xonotlite synthesized over 4 hours of reaction (xonotlite_SBS 4h).

One way to explain the presence of SiO_2 is that solubility and reactivity of SBS is very different in respect to levasil. Methoxy groups are very reactive to the presence of hydroxyl groups in the reactor medium. Then it could be thought that SBS reacted to silica and precipitated at the beginning of the hydrothermal reaction changing the kinetics of the overall process.

With the idea of improving the crystallinity of the xonotlite the reaction time was increased from 4 to 8 hours. Figure III.26 shows the XRD of the product obtained at 8 hours. As it can be seen there is an increase of the intensity of the characteristic diffractions of xonotlite compare to the sample obtained at 4 hours. Moreover, new

peaks associated to crystalline xonotlite can be observed in the diffractogram. This result suggests that when using SBS more reaction time is needed to form crystalline xonotlite.

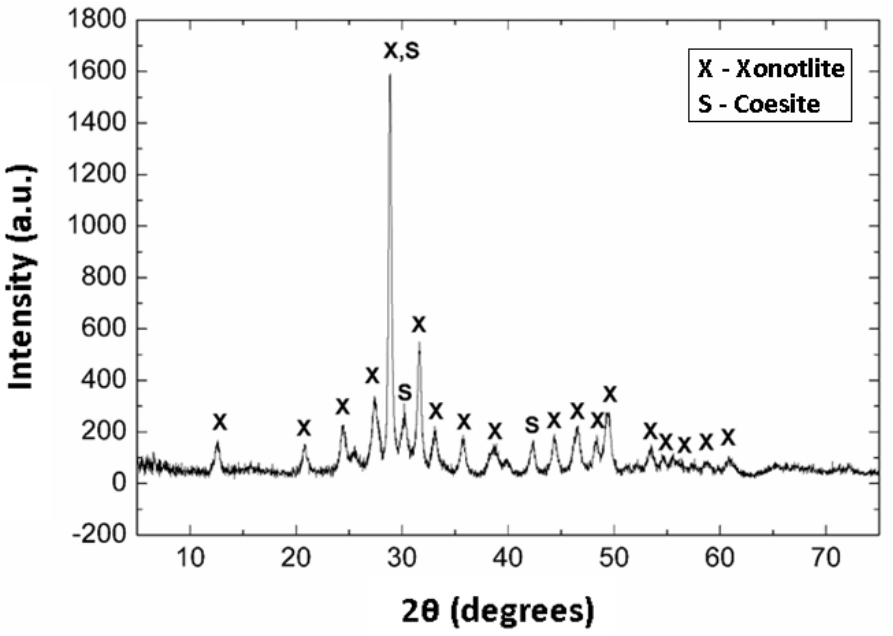

Figure III.26: XRD curve of SBS functionalized xonotlite synthesized in 8 hours of reaction (xonotlite_SBS 8h).

From this point a quantification by Rietveld analysis was carried out to quantify the phases present in the powder, as well as the amorphous part. Detailed results obtained are in appendix A.4.

In the case of the X_SBS 4h sample the amorphous phase was quantified in 66% of the weight and in the case of X_SBS 8h in 64%. Thus, xonotlite was quantified as well as 20% of weight in xonotlite_SBS 4h and 22% in xonotlite_SBS 8h sample. In both samples 5% of SiO_2 (coesite and stishovite) was also found. The rest of phases assigned were calcite around 3% and other phases related to magnesium impurities which are due to the use of CaO obtained from the calcination of commercial $CaCO_3$ which contains magnesium impurities.

Elemental analysis for samples modified with sulfobetaine siloxane was carried out by EDS and results are shown in Table III.9. From this data it was calculated molar ratios of Ca/Si for products obtained after 4 hours and 8 hours of reaction time. In both cases a deficit of calcium is observed, which increases when the reaction time is longer.

Furthermore, from elemental analysis the presence of sulfur can be measured which is part of the SBS molecule, but the quantity is very small. The total amount of sulfur was below 1%. The higher concentration of sulfur in structure could be explain as a higher amount of siloxane reacted to form the reaction product but is not possible to distinguish how is interacting exactly in the structure.

Table III.9: EDS elemental analysis of xonotlite samples functionalized with SBS.

Sample	Ca atomic %	Si atomic %	O atomic %	S atomic %	Ca/Si
xonotlite_SBS 4h	17.77	18.75	62.78	0.70	0.95
xonotlite_SBS 8h	17.04	18.71	63.44	0.82	0.91

All the characterizations carried out for xonotlite_SBS 4h and xonotlite_SBS 8h suggest that mainly two products are formed when SBS is added to the reaction, xonotlite-like compound and silica. At low time reactions (4h) calcium oxide, Levasil and SBS react to give an amorphous calcium silicate hydrate and some silica. If longer reaction time is used (8h) the amorphous calcium silicate hydrate evolves forming a more crystalline xonotlite-like product and amorphous silica as well.

FT-IR measurements of xonotlite_SBS 4h and xonotlite_SBS 8h were also carried out (Figure III.27). First in both cases we can find contributions associated to asymmetric stretching vibrations of Si-O bonds due to Q^2 silicate tetrahedra (pairing silicate tetrahedra) at 1087cm^{-1} and 975cm^{-1}. Bands at 457cm^{-1} and around 670cm^{-1} can be assigned to O-Si-O and Si-O-Si bending vibrational modes respectively. Moreover, the bands at 3400cm^{-1} due to stretching modes of -OH and the band at 1641cm^{-1} due to bending mode of H-O-H confirm the presence of silanol groups and water in both cases.

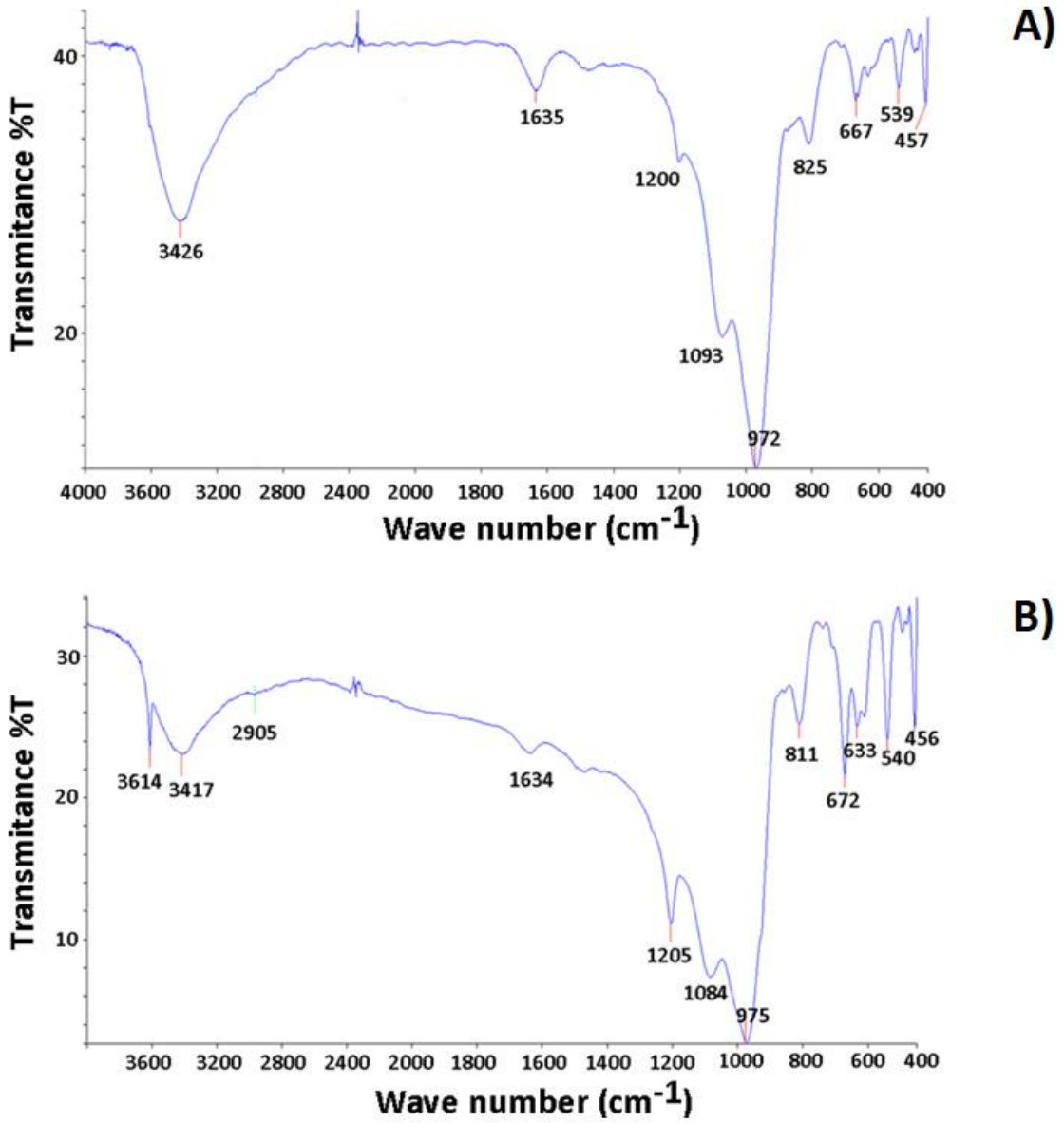

Figure III.27: FT-IR of xonotlite samples functionalized with SBS. A) samples obtained after 4 hours of reaction (xonotlite_SBS 4h). B) samples obtained after 8 hours of reaction (xonotlite_SBS 8h).

However, significant differences can also be observed between both spectra. xonotlite_SBS 8h sample presents a band around 3600cm^{-1} assigned to the stretching mode of Ca-OH bond of xonotlite. This contribution is not so significant in sample xonotlite_SBS 4h which it can be observed as a small shoulder.

The band around 1200cm^{-1}, related to the presence of double silicate chains, is more intense in xonotlite_SBS 8h than in xonotlite_SBS 4h and the bands at 457cm^{-1} and around 670cm^{-1} are more intense in the case of the sample synthesized at 8 hours. This

could indicate that xonotlite structure is evolving in time and increasing its crystallinity. Nevertheless, the presence of stretching vibrational mode of $-CH_2$ is difficult to identify in any of the spectra.

Both samples were also characterized by ^{29}Si ss-NMR. Figure III.28 shows the spectrum obtained for xonotlite_SBS 4h sample. The experimental data were deconvoluted and each signal was adjusted to pseudo-Voigt. In addition to Q^2 (-86.1ppm) and Q^3 (-97.7ppm) signals, a large contribution of Q^1 can be observed which can indicate a short length of silicate chains in structure that is associated to a low crystallinity of these samples, confirming results obtained by XRD. Moreover, a signal at -110ppm can be seen which is associated to the presence of Q^4 silicate tetrahedra [4]. The presence of this contribution can only be assigned to the formation of amorphous silica in the reaction.

However, no presence of T^1, T^2 or T^3 signals between the range of -40 and -70ppm [5, 6] can be seen which would indicate the bonding of the SBS molecule to silicate chain of the xonotlite phase. Therefore, there is no direct evidence of the SBS molecule covalently bound to xonotlite.

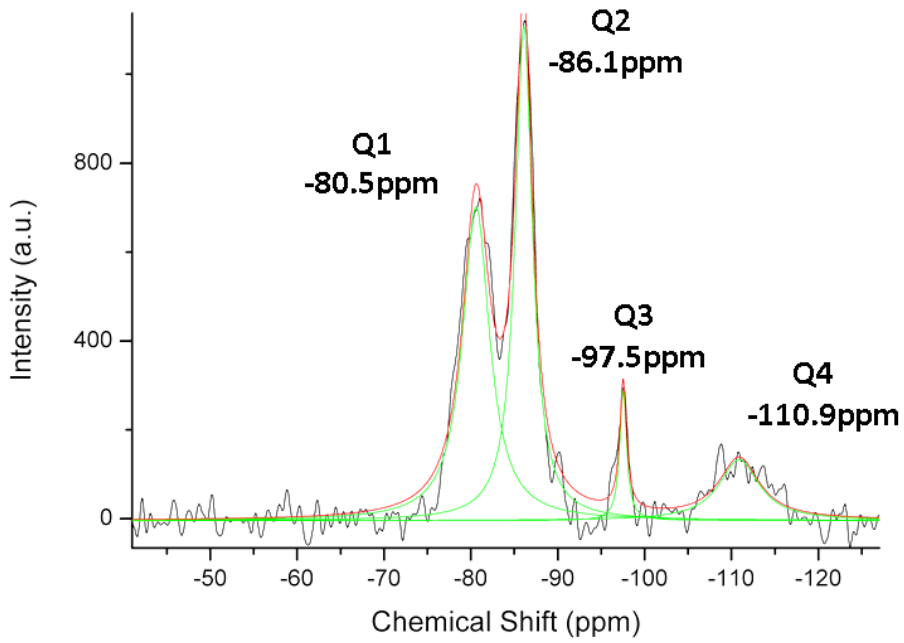

Figure III.28: ^{29}Si NMR curve of SBS functionalized xonotlite obtained after 4 hours of reaction (xonotlite_SBS 4h). Notes: black curve is the experimental, red curve is the adjusted curve and green curve represents the deconvoluted curves of each signal adjusted to pseudo-Voigt.

In Figure III.29 the ^{29}Si NMR of xonotlite_SBS 8h is shown. Here again besides the $Q^2$and Q^3 signals a large Q^1 signal can be seen which suggests the formation of shortened silicate chains. Furthermore, the sample also shows a Q^4 signal which indicates the formation of amorphous silicate. Deconvolution of both spectra were carried out and the relative population of the signals were calculated. showed a decrease of Q^1 signal (expressed as an increase of MCL value calculated by equation 15) and the increase of Q^3 which is more similar to the spectrum shown by crystalline xonotlite. A priori, it could be suggested that the addition of SBS to the reaction slows down the formation of crystalline xonotlite, and longer reaction times would be necessary to obtain a good crystalline xonotlite sample. However, it is also important to highlight that Q^4 signal (quantified by deconvolution of ^{29}Si NMR spectrum) also increases when the reaction time is 8 hours (Table III.10).

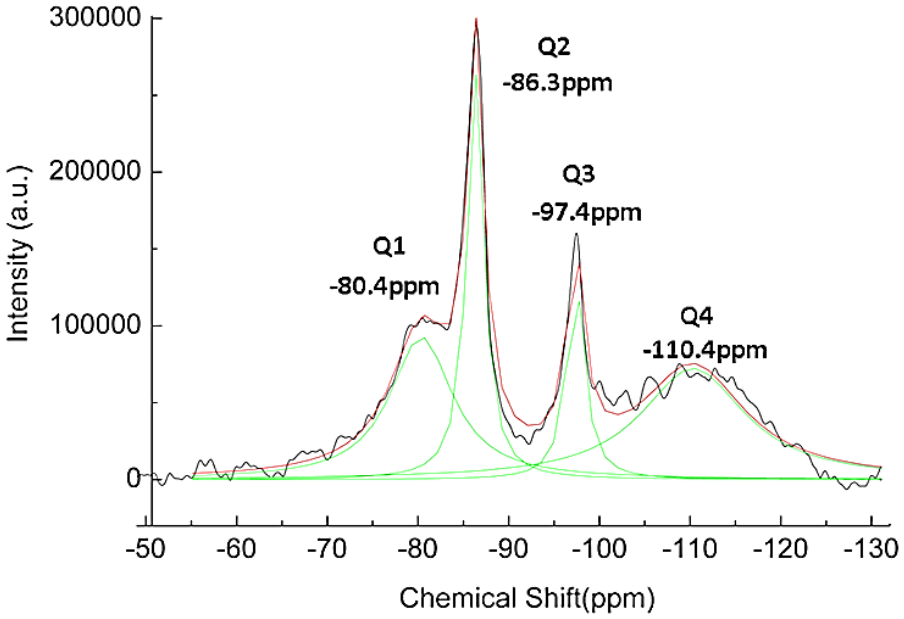

Figure III.29: ^{29}Si NMR curve of SBS functionalized xonotlite obtained after 4 hours of reaction. Notes: black curve is the experimental, red curve is the adjusted curve and green curve represents the deconvoluted curves of each signal adjusted to pseudo-Voigt.

Table III.10 shows the MCL, Q^2/Q^3 and Q^4 population calculated from the deconvoluted peaks. It can be observed that the longer the reaction time the lower is the ratio Q^2/Q^3. MCL values on the other hand increase from 4.87 in xonotlite_SBS 4h sample to 6.89 in xonotlite_SBS 8h sample. Moreover, xonotlite_SBS 4h has low population of Q^3 silicate tetrahedra groups however when the reaction time is increased to 8 hours the Q^3

quantity increases giving a Q^2/Q^3 ratio of 1.95 very close to 2.0, which is the ideal value for highly crystalline xonotlite.

This could mean that a higher ordered xonotlite structure is achieved after longer reaction times confirming the tendency observed XRD and FTIR spectroscopy. On the other hand, the longer reaction time is employed the higher the population of Q^4 contribution is obtained. The characterizations carried out so far indicate that both samples (xonotlite_SBS 4h and xonotlite_SBS 8h) contain not very crystalline xonotlite and amorphous silica but it is not very clear if the SBS molecule is covalently bound to xonotlite.

Table III.10: Influence of reaction time in Mean Chain Length, Q^2/Q^3 ratio and Q^4 population of SBS functionalized xonotlite samples.

Sample	MCL	Q2/Q3	Q4/(Q1+Q2+Q3+Q4)
xonotlite_SBS 4h	4.87	9.94	0.115
xonotlite_SBS 8h	6.89	1.95	0.376

^{1}H NMR of both samples was carried out to try to characterize them further. The ^{1}H NMR spectrum of xonotlite_SBS 4h shows three signals (Figure III.30). The signal at 4.8ppm is associated to the water in structure. Two more signals can also be observed in the spectrum, one at 2.0ppm that could be assigned to proton in Ca-OH bond and other at 1.4ppm that could be assigned to the protons in silanol groups [46, 47, 48].

The ^{1}H NMR spectrum of xonotlite_SBS 8h present two main differences from the 4h sample one. First, Ca-OH and Si-OH contributions increase respect to the water contribution at 5.0ppm. Moreover, there is one more signal at 3.8ppm. This peak could be due to silanol groups interacting with molecular water or it could be related to the presence of $-CH_3$ or $-CH_2-$ groups attached to the ammonium cation in the SBS molecule [42].

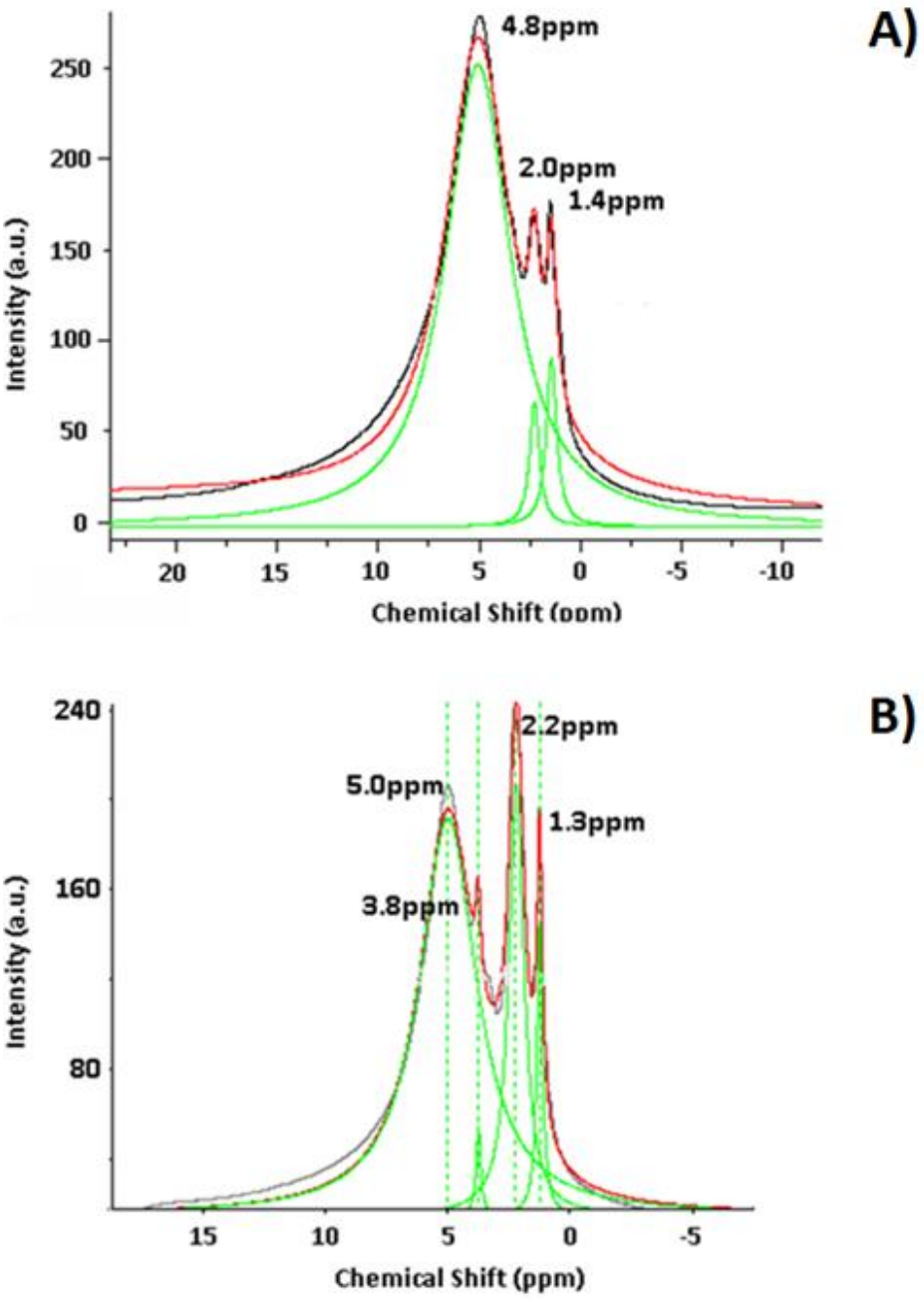

Figure III.30: ^{1}H ss-NMR of xonotlite samples functionalized with SBS. A) samples obtained after 4 hours of reaction (xonotlite_SBS 4h). B) samples obtained after 8 hours of reaction (xonotlite_SBS 8h).

III.3.2. Morphological analysis of xonotlite like samples modified with SBS.

TEM was used to characterize the morphology of xonotlite_SBS-4h and xonotlite_SBS-8h (Figure III.31). The particles observed presented plate shapes or shorter fibers than the ones obtained for pristine xonotlite.

Particle sizes observed in the obtained images are very diverse. The particles of xonotlite_SBS-4h are between 450nm and 1.5um in length and between 80 and 200nm in width. Images taken of samples recovered after 8 hours of synthesis showed an increase in its length from 500nm to 2µm.

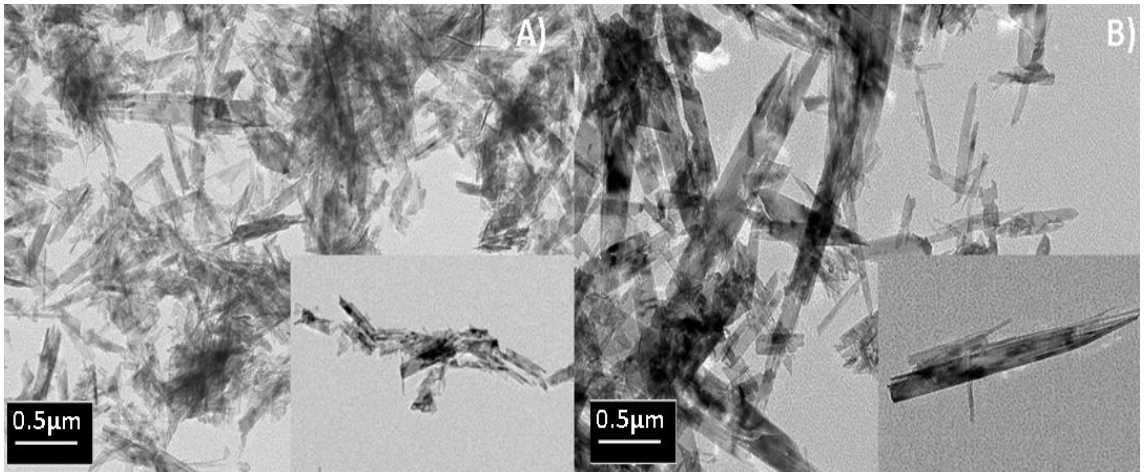

Figure III.31: TEM images of xonotlite particles functionalized with SBS. Xonotlite_SBS 4h (A) and xonotlite_SBS 8h (B).

In conclusion, SBS had different effects in xonotlite precipitation during hydrothermal reaction. On one hand, it was observed that SBS shortens the silicate chains length and generate more chain endings with hydroxyl groups. Moreover, the particle size was also reduced compared to the same particles produced at the same conditions without SBS and after 4 hours of reaction. Differences in XRD patterns and ^{29}Si NMR indicates that SBS is changing the synthesis process and the characterization of the obtained products suggests that more time than 8 hours should be needed to polymerize further the silicate chains and obtain more crystalline xonotlite.

III.4. Addition of xonotlite particles (with and without PEG) in cement pastes.

III.4.1. Dosage of particles. Calculation of organic content by TGA- DSC.

The first step to prepare the experiments with cement pastes was characterizing the polymer content in samples. This way it is possible to adjust better the formulation adding in every experiment the same quantity of inorganic particles that acts as seeds in cement hydration. The organic content in samples was characterized by thermogravimetry (TGA) and differential scanning calorimetry (DSC).

Figure III.32 shows the DSC analysis of PEG MW600, MW1500 and MW4000 employed in synthesis. According to the DSC, an exothermic event occurs in the range of 220 and 300°C. This is associated to exothermic PEG degradation.

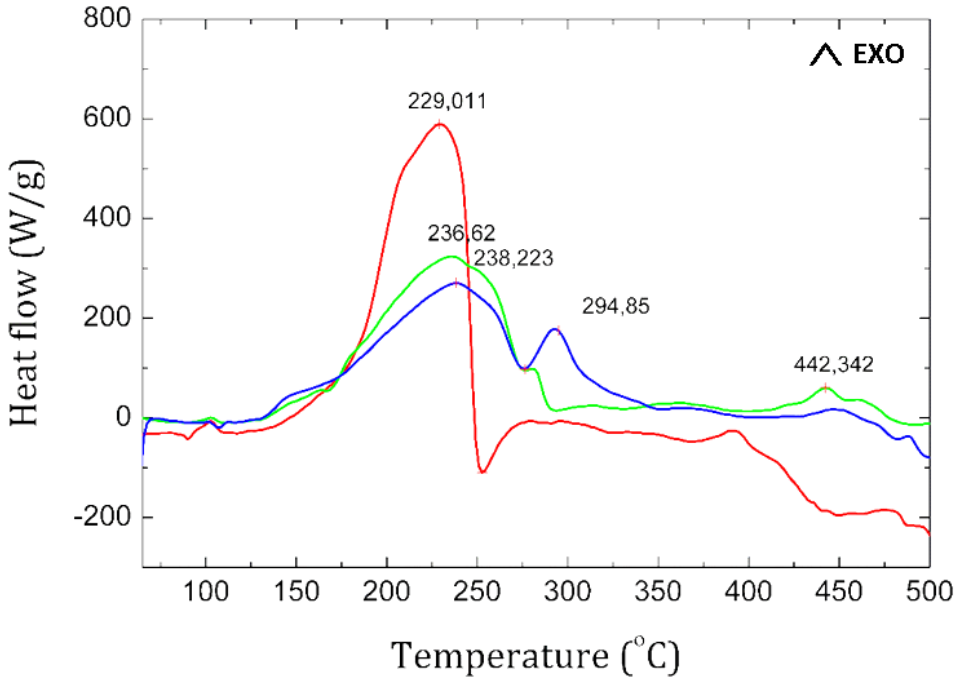

Figure III.32: DSC curves of X_P600 (red line) X_P1500 (green line) and X_P4000 (blue line)

Thermogravimetric analysis was carried out in order to characterize also the presence of PEG and measure its quantity in the PEG functionalized/modified compounds. TGA and DSC curves of xonotlite samples are plotted in Figure III.33. The polyethylene glycol compounds degrade between 220ºC and 300ºC. According to the literature this is the range of temperature where PEG degradation occurs [26, 31]. In Table III.11 the mass percentage range measured by TGA of several samples of each compound is shown. In

the case of X_PEG600 the amount in weight of PEG found in the sample ranges from 16wt% to 38wt%. For the X_PEG the range goes from 27wt% to 31wt% and lastly for X_PEG4000, it ranges between 65wt% and 71wt%. As it can be observed, the amount of PEG in each compound varies from one synthesis batch to the other, especially in the case of PEG600. This result suggests that polyethylene glycol molecule does not seem to have a strong interaction with xonotlite and that the quantity might vary.

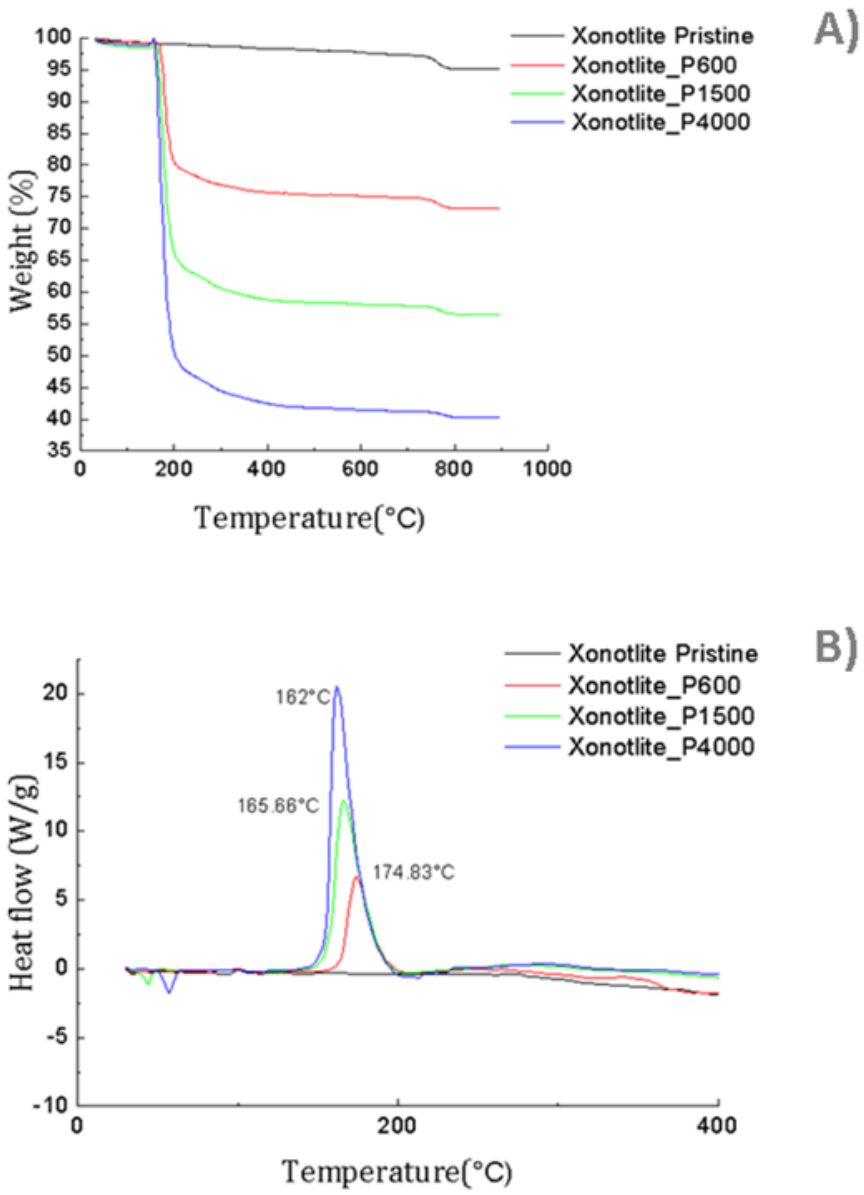

Figure III.33: TGA (A) and DSC (B) curves of pristine and modified xonotlite samples

Moreover, in Table III.20 yield percentages about the mass added in the reaction of are shown. It can be observed that the higher the MW of the PEG added to the reactor medium, the higher is the total amount of polymer found in the final product. However,

according to the yield values only a 6wt% of the initial PEG has remained in X_P600 and X_P1500 samples, and an 8wt% for X_P4000 samples.

Table III.11: Summary of PEG contents in modified xonotlite samples

Sample	Additive	Range of wt% of PEG	Yield (g PEG in solid/g PEG initialx100)
xonotlite Pristine	N/A	-	-
xonotlite_P600	PEG 600	16-38%	5.7%
xonotlite_P1500	PEG 1500	27-31,1%	5.4%
xonotlite_P4000	PEG 4000	64.8-70.8%	8.45%

III.4.2. Stability of particle dispersions in water.

This part of the work also focused on how suspensions of xonotlite and their PEG modifications are stabilized in water. The main idea was simulating exactly the same concentration of particles that will be employed for cement pastes and test the decantation time and zeta-potential. The decantation test tried to analyze in a qualitative way how stable the different suspensions are. Then z-potential measurements were carried out trying to quantify this stability.

In the case of decantation tests suspensions where prepared using two methods, manually and by ultrasound homogenizer probe. 50mg of particles are suspended in 2mL of miliQ water. In Figure III.34 the dispersion stability over time of pristine and modified xonotlites are shown.

PEG modified xonotlite samples showed high stability in water compared to pristine xonotlite. This stability was better if the particles were suspended by ultrasound probe for 30 seconds (70% of power). According to the pictures taken after 7 days xonotlite with higher molecular weights PEG (PEG MW 1500 and PEG MW4000) showed the highest stability even in the case of suspensions mixed without ultrasounds.

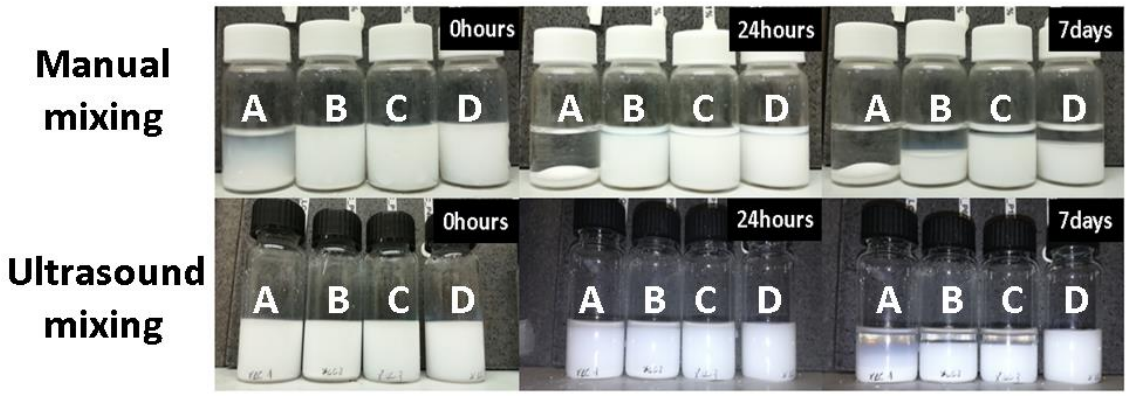

Figure III.34: Decantation experiments for pristine xonotlite and PEG modified xonotlites. Pristine xonotlite (A), xonotlite PEG MW600g/mol (B), xonotlite PEG MW1500g/mol (C) and xonotlite PEG MW4000g/mol (D).

Kumar [63] proposed a range of values for zeta-potential to classify nanoparticles depending on its stability in suspension. Particles with Zeta potential between 0 and ±5mV tend to flocculate easily, between ±10mV and ±30mV have incipient instability and from ±30mV or above are moderately stable or stable.

The Z-potential results for pristine and modified xonotlite samples are shown in Table III.12. These suspensions were prepared by dispersion in an ultrasound bath for 10 minutes using two different concentrations, 2.5% w/w and 1.25% w/w of particles in water. For a suspension equivalent to the one employed in cement pastes (2.5% w/w or 1 gram of particles per 40 grams of water) all tests demonstrate a very poor stability of these suspensions in water. Moreover, dilutions of 1.25%w/w showed a moderate stability in all cases, modified and unmodified particles with PEG.

This could be explained by the morphology of xonotlite. Xonotlite has a fibrillar shape that tends to aggregate very easily under stirring in the reactor and polyethylene glycol is not capable to disaggregate these structures in suspension.

Table III.12: Zeta potential of xonotlite particles suspensions.

Sample	Mean ZP (mV)	Standard Deviation (mV)	Sample	Mean ZP (mV)	Standard Deviation (mV)
1.25%w/w particles in water			**2.5%w/w particles in water**		
X_Pristine	-20.6	0.954	X_Pristine	-0.2	0.349
X_P600	-19.8	0.737	X_P600	2.21	0.509
X_P1500	-17.9	3.45	X_P1500	-0.125	0.682
X_P4000	-20.1	0.551	X_P4000	2.25	1.18

III.4.3. Modified xonotlite rheological, mechanical and acceleration effect on cement paste.

After preparing 100 grams of Portland cement (OPC) pastes with a 1%w/w of xonotlite particles (W/C=0.4), around 10 grams of the mix were employed to analyze its rheology. In Figure III.35 viscosity and stress versus shear rate of pastes with different PEG modified molecules are shown. The viscosity plot gives us information about the real viscosity in all the ranges of shear forces applied to the cement paste and the stress gives parameters such as yield stress (which is the minimum stress needed for the paste to start flowing) and apparent viscosity (the slope of stress versus shear rate curve) for a Bigham like non-Newtonian fluid. In both cases it is possible to compare the fluidity and workability of cement pastes and the effect of PEG when it is present in samples.

According to the results obtained, the presence of PEG modified xonotlite additions in pastes lowers de viscosity and enhances the workability of the cement mixes. The viscosity and yield stress values decrease comparing to the same cement paste with 1%wbc (weight based on cement) of pristine xonotlite. The use of modified xonotlite

samples has viscosity values near or even lower than the cement pastes without any addition. However, no significant differences in the viscosity were observed between the different molecular weight of PEGs employed.

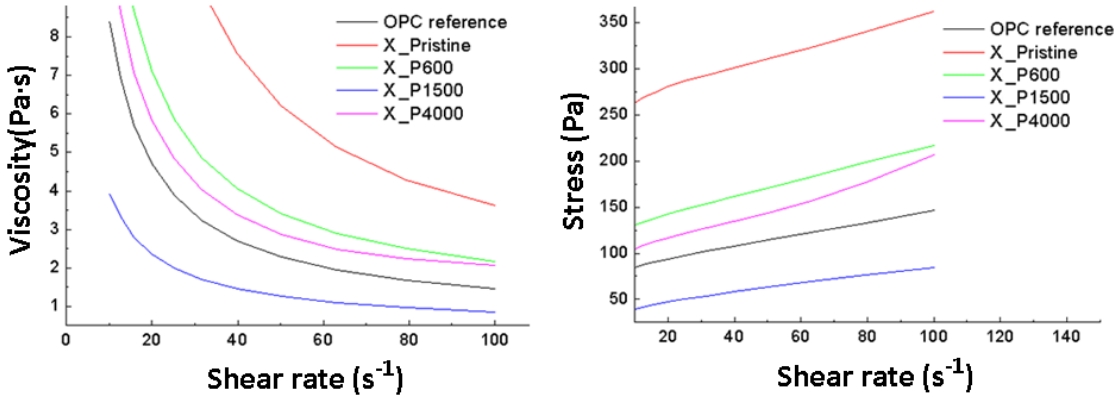

Figure III.35: Viscosity (left) and Stress (right) curves of prepared cement pastes with additives.

The hydration of cement pastes with the different xonotlite additives were also characterized by isothermal calorimetry (Figure III.36). A certain acceleration of the hydration can be observed when X_P600 and X_P1500 were used. This acceleration is similar to the one obtained by addition of pristine xonotlite. In the case of X_P600 the acceleration was slightly higher than the rest of tests.

However, xonotlite modified with PEG MW 4000 presented a negative effect on the cement hydration. This means that a high quantity of PEG retained in the solid could have an undesired effect.

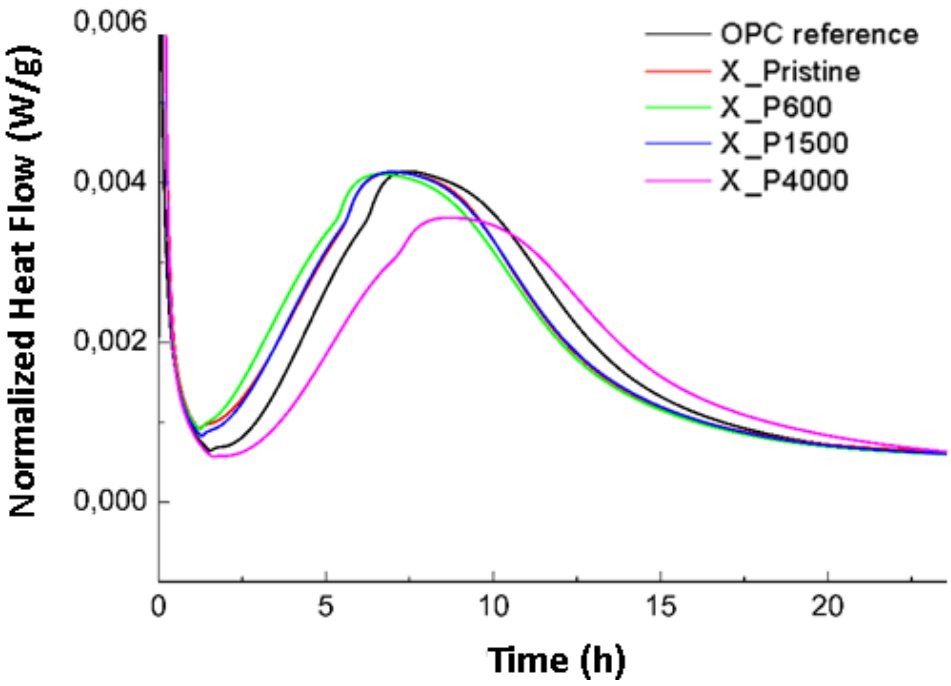

Figure III.36: Isothermal calorimetry curves of mixed cement pastes with additions.

Mechanical properties of the pastes with different xonotlite additions (1%wt/wt cement) were characterized at 8h and 24h of curing (Figure III.37). After 8 hours unmodified xonotlite and samples modified with PEG MW600 (X_P600) and PEG MW1500 (X_P1500) showed an increase of flexural strength over the reference paste. In the case of cement paste specimens with X_P4000 the flexural strength was worse than in the other specimens. Due to the brittle properties of the specimens, reference sample and pastes with xonotlite modified by PEG MW4000 (X_P4000) broke even before starting the test. Nevertheless, it is not very clear the effect of additions in flexural strength at very short curing time. No significant changes were found in flexural strength after 24 hours.

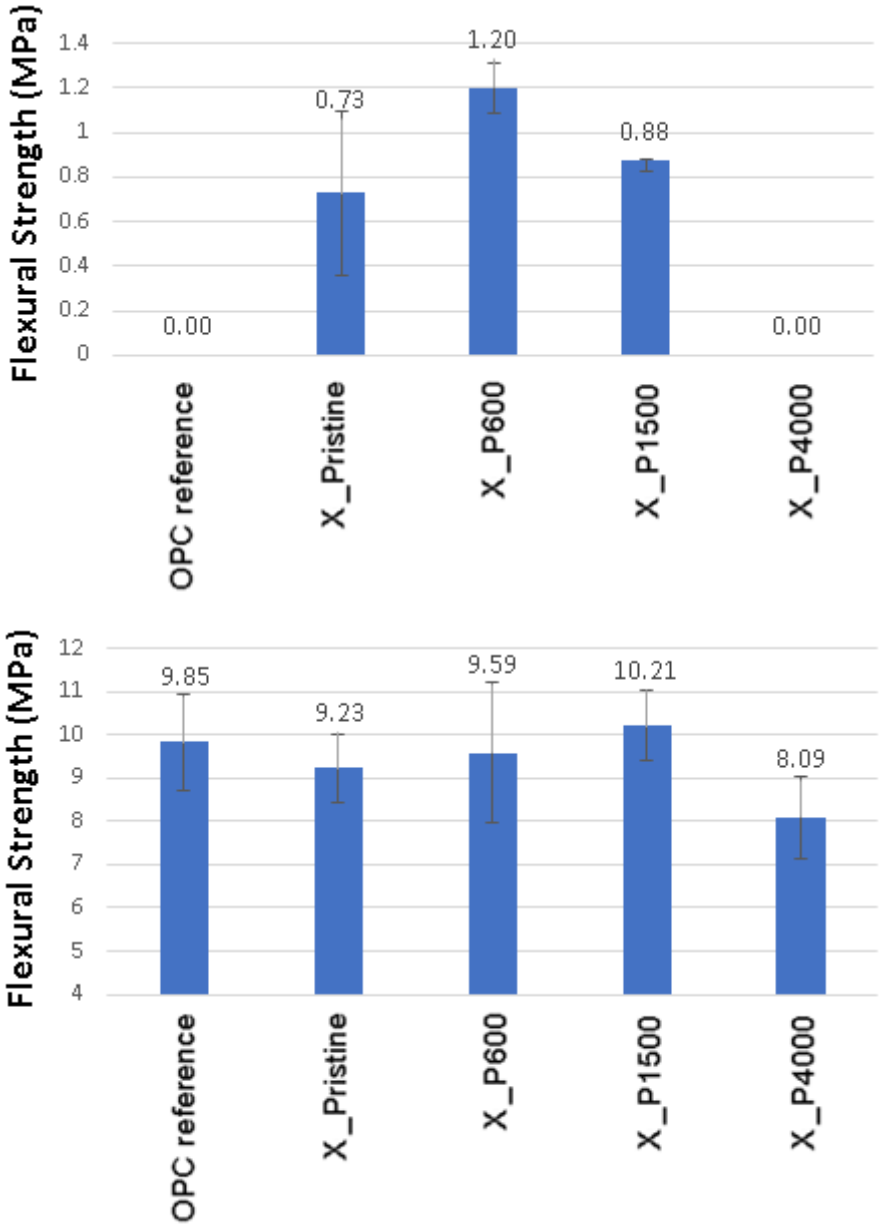

Figure III.37: Flexural strength of pastes with different xonotlite additions. Prisms tested after 8 hours (above) and 24 hours (below).

Compressive strength values of cement specimens plotted in Figure III.38 show a similar trend to the bending tests. After 8 hours the specimens with pristine xonotlite and modified xonotlite additions showed an increase in the compression resistance respect to the reference paste. The highest compressive strength was obtained with xonotlite modified with PEG MW600. However, as it was measured for flexural test xonotlite modified with PEG MW 4000 (X_P4000) showed a low value for compressive strength even lower than the reference. This confirmed the retardation effect observed in isothermal calorimetry for cement paste with X_P4000 addition.

It is important to remark that just adding PEG in the mixture to enhance its rheological behavior is not a solution because of the negative effect of the PEG on the hydration reaction. It is preferable to obtain samples with enough amount of PEG capable to disperse xonotlite fibers without worsening the seeding effect of xonotlite.

On the other hand, the specimens tested in compression after 24h did not show any significant difference respect to the reference. This tendency agrees with the results obtained by isothermal calorimetry where curves converged after 24h.

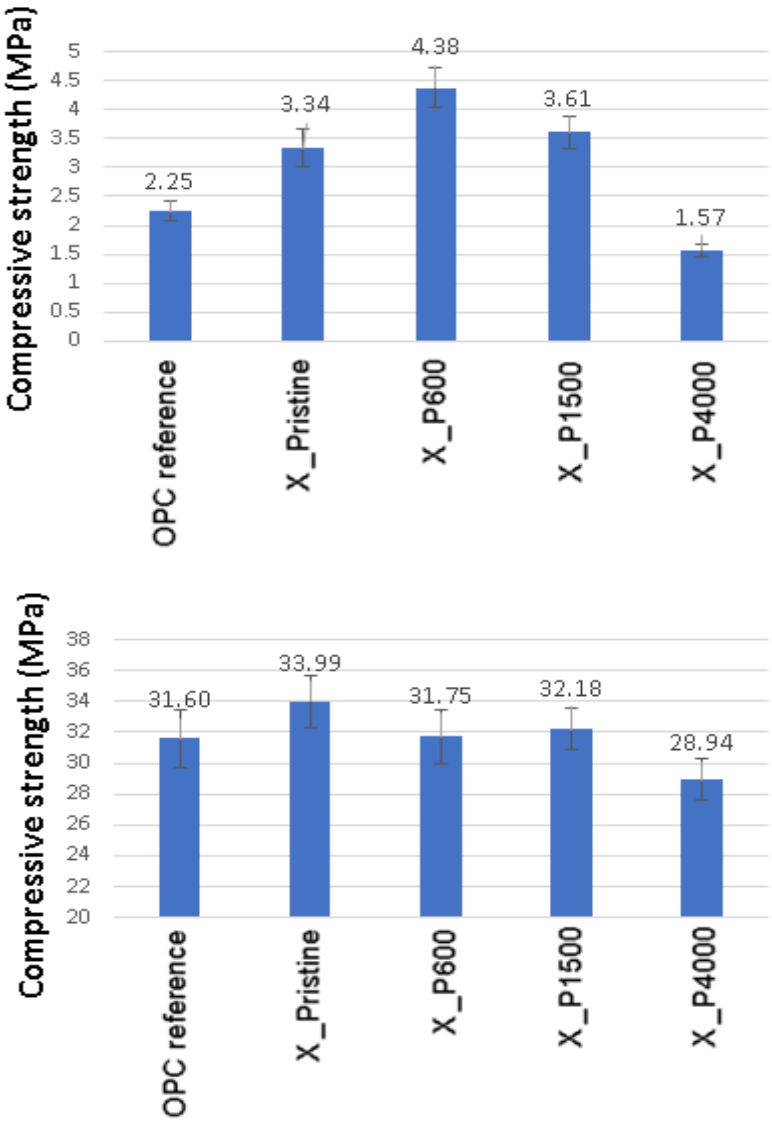

Figure III.38: Compressive strength of pastes mixed with subcritical xonotlites. Prisms tested after 8h (above) and 24h (below).

According to rheological tests carried out, it can be concluded that PEG is a good option to stabilize xonotlite particles in cement suspension. The introduction of PEG in batch reactor during precipitation of xonotltie limits the content of polymer retained. This limitation is crucial if the deceleration effect of PEG in cement hydrations has to be minimized. The higher the molecular weight of the polymer the slower is the hydration reaction.

III.5. Addition of SBS functionalized xonotlite samples to cement pastes. Rheology, mechanical behavior and acceleration effect.

Table III.13 shows the SBS content obtained from thermal degradation of samples in the range of 250 and 400°C measured by TGA/DSC. This degradation was associated to an exothermic event associated to the degradation of SBS [43]. Moreover, it was calculated the yield of SBS found in samples powder in respect to the total SBS added to the reactor medium. In both cases for xonotlite like samples and tobermorite like samples the yield was below 20%. That means that more than 80% of SBS did not react and could be still as part of reaction solution.

Table III.13: Sulfobetaine siloxane content in prepared xonotlite samples characterized by TGA /DSC.

Sample	SBS content (weight %)	Yield (g of SBS in solid/g of SBS added)%
Xonotlite_SBS-4h	3.94	15.68
Xonotlite_SBS-8h	3.54	16.40

In every case the amount of SBS calculated from TGA was very low. No significant differences were found between xonotlite like particles with SBS synthesized in 4 and 8 hours. Nevertheless, this content of SBS is very low compared to the total amount added to reactor medium (according to the yield values obtained) and there is no evidence of what is happening to the rest of the SBS.

Zeta potential measurements were carried out to study the behavior of these particles in suspension. In Table III.14 the Z potential of the xonotlite_SBS samples are shown. In

general, in the case of xonotlite samples, the particles demonstrated moderate stability (around 20mV) in water. In the case of suspensions prepared with 2.5%w/w of xonotlite particles there are no significant difference of stability if particles are modified with SBS or not (Table III.14). However, when using a concentration of 5%w/w, equivalent to a 1% of particles in cement pastes, pristine xonotlite showed high instability according to its low zeta potential (near to 0mV), while xonotlite modified with SBS shows incipient stability. This increase to more negative zeta potential was also reported for silica nanoparticles modified with SBS [49, 50].

Table III.14: Zeta potential values of SBS functionalized xonotlite samples in water suspensions.

Sample	Mean ZP (mV)	Standard Deviation (mV)	Sample	Mean ZP (mV)	Standard Deviation (mV)
2.5%w/w particles in water			**5%w/w particles in water**		
Pristine xonotlite	-20.6	0.954	Pristine xonotlite	-0.2	0.349
Xonotlite SBS-4h	-18.8	2.26	Xonotlite SBS-4h	-18.2	3.12
Xonotlite SBS-8h	-25.9	2.41	Xonotlite SBS-8h	-16.7	0.231

In Figure III.39 rheological test carried out in pastes with xonotlite modified with SBS are shown. As it can be seen the addition of SBS modified xonotlites shows a reduction in viscosity compared to cement paste with pristine xonotlite.

Isothermal calorimetry, on the other hand, showed similar acceleration effect for addition of SBS modified particles and pristine ones (Figure III.40). This seems to indicate

that there is not a negative effect of SBS in the hydration of cement. As in previous cases the acceleration effect is only observed during the first 12 hours of hydration. After 24 hours all isothermal calorimetry curves tend to converge to the same values.

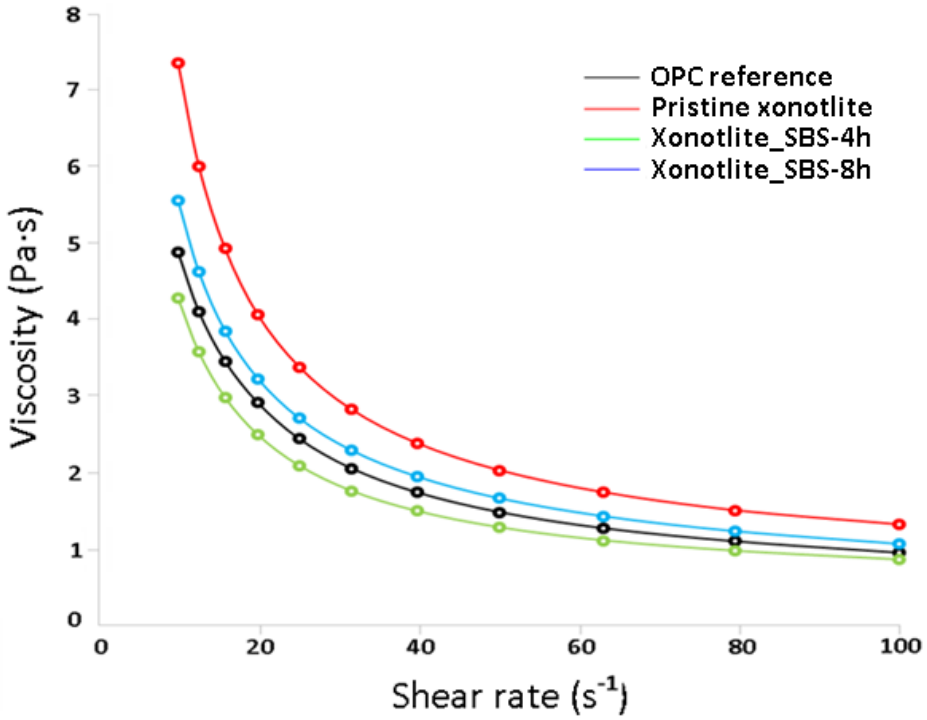

Figure III.39: Viscosity curves of prepared cement pastes with xonotlite additions.

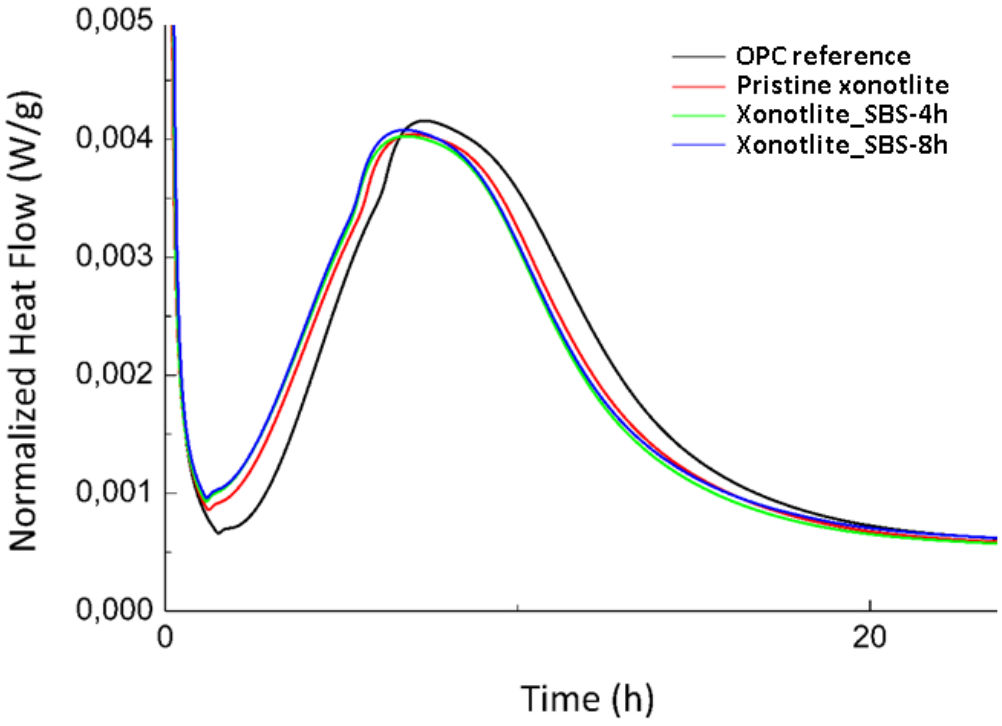

Figure III.40: Isothermal Calorimetry curves of prepared cement pastes with xonotlite additions.

Flexural tests were carried after 8 hours and after 24 hours of curing time. However, no significant effect was observed due to the addition of xonotlites. After 8 hours of curing specimens broke right at the beginning of the test and after 24 hours, differences of flexural strength among the different specimens are negligible.

Figure III.41 shows the compressive tests carried out for xonotlite additions in cement pastes after 8 and 24 hours of curing time. After 8 hours of curing significant increases of compressive strength were observed when xonotlite particles are added. However, no changes were observed between pristine xonotlite or xonotlite samples modified with SBS. After 24 hours of curing time the difference of compressive resistance between the reference paste and the paste with the addition is reduced confirming the tendency found in isothermal calorimetry curves where every curve tends to converge.

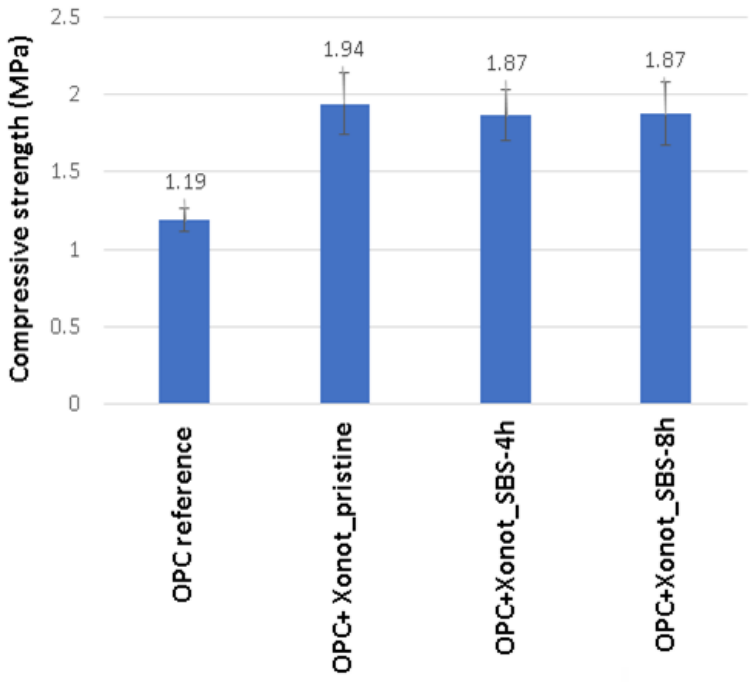

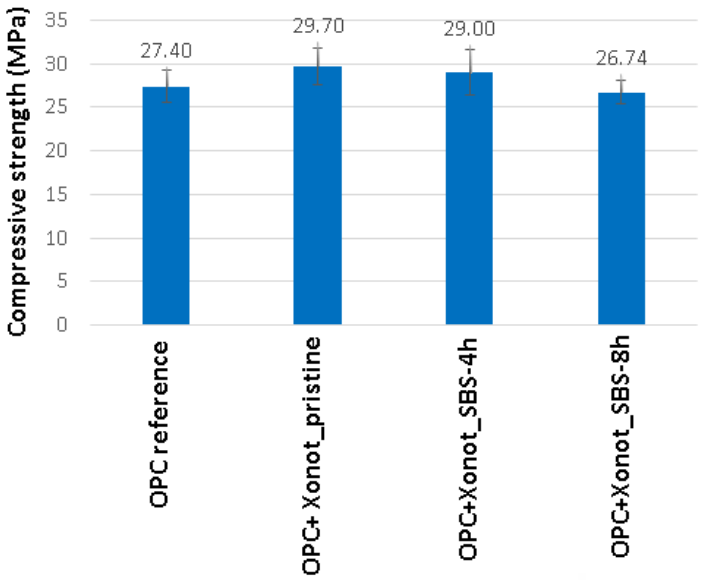

Figure III.41: Compressive test of cement pastes with SBS modified xonotlite after 8 hours (above) and after 24 hours curing (below).

In conclusion, it is important to remark that modification of xonotlite with SBS, has a positive effect in workability properties of cement pastes according to reduction of viscosity obtained in rheometric measurement. Moreover, it was demonstrated by zeta potential measurements that the SBS modified particles have a higher stability in water suspension, in particular particles at high concentration. However, it is difficult to analyze if xonotlite-like particles have a significant effect in suspension stability or is more related to the presence of silica impurities. Nevertheless, in all cases products with SBS accelerated cement hydration as much as the pristine addition. This acceleration was also observed in compressive tests where compressive strength is increased in the same way pristine samples do when they are added to cement matrix.

III.6. References.

[1] Y. Kudoh, Y. Takeuchi, *Miner. J. (Japan) 9* (**1979**), pp349–373.

[2] N. B. Milestone, K. Ghanbari Ahari*, Adv. App. Ceram., 106(6)* **(2007)**, pp. 302-308

[3] F.Liu, L.K. Zeng, J.X. Cao, B. Zhu, A. Yuan, *Adv. Mater. Res.,* Vol. 105-106 (**2010**), pp. 841-843.

[4] S. Shaw, S.M. Clark, CMB Henderson, *Chem. Geol. 167* (**2000**), pp. 129–140.

[5] N.Y. Mostafa, A.A. Shaltout, H. Omar, S.A. Abo-El-Enein, *J. Alloy. Compd. 467* (**2009**), pp. 332–337.

[6] Z. Zhao, J. Wei, F. Li, Q. Yu, *Adv. Cem. Res., 29(9)* (**2017**), pp. 359–372.

[7] J. J. Beaudoin, H. Dramé, L. Raki, R. Alizadeh*Mater. Struct. 42* (**2009**), pp. 1003-1014.

[8] M. Diez-Garcia **2017**. *"Synthesis by supercritical fluids methods of advanced additions for cementitious materials"* Universidad del País Vasco/Université de Bordeaux. Repositorio institucional ADDA EHU Biblioteka UPV/EHU.

[9] M. Li and H. Liang, CHINA PARTICULOGY Vol. 2, No. 3 **(2004),** pp. 124-127.

[10] K. Suzuki, T. Nishikawa, S. Ito, *Cem. Concr. Res., 15,* (**1985**); pp. 213–24.

[11] G. Smalakys and R. Siauciunas, *J. Therm. Anal. and Calorim.,* 142 (**2020**), pp. 1671-1679.

[12] P. Yu, R.J. Kirkpatrick, B. Poe, P.F. McMillan, X. Cong, *J. Am. Ceram. Soc. 82* (**1999**)742.

[13] I. García-Lodeiro, D. E. Macphee, A. Palomo, A. Fernández-Jiménez, *Cement and Concrete Research* 39 (**2009**) pp. 147–153.

[14] R. L. Frost, M. Mahendran, K. Pologanathan, Y. Xi, *Mater. Res. Bull.* 47 (**2012**) pp. 3644–3649.

[15] X. Cong and R. Kirkpatrick. *Advn. Cem. Bas. Mat*. 3 (**1996**), pp. 133-143.

[16] Ian G. Richardson. *Acta Cryst.* (**2014**). B70, pp. 903–923.

[17] T. F. Sevelsted and J. Skibsted. *Cem. Concr. Res.,* 71 (**2015**) pp. 56–65.

[18] H. Noma, Y. Adachi, Y. Matsuda, T. Yokoyama, *Chem. Lett.27, 3* (**1998**), pp. 219-220.

[19] J. J. Chen, J. J., Thomas, H. F. W. Taylor, H. M. Jennings, *Cem. Concr. Res.* 34, 9 (**2004**), pp. 1499–1519.

[20] Y. Chiang and S.W. Chang, *Cem. Concr. Res. 140* (**2021**) 10626

[21] I. S. Protsak, Y. M. Morozov, W. Dong, Z. Le, D. Zhang, *Nanoscale Res. Lett.* 14:160 (**2019**).

[22] A. Putnis, Introduction to Mineral Sciences, 4th ed., Cambridge Univ. Press, Cambridge, **1992**.

[23] L. Black, K. Garbev, P. Stemmermann, K.R. Hallam, G.C. Allen. *Cem. Concr. Res. 33* (**2003**) pp. 899–911.

[24] L. Black, K. Garbev, P. Stemmermann, K.R. Hallam, G.C. Allen, *Phys. Chem. Miner.* (**2004**) 31: pp. 337–346

[25] M. Diez-Garcia, J.J. Gaitero, J.I. Santos, J.S. Dolado *J., C. Aymonier, Flow. Chem.* 8, (**2018**), pp. 89–95.

[26] X. Guo, F. Meng, H. Shi, *Constr. Build. Mater., 133* (**2017**) pp. 253–260.

[27] J. Blummel, N. Perschmann, D. Aydin, J. Drinjakovic, T. Surrey, M. Lopez-Garcia, H. Kessler, J. P. Spatz, Biomater., 28 (**2007**) pp. 4739–4747

[28] L. Black, A. Stumm, K. Garbev, P. Stemmermann, *Cem. Concr.Res. 35* (**2005**) pp. 51–55.

[29] O. Hourri,J. Masse, *J. Therm. Anal., 39, 507,* (**1993**).

[30] J. Ha, S. Chae, K.W. Chou, T. Tyliszczak, *J. Mater. Sci. 47* (**2012**), pp. 976–989.

[31] Y. Zhou, C. A. Orozco, E. Duque-Redondo, H. Manzano, G. Geng, P. Feng, P. J.M. Monteiro, C. Miao, Cem. Concr. Res. *115 (***2019***)* pp.20-30.

[32] W. Guan, F. Ji, *Materials*, 6 (**2013**), pp. 2846-2861.

[33] F. Branda, B. Silvestri, G. Luciani, A. Costantini, F. Tescione, *Colloids and Surfaces A: Physicochem. Eng. Aspects 367* (**2010**) pp. 12–16.

[34] J. Meng, X. Tang, W. Li, X. Zhang, *Thermochimica Acta 558* (**2013**) pp. 83–86.

[35] J. J. Beaudoin, L. Raki, R. Alizadeh, *Cem. Concr. Comp. 31* (**2009**) pp. 585–590

[36] S. Sharma, R. W. johnson, T. A. Desai, *Biosens. Bioelectron. 20 (**2004**)* pp*. 227–239.*

[37] L. Black, K. Garbev, A. Stumm, *Adv. Appl. Ceram.* 108, 3 (**2009**).

[38] K. Horikoshi *et al.*, *J. Mol. Struct., 239* (**1990**) pp. 33-42.

[39] A. Kumar, C. K. Dixit, "Methods of Characterization of Nanoparticles" (**2017**) pp.43-58. ISBN 9780081005576.

[40] J. J. Chen, J. J. Thomas, H.F.W. Taylor, H. M. Jennings, *Cem. Concr. Res.* 34,9 (**2004**), pp. 1499–1519.

[41] Z. G. Estephan, H.H Hairi and J.B. Schlenoff, *Langmuir, 29, 8,* (**2013**) pp. 2572–2579.

[42] V. Hildebrand, A. Laschewsky, M. Päch, P. Muller-Buschbaum, C. M. Papadakis, *Polym. Chem., 8,* **(2017)** pp. 310–322.

[43] Z. G. Estephan and J. B. Schlenoff, "Stable iron oxide nanoparticles and method of production" patent n°: US 9196405 B2 Nov 24, 2015.

[44] B. Walkley and J. L. Provis, *Materials Today Advances, Volume 1,* (**2019**), article. 100007.

[45] M. Monasterio, J. J. Gaitero, E. Erkizia, A. M. Guerrero Bustos, L. A. Miccio, J. S. Dolado, S. Cerveny, *Journal of Colloid and Interface Science 450,* (**2015**) pp. 109-118.

[46] A. Franceschini, S. Abramson, V. Mancini, B. Bresson, C. Chassenieux, N. Lequeux, *J. Mater. Chem., 17,* (**2007**), pp. 913–922.

[47] H. Rosenberger, A. R. Grimmer, U. Haubenreißer, B. Schnabel, *Magn. Reson. Relat. Phenom.*, Springer, Heidelberg, Berlin, (**1979**), pp. 106-106.

[48] D. Heidemann, W. Wieker, *Nucl. Magn. Reson. Spectrosc. Cem. Mater.*, Springer, Berlin, (**2012)**, p. 169.

[49] B. R. Knowles, D. Yang, P. Wagner, S. Maclaughlin, M. J Higgins, P. J. Molino, *Langmuir, 35, 5*(**2019**) pp. 1335-1345.

[50] Z. G. Estephan, J. A. Jaber, J. B. Schlenoff, *Langmuir, 26, 22* (**2010**), pp. 16884–16889.

[51] S. V. Churakov and P. Mandaliev, *Cem. Concr. Res., 38* (**2008**) pp. 300-311.

CHAPTER IV. SYNTHESIS OF TOBERMORITE MODIFIED WITH ORGANIC COMPOUNDS IN BATCH REACTOR.

IV.1. Pristine tobermorite synthesized in subcritical conditions.

IV.1.1. Structural analysis of pristine tobermorite.

Tobermorite structure has been the object of numerous studies over the years due to its structural similarities to cement hydration product. Although its silicate chains and calcium oxide layers arrangements have similarities to xonotlite, tobermorite presents significant differences. From the first models proposed by McConnel (1954) [9] or Hamid (1981) [10] to Merlino's model [11], different interpretations have been made about its crystallographic structure.

Moreover, the existence of different hydration states in tobermorite complicates its analysis. As it was mentioned before tobermorite can be found as 14Å, 11Å or 9Å - tobermorite phases.

After 4 hours of reaction at 215°C, the obtained powder was characterized by XRD (Figure IV.1). The XRD pattern matched to 11Å-tobermorite Powder Diffraction File (PDF 00-045-1480). This reference was obtained from a natural tobermorite sample obtained in Fuka, Japan [12].

The main phase obtained using these conditions of synthesis was tobermorite, although some presence of residual calcite was also detected. No other byproduct was identified by XRD.

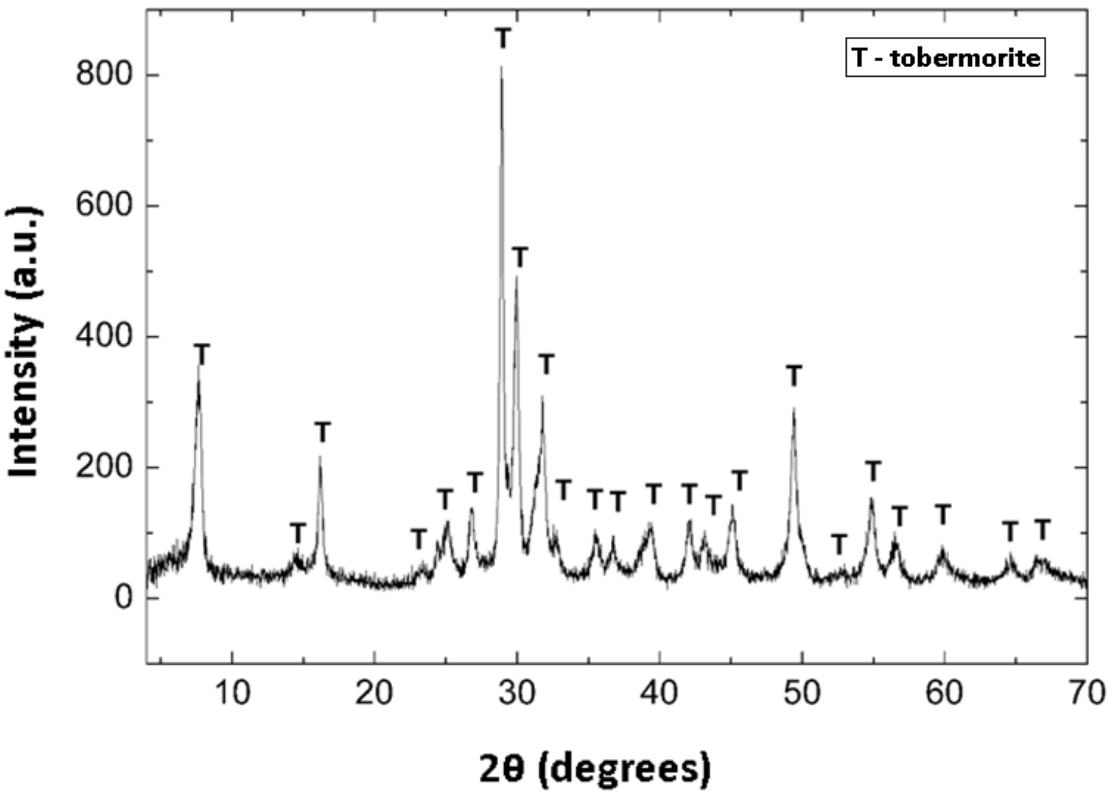

Figure IV.1: XRD diffractogram of 11Å - tobermorite obtain under 215°C and 18 bar of pressure for 4 h.

If we compare our result with the reference in ICDD database, no significant shift was observed in the basal peak associated to crystallographic plane (002) that is located at 11.54Å (signal at 7.6° in Figure III.9). It can be concluded that as expected this is a good synthetic route to obtain 11Å-tobermorite with good crystalline properties, by using only 4 hours of reaction and 15%w/w of aluminum as stabilizing element.

FT-IR spectrum of pristine tobermorite is shown in Figure IV.2. The most intense peaks at 1057cm^{-1} 975cm^{-1} and 903cm^{-1} can be assigned to Si-O stretching mode. This signal is generally assigned in the literature to the pairing/bridging silicate tetrahedra (the silicate tetrahedra that gives theQ^2 signal in the ^{29}Si NMR). O-Si-O bending modes, which occur in the 556–400cm^{-1} region and the band at ∼672 cm^{-1} which is due to Si-O-Si bending vibrations [1] can also be observed in the FT-IR spectrum. The band at 1180 cm^{-1} can be also assigned to Si-O stretching mode. This band is generally assigned in the literature to the branching silicate tetrahedra (the silicate tetrahedra that gives the Q^3 signal in the 29Si NMR). tetrahedral silicate also appears at 1200cm^{-1} but is lower than

the one for xonotlite and it is a bit shifted to 1180 cm^{-1}. This shift in Q^3 contributions have been previously reported for aluminum substituted tobermorites [4].

Although infrared spectroscopy showed results similar to xonotlite, tobermorite particles present more intense contributions associated to water. This can be seen in the more intense peak than in the case of xonotlite around 1600cm^{-1} which can be assigned to bending vibrational mode of water. The stretching contributions for hydroxyl groups around 3400cm^{-1} are also more intense than the ones observed for xonotlite.

The band at 1450cm-1 can be assigned to carbonate groups. It is interesting to mention that the intensity of the carbonate band in tobermorite is higher than in the case of xonotlite. This could be due to the fact tobermorite has higher amounts of hydroxyl groups and eater in the structure which makes it easier to carbonate.

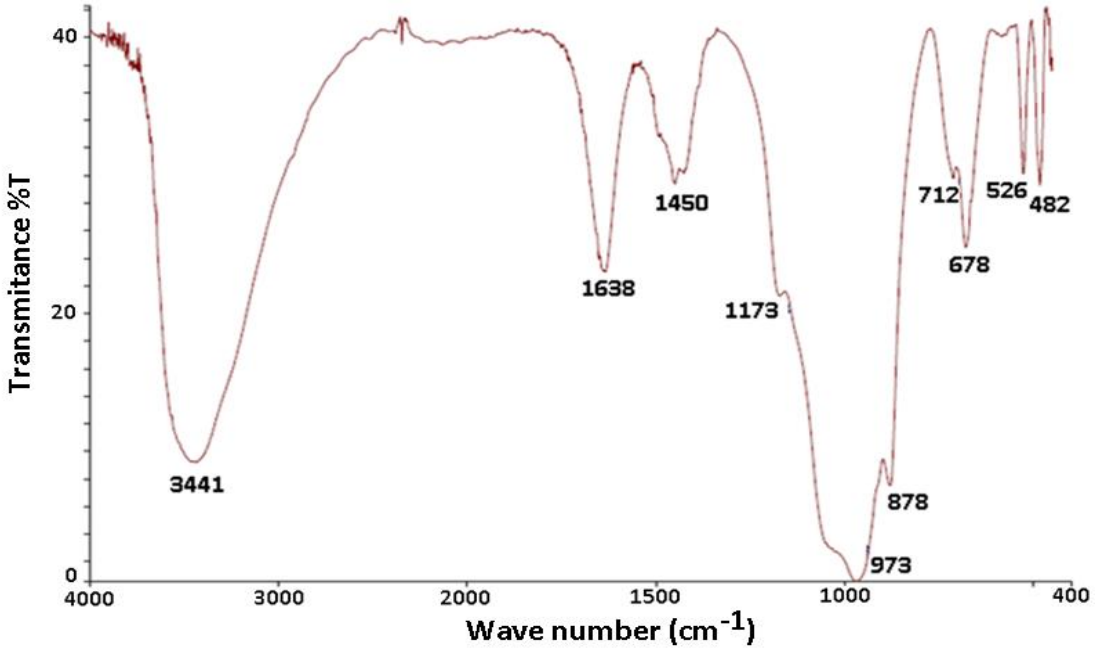

Figure IV.2: FT-IR spectrum of 11Å-tobermorite obtain under 215°C and 18bars for 4 hours.

Pristine tobermorite was also analyzed by ^{29}Si ss-NMR and its results (Figure IV.3) matched to previous measurements in literature [12, 17-19]. Besides the characteristic peaks, Q^1, Q^2 and Q^3, associated to silicate tetrahedra in Dreierketten double chain, there are two extra signals at -84ppm and -93ppm. They are associated to Q^2(1Al) and

Q^3(1Al), respectively, and the signals are due to the silicate tetrahedra that are bound to an aluminate tetrahedra through an oxygen atom along the chain [12, 28].

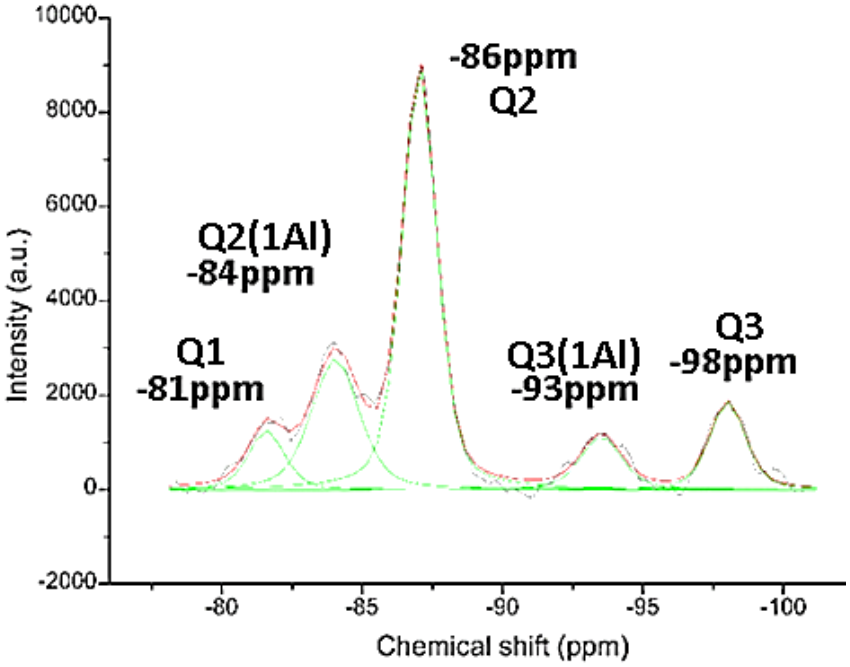

Figure IV.3: ^{29}Si Solid State NMR for aluminum substituted tobermorite.

The spectrum has been deconvoluted using 5 peaks, one per each signal. The average or mean chain length can be calculated from the areas under the deconvoluted curves. In this case the calculation follows equation 16. (It can be considered that xonotlite MCL formula is just a specific case where Q^2(1Al) and Q^3(1Al) are equivalent to zero). The average chain obtained for tobermorite is 30, lower than the MCL obtained for xonotlite.

$$\mathbf{MCL} = \frac{2}{\frac{\mathbf{Q^1}}{(\mathbf{Q^1}+\mathbf{Q^2}+\mathbf{Q^3}+Q^3(\mathbf{1Al})+\frac{3}{2}Q^2(\mathbf{1Al}))}} \qquad (16)$$

The sample was also characterized by ^{27}Al NMR in order to further study its structure. The ^{27}Al ss-NMR spectrum for pristine tobermorite pristine (Figure IV.4) presents two signals, one at 63ppm and the other at 56ppm.

Aluminum can have different coordination numbers. It can be tetracoordinated (coordination number 4, Al (4)), pentacoordinated (coordination number 5, Al (5)) and even octahedrally coordinated (coordination number 6, Al (6)). Depending on the

coordination number the chemical shift of the aluminum changes. According to literature [16- 18, 21, 22] Al (4) signals show in the range of 50-75ppm, Al (5) is identified with chemical shifts between 30ppm and 40ppm and octahedral aluminum Al (6) around 0ppm.

Contributions observed in Figure IV.4 can be found around 60ppm and no contributions were found between 0 and 40ppm. Then, it can be interpreted that tobermorite with a Ca/(Si+Al) =0.83 and Al/(Si+Al) =0.15, only contains aluminum in tetrahedral coordination. This result agrees with other literature studies [18, 20]. In fact, Sun *et al.* [18] and Pardal *et al.* [20] previous studies indicated that these high coordinated contributions are only found in systems with Ca/(Si+Al) ratios above 0.90 and Al/(Si+Al) above 0.15.

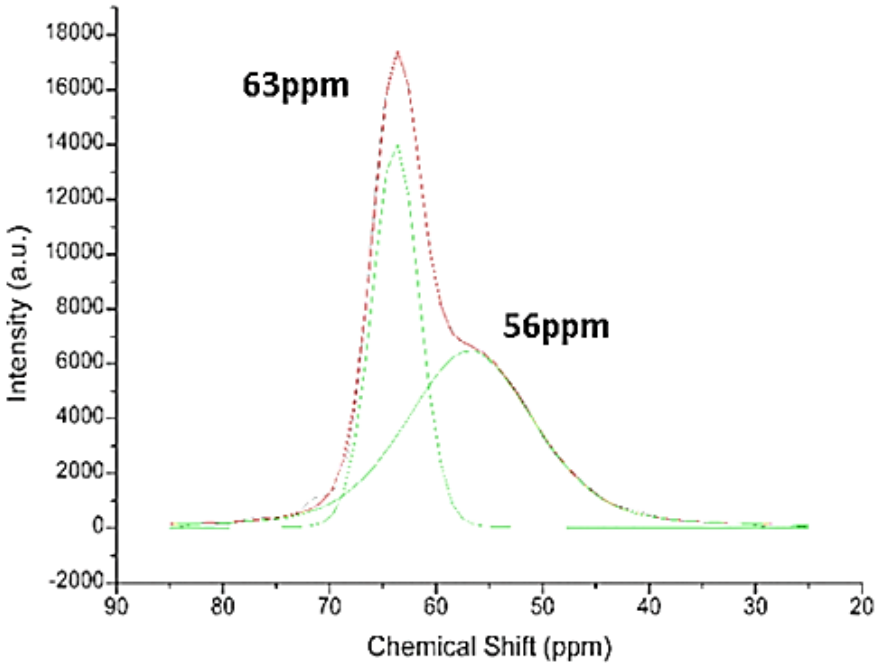

Figure IV.4:^{27}Al ss-NMR of aluminum substituted pristine tobermorite.

There are some ^{27}Al NMR studies carried out in different calcium silicate hydrate phases [17, 18] where they obtained aluminum signal around 74ppm. The authors assigned this signal to the aluminum of the aluminate tetrahedra in Q^2 pairing position (substituting a Q^2 silicate tetrahedra in pairing position). They also indicated that this signal is only obtained with a high Ca/Si ratio. The ^{27}Al NMR spectrum of synthesized pristine

tobermorite in the actual study only shows a signal at 63ppm which has a big shoulder, which could be another signal, at 56ppm. No signals were obtained at higher chemical shifts which, taking into account the previous studies, indicates that the aluminum in the pristine tobermorite structure is in aluminate tetrahedra form and the tetrahedra is in branching or/and bridging position.

Aluminum in tetrahedral coordination substituted in tobermorite structure is not totally described yet. According to some authors there are two signals at 56ppm and 63ppm associated to aluminum with this coordination [16, 17]. These signals fits with the signals obtained in this study. However, other authors do not even distinguish the two contributions in that region [20, 22].

Some authors did assign these two signals to different positions along the double silicate chains [18, 21]. They assigned aluminum in bridging position to the 63ppm signal and the 56ppm signal to aluminum located in a branching position. However, aluminum in branching or in bridging positions can be difficult to distinguish because these arrangements only differ in few neighbors and the differences found in chemical shift are minimal.

Due to the lack of knowledge about the asymmetry degree of aluminum tetrahedra and a huge overlap between both tetrahedral contributions, authors like Schneider [17], do not recommend the quantification of tetrahedral aluminum with NMR. However, assuming that both signals were adjusted to a pseudo-Voigt function, a rough estimation could be performed. In this work a 62.9% of aluminum in bridging position versus a 37.1% of aluminum in branching position, were calculated from the deconvoluted curves in ^{27}Al ss-NMR.

Taking into account the different silicon tetrahedra types seen in the ^{29}Si NMR and the different aluminum tetrahedra from ^{27}Al NMR, it is possible to estimate where the aluminum is introduced in the different structural positions in pristine tobermorite using the areas of deconvoluted peaks from ^{29}Si NMR and a proposed structural model. Then, the result can be compared to the estimated quantification of the deconvoluted peaks in the different aluminum signals observed in ^{27}Al NMR.

A basic model was built considering that aluminum atoms cannot be located in CaO layers or pairing positions along silicate chains [3]. The model showed in Figure IV.5 divides the double Dreierketten chains in segments or elemental units of six atoms that repeat along the total silicate chain. This means that the model shows all the plausible configurations were aluminum tetrahedra can be located in tobermorite.

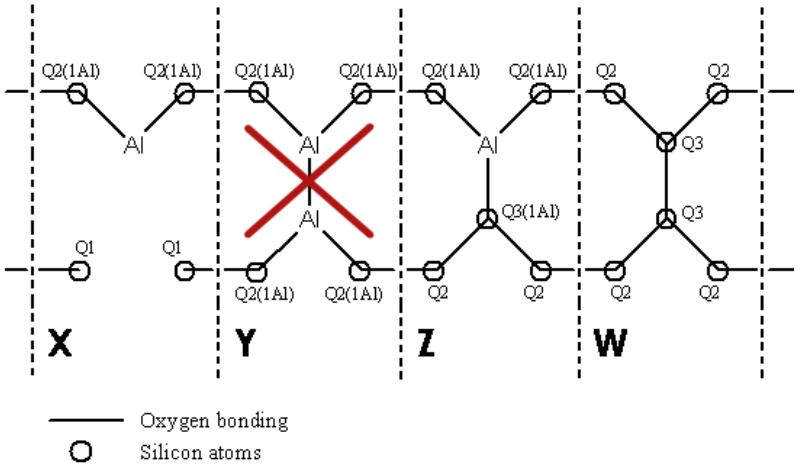

Figure IV.5: Scheme of aluminum substitution cases for proposed Dreierketten silicate chain in aluminum substituted tobermorite.

Subsequently, a percentage "X", "Y", "Z" and "W" to each configuration was assigned as it can be seen in Figure IV.5. "X" and "Z" are associated to structural units with aluminum in bridging and branching positions. "W" is the percentage of units without aluminum and finally "Y" is the percentage of structures with two aluminum atoms located in Q^3 positions and bound by an oxygen atom. This kind of structures are not energetically favorable, according to Loewenstein's rule [23], and it was only introduced as a method to check if the model gives a sound result.

The proposed model with function objective and boundary conditions is shown in equations 17 to 20. It was scripted, compiled and run in a demo version of GAMS vr. 26.1.0. This system has been solved as a nonlinear programming problem where the ratio $Q^2(1Al)/Q^2$ is the function objective that has to approximate as much as possible to the values obtained by deconvolution of the signals shown in ^{29}Si NMR measurement. Boundary conditions were fixed for $Q^2(1Al)/Q^3(1Al)$, $Q^1/Q^3(1Al)$ and Q^1/Q^3. Moreover, two more restrictions were added; first the sum of all percentage must be 100% and each percentage value cannot be negative.

The results obtained are shown in Table IV.1. From these results it was calculated the population of aluminum tetrahedra in bridging and branching positions. Then they are compared to population ratios of the different aluminum atoms (bridging and branching) calculated from ^{27}Al ss-NMR measurements carried out previously.

$$Function\ objective:\ \frac{Q_2(1Al)}{Q_2} = \frac{2X+4Y+2Z}{4W+2Z} \quad (17)$$

$$Boundary\ condition\ \#1:\ \frac{Q_2(1Al)}{Q_3(1Al)} = \frac{2X+4Y+2Z}{Z} \quad (18)$$

$$Boundary\ condition\ \#2:\ \frac{Q_1}{Q_3(1Al)} = \frac{2X}{Z} \quad (19)$$

$$Boundary\ condition\ \#3:\ \frac{Q_1}{Q_3} = \frac{X}{W} \quad (20)$$

Table IV.1: Composition of different locations of aluminum in the structure. Converged result from nonlinear program in GAMS.

X (Bridging Al)	Y	Z (Branching Al)	W	Branching Al/ Bridging Al from model	BranchingAl/ Bridging Al from ^{27}Al ss-NMR first assignation	BranchingAl/ Bridging Al from ^{27}Al ss-NMR second assignation
16.06%	0%	26.54%	57.39%	1.65	0.59	1.69

On one hand, if aluminum in bridging position is assigned to the signal at 63ppm and the aluminum in branching position is assigned to 56ppm as reported in previous studies, branching aluminum/bridging aluminum ratio is 0.59 (named first assignation in table IV.1) far from the result of 1.65 obtained from the model. On the other hand, if the peak at 63ppm is assigned to branching positions and the peak at 56ppm is assigned to bridging positions then branching aluminum/bridging aluminum ratio is 1.69. This result is closer to the value obtained from the ratio given by the proposed model. In order to know where the aluminate sites are in the structure, we believe that more work should be carried as a way to unequivocally assign the two aluminum tetrahedral signals.

Besides ^{29}Si and ^{27}Al ss-NMR, pristine tobermorite was also characterized by ^{1}H ss-NMR (Figure IV.6). Several signals were observed in the spectrum although they overlap. The

spectrum was deconvoluted and fitted with four peaks. The wide contribution around 4-5ppm was associated to the presence of water molecules in the solid the same as in the case of xonotlite. Nevertheless, this signal is larger in tobermorite than in xonotlite. In fact, in the case of tobermorite the signal is quite large and. can overlap the other contributions making the deconvolution and spectra analysis complicated.

A smaller contribution around 2.02ppm can be observed like in the xonotlite case. Following the assignation of xonotlite this signal could be due to the protons of Ca-OH. The other peak around 0.98 ppm that could be related to free silanol groups in silicate chains. Furthermore, a new contribution at 3.5ppm is found. It is possible to assign this peak to the interaction of water molecules and surface silanol groups or hydrogen bonds interaction between close silanol groups [6].

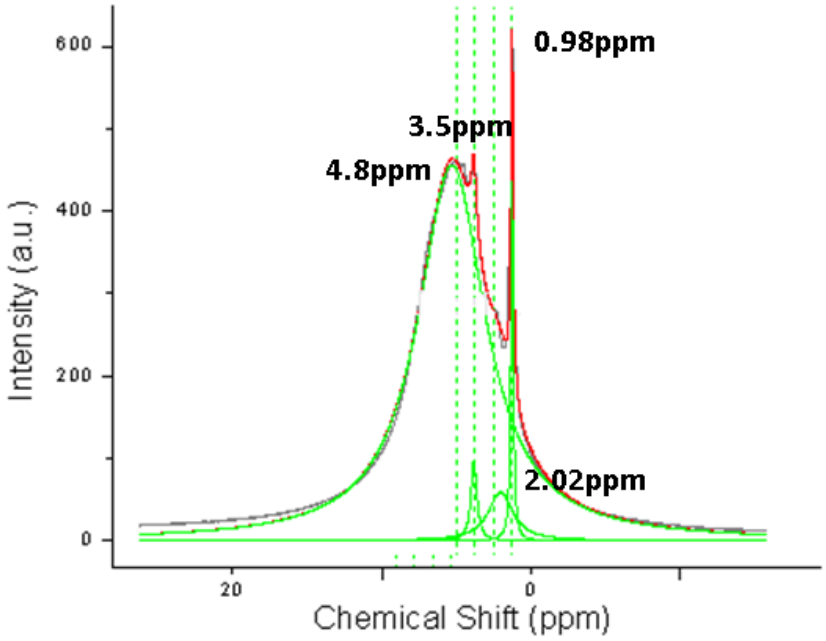

Figure IV.6: ^{1}H ss-NMR of aluminum substituted tobermorite sample.

Pristine tobermorite was characterized by XPS. First elemental analysis of tobermorite was carried out by XPS. Thus, it was confirmed the presence of silicon, calcium, oxygen, and aluminum elements in its composition. Figure IV.7 shows XPS deconvoluted spectra obtained from Si2p, Ca2p, O1s, C1s and Al2p. According to Si2p signal deconvolution there are three main contributions associated to electrons in orbital 2p 3/2. One at 101.4eV, another around 102.5eV and the last one on 103.5eV. If we consider that Si-O-

Si and Si-O-Ca are more abundant than the Si-OH in the tobermorite structure, we could interpret that the peak at 103.5eV is associated to silanol groups.

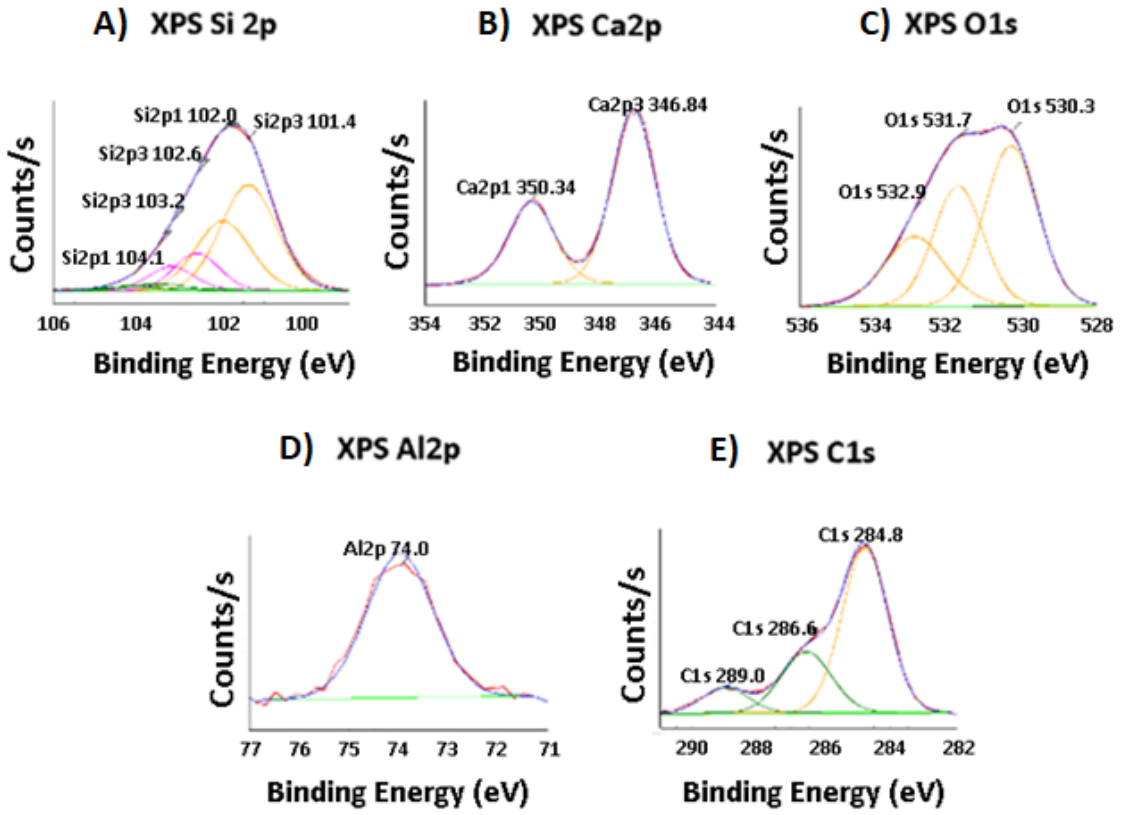

Figure IV.7: XPS spectra of different elements in pristine tobermorite surface.

Moreover, we could assume that an atomic bonding with more distributed electrical charge has a higher binding energy. Following this assumption, we associate the peak around 102.5eV to Si-O-Si bonding and the peak around 101.4eV to Si-O-Ca. Seyama and Soma [7] concluded that substitution of Al^{3+} for Si^{4+} in silicate chains brings a negative charge responsible for a shielding effect of silicon nuclei and a decrease in binding energies.

Faucon *et al.* [22] defended that an increase of aluminum content in the structure drives a shortening effect in silicate chains and Barr *et al.* [25] correlated the increase of aluminum content in structure to a reduction of Si2p binding energies as well. However, in this case the signal Si2p of pristine tobermorite showed similar binding energies compared to the ones observed for xonotlite. So, no significant changes about silicate chain length were observed by XPS.

Black *et al.* [8] showed that Ca2p3 have a low dependency of calcium silicate hydrate structure. Regarding the calcium signal (Figure IV.7 B) two main contributions have been obtained, one at 346.85eV (Ca2p3) and the other at 350.35eV (Ca2p1). Analyzing Ca2p3 it was found that this binding energy is slightly lower than the same contribution for xonotlite, but the difference is not significant and could be part of measurement error.

In the case of O1s peak (Figure IV.7 C) the signal was deconvoluted using fitting three peaks, at 530.3eV, 531.7eV and 532.9eV. The two first contributions, associated to non-bridging (NBO) and bridging oxygens (BO) respectively, did not show any difference to the position values obtained for xonotlite.

However, it is interesting to mention that the relative areas of oxygen in Si-O-Si or Si-O-H groups seem to decrease, and non-bridging contribution tends to increase comparing to the same signals obtained in xonotlite. This tendency was observed by Black *et al.* [34] studying by XPS the degree of polymerization for silicate chains in calcium silicate hydrates. He observed a shielding effect in no-bridging oxygen contributions when silicate chain polymerizes. Figure IV.8 compare both curves for xonotlite and tobermorite and shows effect for non-bridging oxygens in tobermorite. This confirmed the mean chain length values obtained by ^{29}Si ss-NMR that was 41 for pristine xonotlite and less than 30 for pristine tobermorite.

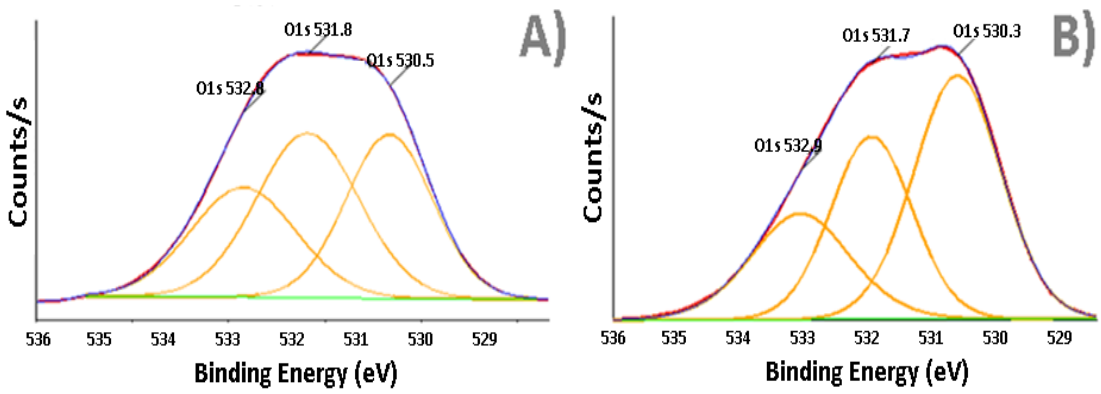

Figure IV.8: Detailed O1s XPS spectra for pristine xonotlite (a) and pristine tobermorite (b)

Other signal that should be expected to be measured for tobermorite is the oxygen in Si-O-Al bond. The electronegativity of aluminum is an intermediate value between Si and Ca elements, so it would be expected to be among Si-O-Si and Si-O-Ca. However, due to the XPS equipment and its resolution, the Si-O-Al contribution is not possible to distinguish through the O1s analysis.

In the case of the Al signal XPS data showed a small peak around 74eV associated to tetrahedral aluminum which is well reported in literature [34]. As it was observed in ^{27}Al ss-NMR, there was no presence of octahedral aluminum in the XPS results either.

IV.1.2. Heat treatment of pristine tobermorite.

As it was introduced in chapter I, there are two different types of 11Å-tobermorite, normal and anomalous. The only reported method to distinguish the specific form of 11Å-tobermorite is heating the samples at 300°C for 24h [13, 14]. This way it can be seen if tobermorite dehydrate to become 9Å-tobermorite or not, to clarify a normal or anomalous behavior, respectively.

In order to find out if the synthesized pristine tobermorite is normal or anomalous tobermorite a heating treatment was carried out. The sample was heated at 300°C for 24 hours under air atmosphere. The treated sample was characterized again by XRD to study possible changes in its structure, through diffraction peak positions. According to the results obtained (Figure IV.9) samples behaved as normal 11Å-tobermorite dehydrating to 9Å-tobermorite phase. This change can be observed in the shift of the peak associated to basal plane (002) which moved from 11Å to around 9.6 Å.

This effect can only be possible if there is a break of the bond of the two branching tetrahedra in the double silicate chain collapsing the structure and reducing the distance between the two CaO layers. Moreover, the XRD showed a significant loss of crystallinity due to the rearrangement of the structure and loss of water.

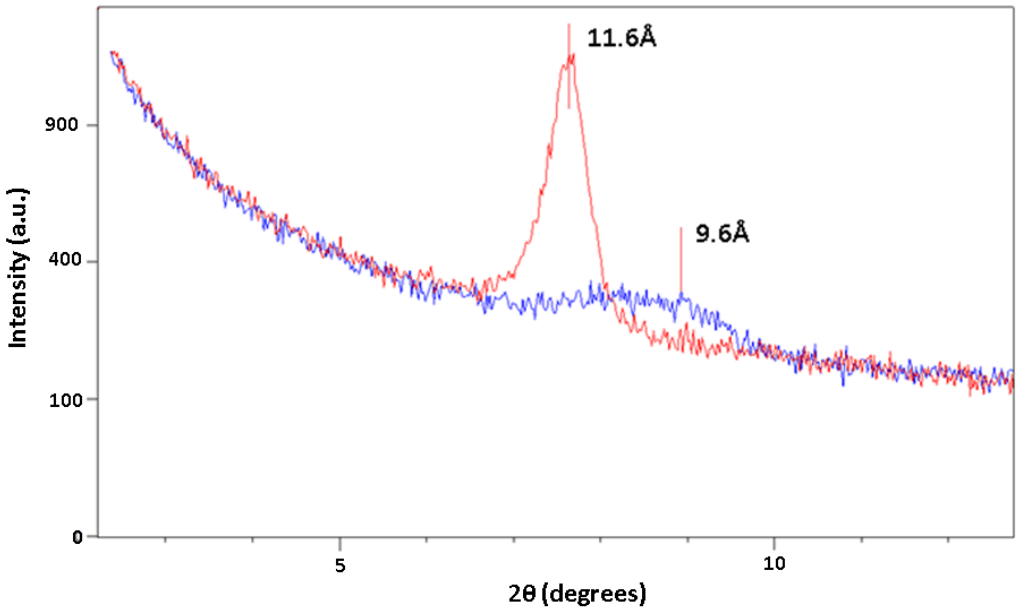

Figure IV.9: Detailed XRD contribution of basal peak associated to plane (002). Effect of temperature treatment in 11Å-tobermorite structure. Red line: untreated sample. Blue line: sample treated at 300°C in air for 24h.

Heating treatment at 300°C for 24 hours caused changes in FT-IR spectra as well. Figure IV.10 shows that Q^3 contribution at 1173 cm^{-1}decreases. This reduction of the band might be due to the reduction of silicon atoms in Q^3 positions due to the breaking of the branching tetrahedra.

Some reduction of water bending at 1600 cm^{-1} were also detected due to the partial dehydration of 11Å - tobermorite. Furthermore heating treatment in air atmosphere provoqued an increase of carbonation signal at 1450 cm^{-1}.

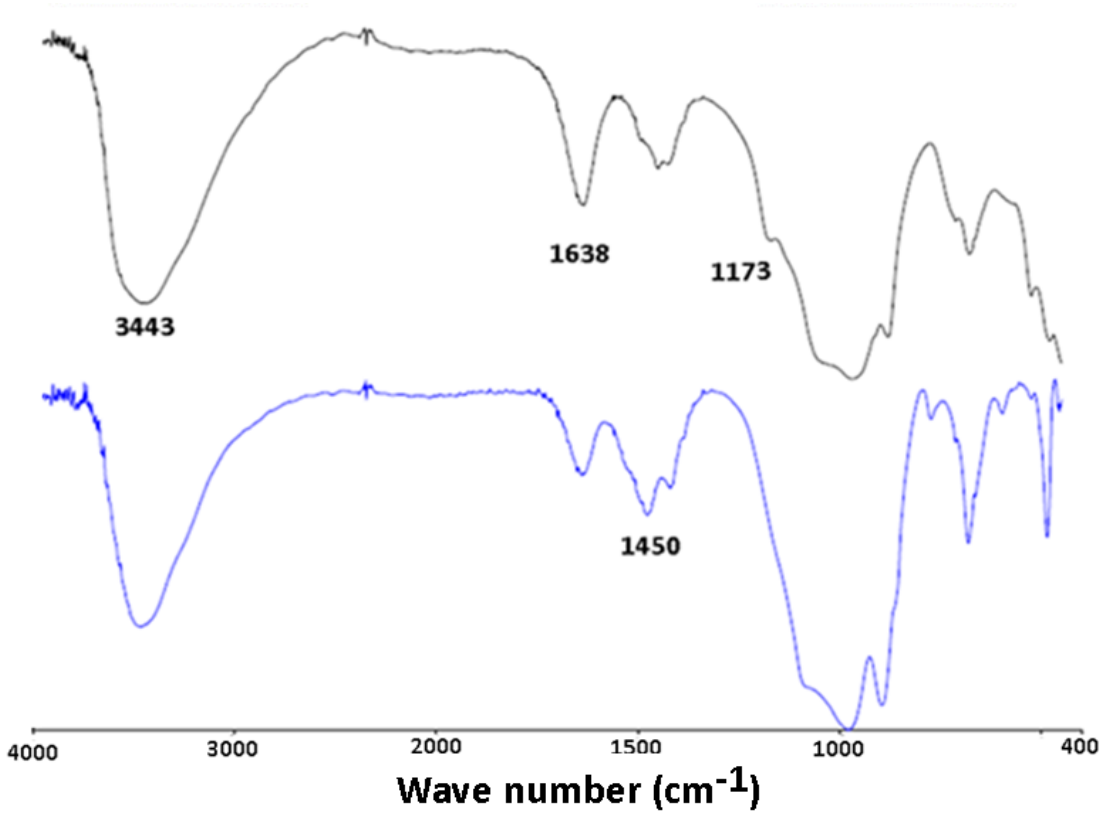

Figure IV.10: Effect of heat treatment in IR spectrum of prepared pristine tobermorite. Black line: Nontreated samples. Blue line: treated at 300°C for 24 h.

^{29}Si ss-NMR was carried out for the same sample of pristine tobermorite treated at 300°C for 24 hours. The results (Figure IV.11) showed an almost total disappearance of Q^3 and Q^3(1Al) signals. As it was mentioned in previous sections, this is due to the structure collapse of 11Å-tobermorite that becomes 9Å-tobermorite where double chains rearranged and split in single Dreierketten chains. This confirms the XRD and FT-IR spectra that indicated a normal tobermorite behavior where basal lattice distance is reduced from 11Å to 9Å.

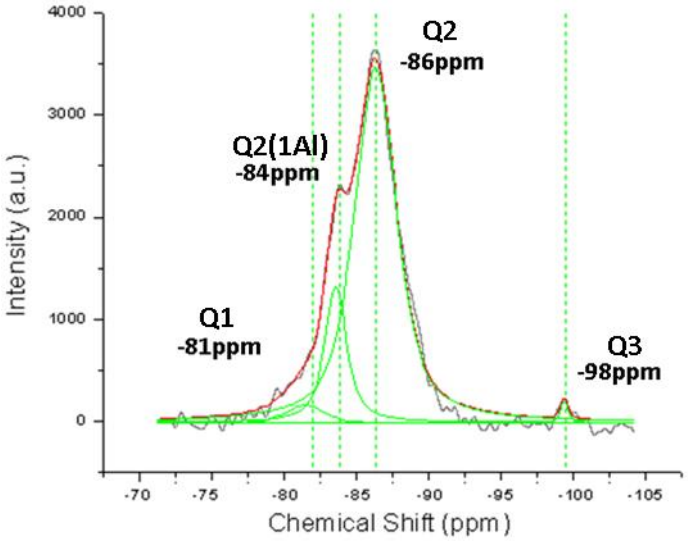

Figure IV.11: ^{29}Si ss-NMR of tobermorite pristine treated at 300°C for 24 hours.

The thermally treated pristine tobermorite was also characterized by ^{27}Al ss-NMR (Figure IV.12). The spectrum obtained was deconvoluted using two peaks, one at 63 ppm and the other one at 53 ppm. The chemical shifts of the peaks are the same as the ones obtained in the nontreated pristine tobermorite but the relative intensities have changed after the treatment. The intensity of the peak at 63 ppm is reduced. This can be explained due to the degradation of tobermorite 11Å to tobermorite 9Å as well. After heat treatment, remaining tetrahedral aluminum at 63ppm is around 17.3% versus 82.7% of contribution at 56ppm. Since both signals are very close to each other, the difficulties to deconvolute both signals could vary slightly the quantification. In the literature the signal at 63ppm is usually assigned to bridging position and the one at 53ppm to branching position. However, if the reduction of the basal distance is due to the break of the bonding between two branching silicate structures, then the 53ppm signal should decrease relative to de other signal. In this case the opposite result is obtained. If the mechanism proposed for the distance reduction is correct this result suggests that the assignation of the signals might not be correct. In any case, more work must be done to clarify this assignation.

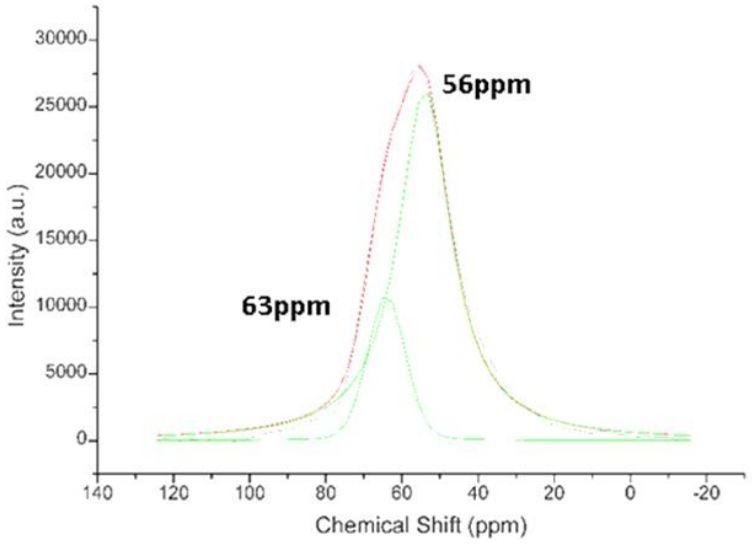

Figure IV.12: ^{27}Al ss-NMR of tobermorite treated at 300°C in air for 24 h.

^{1}H ss-NMR of treated samples at 300°C gave a similar spectrum than non-treated sample, although, some differences where observed (Figure IV.13). First, the main signal around 4.8ppm remains. This suggests the bonding strength of water inside this structure and shows that the source of water molecules is not from only moisture.

The intensity of the high and narrow peak around 0.9ppm decreased, so it could be considered that free silanol groups in 11Å tobermorite have during the thermal treatment. Moreover, the peak at 3.45ppm found in non-treated samples has disappeared. This contribution, as it was said previously, could be associated to physiosorbed water inside tobermorite structure and it could have desorbed when the temperature was increased.

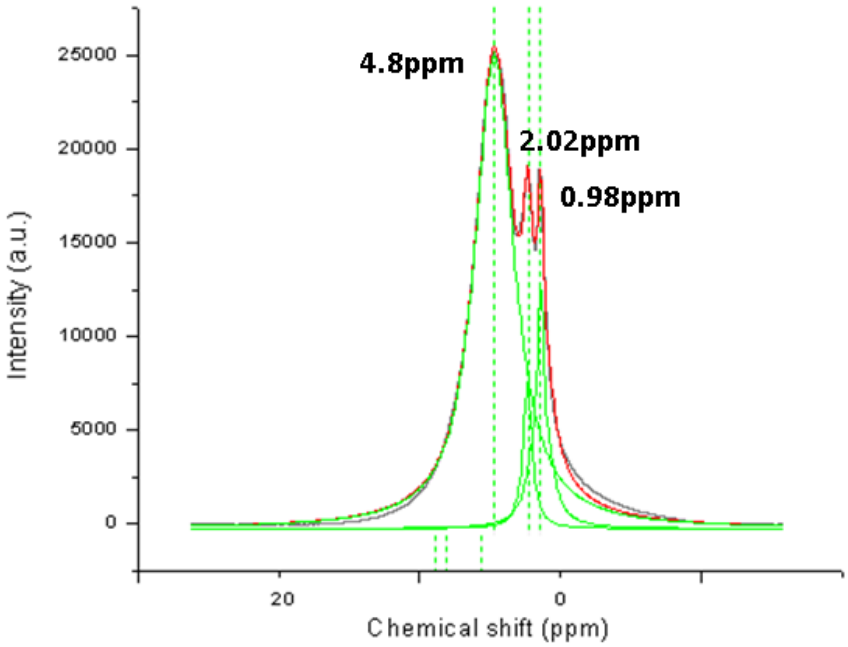

Figure IV.13: 1H ss-NMR of tobermorite treated at 300°C in air for 24 h.

In conclusion, according to the different characterizations carried out in this study, synthesized pristine tobermorite at 215°C for 4h gave a well crystalline structure. The aluminum was found as tetrahedral aluminate in branching or bridging positions. The heat treatment experiment shows that the synthesized pristine tobermorite is a normal 11Å-tobermorite since the treatment produced the reduction of the basal distance to 9Å. FT-IR, ^{1}H NMR and XPS confirmed the presence of hydroxyl groups and its interaction with water molecules.

IV.1.3. Elemental analysis of pristine tobermorite.

Elemental composition of pristine tobermorite has a huge relevance in crystallinity and morphology. As it was mentioned for xonotlite, tobermorite has a specific elemental molar ratio, in this case it is equal to 0.83. Then this section will focus on the Ca/(Si+Al) and Al/(Si+Al) ratios, and possible changes from the expected values due to hydrothermal synthesis conditions or reaction times employed.

Electronic and Energy Dispersive Spectroscopy (Figure IV.14), was carried out to determine elemental composition of the synthesized pristine tobermorite. Table IV.2

shows the results obtained from EDS. With these results a Ca/(Si+Al) ratio equals of 0.83 and Al/(Si+Al) ratio equals to 0.12 were calculated. The Ca/(Si+Al) ratio was very close to the theoretical value in literature, but the Aluminum content was lower than 15%.

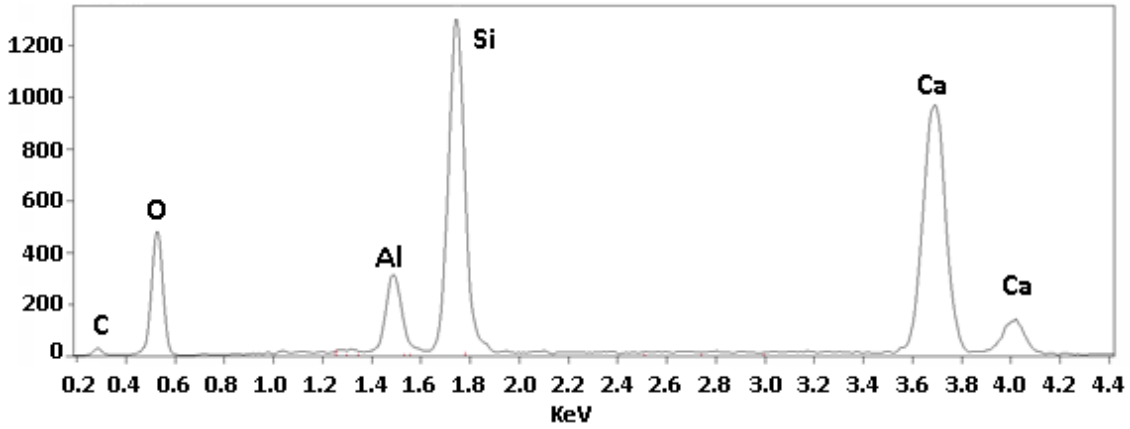

Figure IV.14: EDAX (EDS) elemental analysis for pristine tobermorite samples.

Table IV.2: Elemental analysis by EDS measurements for pristine tobermorite.

Element	Atomic % by EDS
Calcium	15.17
Silicon	15.93
Oxygen	66.71
Aluminum	2.19
Molar ratios	Values
Ca/(Si+Al)	0.83
Al/(Si+Al)	0.12

Considering this result is important to analyze further the yield of the reaction. This yield could be estimated comparing the amount of tobermorite obtained versus the theorical moles of tobermorite that can be produced according to the total amount of precursors added initially. The calculated yield for the production of tobermorite pristine was 96%. Then after 4 hours of reaction a 4% of tobermorite did not react.

IV.1.4. Morphological analysis of pristine tobermorite.

Pristine tobermorite sample was also characterized by scanning and transmission electron microscopy (TEM). Images taken (Figure IV.15) show that most of the morphologies observed were plate shape. These structures are irregular and present a wide range of sizes. Moreover, they tend to aggregate forming particles between 1µm or 3µm size even after ultrasound suspension.

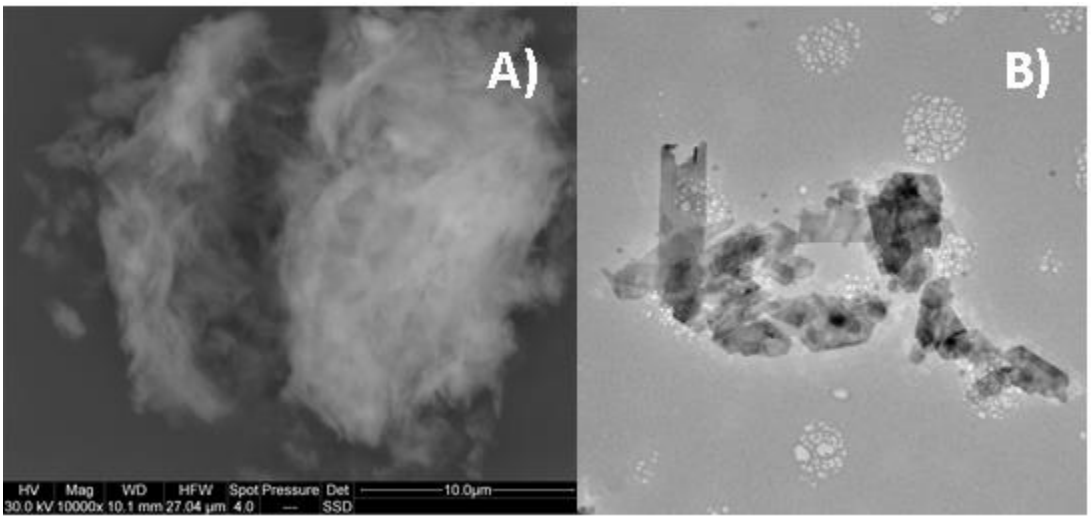

Figure IV.15: Scanning (A) and transmission (B) electron microscopy images of pristine tobermorite plates.

High resolution TEM of the pristine tobermorite was carried out in order to analyze more in depth the crystalline structure of the particles. However, during the characterization degradation of the sample did occur by dehydration due to the high focalized energy of the electron beam. Nevertheless, it was possible to take a few images and characterize the crystalline planes by selected area electron diffraction (SAED) (Figure IV.16). This procedure was carried out in different parts of the sample. When the SAED images were analyzed the lattice distance found was around 9Å instead of 11Å indicating that a degradation of the pristine tobermorite structure occurred.

SAED images were analyzed further to check this effect. From diffraction rings in SAED, it was calculated the reciprocal distance and then the lattice distance of degraded structure. Every distance obtained was compared to the lattice distances present in 11Å-tobermorite and 9Å-tobermorite Phase Diffraction File in ICDD crystallographic database. The comparison between contributions and assignations appears in Table

IV.3. Every ring in diffraction image was associated to planes of riversideite or 9Å-tobermorite (PDF 00-029-0329). This also confirmed the normal behavior of tobermorite synthesized under subcritical conditions and observed in XRD.

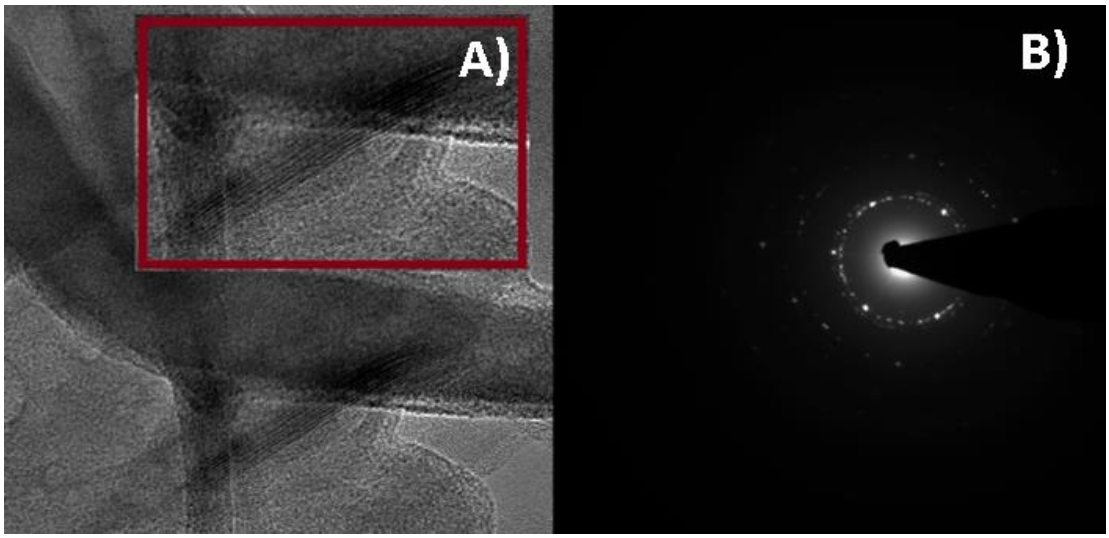

Figure IV.16: High magnification images of tobermorite pristine (A), SAED images of the same sample (B).

In this section it was established the synthesis conditions to obtain a crystalline phase of tobermorite. Moreover, it was carried out a comprehensive analysis about its structure. This information will be useful in the following sections to compare the effect of PEG and other molecules in structure and morphology of tobermorite.

Table IV.3: Comparative table and assignation of lattice distance found in SAED image for pristine tobermorite.

XRD sample distance	XRD pattern distance	Crystallographic plane	Phase associated
2.78Å	2.79Å	(2 0 0)	Riversideite (9Å tobermorite)
2.75Å	2.75Å	(1 1 3)	Riversideite (9Å tobermorite)
1.77Å	1.78Å	(3 0 3)	Riversideite (9Å tobermorite)
1.70Å	1.71Å	(0 0 11)	Riversideite (9Å tobermorite)
1.53Å	1.52Å	(2 2 1)	Riversideite (9Å tobermorite)

IV.2. Tobermorite modified with polyethylene glycols. Synthesis under subcritical conditions.

IV.2.1. Structural analysis of modified tobermorite with PEG.

Tobermorite modified with three different PEG polymers (MW600 g/mol, MW1500g/mol and MW4000g/mol) were synthesized following the same reaction temperature and time as in the case of pristine tobermorite (T_P600, T_1500 and T_P4000). The obtained products were characterized by XRD (Figure IV.17). In all cases the diffraction peaks were match to crystalline tobermorite (PDF 00-019-1364) [2, 13, 14, 16] and in the case of T_P1500 and T_P4000 two extra diffraction peaks (at 19° and 23°) were observed which were matched to diffraction peaks of polyethylene glycol [26].

This confirms the presence of organic polymer in the sample although it does not indicate where the PEG is. In fact, no significant changes in crystallinity or shifts in basal peak were observed in the XRD patterns of the PEG modified products suggesting that the PEG is not intercalated.

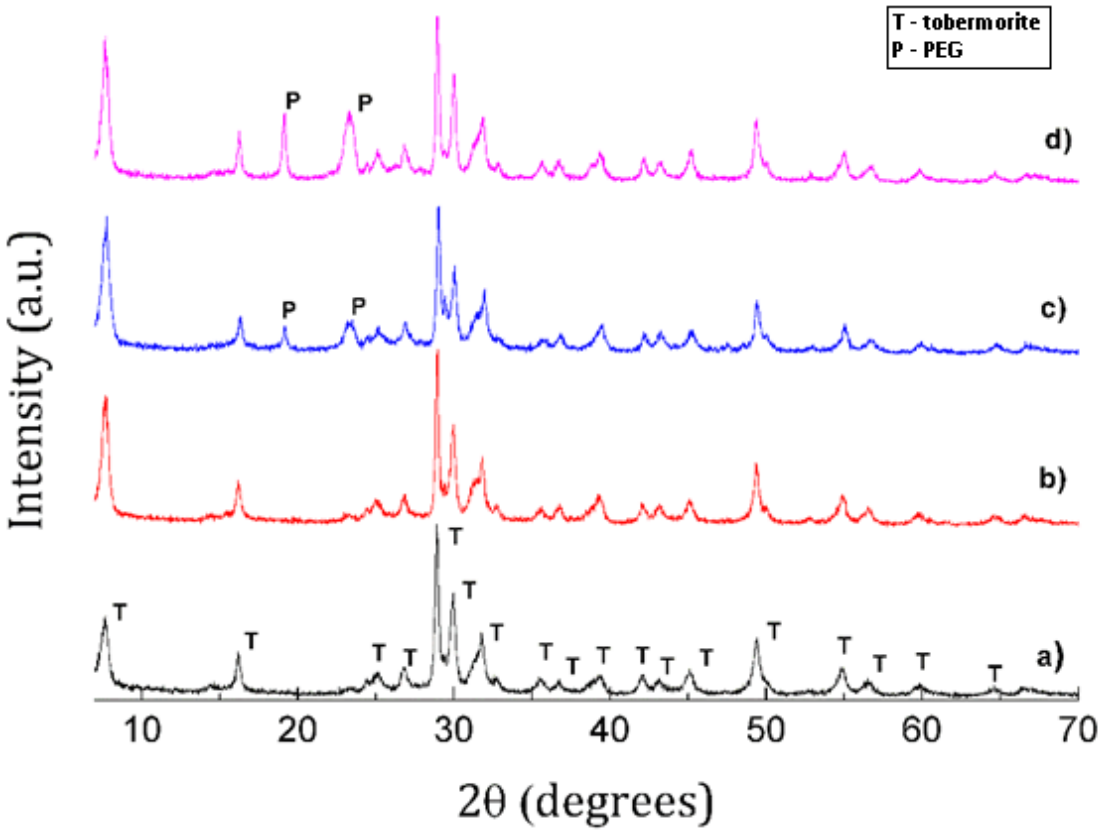

Figure IV.17: XRD spectra of T_Pristine (a) T_P600 (b), T_P1500(c) and T_P4000 (d).

Unlike xonotlite samples, pristine tobermorite and modified samples present high contributions of water vibrational modes in FTIR (Figure IV.18). Around 1600cm^{-1} there is an intense peak related to water bending mode and around 3400cm^{-1} the stretching mode of H-OH of water or hydroxyl groups from silanol groups. Si-O stretching vibrational mode is measured around 975 cm^{-1} for Si in Q^2 positions in silicate chains. Q^3 silicon tetrahedra were measured by the presence of the peak around 1200cm^{-1} as well. There is a band at 2900 cm^{-1} which can be assigned to C-H stretching mode. This indicates the presence of PEG in the samples.

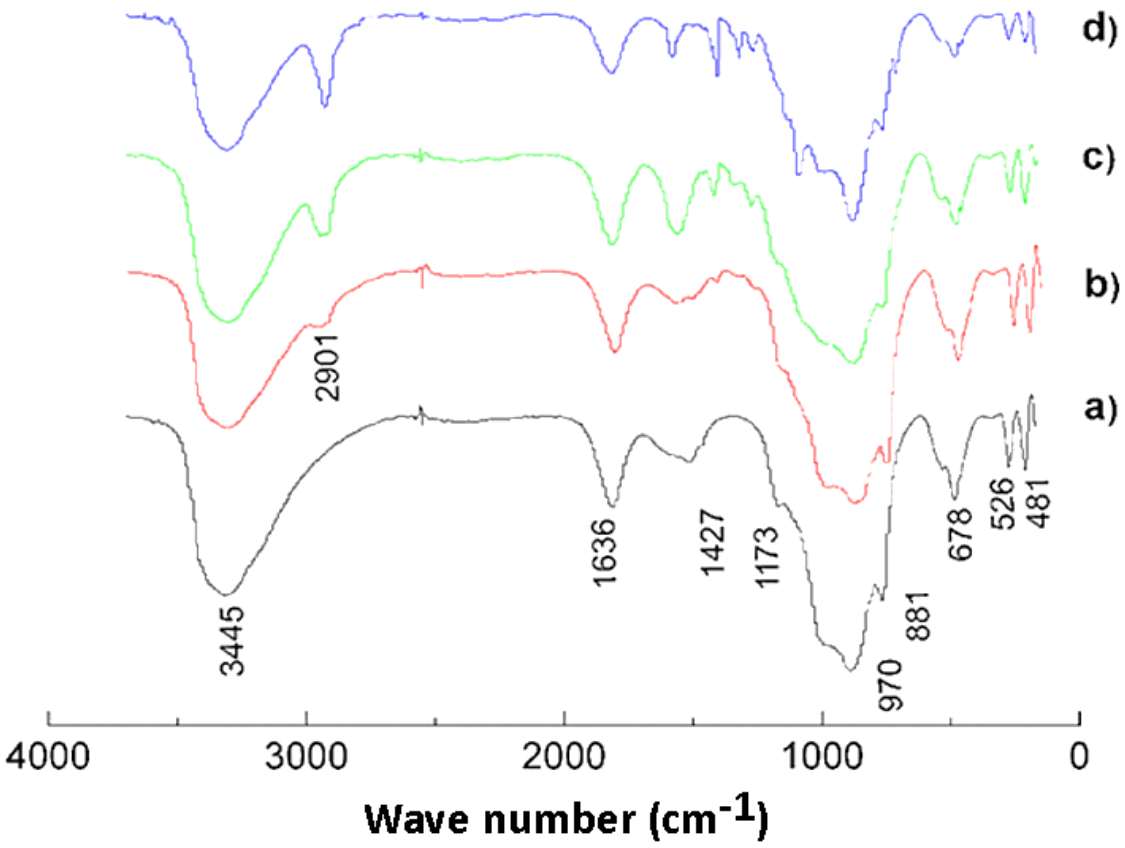

Figure IV.18: FT-IR spectra of unmodified tobermorite (a) and PEG MW 600 (b), (c) PEG MW 1500g/mol and PEG MW 4000g/mol (d) modified tobermorite samples.

^{29}Si NMR were measured for every tobermorite samples (Figure IV.19 A). The results obtained confirmed a typical NMR for Al substituted tobermorite [17, 18]. Besides the characteristic signals associated to Q^1 (-81ppm), Q^2 (-86ppm) and Q^3 (-98ppm) silicon tetrahedra in silicate chains for C-S-H structures, two extra peaks are also observed at -93ppm and -84ppm, associated to Q^3 and Q^2 silicon tetrahedra bound to Al atom by an oxygen atom in the chain, respectively [12].

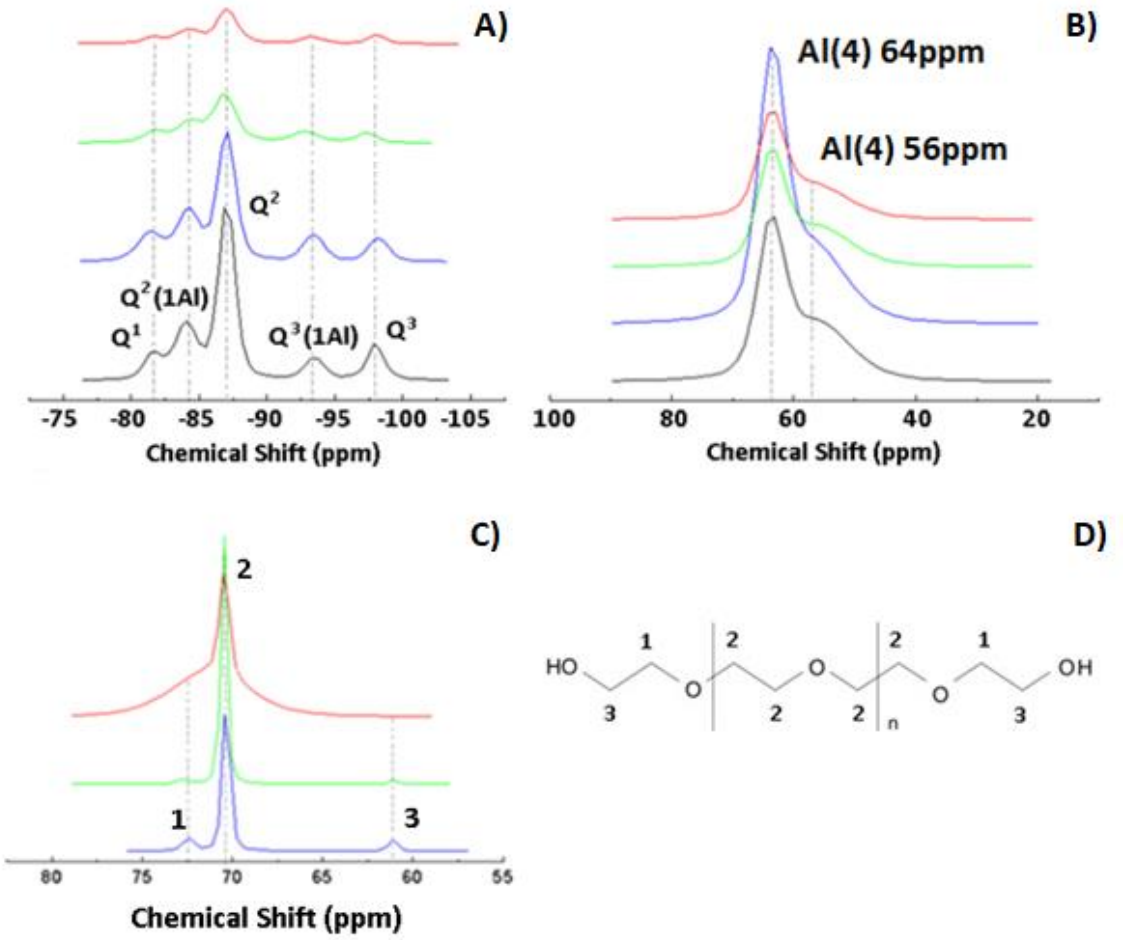

Figure IV.19: ^{29}Si (A) ^{27}Al (B) ^{13}C (C) of hydrothermal synthesized tobermorite samples and carbon assignment for ^{13} C NMR (D). T_Pristine (black curve), T_P600 (blue curve), T_P1500 (green curve) and T_P4000 (red curve).

Deconvolution of all the spectra was carried out and the relative intensities of the fitted peaks were measured (see appendix A.12-A.14). Using these data, the MCL of the different samples was calculated (Table IV.4). The calculated MCL show that the presence of PEG MW600 decreases the MCL value comparing to pristine tobermorite. However, the higher the molecular weight of the PEG, the longer the silicate chain. This is the opposite effect to the one observed in xonotlite-PEG samples and other C-S-H samples in literature modified at room temperature with PEG [5, 27].

Table IV.4: Mean chain length values for unmodified and modified tobermorite prepared under subcritical conditions.

Sample	MCL	$Q^3(1Al)+Q^2(1Al)$ /($Q^1+Q^2+Q^3+Q^2(1Al)+Q^3(1Al)$)	$Q^3(1Al)/Q^2(1Al)$
T_Pristine	29.67	0.36	0.35
T_P600	16.83	0.39	0.49
T_P1500	25.97	0.34	0.65
T_P4000	30.18	0.31	0.43

This effect in MCL could be related to the addition of aluminum as stabilizing element in the structure. The amount of aluminum introduced in the structure was analyzed indirectly through the ratio of deconvoluted area of $Q^2(1Al)$ and $Q^3(1Al)$ and their total population in ^{27}Si ss-NMR spectra. Results are shown in Table IV.5 as well. As it can be observed the total amount of silicate tetrahedra bound to aluminate tetrahedra remains stable in the tobermorite samples modified with PEG. However, a higher content of silicate tetrahedra in branching position and bound to an aluminum tetrahedra ($Q^3(1Al)$) respect to silicate in bridging position and bound to aluminum ($Q^2(1Al)$) is obtained for samples with PEG.

According to elemental analysis carried out, the total amount of aluminum remains equal in bulk for modified samples (see Table IV.11). Then it could be assumed that this increase of $Q^3(1Al)$ signals could be related to an increase of the number of interactions between silicon and aluminum atoms along silicate chain.

The samples were also characterized by ^{27}Al NMR (Figure IV.19 B). Similar signals as in the case of pristine tobermorite were obtained. Deconvolution of the spectra was carried out fitting two peaks for every spectrum, one at 63ppm and the other one at 56ppm. As it can be observed the relative areas of both peaks are very similar among the modified tobermorites and also with the pristine tobermorite.

Table IV.5: Percentage of different aluminum tetrahedra calculated from deconvolution of curves in ^{27}Al ss-NMR.

Sample	%Al at 63ppm Non heated	%Al at 56ppm Non heated	%Al at 63ppm Heated*	%Al at 56ppm Heated*
Pristine tobermorite	51.45	48.55	9.49	90.51
T_P600	58.70	41.30	17.38	82.62
T_P1500	52.94	47.06	14.36	85.64
T_P4000	53.75	46.25	17.79	82.21
***Samples treated at 300°C for 24 h.**				

^{13}C ss-NMR of the samples was carried out to evaluate the presence of polyethylene glycol. Three signals at 72.75ppm, 70.47ppm and 61.15ppm were found the same as in PEG functionalized xonotlite samples.

In this work ^{1}H ss-NMR has been analyzed for tobermorite samples as well (Figure IV.20). There is one wide contribution around 4ppm that could be associated to the presence of hydroxyl groups of molecular water in the solid. There is a lower contribution around 2.02 ppm like the Ca-OH signal found in xonotlite samples and other peak around 0.94-1.1 ppm that could be related to free silanol groups in silicate chains [6]. In samples modified with PEG there is a huge contribution around 3.5ppm that hides the rest of signals. This contribution is associated to the presence of protons attached to carbon atoms in polymer chains. In these curves can be also observed a small contribution at 1.12ppm which could be associated to the presence of free silanol groups.

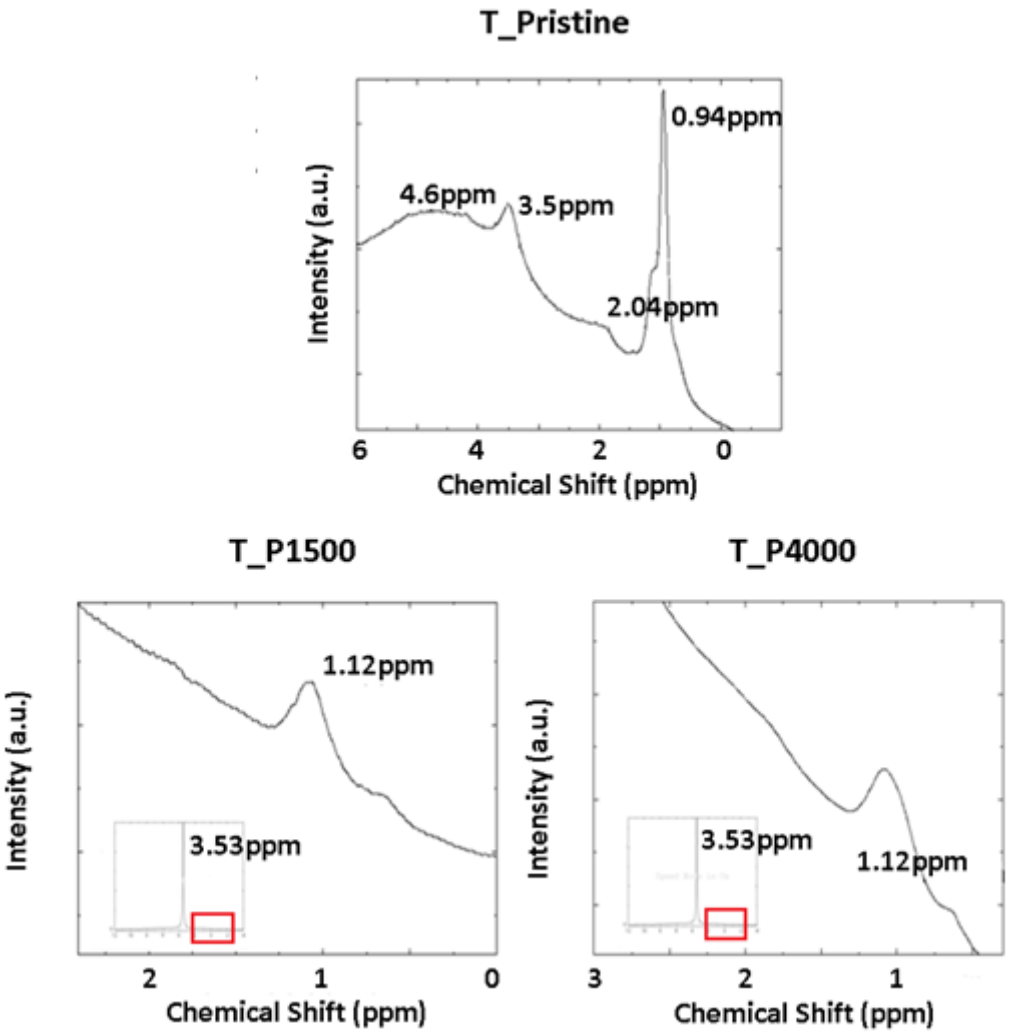

Figure IV.20: ^{1}H ss-NMR for unmodified and modified tobermorite. Note: figure shows a zoomed detail of red area

As mentioned before, XPS can give elemental composition of the surface. XPS elemental analysis was carried out for the PEG modified tobermorite samples (Table IV.6). However, XPS is a semiquantitative technique and absolute values cannot be reliable if corrections in sensitivity factors is not well applied. The important information obtained from this analysis should be the tendency of composition when different PEG molecules are added.

In Table IV.6 can be observed an increase of Ca/(Si+Al) ratio due to the presence of PEG in samples. This tendency does not match the elemental analysis in bulk obtained with X-ray fluorescence technique and EDS analysis (section IV.2.2.). If it is considered that fitting parameters are well adjusted, this increase only can be interpreted as a higher

calcium concentration on samples surface due to the coordination of calcium to polyethylene glycol located in this region. However, this is only a hypothesis and further analysis should be carried out.

Table IV.6: Elemental quantification by XPS analysis in tobermorite samples.

Samples	Si2p (%)	C1s (%)	Ca2p (%)	O1s (%)	Al2p (%)	Ca/ (Si+Al)	Al/ (Si+Al)
T_Pristine	18.2	1	17.41	60.68	2.71	**0.832**	**0.114**
T_P600	16.05	12.99	15.87	52.26	2.82	**0.841**	**0.149**
T_P1500	17.20	5.02	17.00	57.57	3.20	**0.833**	**0.156**
T_P4000	12.41	26.65	13.45	45.46	2.02	**0.93**	**0.139**

A high resolution spectra for Si2p, O1s, Ca2p, C1s and Al2p was obtained in order to identify chemical environment of those elements. According to Si2p signal deconvolution (Figure IV.21) there are three main contributions associated to electrons in orbital 2p 3/2. One around 101.4eV, another around 102.5eV and the last one near to 103.5eV.

If it is considered that Si-O-Si bonding and Si-O-Ca are more abundant inside the sample, we could interpret that the peak at 103.5eV could be associated to silanol groups. Moreover, bonding with more distributed electrical charge like Si-O-Si has a higher binding energy than Si-O-Ca. Following this assumption, the signal around 102.5eV can be associated to Si-O-Si bonding and the signal around 101.4eV to Si-O-Ca.

It was detected a reduction from 102.6eV to 102.4eV in Si2p3 binding energies for silicon bound to other silicon through oxygen atoms (Si-O-Si). As it was mentioned in previous sections Barr *et al.* [25] correlated the increase of aluminum in structure to a reduction of Si2p binding energies as well.

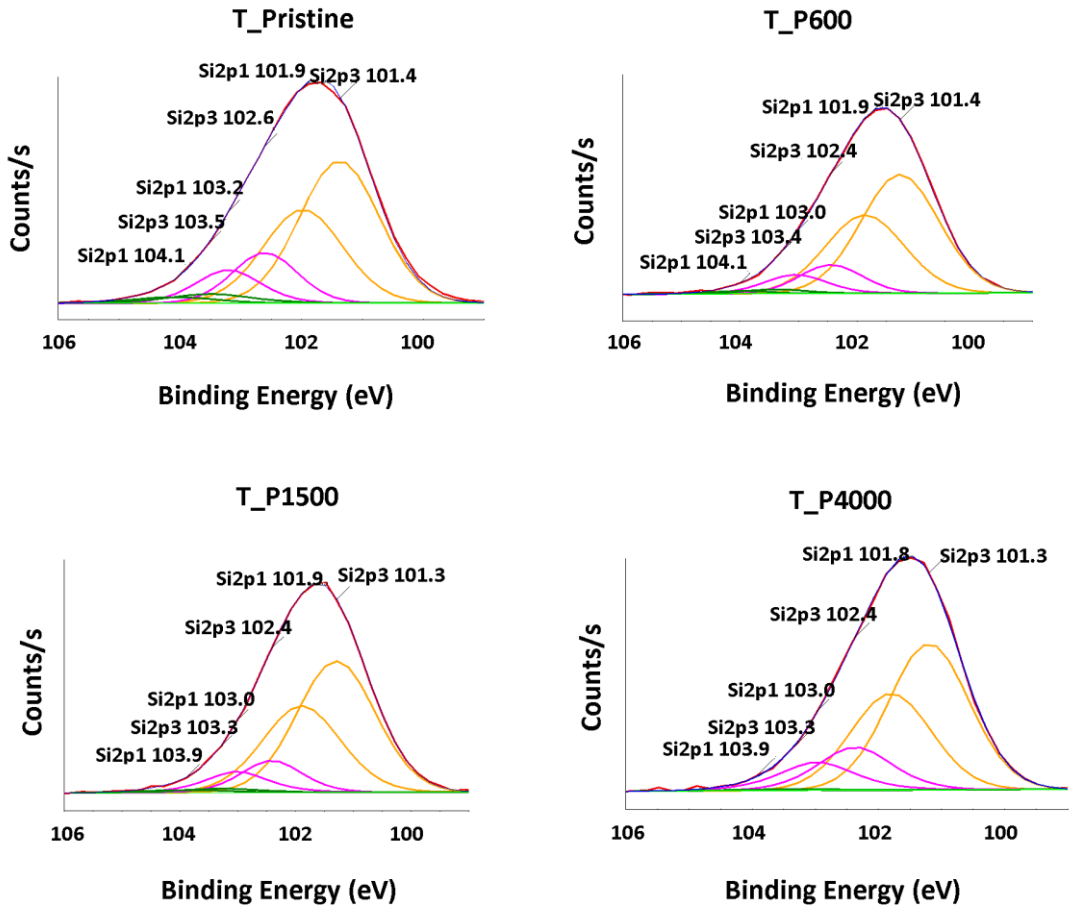

Figure IV.21: Deconvoluted curves from XPS data analysis Si2p contributions in T_Pristine, T_P600, T_P1500 and T_P4000.

Three main contributions at 530.3eV, 531.7eV and 532.8eV were detected from deconvolution of O1s XPS curve (Figure IV.22) the same as in case of the xonotlite samples. The two first contributions are associated to non-bridging (NBO) and bridging Oxygens (BO), respectively, and the last one at 532.8eV could be associated to molecular water. The Non-Bridging/Bridging oxygen ratios are shown in Table IV.7.

We observed the opposite tendency of NBO/BO ratio to the one found for xonotlite modified samples. The modification of tobermorite with PEG causes a decreasing effect in NBO/BO ratio. In this case the analysis is more complicated. It must be considered that part of bridging oxygens is attached now to aluminum so the binding energy of this oxygens and its contribution on NBO/BO ratio changes completely.

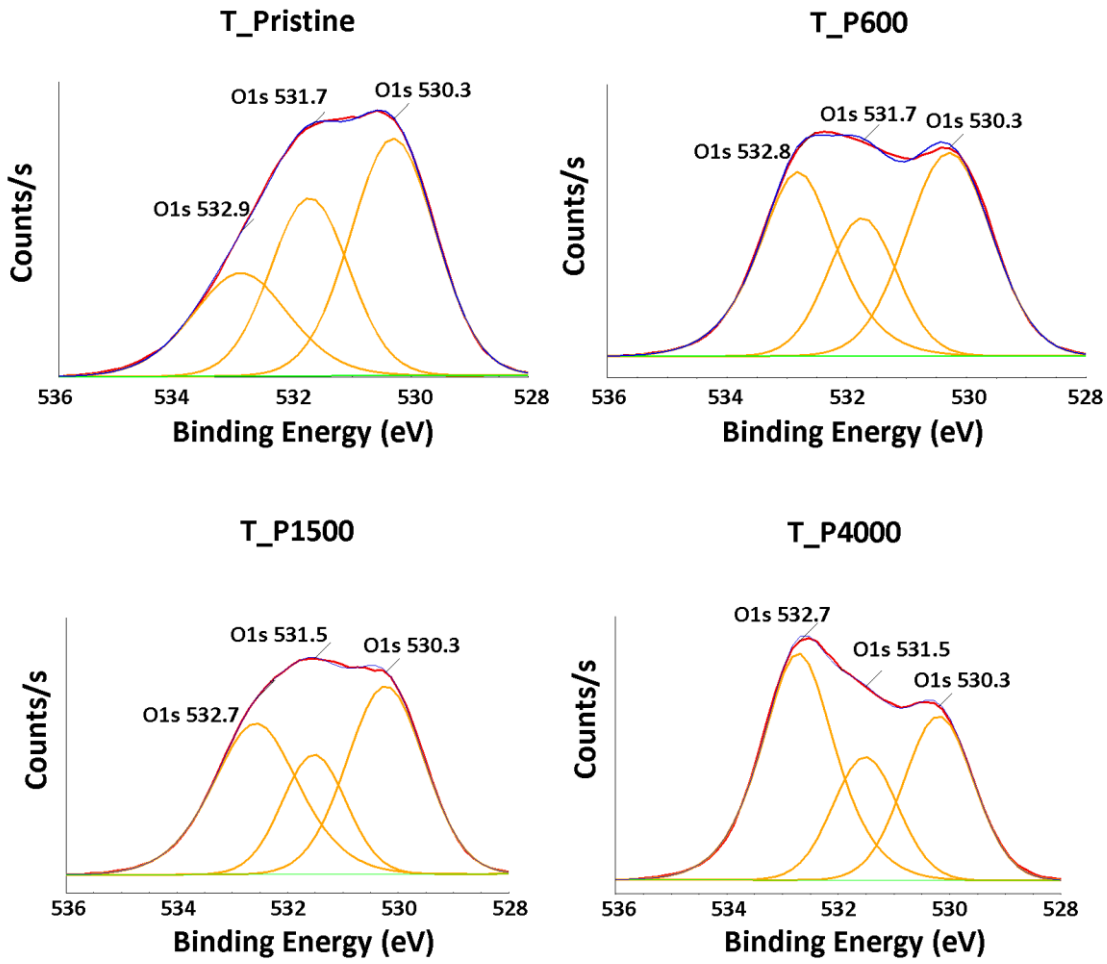

Figure IV.22: Deconvoluted curves from XPS data analysis of O1s signal in pristine tobermorite (T_Pristine) and tobermorite modified with PEG MW600 (T_P600), PEG MW1500 (T_P1500) and PEG MW4000 (T_P4000) .

Table IV.7: Non-bridging over bridging ratio for Oxygen analyzed by high-resolution XPS.

Samples	NBO/BO
T_Pristine	3.39
T_P600	**1.76**
T_P1500	**1.65**
T_P4000	**1.11**

After analyzing the Ca2p3 binding energies in every synthesized tobermorite samples (Figure IV.23), we realize that there is a slight shift to lower values in samples prepared with PEG, from 346.85eV to 346.7eV. However, this displacement is not so significant if it is compared to the one obtained in xonotlite samples modified with the same polymer.

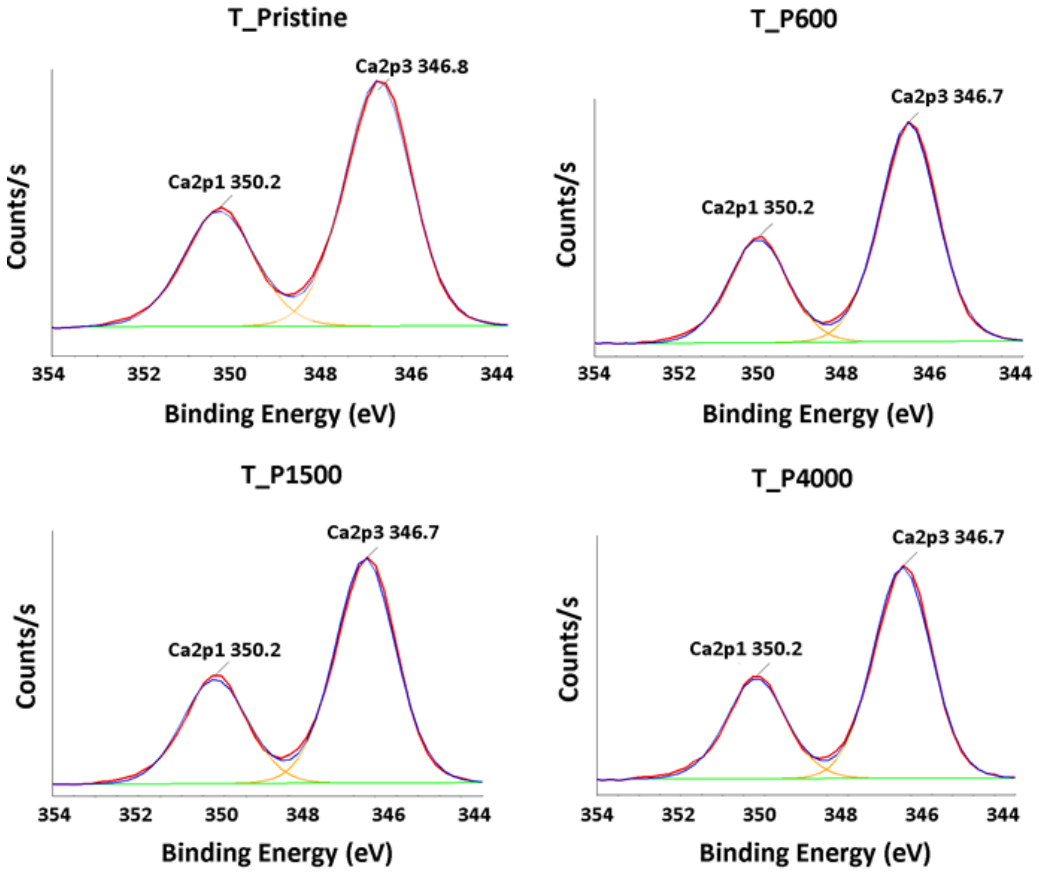

Figure IV.23: Deconvoluted curves from XPS data analysis Ca2p contributions in pristine tobermorite (T_Pristine) and tobermorite modified with PEG MW600 (T_P600), PEG MW1500 (T_P1500) and PEG MW4000 (T_P4000).

Although we could distinguish some effect of polymer in calcium interactions, is not as significant as in the case of xonotlite. One way to interpret this is that the silicate tetrahedra in Q^3 position in tobermorite structure are not bound to CaO layers like in xonotlite structure, therefore the effect of PEG and the increase of vacancies in Q^3 positions does not affect to the interaction with calcium in the same way.

In the case of carbon, the signal was fitted by three peaks, one at 284.8 eV associated to C-C and C-H bonding, another one at 286.5eV due to C-O bonding and another small peak at 289eV which is associated to carbonation in samples (Figure IV.24).

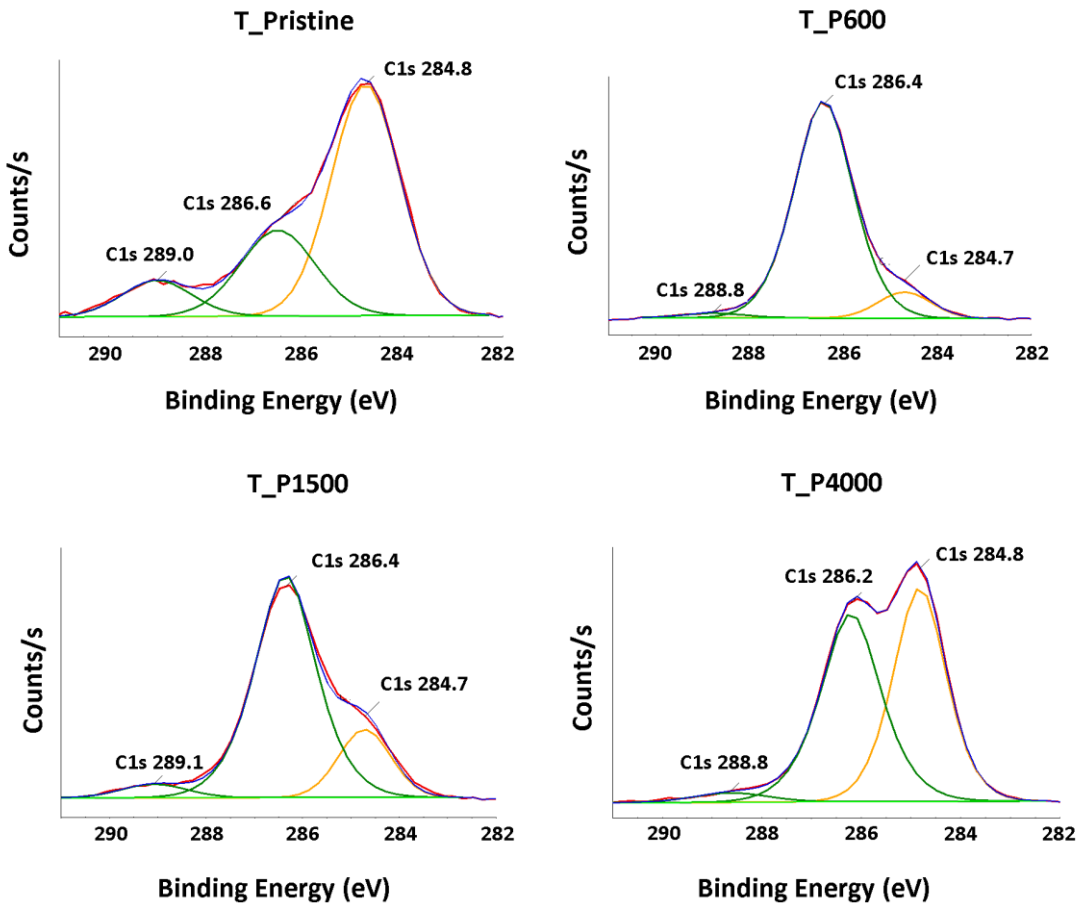

Figure IV.24: Deconvoluted curves from XPS data analysis of C1s signal in T_Pristine, T_P600), T_P1500 and T_P4000.

A slight shift to lower binding energies for the C-O contribution can be observed as the molecular weight of the PEG increases (Table IV.8). A decrease of 0.2eV for samples with PEG MW 600 and PEG MW1500 can be observed and of 0.4eV for tobermorite modified with PEG MW4000.

Table IV.8: C1s Binding energies for C-O bonding in PEG modified tobermorite.

Sample	Binding Energy for C-O bonding (eV)
Pristine tobermorite	**286.6**
T_P600	**286.4**
T_P1500	**286.4**
T_P4000	**286.2**

In the case of the aluminum signal (Figure IV.25) it is not possible to interpret clearly if this curve can be deconvoluted in more than one peak from the signal. Because of this the Al spectrum cannot be used to clarify the presence of aluminum in Q^2 or Q^3 positions along the silicate chain observed in NMR measurements. Nevertheless, it can be observed that this signal is shifted from values around 74eV for pristine tobermorite to values around 73.7eV for tobermorite with PEG.

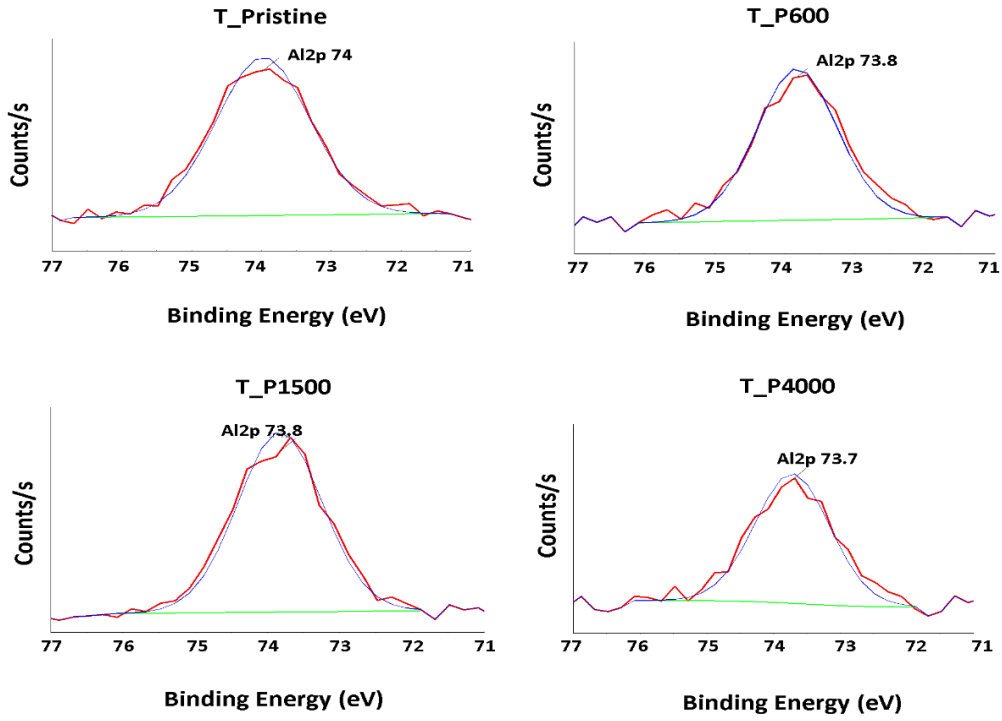

Figure IV.25: Deconvoluted curves from XPS data analysis of Al2p signal in T_Pristine, T_P600, T_P1500 and T_P4000.

This way it could be interpreted that PEG is generating imperfections inside the crystal during tobermorite precipitation in the reactor that is modifying the way that aluminum interacts in structure. These changes in Al2p XPS curves complement the results of NMR obtained in this study and confirms that crystalline structure in tobermorite is modified when PEG is added to the reaction medium.

IV.2.2. Heat treatment of tobermorite modified with PEG.

Tobermorite particles with polyethylene glycol were heated at 300°C to check if they present a normal or anomalous behavior. Then de basal peak associated to the plane (002) was compared before and after treatment (Figure IV.26). The results for each sample are shown in Table IV.9.

At first these results could indicate that tobermorite modified with PEG MW1500 and PEG MW4000 do not shrink their basal lattice distance after 24-hour heating. However, even for samples modified with PEG MW1500 and MW4000 there is a small shift to lower 2θ and peaks get wider as well.

This result was reproduced using 400°C as temperature condition and using longer period of times (48 hours) (samples 2 in Table IV.9). From these results it can be concluded that PEG has an influence in the stability of tobermorite structure. Nevertheless, a more comprehensive study will try to describe this effect through NMR analysis.

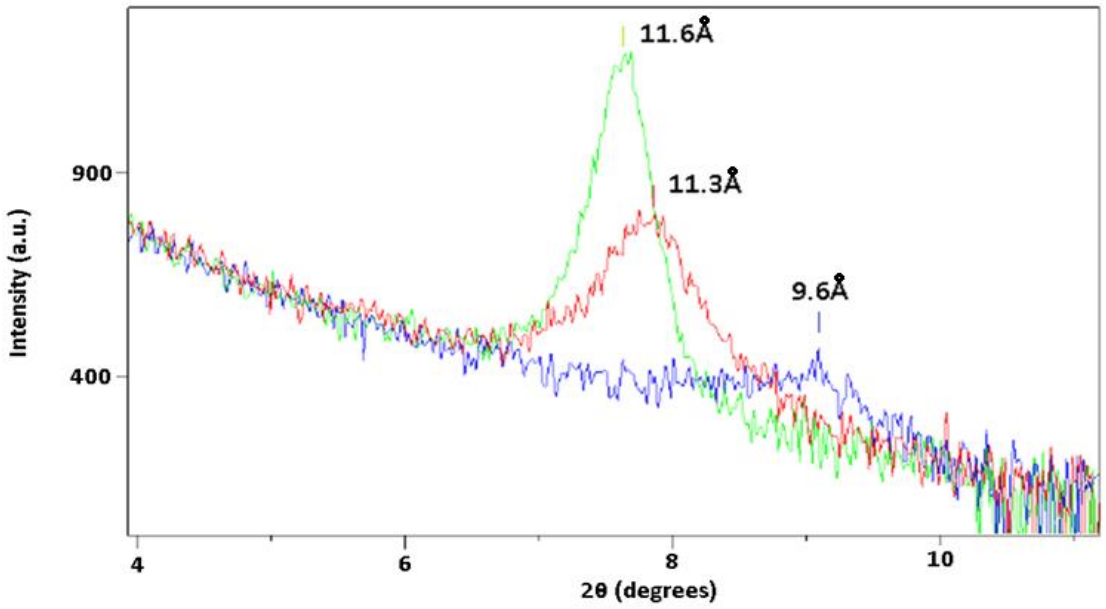

Figure IV.26: Amplified image of basal peaks of pristine tobermorite and T_P4000 without heat treatment and after 24h at 300°C. Blue curve: tobermorite pristine, red curve tobermorite with PEG MW4000 (T_P4000). Green line: tobermorite pristine without heating treatment.

Table IV.9: Effect of heating treatment on basal peak position (002) for unmodified and modified tobermorites.

	T_Pristine	T_P600	T_P1500	T_P4000
No Heated (sample 1)	11.5	11.5	11.5	11.6
No Heated (sample 2)	11.5	11.5	11.4	11.6
Heated 300˚C (sample 1)	9.6	9.7	11.1	11.3
Heated 400˚C (sample 2)	9.6	9.7	11.3	11.2

Samples with polyethylene glycols treated at 300°C, on the other hand, showed a different behavior in ^{29}Si NMR compared to pristine tobermorite. Figure IV.27 shows the ^{29}Si NMR of the treated pristine tobermorite and T_P4000.

As it can be seen in the figure III.47 the presence of contributions at -94ppm and -98ppm associated to silicate tetrahedra Q^3(1Al) and Q^3, respectively are still remaining in T_P4000 sample after the temperature treatment. Then polyethylene glycol could have any effect on dehydration of tobermorite and could inhibit the breakage of the silicate double chains.

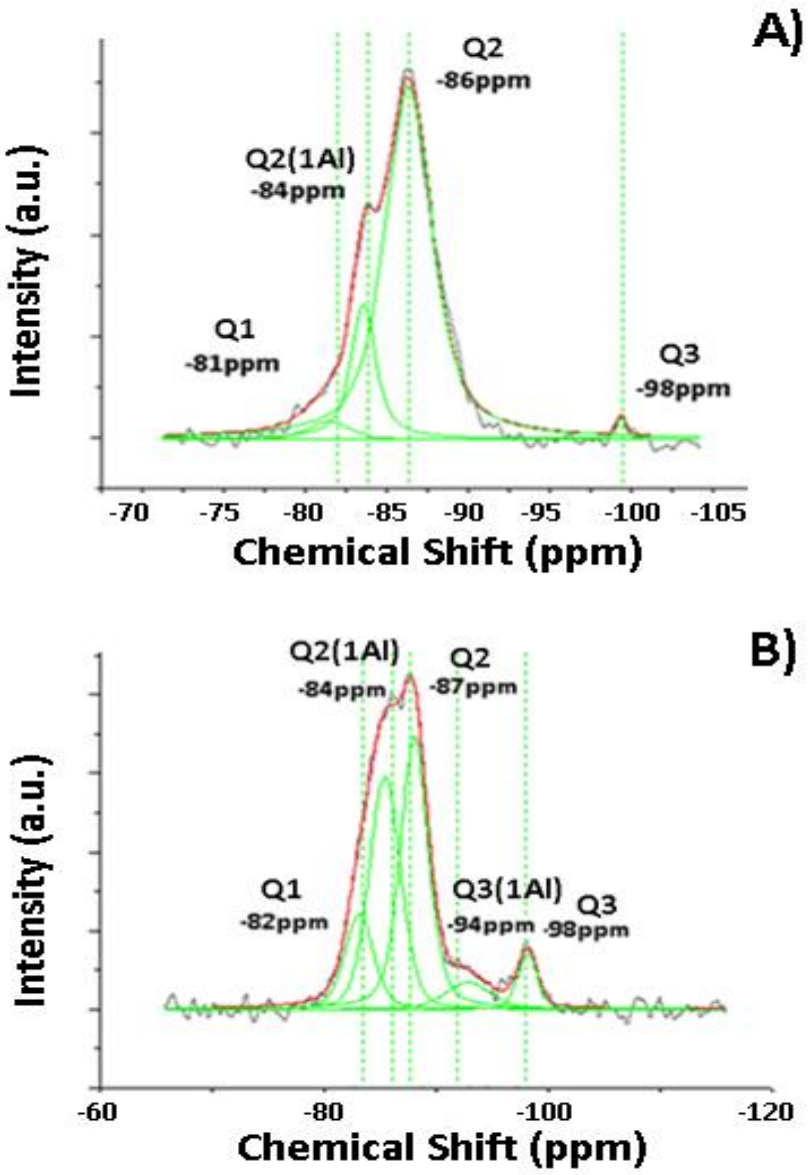

Figure IV.27: ^{29}Si NMR of tobermorite pristine (A) and tobermorite modified with PEG MW4000 (B) treated at 300°C for 24h.

Samples treated at 300°C where also characterized by ^{27}Al ss-NMR. The quantification of deconvoluted curves (Table IV.10) showed a reduction of signal at 64ppm. However, this reduction is lower in the case of tobermorite that was synthesized in the presence of PEG. This result confirms the ^{29}Si NMR analysis that showed remaining Q^3 (1Al) and Q^3 signals for tobermorite-PEG samples treated at 300°C. It can be concluded that PEG molecule has an effect in the structure of the tobermorite and it helps to form the anomalous 11Å tobermorite structure.

Table IV.10: Quantification of aluminum signals in ^{27}Al NMR for obtained tobermorites.

Sample	%Al signal at 64ppm	%Al Signal at 56ppm Non heated	%Al signal at 64ppm Heated*	%Al Signal at 56ppm Heated*
Pristine tobermorite	51.45	48.55	**9.49**	90.51
T_P600	58.70	41.30	**17.38**	82.62
T_P1500	52.94	47.06	**14.36**	85.64
T_P4000	53.75	46.25	**17.79**	82.21
				***Samples treated at 300°C for 24h.**

IV.2.3. Elemental analysis of modified tobermorite with PEG.

Table IV.11 shows the elemental composition carried out using EDS technique. The Ca/(Si+Al) ratios in this table show a decreasing tendency for calcium composition when polyethylene glycol MW4000 is added. These results match the effect of PEG observed for modified xonotlites but the effect seems to be lower in this case. On the other hand, Al/(Si+Al) ratio does not change significantly after PEG addition.

Table IV.11: Molar ratios obtained from EDS analysis.

Samples	Ca/(Si+Al)	Al/(Al+Si)
Tobermorite pristine	0.837	0.121
Tobermorite_P600	0.839	0.121
Tobermorite_P1500	0.840	0.120
Tobermorite_P4000	0.804	0.112

Nevertheless after 4 hours of synthesis is observed that only 12% of aluminum in respect to silicon (Al/(Si+Al)) molar ratio are in tobermorite products. A low decrease of aluminum was also observed due to the presence of polyethylene glycol MW4000, but this decrease is negligible (lower than 1% of moles). So, no significant changes can be

obtained from elemental analysis if pristine tobermorite compared to tobermorites prepared with PEG.

IV.2.4. Morphological analysis of modified tobermorite with PEG.

Figure IV.28 shows the LR-TEM images of the pristine tobermorite and the PEG modified tobermorite samples. No significant changes in crystal morphologies were found when PEG is added.

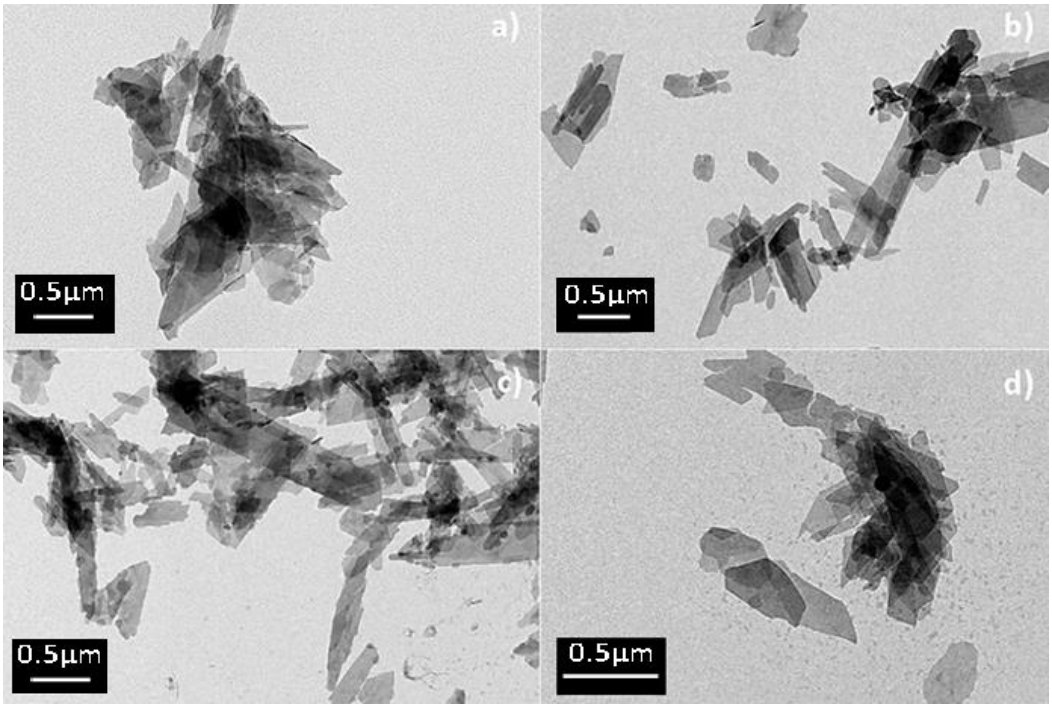

Figure IV.28: LR-TEM images of tobermorite plates Unmodified (a), PEG MW 600(b), PEG MW1500 (c) and PEG MW 4000 (d) modified particles.

High Resolution TEM was also used to obtain more detailed images of tobermorite particles with PEG. In this occasion, the same as with pristine tobermorite, it was difficult to get well defined images, due to the degradation of the tobermorite structure by the electron beam. Figure IV.29 shows SAED images for every tobermorite sample analyzed. In a first glimpse it can be seen a higher crystallinity of structures in the presence of PEG than in unmodified sample.

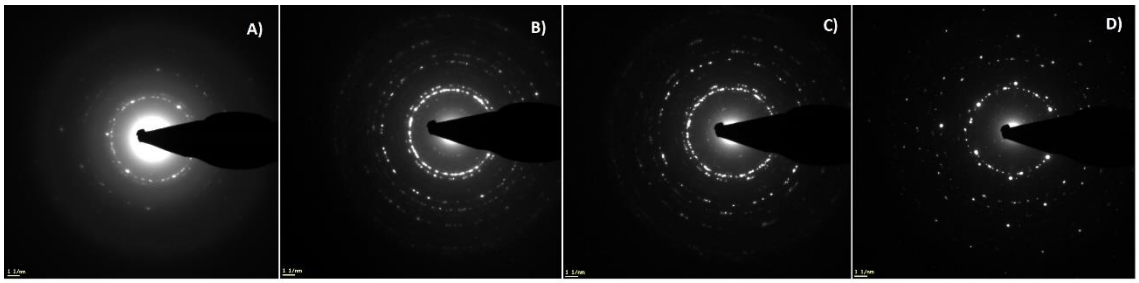

Figure IV.29: SAED images for pristine (A), PEG MW600 (B), PEG MW1500 (C) and PEG MW4000 (D) modified tobermorites.

In conclusion, in the tobermorite case, as in the case of xonotlite, it has been observed that the addition of PEG has an effect in the length of the silicate chain. The calculated MCL values show that the presence of PEG MW600 decreases the MCL value comparing to pristine tobermorite. However, the higher the molecular weight of the polymer, the longer the silicate chain. Moreover, according to the heat treatment experiments, tobermorites with PEG seem to have an anomalous behavior comparing to pristine tobermorite that has a normal behavior. XPS results of PEG modified samples showed some influence of PEG in aluminum.

Then, it was not proved an increase of aluminum inside the structure but the results from ^{29}Si NMR could give information about an effect of PEG in the location of aluminum along the silicate chain. This change could have an influence related to how samples dehydrate and degrade into 9Å- tobermorite under high temperature conditions (300˚C). However, this effect is not completely well understood and a further analysis should be carried out.

IV.3. Tobermorite samples modified by sulfobetaine siloxane.

IV.3.1 Structural analysis.

Thesamples were synthesized with Ca/(Si+Al)= 0.83 and 15% of aluminum, in presence of SBS as part of silicon source in order to obtain crystalline samples of tobermorite modified with this SBS. The ratio SBS/SiO_2 was 1/4 as it was done for xonotlite ones and experiments were carried out for 4h and 8 h.

In Figure IV.30 the XRD of tobermorite_SBS-4h is shown. There are no significant contributions associated to crystalline phases, but some contributions can be assigned

to the presence of tobermorite (PDF 00-045-1480), calcite, and phases related to coesite (SiO_2).

More comprehensive analysis by Rietveld refinement technique (Appendix A.4) gave information about the existence of phases in the sample associated to the presence of magnesium impurities that come from the calcium precursor besides the phases mentioned above. Nevertheless, Rietveld analysis carried out quantified the amorphous part as 80% (of the product) (in weight), which is higher than the amorphous percentage found in xonotlite.

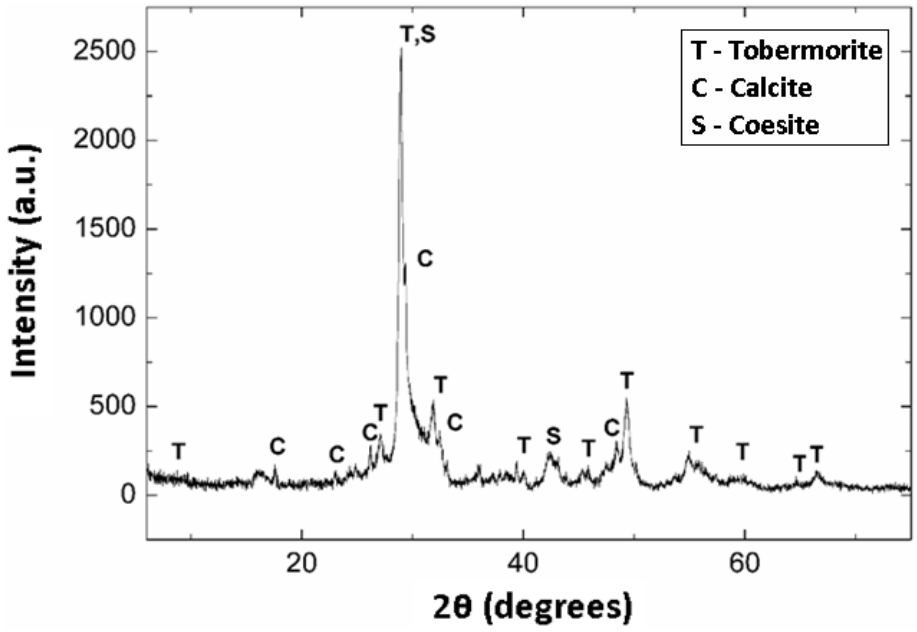

Figure IV.30: XRD curve of SBS functionalized tobermorite synthesized in 4 hours of reaction (tobermorite_SBS-4h).

After 8 hours of reaction the XRD diffractogram (Figure IV.31) of the tobermorite_SBS-8h sample show a slightly more intense diffractions, but the signals are still quite amorphous. Basal peak associated to plane (002) is more defined than in the case of tobermorite_SBS-4h. From Rietveld analysis, no significant changes in phase composition or quantity were found between both samples, except for an increase in carbonate phases in the tobermorite_SBS-8h sample.

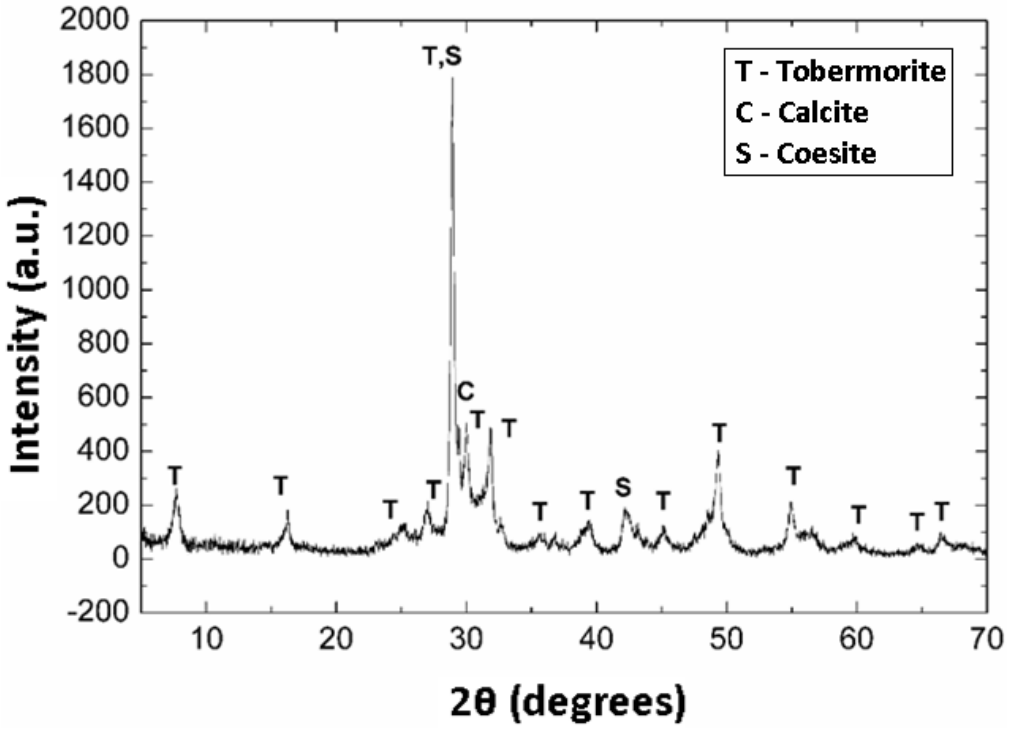

Figure IV.31: XRD curve of SBS functionalized tobermorite recovered after 8 hours of reaction (tobermorite_SBS-8h).

Infra-red spectrum (Figure IV.32) shows bands that can be assigned to Si-O stretching modes for silicate tetrahedra in Q^2 position at 975 cm^{-1} and around 1057 cm^{-1}. Bands in the range of 556 and 400 cm^{-1} were also found which were reported in previous sections and associated to Si-O-Si and O-Si-O bending vibrational modes. Bands around 3400 cm^{-1} and around 1641 cm^{-1} assigned to hydroxyl groups of silanol groups and molecular water present in samples were very intense as it was measured in previous analysis for tobermorite samples. In this case it is important to remark that the peak at 1173 cm^{-1} associated to the presence of double silicate chain is only observed for tobermorite_SBS-8h.

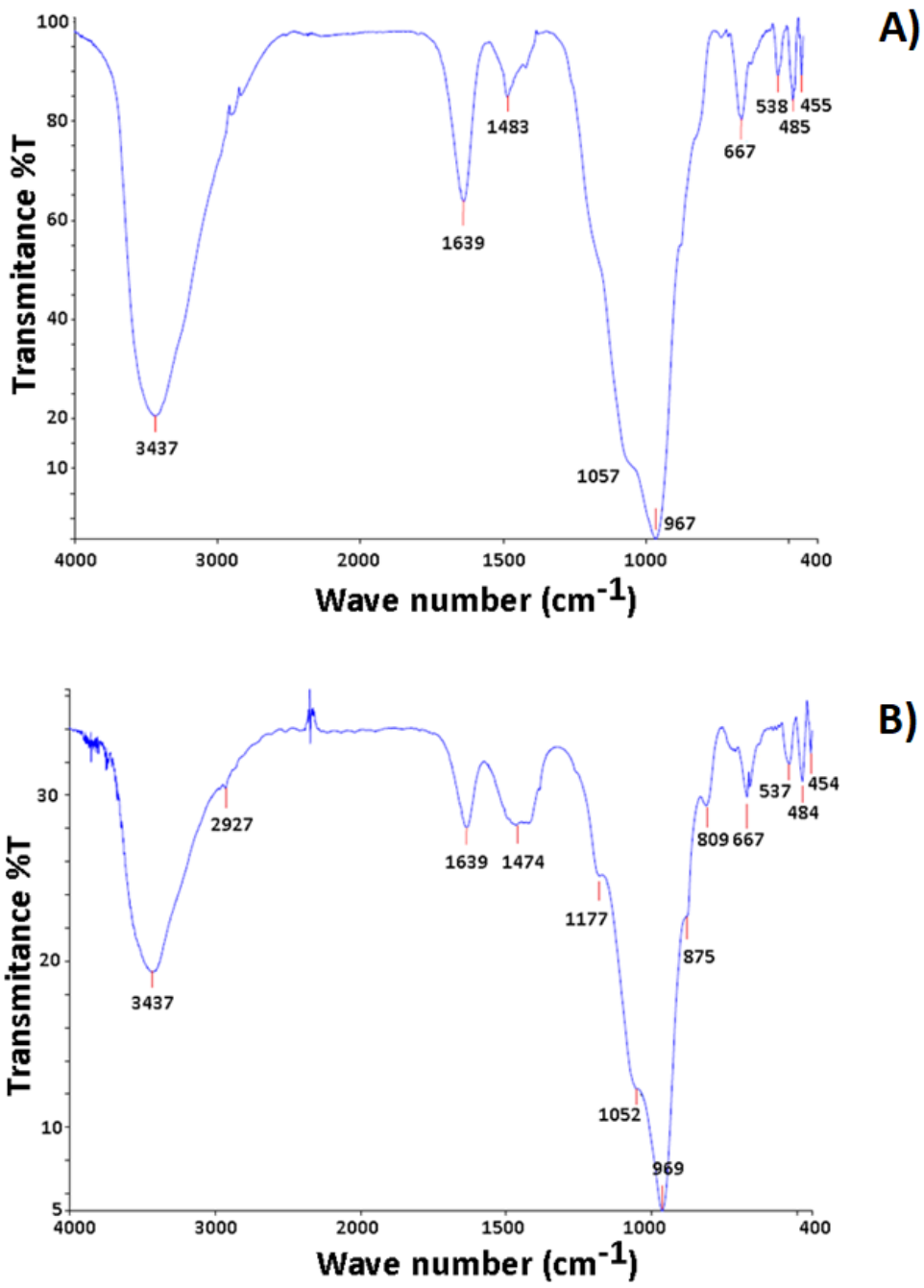

Figure IV.32: FT-IR of tobermorite samples functionalized with SBS. A) tobermorite_SBS-4h. B) tobermorite_SBS-8h.

^{29}Si NMR presented significant differences comparing to pristine tobermorite prepared using the same conditions. The deconvoluted NMR spectrum in Figure IV.33 shows Q^1, Q^2 and Q^3 contributions associated to silicate chain. Moreover, contributions Q^2(1Al) and Q^3(1Al) related to silicate tetrahedra in chains bound to aluminate tetrahedra by oxygen bonds were also observed.

However, as in the case of xonotlite_SBS samples, a signal around -110ppm was also observed and associated to the presence of Q^4 silicate tetrahedra in an amorphous structure. This result suggests that during the reaction amorphous silica has also formed or it could be interpreted as amorphous silica precipitated at the beginning of the reaction and not part of tobermorite-like product.

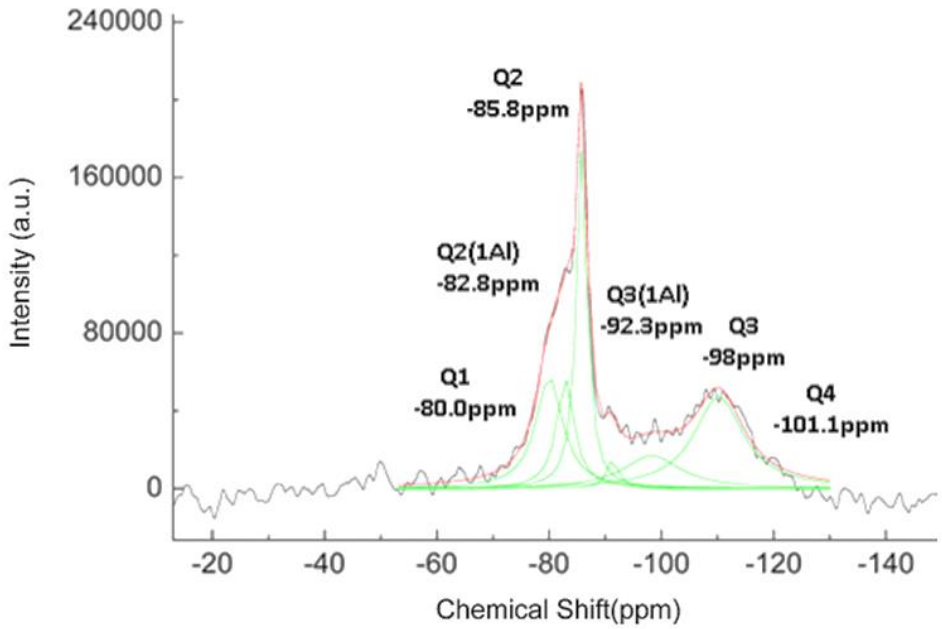

Figure IV.33: ^{29}Si NMR spectrum of SBS functionalized tobermorite (tobermorite_SBS-4h). Notes: black curve is the experimental, red curve is the adjusted curve and green curve represents the deconvoluted curves of each signal adjusted to pseudo-Voigt.

The ^{29}Si NMR of tobermorite_SBS-8h is shown in Figure IV.34. The spectrum was deconvoluted using seven peaks to fit the curve. Besides the typical four signals shown by pristine tobermorite, Q^1, Q^2, Q^3, Q^2(1Al) and Q^3(1Al), two more peaks are observed in the deconvoluted spectrum, one at -101.6ppm and the other one at -113.1ppm. These two signals are often found in amorphous silica samples. The chemical shift at -101.6ppm can be assigned to silicate tetrahedra that are bound to 3 other silicate tetrahedra through oxygens ($Q^{3'}$) and the signal at -113.1ppm can be assigned to silicate tetrahedra bound to 4 silicate tetrahedra (Q^4) [29]. Deconvolution areas gave more information about influence of reaction time. Q^3 and Q^3(1Al) increases as well as Q^4 contribution.

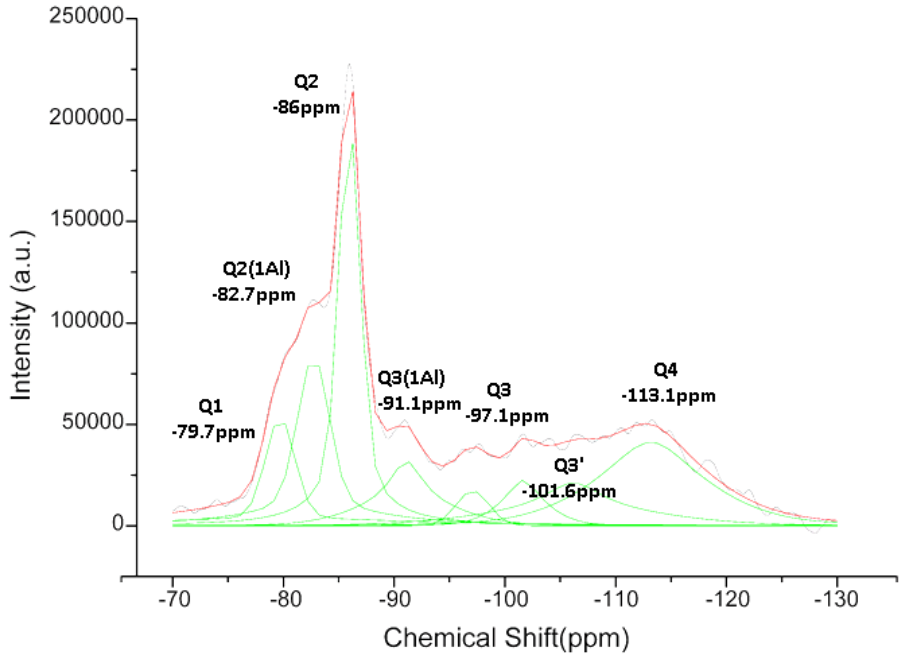

Figure IV.34: ^{29}Si NMR curve of SBS functionalized tobermorite recovered after 8 hours of reaction (tobermorite_SBS-8h).

It is difficult to understand how the reaction is evolving in presence of SBS but it could be possible that, according to XRD, FT-IR and ^{29}Si-NMR, product is still reacting after 8 hours. The characterization indicates that after 8 hours of reaction silica is still formed in the reaction besides the tobermorite like structure. Longer reaction time does not remove the formation of amorphous silica. It could be assumed then that a further analysis should be carried out with even longer reaction times to describe better the effect of SBS in reaction.

^{1}H NMR in Figure IV.35 gave similar results than pristine tobermorite. First, a large contribution appears at 4.8 ppm due to the presence of water in structure. Then a shoulder, associated to protons in Ca-OH groups, appears around 2.1ppm [33]. ^{1}H NMR could distinguish two contributions associated to silanol groups. First a signal at 1.1ppm chemical shift that can be assigned to isolated silanol groups. This contribution was also found in pristine tobermorite. Moreover, a second signal at 1.2ppm chemical shift can be seen. This signal decreased with reaction time and according to literature could be related to protons of Si-OH groups weakly hydrogen bound [30, 31].

As it was observed for xonotlite modified with SBS, in the case of tobermorite_SBS-8h there is a signal at 3.6ppm that could be assigned to the methyl groups of SBS. However,

in this case, this region overlaps with the signals associated to adsorbed water in silanol groups [32] and therefore it is impossible to conclude that the 3.6ppm signals is due to SBS.

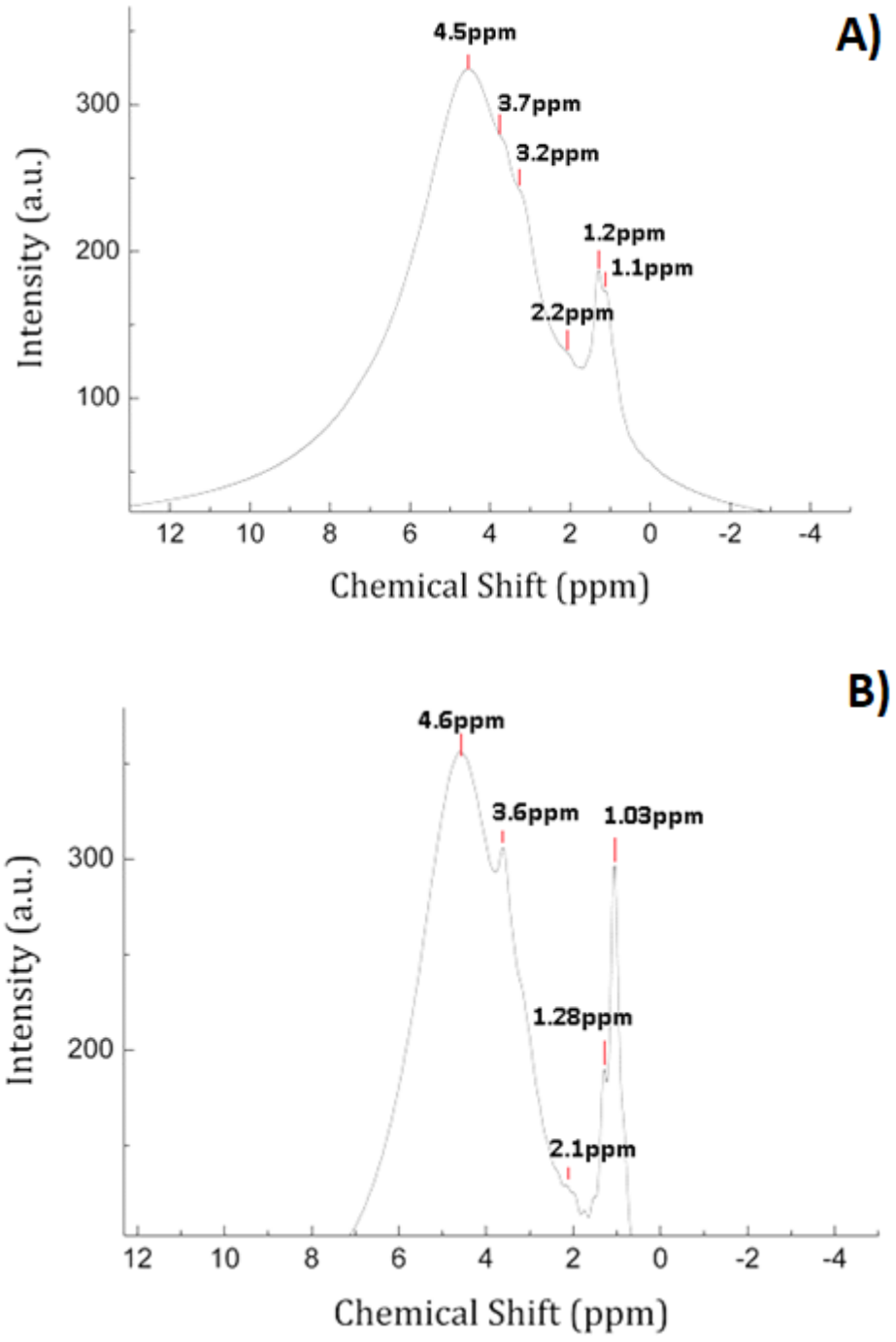

Figure IV.35: A) ^{1}H NMR curve of tobermorite_SBS-4h. B) ^{1}H NMR curve of tobermorite_SBS-8h

IV.3.2. Elemental analysis.

Table IV.12 shows the atomic composition of tobermorite samples obtained in presence of SBS. Ca/(Si+Al) ratios gave lower values than expected for perfect tobermorite (Ca/(Si+Al) =0.83). Moreover, the aluminum content was half the amount introduced in the reactor. No significant changes were observed in elemental composition when the reaction time is increased from 4 hours to 8 hours.

Table IV.12: EDS elemental analysis of tobermorite samples functionalized with SBS.

Sample	Ca atomic %	Si atomic %	O atomic %	Al atomic %	S atomic %	Ca/ (Si+Al)	Al/ (Si+Al)
Tobermorite SBS 4h	14.61	16.92	66.72	1.23	0.51	**0.805**	**0.073**
Tobermorite SBS 8h	14.65	17.01	66.63	1.37	0.35	**0.797**	**0.080**

There is not an easy explanation to justify the calcium and aluminum deficit. However, analyzing these results and results obtained in previous sections it could be assumed that there is a relation between calcium deficit, double silicate chain length and aluminum incorporation. In this case it could be interpretated that SBS inhibits silicate chain growth and aluminum incorporation as well. Contrary to results from xonotlite synthesized in presence of SBS, it seems that the sulfur content in the sample is reduced when time of reaction is increased.

IV.3.3. Morphological analysis.

TEM images of these samples prepared in presence of SBS showed amorphous structures more similar to C-S-H gel than plates like tobermorite structures. Moreover, little spherical structures with nanometer size were also found in these images. These could suggest the presence of SiO_2 byproduct suggested by ^{29}Si NMR.

Nevertheless, differences between samples obtained after 4 and 8 hours can be observed (Figure IV.36). After 4 hours of reaction TEM images show irregular particles

with an average size of 0.5µm. When the reaction time is 8 hours the particles obtained are larger, between 2µm and 3µm in size.

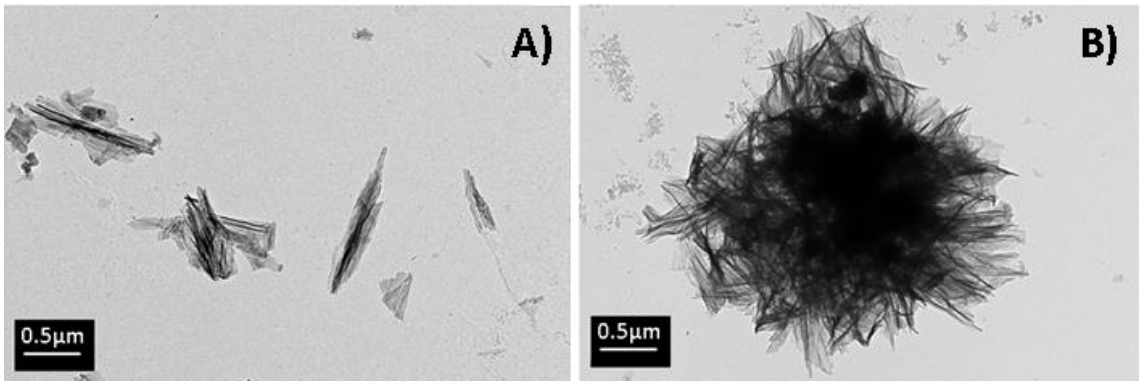

Figure IV.36: TEM images of tobermorite particles functionalized with SBS. Samples synthesized in 4 hours of reaction (A) and samples synthesized in 8 hours of reaction (B).

From all these results it was concluded that SBS inhibits the crystallization of tobermorite. On one hand, it was observed a reduction of calcium and aluminum inside the structure. Then it could be possible that part of reactants is still unreacted in liquid medium after 4 and 8h of reaction. On the other hand, it was observed the formation of byproducts that could be associated to the precipitation of silica. It is not clear at all if SBS has an effect in the mechanism of tobermorite precipitation or it changes the synthesis process. Moreover, it is not clear where the SBS is either. IF it is bound to silica by product or tobermorite-like amorphous product. Nevertheless, a more in-depth study should be carried out to better analyze this effect.

IV.4. Addition of tobermorite particles (with and without PEG) in cement pastes.

IV.4.1. Dosage of particles. Calculation of organic content by TGA- DSC.

Tobermorite modified with PEGs, as it was observed for xonotlite samples, present a significant loss of mass around 200°C in air (Figure IV.37). This temperature decreases as it was observed for xonotlite samples depending on the molecular weight of the PEG employed to functionalize tobermorite. However, the DSC curve shows that exothermic events happened between 180°C and 270°C a range higher than the same event for xonotlite with PEG. This means that thermal stability of PEG grafted on tobermorite is higher than PEG on xonotlite surface. This could suggest a higher interaction of PEG in

tobermorite or a partial degradation occurred during hydrothermal synthesis in batch reactor.

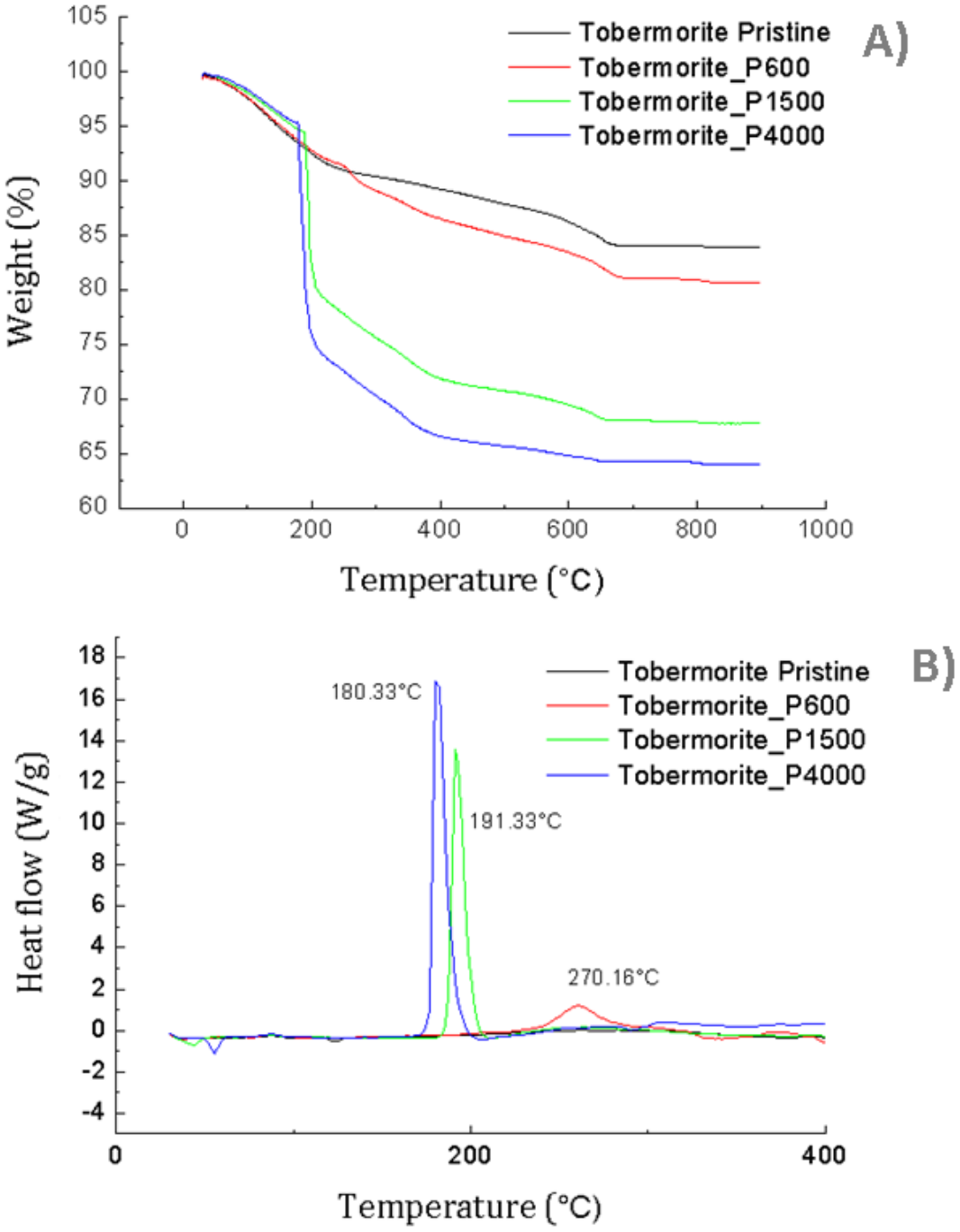

Figure IV.37: TGA (A) and DSC (B) curves of hydrothermal tobermorite samples.

However, the quantity of remaining polymer in the solid is much lower compared to the contents obtained for xonotlite. The calculated yield for PEG added that remains attached in solid is below 2% (Table IV.13).

There is not a clear explanation about why xonotlite samples retain more polymer than tobermorite but maybe their morphology could explain it. In TEM images xonotlite showed a grid arrangement of fibers. This structures generate holes or spaces between fibers where polyethyleneglycol could be retained during the precipitation of the particles. However in tobermorite samples particles do not aggregate this way and do not form larger porous aggregates. Therefore, in the case of tobermorite the remaining PEG could be only adsorbed or interacting on tobermorite surface directly.

Table IV.13: Summary of PEG contents in modified tobermorite samples.

Sample	Additive	%PEG in sample	Yield (gPEG solid/gPEG initial)x100
T_Pristine	N/A	-	-
T_P600	PEG 600	**3.3%**	**1.01%**
T_P1500	PEG 1500	**19.64%**	**3.24%**
T_P4000	PEG 4000	**27.4%**	**2.17%**

IV.4.2. Stability of particle dispersions in water.

On the other hand, Figure IV.38 shows the dispersion stability tests carried out for pristine and modified tobermorite. Tobermorite samples showed a lower stability than xonotlite samples when they were mixed manually. This could be explained due to the low quantity of polyethylene glycol adsorbed on tobermorite particles. After 24 hours these suspensions tend to aggregate and precipitate. However, if pristine tobermorite pristine and modified ones are compared, the unmodified particles tend to sediment sooner. This precipitation is lower if the suspension is prepared by ultrasound homogenizer, but the tendency is similar. In this case the samples that showed the best stability were tobermorites modified with PEG MW600 and PEG MW4000.

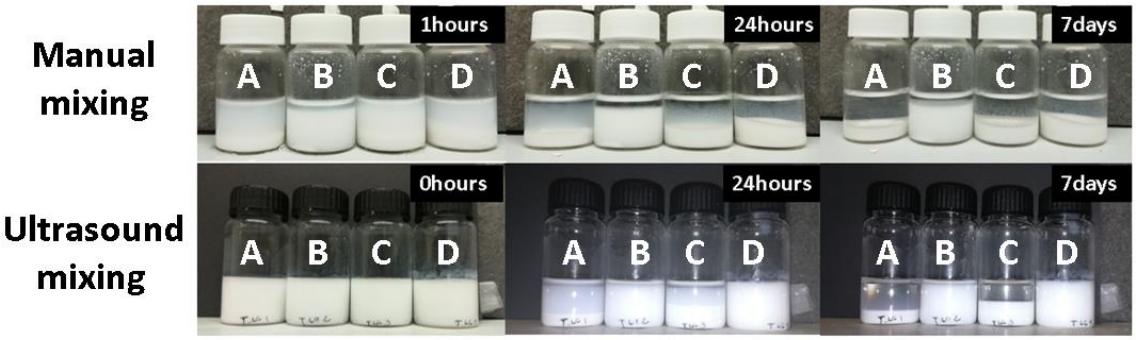

Figure IV.38: Decantation experiments for tobermorite pristine and PEG modified tobermorites. Pristine tobermorite (A), tobermorite PEG MW600g/mol (B), tobermorite PEG MW1500g/mol (C) and tobermorite PEG MW4000g/mol (D).

Zeta potential values of tobermorite samples are shown in Table IV.14. In this case the effect of PEG in particles stability can be observed clearly. Using the same concentration of particles that it was employed to prepare cement pastes the stability is poor except for T_P600. This result matches the result obtained in the decantation experiment which showed the same tendency. For suspensions of 1.25%w/w of particles in water all the PEG modified increased the stability comparing to the pristine tobermorite suspension. Therefore, the PEG functionalization improved the dispersion of the tobermorite.

Table IV.14: Zeta potential of tobermorite particles suspensions.

Sample	Mean ZP (mV)	Standard Deviation (mV)	Sample	Mean ZP (mV)	Standard Deviation (mV)
1.25%w/w particles in water			**2.5%w/w particles in water**		
T_Pristine	-1.56	2.36	T_Pristine	3.76	3.32
T_P600	-18.8	0.153	T_P600	-13.5	0.751
T_P1500	-15.6	0.643	T_P1500	-1.75	6.56

T_P4000	-12	0.52	T_P4000	-0.366	0.941

IV.4.3. Tobermorite rheological, mechanical and acceleration effect on cement paste.

The rheology behavior of tobermorite samples mixed in cement pastes were analyzed and compared with the reference cement paste without additives. 1% wbc of pristine and modified tobermorite samples were added to the cement paste. When pristine tobermorite is added to the cement paste the viscosity and yield stress are increased compare to the reference paste (Figure IV.39). However, when PEG modified tobermorites were added, the workability of pastes is improved reducing the viscosity below the viscosity of the reference paste. This effect could be explained because PEG could be desorbed from tobermorite surface and dispersed among the Portland cement particles.

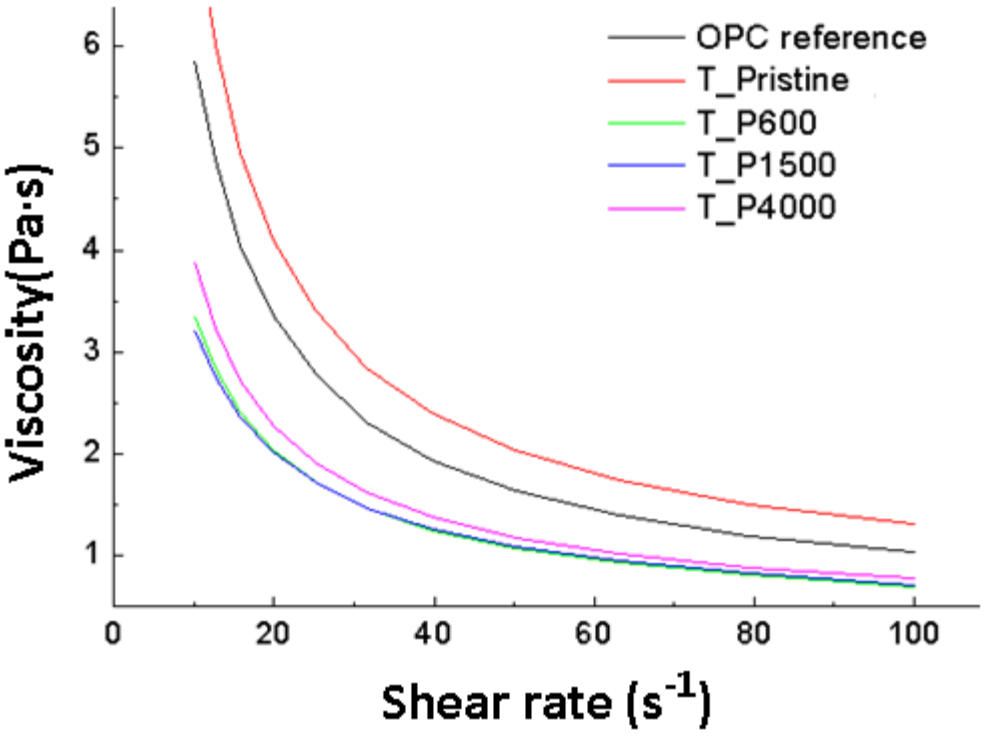

Figure IV.39: Viscosity curve of prepared cement pastes with tobermorite particles.

Figure IV.40 shows the isothermal calorimetry measurements of the cement pastes with the different tobermorite samples. Similar acceleration of the cement hydration was

observed for all cement pastes that contain the different tobermorite additions. Although good results in rheology were obtained using tobermorite particles modified with PEG, in the case of the cement hydration, the same acceleration as with the pristine tobermorite is obtained. We could conclude that the PEG molecules that contain the different tobermorite samples (T_P600, T_P1500 and T_P4000) help improve the rheology of the workability without retarding the hydration contrary to what occurred when X_P4000 was added to the cement paste. Moreover, the addition of PEG does not seem to cause a significant retardation of cement hydration as it was observed for xonotlite additions with PEG. This makes sense because the tobermorite compounds contain less PEG quantity than the xonotlite compounds.

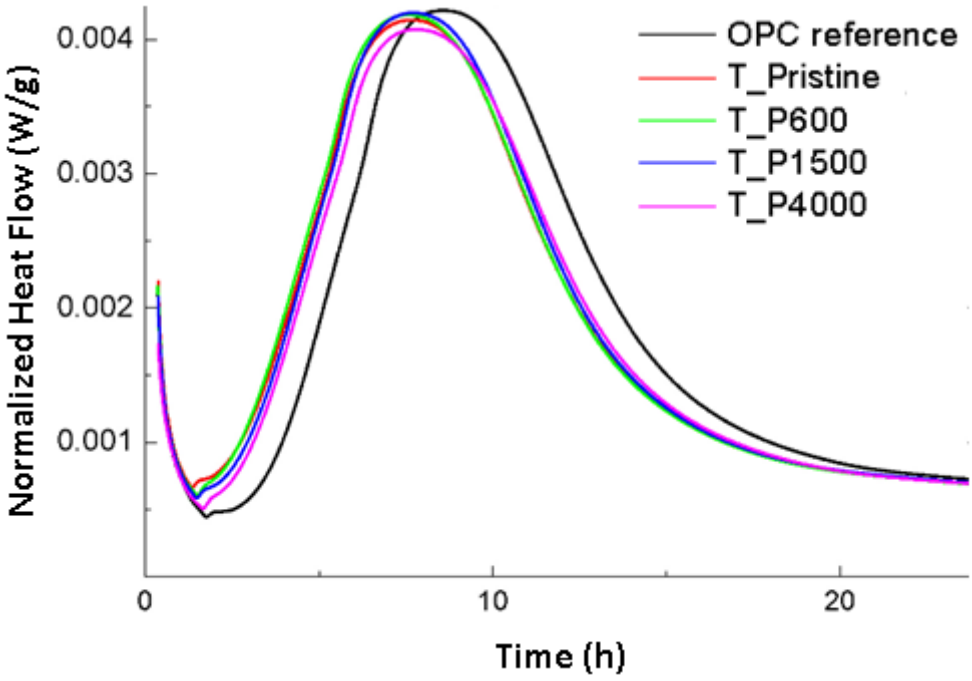

Figure IV.40: Isothermal calorimetry curves of mixed cement pastes with tobermorite additions.

Cement pastes with tobermorite particles showed a good flexural strength after 8h of curing if they are compared to the reference (Figure IV.41). There are no significant changes between cement pastes with pristine tobermorite and with the different PEG modified tobermorite additions after 8 hours of curing. On the other hand, bending tests carried out after 24h did not showed significant increase of flexural resistance of the

specimens with pristine tobermorite, and a slight reduction was observed in specimens that contain T_P600, T_P1500 and T_P4000 as additions.

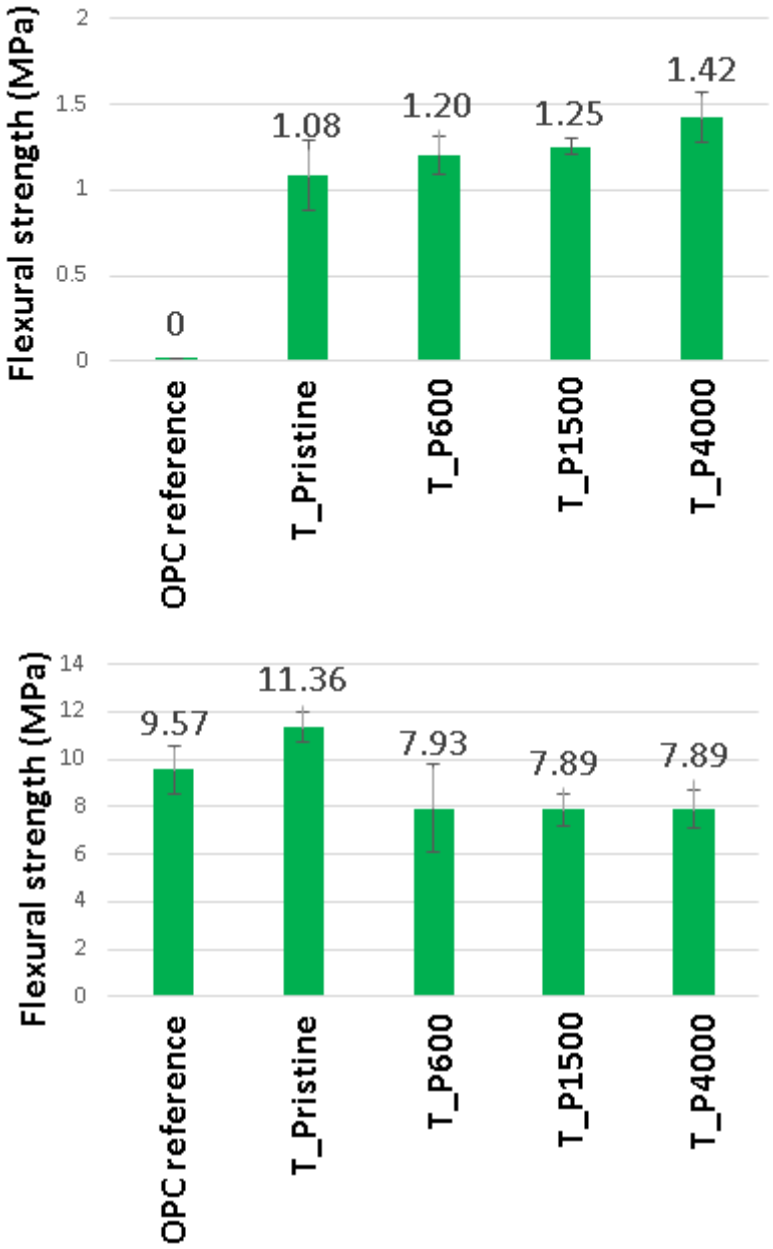

Figure IV.41: Flexural strength of pastes modified with the different tobermorite samples. Prisms tested after 8h (above) and 24h (below).

In the case of compression tests, addition of the different tobermorite samples have an improvement in compressive strength values comparing to the reference cement after 8h of curing (Figure IV.42). However, no enhancement was observed after 24h of curing time. This confirms the results obtained in isothermal calorimetry as well where the hydration curves tend to converge after 20h of hydration.

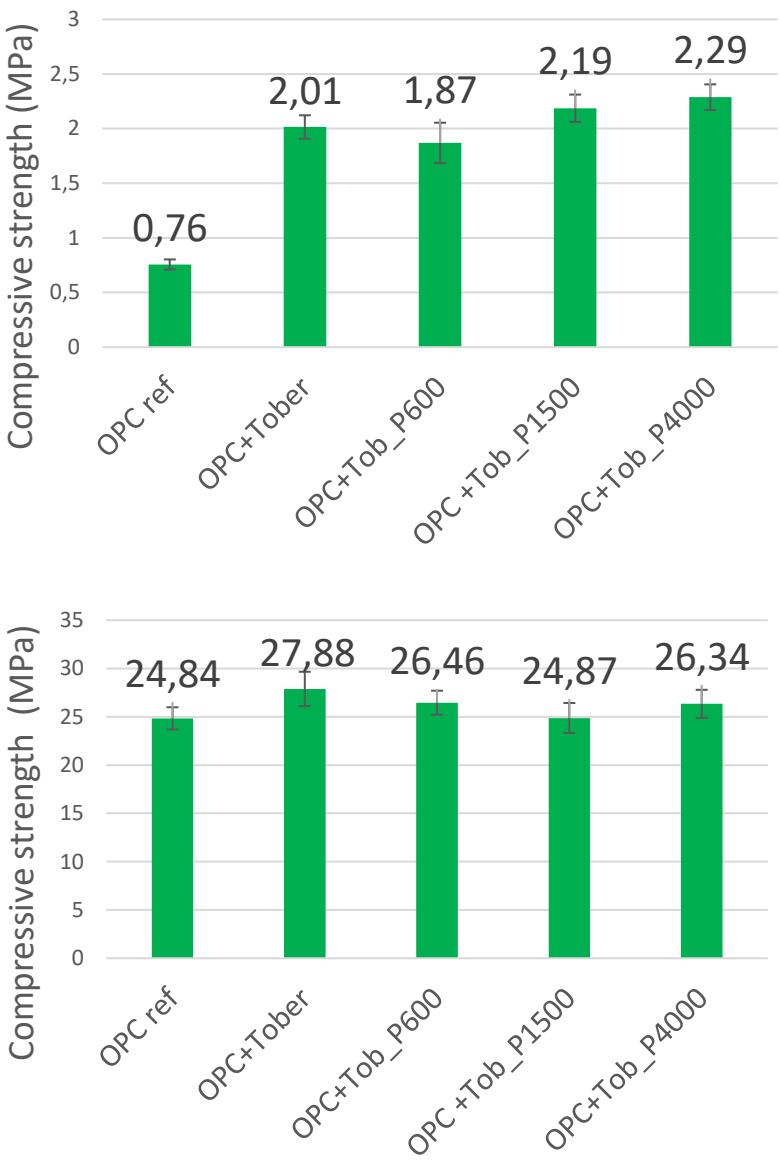

Figure IV.42: Compressive strength of pastes modified with subcritical tobermorites. Prisms tested after 8h (above) and 24h (below).

From mechanical tests several things can be concluded. First, samples modified with PEG MW 1500and PEG MW4000 increased slightly the flexural and compressive strength after the first 8 hours of curing. Nevertheless, the increase of mechanical properties after 24h using the different xonotlite and tobermorites samples is almost negligible compare to the reference cement, most of the effect is observed at earlier ages.

IV.5. Addition of SBS functionalized tobermorite to cement pastes. Rheology, mechanical behavior and acceleration effect.

Table IV.15 shows the SBS content obtained from thermal degradation of samples in the range of 250°C and 400°C measured by TGA/DSC. Moreover, the yield of SBS found in samples respect to the total SBS added to the reactor medium was calculated. As it was observed for xonotlite like samples, in tobermorite like samples the yield was also below 20%. Therefore more than 80% of SBS did not react and could be still as part of reaction solution.

Table IV.15: Sulfobetaine siloxane content in tobermorite like samples characterized by TGA /DSC.

Sample	SBS content (weight %)	Yield (g of SBS in solid/g of SBS added)
Tobermorite_SBS-4h	5.79	14.30
Tobermorite_SBS-8h	4.30	18.24

According to z-potential tests, in the case of tobermorite-like amorphous particles with SBS, the stability in water is slightly different than the one observed for xonotlite-like samples (Table IV.16). Pristine tobermorite particles tend to aggregate easily even using a 2.5% w/w concentration, therefore they do not seem to be very stable in suspension according to the very low values of zeta potential obtained (lower than 10mV). Both tobermorite_SBS samples showed incipient stability (higher than 10mV) using 2.5% w/w but higher concentration suspensions present low Z potentials and fast precipitation as well. These results show that tobermorite_SBS samples are less stable than xonotlite_SBS samples.

Table IV.16: Zeta potential values of SBS functionalized tobermorite samples in water suspensions.

Sample	Mean ZP (mV)	Standard Deviation (mV)	Sample	Mean ZP (mV)	Standard Deviation (mV)
2.5%w/w particles in water			**5%w/w particles in water**		
Pristine tobermorite	-1.56	2.36	Pristine tobermorite	3.76	3.32
Tobemorite SBS-4h	-13.5	0.208	Tobermorite SBS-4h	1.08	0.196
Tobermorite SBS-8h	-11.5	1.11	Tobermorite SBS-8h	1.16	0.982

Rheological test carried out with cement pastes that contain the different tobermorite samples (Figure IV.43) showed significant effect of SBS molecule. The presence of SBS caused a reduction in viscosity compared to pristine tobermorite. This reduction is higher in the case of samples modified with SBS obtained after 8h of reaction.

Calorimetry results demonstrated acceleration effects in cement hydration for tobermorite samples modified with SBS as well. The higher acceleration was obtained in pastes with tobermorite_SBS-8h (Figure IV.44).

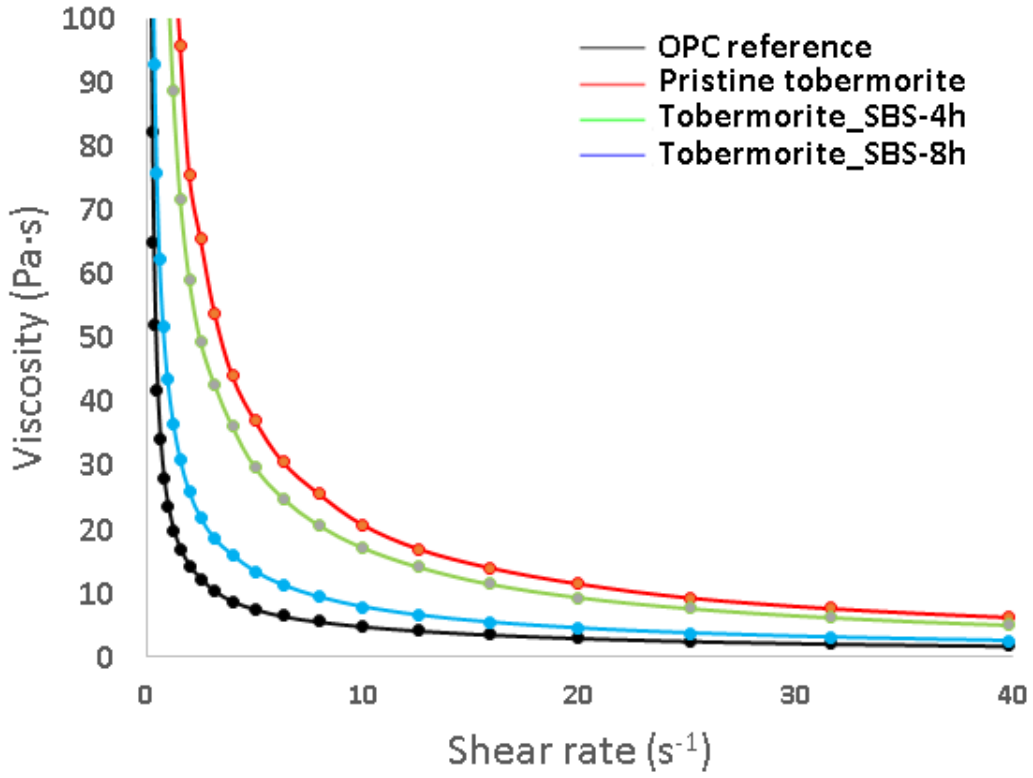

Figure IV.43: Viscosity curves of prepared cement pastes with tobermorite additions.

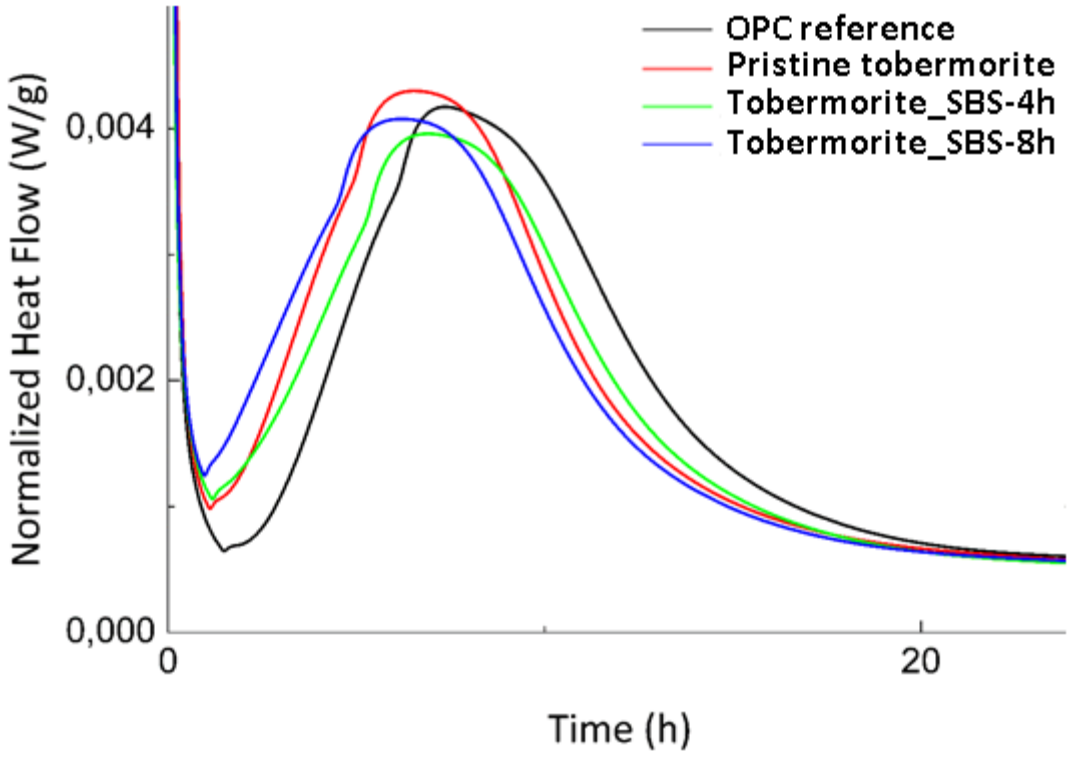

Figure IV.44: Isothermal calorimetry curves of prepared cement pastes with tobermorite additions.

Flexural tests carried out did not give conclusive results. After 8 hours of curing time all specimens broke even before starting the test. Moreover, no significant differences were found in pastes with unmodified and modified samples after 24 hours of curing.

Compressive strength on the other hand showed a similar tendency found in specimens with xonotlite samples. Addition of tobermorite with and without SBS increased compressive strength. In this case tobermorite-like particles with SBS that was synthesized in 8 hours showed a higher increase of compressive strength (Figure IV.45).

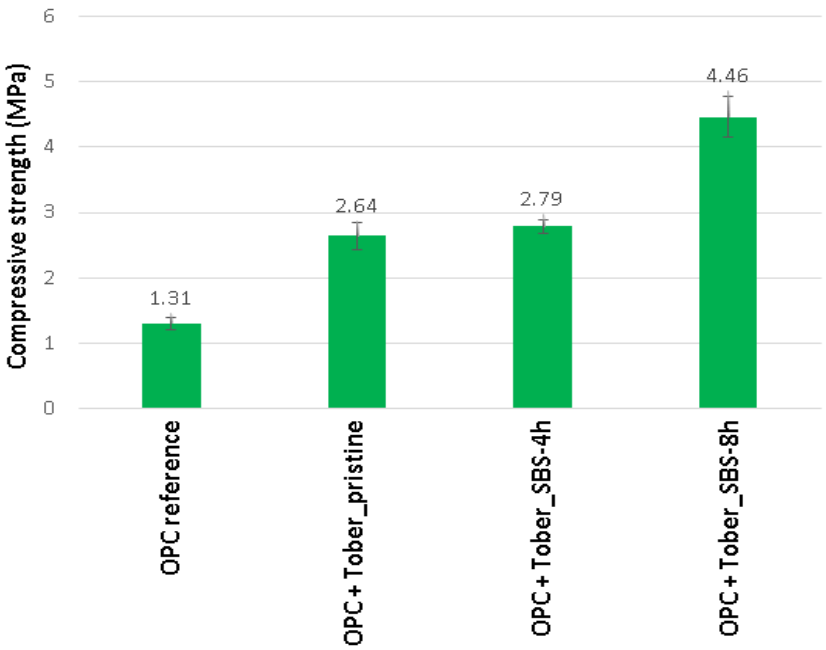

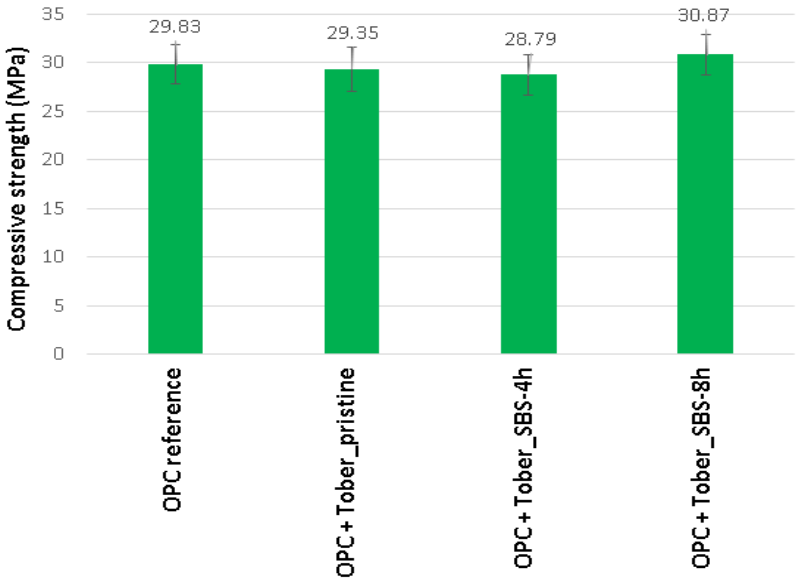

Figure IV.45: Compressive test of cured cement pastes with tobermorite modified by SBS after 8 hours (above) and after 24 hours curing time (below).

In conclusion the partial substitution of SBS as silicon source in batch reactor has generated particles employed as seeds with interesting properties in workability and acceleration effect in cement pastes. Although a deeper study should be carried out in future work to understand the effect of SBS in tobermorite formation, this could be a first step to obtain modified seed particles without the use of polymers or other conventional surfactants as tween 20, sodium dodecylsulfate (SDS) or Cetyltrimethylammonium (CTAB).

IV.6. References.

[1] N.Y. Mostafa, A.A. Shaltout, H. Omar, S.A. Abo-El-Enein, *J. Alloy. Compd. 467* (**2009**), pp. 332–337.

[2] Z. Zhao, J. Wei, F. Li, Q. Yu, *Adv. Cem. Res., 29(9)* (**2017**), pp. 359–372.

[3] M. Diez-Garcia **2017**. *"Synthesis by supercritical fluids methods of advanced additions for cementitious materials"* Universidad del País Vasco/Université de Bordeaux. Repositorio institucional ADDA EHU Biblioteka UPV/EHU.

[4] I. García-Lodeiro, D. E. Macphee, A. Palomo, A. Fernández-Jiménez, *Cement and Concrete Research* 39 (**2009**) pp. 147–153.

[5] J. J. Chen, J. J., Thomas, H. F. W. Taylor, H. M. Jennings, *Cem. Concr. Res.* 34, 9 (**2004**), pp. 1499–1519.

[6] I. S. Protsak, Y. M. Morozov, W. Dong, Z. Le, D. Zhang, *Nanoscale Res. Lett.* 14:160 (**2019**).

[7] H. Seyama, M. Soma, A. Tanaka, *Chem. Geol. 129* (**1996**) pp. 209–216.

[8] L. Black, K. Garbev, P. Stemmermann, K.R. Hallam, G.C. Allen. *Cem. Concr. Res. 33* (**2003**) pp. 899–911.

[9] J. D. C. McConnell, *Mineral. Mag.* **1954**, *30*, 293–305.

[10] S. A. Hamid, *Zeitschrift für Krist. - Cryst. Mater.* **1981**, *154*, 189–198.

[11] S. Merlino, E. Bonaccorsi, T. Armbruster, *Am. Mineral.* **1999**, *84*, 1613–1621.

[12] T. Maeshima, H. Noma, M. Sakiyama, T. Mitsuda, *Cem. Concr. Res.* **2003**, *33*, 1515–1523.

[13] S. A. S. El- Hemaly, T. Mitsuda, H. F. W. Taylor, *Cem. Concr. Res. Vol. 7* (**1977**), pp. 429-438.

[14] N. Y. Mostafa, S. A. S. El-Hemaly, E. I. Al-Wakeel, S. A. El-Korashy, P. W. Brown, *Cem. Concr. Res. 31* (**2001**) p. 905.

[15] D. S. Klimesch, A. Ray*, Thermochim. Acta 334* (**1999**) 115.

[16] X. Guo, F. Meng, H. Shi, *Constr. Build. Mater., 133* (**2017**) pp. 253–260.

[17] J. Schneider, M. A. Cincotto, H. Panepucci, *Cem. Concr. Res. 31, 7* (**2001**), pp. 993–1001.

[18] G. K. Sun, J. F. Young, R. J. Kirkpatrick, *Cem. Concr. Res. 36, 1* (**2006**), pp. 18–29.

[19] X. Qu, Z. Zhao and X. Zhao., *RSC Adv.,* 8 (**2018**), pp. 28198–28208.

[20] X. Pardal, F. Brunet, T. Charpentier, I. Pochard, A. Nonat, *Inorg. Chem*., 51, (**2012**) pp. 1827−1836.

[21] R. Komarneni, R. Roy, D. M. Roy, C. A. Fyfe, G. J. Kennedy, A. A. Bothner-By, J-Dadok, A. S. Chesnick, *J. Mater. Sci. 20* (**1985**) pp. 4209–4214.

[22] P. Faucon, A. Delagrave, C. Richet, J. M. Marchand, H. Zanni, *J. Phys.Chem., B 103* (**1999**) pp. 7796–7802.

[23] R. Loewenstein, *Am. Mineral.*, 39, (**1954**), pp. 92 —96

[24] J. Blummel, N. Perschmann, D. Aydin, J. Drinjakovic, T. Surrey, M. Lopez-Garcia, H. Kessler, J. P. Spatz, Biomater., 28 (**2007**) pp. 4739–4747

[25] T. L. Barr, E. E. Hoppe, S. Hardcastle, *J. Vac. Sci. Technol., A, Vac. Surf. Films 17 (4)* (**1999**) 1079–1085

[26] O. Hourri,J. Masse, *J. Therm. Anal., 39, 507,* (**1993**).

[27] Y. Zhou, C. A. Orozco, E. Duque-Redondo, H. Manzano, G. Geng, P. Feng, P. J.M. Monteiro, C. Miao, Cem. Concr. Res. *115 (***2019***)* pp.20-30.

[28] M. D. Andersen, H. J. Jakobsen, J. Skisped, *Inorg. Chem., Vol. 42, No. 7,* (**2003**).

[29] M. Monasterio, J. J. Gaitero, E. Erkizia, A. M. Guerrero Bustos, L. A. Miccio, J. S. Dolado, S. Cerveny, *Journal of Colloid and Interface Science 450,* (**2015**) pp. 109-118.

[30] H. Rosenberger, A. R. Grimmer, U. Haubenreißer, B. Schnabel, *Magn. Reson. Relat. Phenom.*, Springer, Heidelberg, Berlin, (**1979**), pp. 106-106.

[31] D. Heidemann, W. Wieker, *Nucl. Magn. Reson. Spectrosc. Cem. Mater.*, Springer, Berlin, (**2012)**, p. 169.

[32] I. S. Protsak, Y. M. Morozov, W. Dong, Z. Le, D. Zhang, *Nanoscale Res. Lett.* 14:160 (**2019**).

[33] P. Colombet, "Nuclear Magnetic Resonance Spectroscopy of Cement-Based Materials" Springer-Verlag Berlin Heidelberg, (**1998**) ISBN: 978-3-540-63134-7.

[34] L. Black, A. Stumm, K. Garbev, P. Stemmermann, *Cem. Concr.Res. 35* (**2005**) pp. 51–55.

CHAPTER V: SUPERCRITICAL SYNTHESIS.

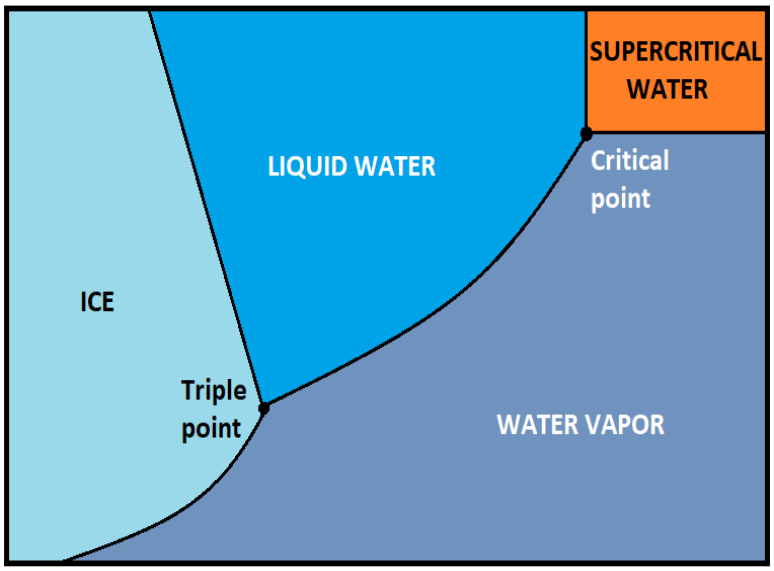

As it was mentioned in previous chapters one of the reasons to use supercritical technique for synthesis of calcium silicate hydrates particles is controlling better the average size. Products obtained by this method have narrower size distribution and a more reduced size. This have significant advantages in acceleration of cement when these particles are added to cement matrix [1].

This part of the work started using reaction conditions observed in previous studies [2]. However, the reactor employed for these experiments was scaled up from the reactor used in reference 2 and required a previous optimization of reaction parameters.

V.1. Pristine xonotlite synthesized under supercritical hydrothermal conditions.

The first experiments carried out tried to reproduce the synthesis of xonotlite using supercritical conditions at 400°C, 235 bars and a residence time of 20 seconds (obtained by setting the flow rate to 3.3mL/min for each HPLC pump). As it was mentioned in chapter II, the precursor solutions were prepared using a Ca/Si molar ratio equal to 1.0 and a molar concentration of Ca and Si equal to 0.01M.

In Figure V.1 the XRD pattern of the product obtained using these conditions in the continuous reactor setup is shown. It can be observed that in the product there is xonotlite (PDF 00-023-0125) contaminated with the presence of wollastonite phase (PDF 01-075-1396). The latter phase could be the result of dehydration of xonotlite under high temperature conditions. Calcite traces also are observed in XRD diffractogram

Some authors in the literature employed a calcination treatment above 800°C to dehydrate xonotlite into wollastonite [3-5]. However, others reported wollastonite formation after few days of hydrothermal treatment at 400°C and 34MPa of pressure [6]. Therefore, these studies indicate that xonotlite is able to evolve into its dehydrated form near or above the critical temperature of water (>374ºC) [7].

It is possible that part of the material that is attached to the inner reactor wall spends more time inside the reactor. This causes that this material reacts further into its dehydrated form.

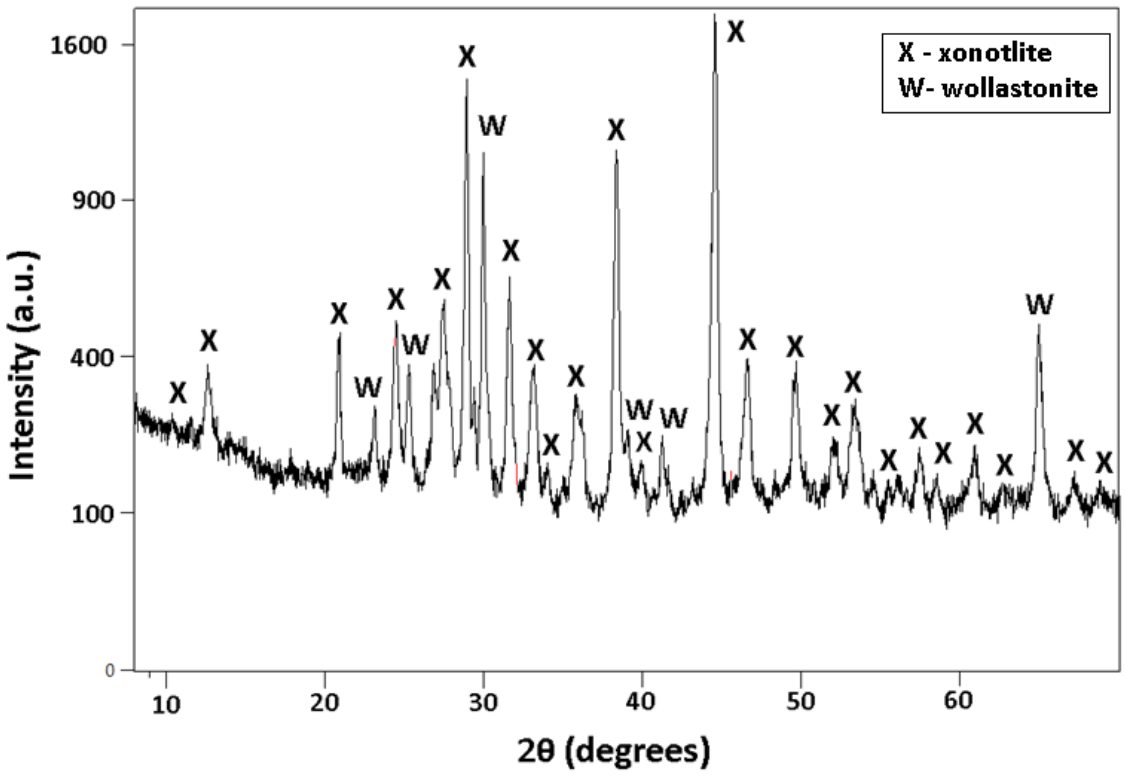

Figure V.1: XRD pattern of xonotlite synthesized at 400°C and 235bars. Residence time equal to 20 seconds.

One solution proposed to avoid, or at least reduce, the contamination of wollastonite was decreasing the residence time of the material in the reactor tube. By increasing the total flow rate (reduction of the residence time), it is also possible to reduce the amount of material stuck or clogged on the inner wall. The next experiment carried out consisted in increasing the flow rate from 3.3mL/min to 4.3 mL/min per pump. This latter flow rate gives a residence time of 17 seconds. The concentration, temperature and pressure conditions were maintained constant.

In Figure V.2 the XRD pattern of the product obtained with the new residence time is shown. As it can be observed in this pattern, the presence of wollastonite has been reduced significantly. However, a reduction of residence time has a negative effect on xonotlite crystallinity, therefore larger reduction of residence time could generate undesired amorphous byproducts. Taking into account this result it was decided to use 4.3mL/min as flow rate for the synthesis of xonotlite.

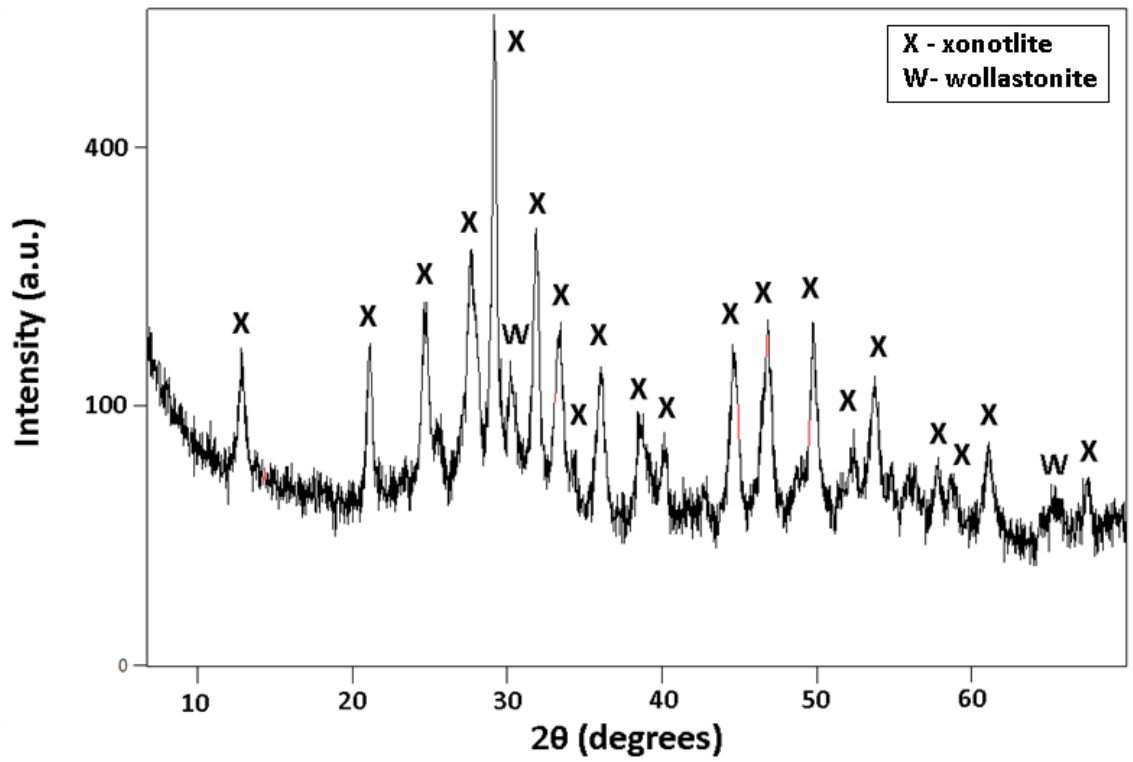

Figure V.2: XRD spectrum of xonotlite synthesized at 400°C and 235 bars. Residence time equals to 17 seconds.

V.2. Xonotlite modified with polyethylene glycol synthesized under supercritical conditions.

The same conditions (400°C, 235bars and 17seconds of residence time) were employed to synthesize xonotlite in presence of different polyethylene glycol (PEG) polymers. Xonotlite particles were prepared with polyethylene glycol of MW 600g/mol, MW 1500g/mol and MW 4000g/mol. The molar ratio Ca/PEG used was equal to 1.5 as it was employed for subcritical experiments.

XRD patterns from Figure V.3 shows the products obtained in the presence of different polyethylene glycol polymers. The analysis of the XRD diffraction shows that besides xonotlite, calcite (PDF 01-081-2027) is also present in all samples. Besides the calcite contribution seems to be more intense when the molecular weight of the PEG used is higher.

The most plausible explanation for this effect is that part of polyethylene glycol is degraded in these temperature conditions, even for such a short residence time. This

degradation can be observed during the experiment with bubbles that leaves the system through the back-pressure regulator (BPR) outlet.

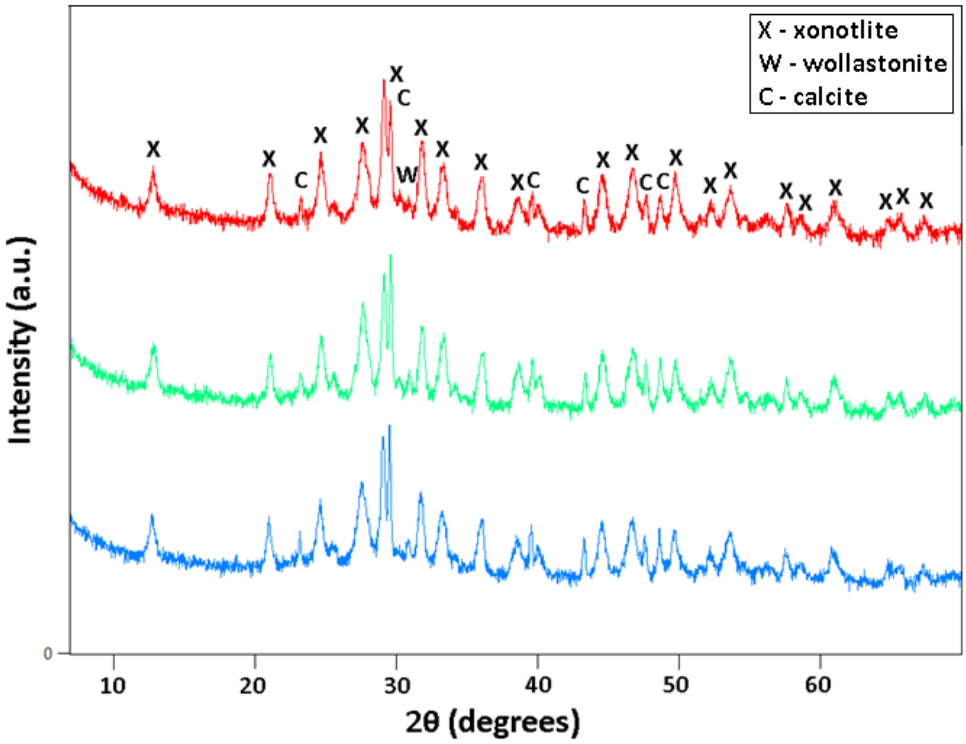

Figure V.3: XRD patterns of xonotlite synthesized at 400°C and 235bars in presence of PEG MW 600g/mol (red curve) PEG MW 1500g/mol (green curve) and PEG MW 4000g/mol (blue curve). Residence time equal to 17 seconds.

From this result, it was decided to test which is the maximum allowed temperature in which polyethylene glycol does not degrade. To do this polyethylene glycol solutions were flowed through the reactor at different temperatures from 50 to 400°C. Flow rate and pressure conditions were maintained fixed. Experiments consisted in making a visual inspection of BPR outlet while the temperature conditions in the reactor were increased. Then it was determined at which temperature the bubbling starts.

Results gathered in Table V.1 showed that below 350°C bubbling was not observed and near to the critical point of water (374°C) little bubbling is detected. Moreover, the experiments confirmed that the bubbling effect is significant at 400°C of temperature, above the critical point.

Table V.1: Visual inspection of bubbling effect at different temperatures.

Reactor Temperature (°C)	Bubbling (Visual inspection)
50	**NO**
100	**NO**
150	**NO**
175	**NO**
200	**NO**
250	**NO**
275	**NO**
300	**NO**
325	**NO**
350	**NO**
360	**VERY LOW**
375	**LOW**
400	**HIGH**

Taking these results into account, it was decided to carry out the synthesis of xonotlite with different PEGs at 325°C. Figure V.4 shows the XRD pattern of xonotlite synthesized in the presence of PEG at these temperature conditions. The presence of calcite, according to XRD spectra, was reduced significantly in samples prepared with PEG MW600, PEG MW1500g/mol and PEG MW4000g/mol.

A temperature of 325°C in the system, required a higher flow rate per pump to maintain a residence time similar to the pristine xonotlite synthesis in supercritical conditions (4.3mL/min). In this case the flow rate was increased to 9.9mL/min per pump, which following the equation 10 corresponds to a residence time equal to 27 seconds. In this case the HPLC pumps in the system are working near to the upper limit for the flow rate and it is not possible to reduce the residence time further.

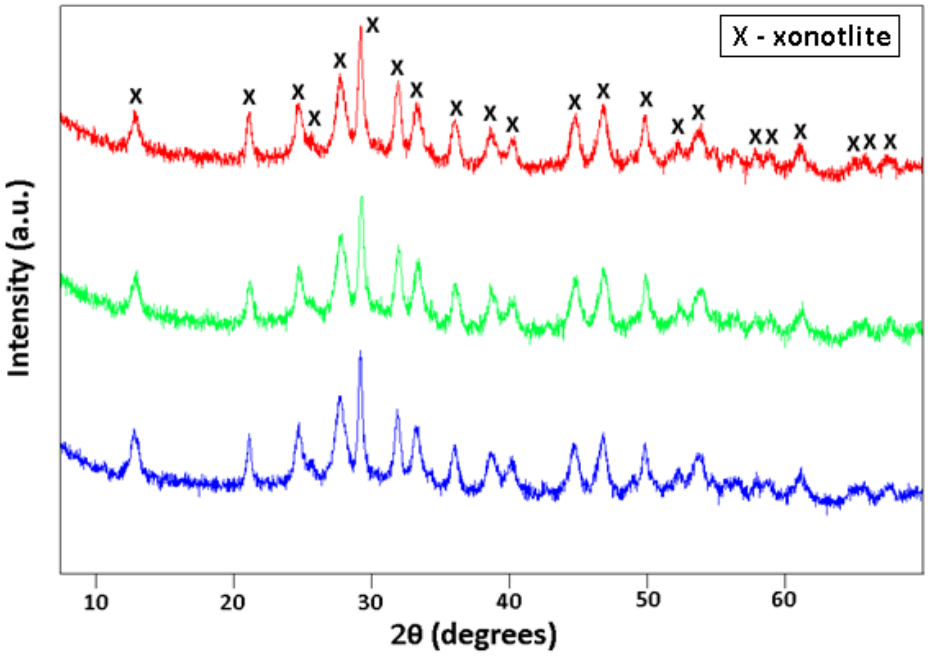

Figure V.4: XRD spectra of samples prepared at 325°C, 235bars and 27 seconds of residence time. Particles prepared in the presence of PEG MW600 (red curve), PEG MW 1500 (green curve) and PEG MW 4000 (blue curve).

All the samples were analyzed by FT-IR (Figure V.5). In all cases a relatively small band between 1400 and 1500 cm^{-1} can be observed which can be associated to CO_3^{2-} groups. As mention before, this is probably due to a certain degradation of the PEG and its reaction with the calcium ion forming $CaCO_3$. However, the intensity of the band is not very large. Nevertheless FT-IR spectroscopy confirms the presence of characteristic peaks of xonotlite at 1200 cm^{-1}, which are associated to double silicate chains and 3600cm^{-1} which are associated to the stretching mode of Ca-OH bond. As it was mentioned in chapter 3, other intense contributions can be found between 457cm^{-1} and 671cm^{-1}. They indicate the bending mode of O-Si-O and Si-O-Si, respectively.

The C-H stretching mode in CH_2 groups associated to the presence of PEG in samples can be distinguished very clearly for samples modified with PEG MW 1500g/mol and PEG MW 4000g/mol at 2900cm^{-1}. In the case of xonotlite modified with PEG MW 600g/mol this contribution appears as a very weak shoulder.

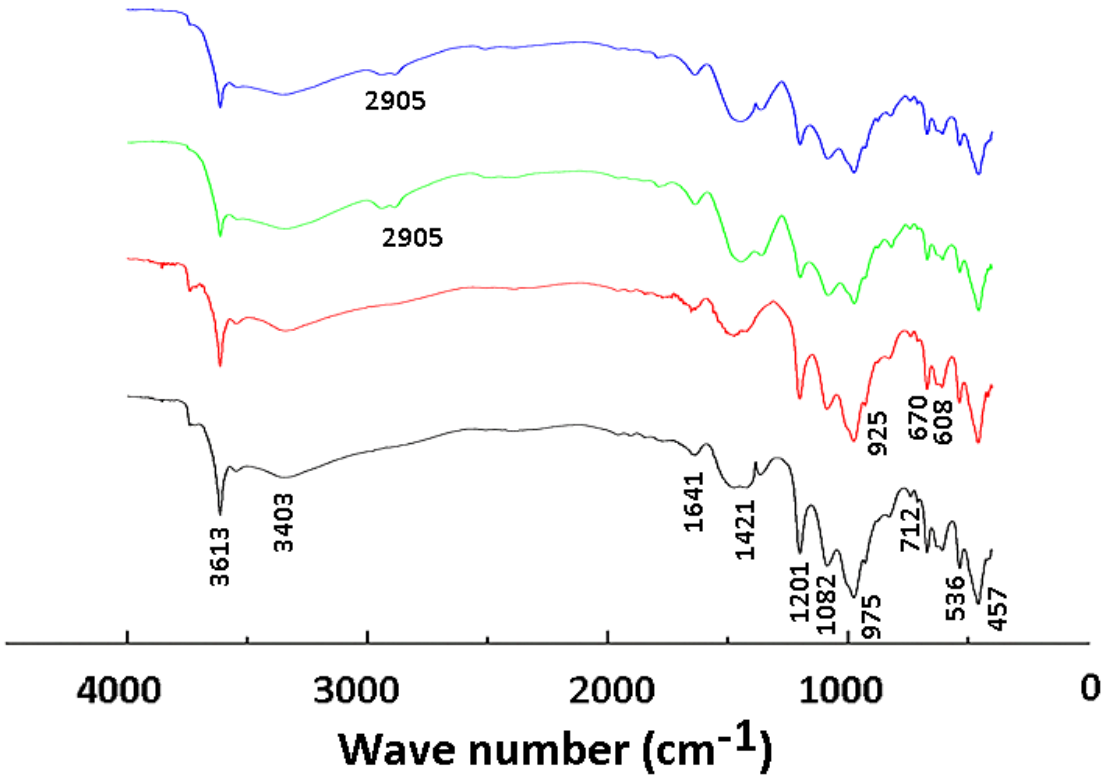

Figure V.5: FT-IR spectra of pristine and modified xonotlite samples obtained at 325°C, 235 bar and a residence time of 27seconds. Pristine xonotlite particles (black curve), and xonotlite particles prepared in the presence of PEG MW 600 (red curve), PEG MW 1500 (green curve) and PEG MW 4000 (blue curve).

^{29}Si ss-NMR was carried out to complement the results obtained by XRD and FT-IR of samples prepared in continuous reactor (Figure V.6). In general, each sample showed the three signals associated to xonotlite structure. Q^2 (-87ppm) and Q^3 (-98ppm) are the most intense signals observed in spectra, then a small Q^1 signal at -81ppm can be measure associated to silicate tetrahedra of the ending of the silicate chains. This contribution is also associated to the presence of defects or vacancies in Q^3 position along the silicate chains.

Unlike samples prepared in batch reactor at 250°C, pristine xonotlite and xonotlite precipitated in the presence of PEG MW 1500 showed an extra contribution at -110ppm associated to silicate tetrahedra in Q^4 position. That means that there are silicates bonded to 4 other silicate tetrahedra through oxygen bonds. This only can be possible if some silicate has reacted and precipitated as amorphous silica.

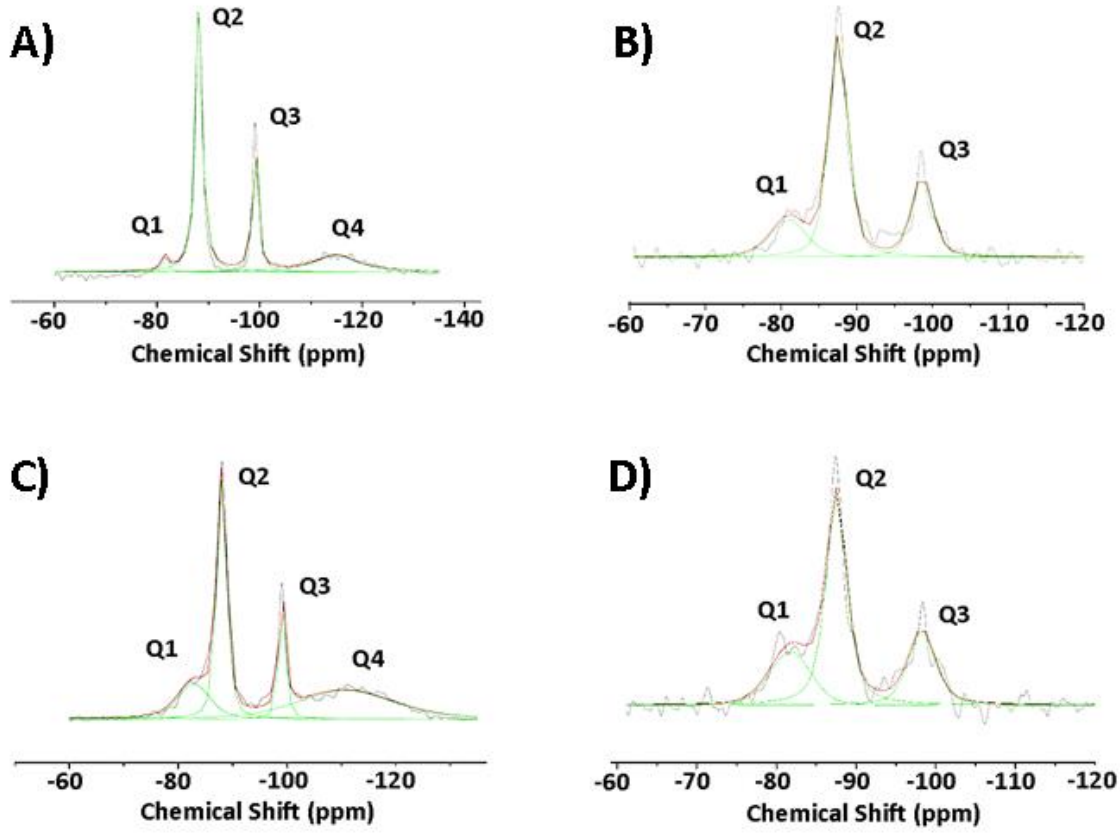

Figure V.6: ^{29}Si ss-NMR spectra of xonotlite samples obtained at 325°C, 235bars and a residence time equal to 27 seconds. Pristine particles (A), and particles prepared in the presence of PEG MW 600 (B), PEG MW 1500 (C) and PEG MW 4000 (D).

First it was thought that residence time was not long enough to react the silicon precursor totally with calcium precursor but other syntheses like xonotlite with PEG MW 600 and PEG MW 4000 did not show Q^4 contributions in their ^{29}Si ss-NMR spectra. Although FT-IR confirmed the presence of carbonate groups that could form calcite, no contributions associated to calcium oxide or calcite crystalline phases were measured in XRD spectra to confirm the presence of non-reacted calcium as byproduct. Then there must be another reason to explain the appearance of amorphous silica as a byproduct in the reaction.

A hypothesis proposed in this study is that some experiments had a deficit of calcium solution due to a flow rate diminution in calcium source HPLC pump. This deficit may have caused a total reaction of calcium as part of xonotlite product and the excess of silicon precursor precipitated as amorphous silica. Other plausible explanation could be

a partial carbonation effect of xonotlite particles in air that could displace the calcium from the structure and make Q^4 contributions appear in ^{29}Si NMR spectra [8].

It was also calculated the population of Q^3 silicate tetrahedra and MCL (following equation 14) from deconvoluted areas of the signals measured by ^{29}Si NMR. Table V.2 shows the values for the different samples prepared in the continuous reactor and compares them to the analog samples obtained in the batch reactor. As it can be observed in the table the MCL values for samples obtained with the continuous setup are lower than the MCL values for samples prepared in batch at lower temperature.

Table V.2: Q^3 population and MCL values for xonotlite samples prepared at 325°C and 235bars in continuous reactor. Comparison with samples prepared at 250°C and 38 bars.

SAMPLE	$Q^3/(Q^1+Q^2+Q^3)$ Continuous	MCL Continuous	$Q^3/(Q^1+Q^2+Q^3)$ Batch	MCL Batch
X_Pristine	0.259	19.39	0.307	40.81
X_P600	0.225	10.03	0.297	28.18
X_P1500	0.211	8.45	0.288	22.72
X_P4000	0.238	8.03	0.218	20.40

^1H NMR was carried out for xonotlite synthesized at 325°C and 235bars in the presence of different polyethylene glycols (Figure V.7). In every sample there is a signal at 4.6ppm which can be associated to molecular water. This contribution tends to increase in samples of PEG modified xonotlites. Moreover, two contributions at 1.73ppm and 2.04ppm are observed which can be associated to protons of silanol and Ca-OH groups, respectively, as it was seen in previous samples of xonotlite obtained in batch reactor. Furthermore, there is a small contribution associated to the presence of isolated silanol groups around 1ppm.

In the case of pristine xonotlite, no signal of the proton of the silanol group can be observed in the spectrum. This could mean that the population of silanol groups is not high enough to be measured by ^1H NMR. This result agrees with the spectrum obtained by ^{29}Si NMR where the Q^1 signal was also quite small. Finally, samples modified with polyethylene glycol showed one more contribution around 3.6ppm that is associated to

protons of the -CH_2- groups present in the polymer chain as it was mentioned in previous chapter.

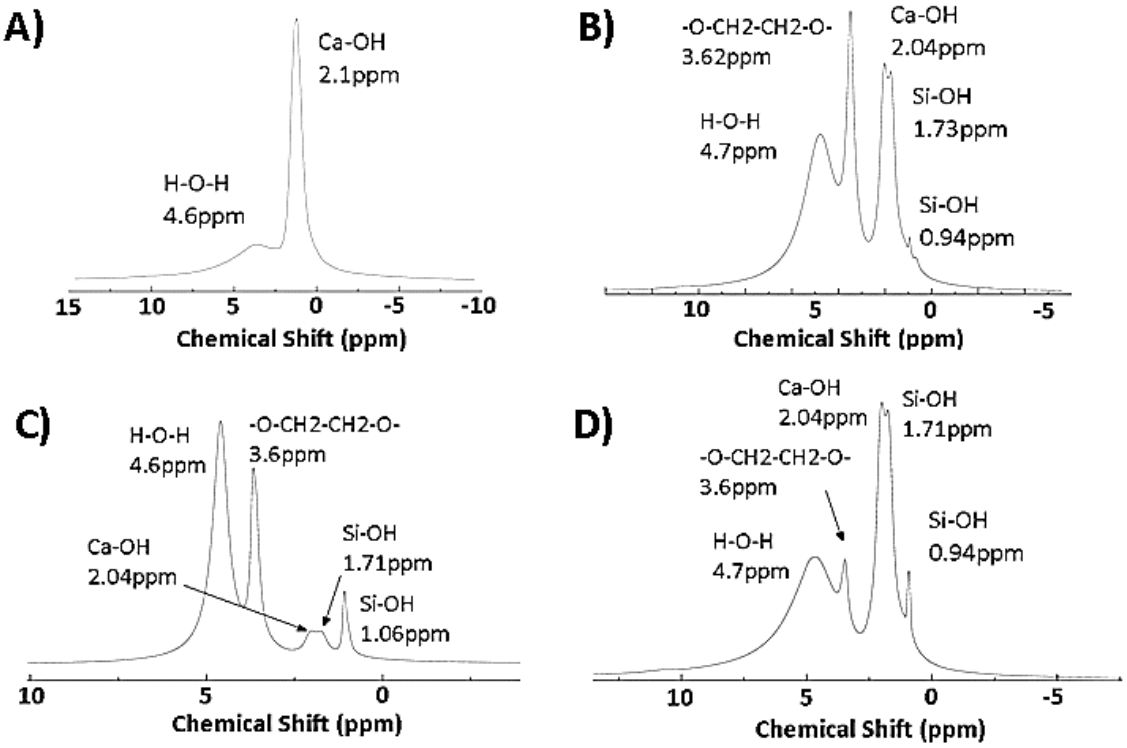

Figure V.7: ^{1}H ss-NMR spectra of pristine and modified xonotlite synthesized at 325°C, 235bars and a residence time of 27 seconds. Pristine xonotlite particles (A), and xonotlite particles prepared in the presence of PEG MW 600 (B), PEG MW 1500 (C) and PEG MW 4000 (C).

Elemental analysis was carried out by EDS technique. In Table V.3, the Ca/Si ratio obtained from elemental analysis is shown. Pristine xonotlite and xonotlite prepared in the presence of PEG show a Ca/Si molar ratio near to 1.0. There are no significant differences between samples with and without PEG but samples with PEG MW1500g/mol and PEG MW4000g/mol present a slightly lower value than 1.0.

Table V.3: Ca/Si molar ratio for xonotlite samples prepared in the continuous reactor.

Samples	Ca/Si
X_Pristine	1.02
X_P600	1.03
X_P1500	0.99
X_P4000	0.98

TEM images taken for pristine and modified xonotlite (Figure V.8) prepared in continuous reactor showed fibrillar shaped particles with heterogeneous size distribution. No significant influence of the presence of PEGs was observed on particle morphology. No other morphologies of amorphous structures were observed, although this does not explain the results of ^{29}Si NMR regarding the presence of Q^4 signals.

Length and width distributions were obtained measuring the dimensions of 150 particles of the pristine and modified xonotlite particles. This task was carried out using Image J software. The results plotted in Figure V.9 show a mean length around 500nm and a mean width of 30nm or 40nm for samples obtained in continuous reactor. As it was expected for samples prepared in the continuous reactor, these values are much lower than the ones obtained for samples prepared in batch reactor (mean length about 1.5µm and mean width around 50nm- 60nm). Moreover, the size distribution of the samples synthesized in the continuous reactor are narrower as well.

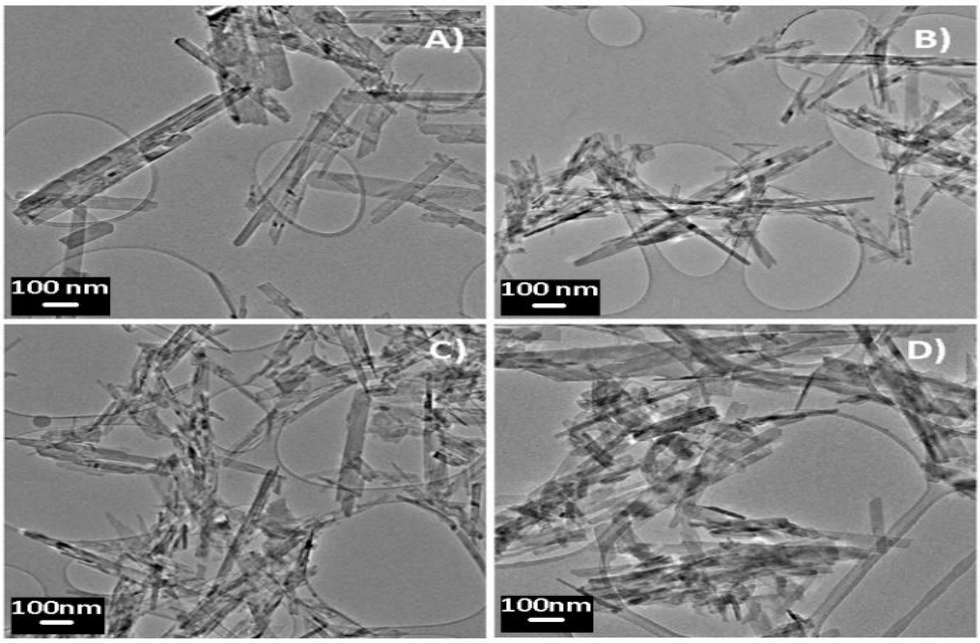

Figure V.8: TEM images of different samples of xonotlite obtained in continuous reactor at 325°C, 235bars and a residence time of 27 seconds. Pristine particles (A), particles prepared with PEG MW 600g/mol (B), PEG MW 1500g/mol (C) and PEG MW 4000g/mol (D).

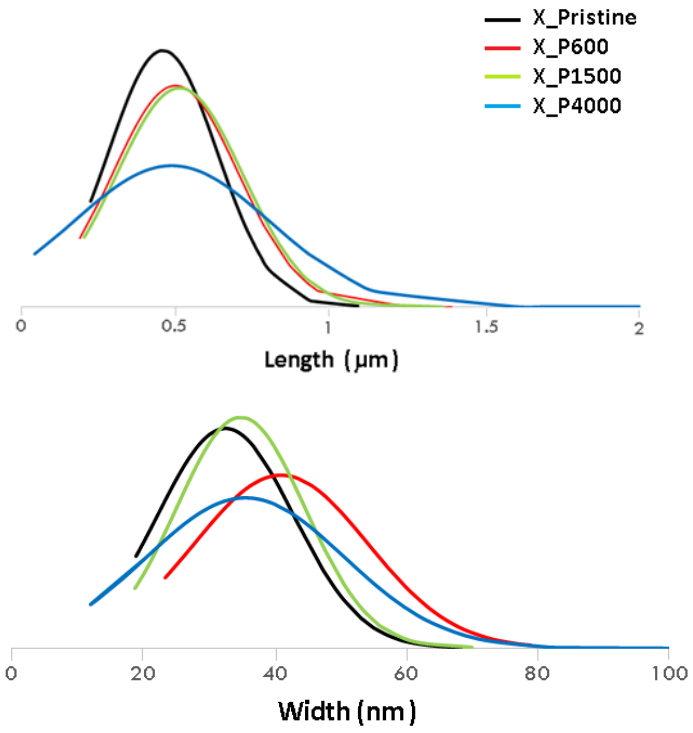

Figure V.9: Length and width distributions of the different xonotlite particles prepared in continuous reactor at 325°C, 235bars and a residence time of 27 seconds. Pristine xonotlite particles (X_Pristine), and xonotlite particles modified with PEG MW 600g/mol (X_P600), PEG MW 1500g/mol (X_P1500) and PEG MW 4000g/mol (X_P4000).

Magnified images were also taken for these samples by High Resolution TEM. The obtained images allowed measuring the lattice distance of crystallographic planes that grow along fiber's length. As it was done in the previous chapter for xonotlite samples obtained in batch reactor, this distance was compared to the value for crystalline xonotlite (0.86nnm).

Table V.4 shows the values of this distance for unmodified and modified samples. On one hand, the lattice distance for pristine xonotlite is near to the expected value. In the case of xonotlite samples modified with PEG polymers this value tends to increase slightly. This increase is not significant but could indicate a kind of broadening of the distance between calcium oxide layers due to the presence of polymer during the precipitation of xonotlite.

Table V.4: Mean lattice distance obtained from high magnification images (HR-TEM).

Sample	Mean Lattice Distance (nm).
X_Pristine	0.862
X_P600	0.878
X_P1500	0.887
X_P4000	0.880

This chapter has demonstrated that is possible to obtain xonotlite samples modified with PEG polymers under near supercritical conditions. Higher temperatures than 325˚C present carbonation problems associated to the fast degradation of the polymer. However, ^{29}Si NMR results concluded that X_pristine and X_1500 products obtained have some traces of silica as byproduct due to the presence of Q^4 in every spectrum. Elemental analysis did not show different values of Ca/Si molar ratio respect to the ideal

value of 1.0. Moreover, TEM images showed the typica fibrillar shaped particles obtained previously in the batch reactor.

V.3. Pristine tobermorite synthesized under supercritical conditions.

Same synthesis conditions employed for xonotlite (325°C, 9.9mL/min for each pump and 235bars) were used to synthesize tobermorite. In this case, only the ratio of Ca/Si was changed, and a percentage of aluminum was added. The concentration of silicon precursor ($Na_2SiO_3 \cdot 9H_2O$) was fixed to 0.01M and the concentration of aluminum ($Al(NO_3)_3 \cdot 9H_2O$) and calcium ($Ca(NO_3)_2 \cdot 4H_2O$) guaranteed an Al/(Si+Al) ratio equal to 0.15 and a Ca/(Si+Al) equal to 0.83. Silicon and aluminum precursors were dissolved in the same solution and added through the same pump. Furthermore, the experiments carried out with polyethylene glycol maintained a Ca/PEG molar ratio equal to 1.5.

However, as it can be observed in Figure V.10, the XRD pattern of tobermorite synthesized at 325°C showed a non-crystalline spectrum. Even if the basal peak associated to the plane (002) is very intense the rest of the characteristic peaks associated to tobermorite phase are too weak or they do not appear at all, showing that an amorphous product has been obtained.

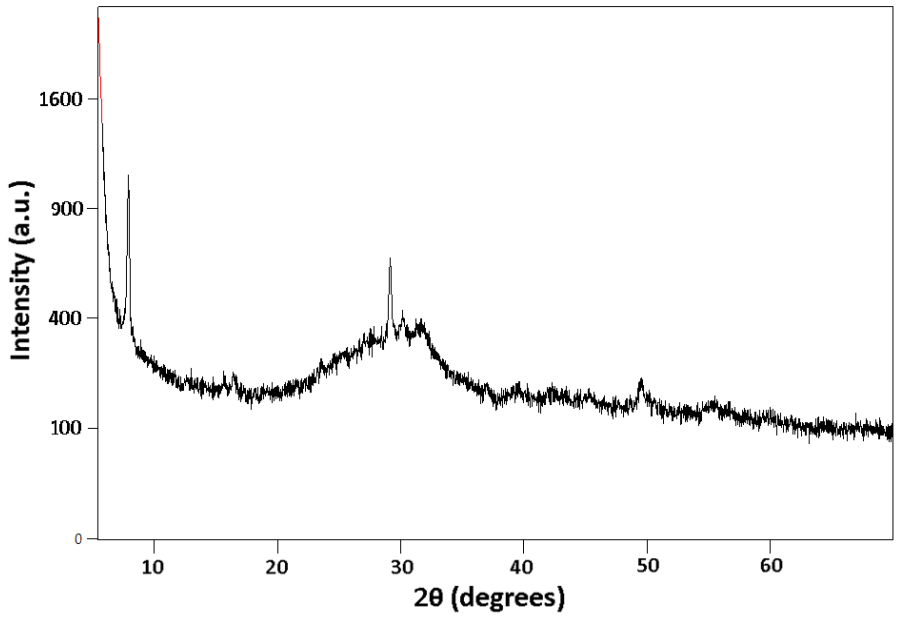

Figure V.10: XRD pattern of sample obtained at 325°C, 235bars and 27 seconds.

It was concluded that the only plausible way to obtain tobermorite in the continuous setup is under supercritical conditions as it was reported in previous studies [2, 9]. However, at 400°C fast degradation of PEG polymer was observed for xonotlite samples. Taking this into account it was decided to divide the reaction into a two-step process. In the first step, the synthesis of tobermorite would be carried out at supercritical conditions (400ºC and 235bar) and in a second step when the temperature of the reaction solution was lower the PEG polymer would be introduced in the system so it could react with the tobermorite synthesized in the first step. In order to carry out the synthesis in two-steps the setup of the reactor was modified (see chapter two, figure II.9). The main goal of this new design was to obtain crystalline tobermorite by the use of supercritical conditions of water but prevent the PEG degradation by introducing it when the temperature of the reaction solution decreased. Tobermorite would crystallize in a first step at 400°C and after it would be quenched below 350°C and mixed with the polymer during a second step.

First, different residence times were tested to guarantee the highest possible crystallinity of tobermorite. Residence times of 4 seconds (7mL/min per pump), 4.3 seconds (6.5mL/min per pump), 5.1 seconds (5.5mL/min per pump) and 6.3 seconds (4.5mL/min per pump) were examined. Figure V.11 shows the XRD results of pristine tobermorite samples prepared in this two-step setup. Samples prepared with a residence time of 6.3 seconds showed the presence of xonotlite as byproduct in the reaction. It is very probable that tobermorite synthesis reaction was still occurring in the second step and increasing the residence time respecting to the theoretical value.

On the other hand, a residence time of 4 seconds gave an XRD diffractogram of an amorphous product. The best results were obtained with samples prepared with residence time equal to 4.3 seconds and 5.1 seconds. The difference between both experiments were minimal, so the samples prepared with the lowest residence time (4.3 seconds) was chosen as the optimum.

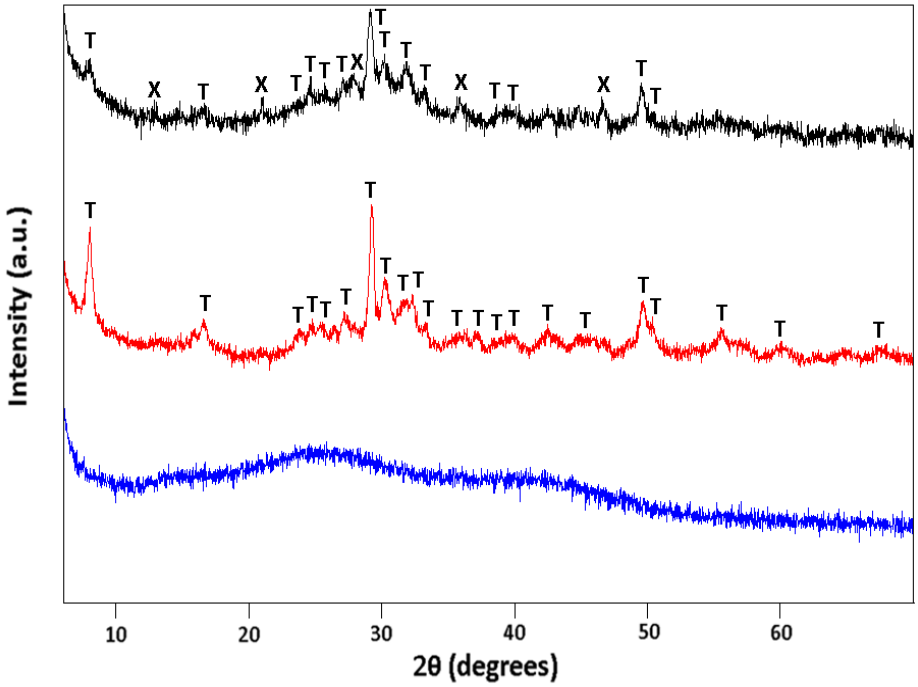

Figure V.11: XRD patterns of pristine tobermorite synthesized at different residence times: 4 seconds (blue curve), 4.3 seconds (red curve) and 6.3 seconds (black curve).

V.4. Tobermorite modified with polyethylene glycol synthesized under supercritical conditions.

Using the two-step reactor, the synthesis of tobermorite with PEG4000 was carried out. A temperature of 400°C, 235bar of pressure and a residence time of 4.3 seconds was employed to obtain tobermorite modified with polyethylene glycol MW 4000. Figure V.12 shows the XRD diffractograms of both pristine tobermorite and tobermorite with PEG MW4000. No significant changes were observed between the diffractions of both samples except for an intensity reduction in the case of T_P4000. No peaks associated

to PEG were detected. Furthermore, no shift in XRD diffractions were measured for T_P4000 in respect to the pristine product.

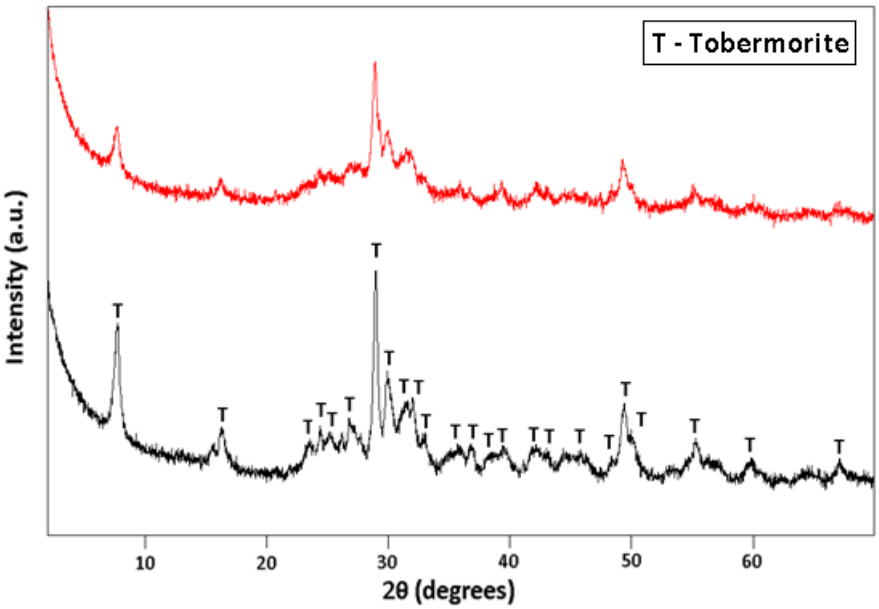

Figure V.12: XRD patterns of pristine tobermorite (black curve) and tobermorite modified with PEG MW 4000 (red curve). Samples prepared at 400°C, 235bar and a residence time equal to 4.3 seconds.

Infrared spectroscopy of pristine tobermorite and tobermorite with PEG MW4000 were also carried out. Both spectra are compared in Figure V.13. As it can be seen in that figure, FTIR of samples modified with PEG showed the characteristic peak of C-H stretching vibrational mode around 2900cm^{-1}.

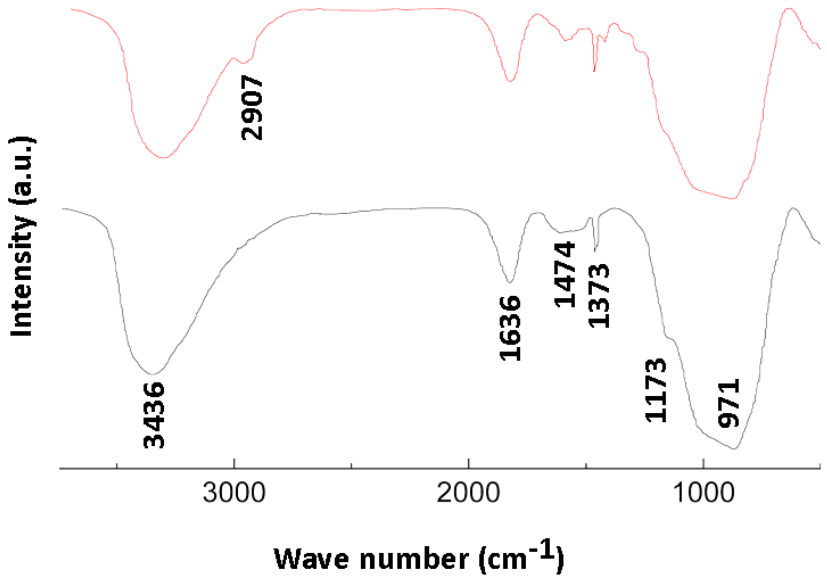

Figure V.13: FT-IR spectra of pristine tobermorite (black curve) and tobermorite modified with PEG MW 4000 (red curve). Samples prepared at 400°C, 235bas and a residence time equals to 4.3 seconds.

Figure V.14 shows the deconvoluted curves obtained from ^{29}Si ss-NMR. Modified and pristine tobermorite showed the same characteristic contributions at Q^1, Q^2, Q^3, Q^2(1Al) and Q^3(1Al).

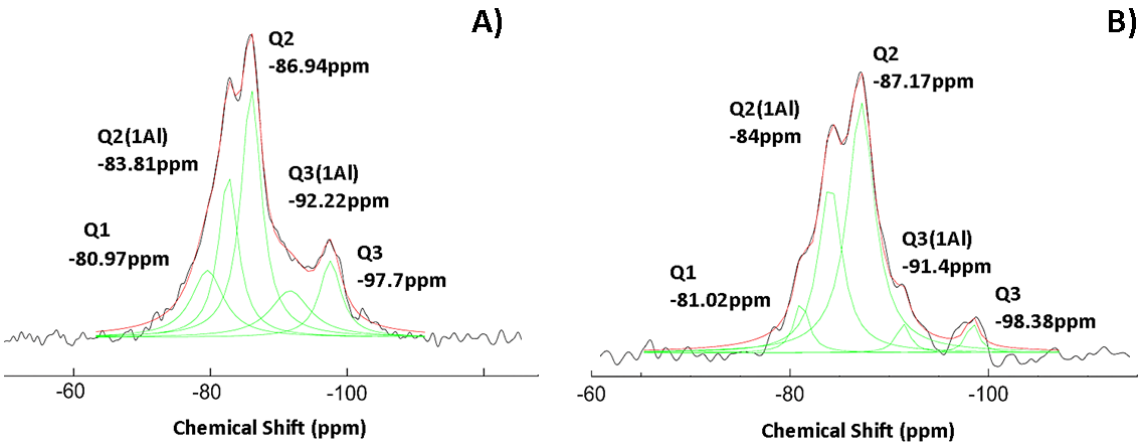

Figure V.14: ^{29}Si ss-NMR spectra of pristine tobermorite and tobermorite modified with PEG MW 4000. Samples prepared at 400°C, 235bar and a residence time equal to 4.3 seconds.

However, in the case of tobermorite modified with PEG MW4000 a significant reduction of Q^3 contribution can be observed. The reduction of Q^3 contribution is related to the

decrease of the signal observed by FT-IR at 1373cm^{-1}. Table V.5 shows this influence of PEG in population of Q^3 signal calculated from deconvoluted areas of the ^{29}Si NMR spectra. This table also compares the Q^3 population for pristine tobermorite and tobermorite with PEG MW4000 prepared in subcritical batch reactor.

As it can be observed in Table V.5, there is no influence of PEG in Q^3 population for samples prepared in batch reactor, however, in samples prepared in continuous setup under supercritical conditions the amount of branching silicate tetrahedra decreases significantly in the presence of polymer (around 8%).

Table V.5: Population of Q^3 signals in ^{29}Si NMR spectra of samples prepared in batch and in continuous reactor.

SAMPLE	Q3/(Q1+Q2+Q3+Q2(1Al)+Q3(1Al)) Continuous reactor	Q3/(Q1+Q2+Q3+Q2(1Al)+Q3(1Al)) Batch reactor
T_Pristine	0.124	0.111
T_P4000	0.040	0.114

Elemental analysis obtained with EDS technique gave the Ca, Si and Al molar percentages which were used to calculate the Ca/(Si+Al) and Al/(Si+Al) ratios for the samples obtained in the continuous reactor (Table IV.6). Values of Ca/(Si+Al) for pristine tobermorite (T_Pristine) as well as tobermorite with PEG MW4000 (T_P4000) are lower than 0.83. So, this indicates that the tobermorite obtained is poorly crystalline as well. Moreover, in both cases the aluminum content is higher than 15%. Nonetheless, tobermorite with PEG MW 4000 shows values nearer to the expected molar ratios.

Table V.6: Molar ratios obtained from elemental analysis for both tobermorite samples obtained in continuous reactor.

Samples	Ca/(Si+Al)	Al/(Si+Al)
T_Pristine	0.671	0.188
T_P4000	0.732	0.172

Pristine tobermorite and T_P4000 were analyzed by transmission electron microscopy (LR-TEM and HR-TEM) as well (Figure V.15). In the images obtained, different morphologies were observed. On one hand fibrillar samples as the ones reported in literature [2, 10, 11] were obtained. Moreover, amorphous structures that could be associated to impurities were also observed. At first, it was thought that these structures were amorphous silica but not presence of Q^4 signals were detected by ^{29}Si NMR technique. No significant differences in morphology were observed between pristine tobermorite and tobermorite prepared with PEG MW4000.

HR-TEM measurement caused the degradation of structure due to the intensity of the focused electron beam. So, it was difficult to measure the lattice distance associated to the basal peak in magnified images. Nevertheless, some images were taken to obtain the lattice distance which are showed in Table V.7. Obtained values were a bit lower than the theoretical value (1.15nm) for 11Å tobermorite.

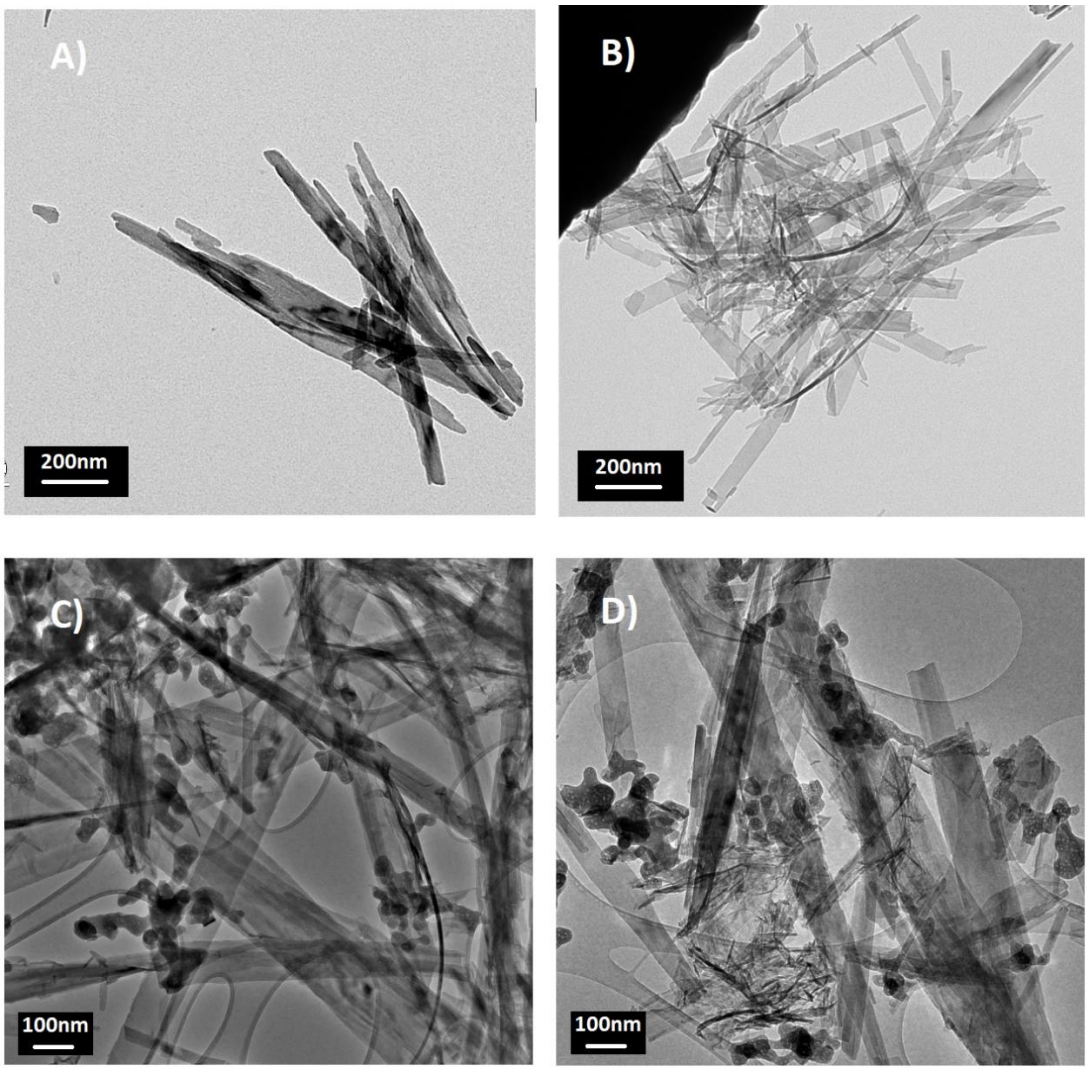

Figure V.15: TEM images taken of pristine tobermorite (A y C) and modified with PEG MW 4000 (B y D) prepared at 400°C, 235bars and a residence time of 4.3 seconds.

Table V.7: Lattice distance calculated from high magnification images taken by HR-TEM

Sample	Mean lattice distance (nm).
T_Pristine	1.088
T_P4000	1.113

In conclusion, tobermorite samples modified with PEG in continuous reactor was the more difficult experiment to carry out. Experiments at 400˚C degradade the polymer instantly and experiments at lower temperature did not produced crystalline enough

products. Expperiments carried out in two steps reactor gave more crystalline samples but silica byproducts were obtained as well. Elemental analysis gave information about some defects or vacancies in the structure when polymer is added in the second step. Then a deeper study should be carried out to optimize the residence time and increase the crystallinity of this kind of samples prepared in continuous setup.

V.5. Xonotlite and tobermorite samples obtained in continuous reactor. Rheological, mechanical and acceleration effect on cement paste.

TGA/DSC analysis was carried out as it was done for samples prepared in batch reactor. The main goal was to characterize the organic content to be able to adjust the dosage of inorganic particles in cement mixes. Thus, it is possible to fix the same dosage of additive for every sample no matter the quantity of PEG attached to the solid.

Tables V.8 and V.9 show the quantity of PEG calculated from TGA curves. As it can be seen these quantities are much lower than the values obtained for xonotlite and tobermorite samples in batch subcritical reactor. This could be due to the partial washing of PEG in retained powder when precursor solutions flow through the filter. Therefore, the total amount of retained PEG and the yield of remaining PEG respect to the initially added polymer is lower than in the case of the batch products. This also indicates that the interaction of the PEG with xonotlite and tobermorite is weak.

Table V.8: Polyethylene glycol content obtained from thermogravimetric analysis. Xonotlite samples prepared at 325°C, 235bar and 27 seconds of residence time.

Sample	PEG content (%)
X_Pristine	-
X_P600	3.2
X_P1500	11.8
X_P4000	15.9

Table V.9: Polyethylene glycol content obtained from thermogravimetric analysis. Tobermorite samples prepared at 400°C, 235bar and 4.3 seconds of residence time.

Sample	PEG content (%)
T_Pristine	-
T_P4000	7.4

Cement pastes with 1%w/w of these xonotlite and tobermorite particles obtained from continuous reactor as additions, and a water cement ratio of 0.4 were prepared to test their rheological behavior. Results plotted in Figure V.16 showed an increase of viscosity due to the addition of pristine xonotlite in cement matrix respect to cement reference without additions.

On the other hand, a decrease of viscosity respect to the reference paste is observed when samples modified with PEG are added. This means that the presence of PEG in samples prepared in continuous reactor, improved the rheological behavior of cement pastes with xonotlite additions. Moreover, viscosity values decreased even below the reference paste without additions, therefore these additions improved the intrinsic workability of OPC cement without using an external superplasticizer additive. In this case no significant differences were observed between the different PEG modified xonotlite samples.

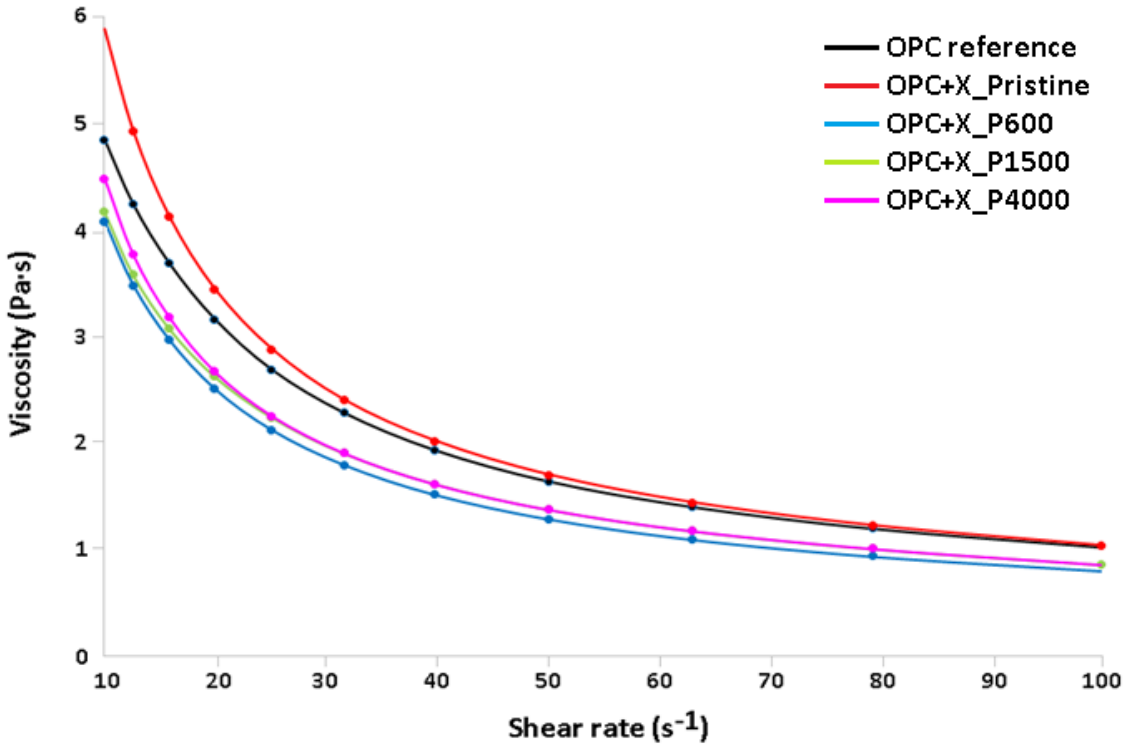

Figure V.16: Viscosity versus shear rate curve of cement paste with xonotlite samples obtained in continuous reactor. OPC cement paste reference (OPC reference), OPC with pristine xonotlite (OPC + X_Pristine), OPC with xonotlite modified with PEG MW 600 (OPC+X_P600), PEG MW 1500 (OPC+X_P1500) and PEG MW 4000(OPC+X_P4000).

Isothermal calorimetry was carried out to analyze the accelerating effect that the synthesized xonotlite samples have in cement hydration. Results in Figure V.17 showed almost no differences between pastes with and without additions.

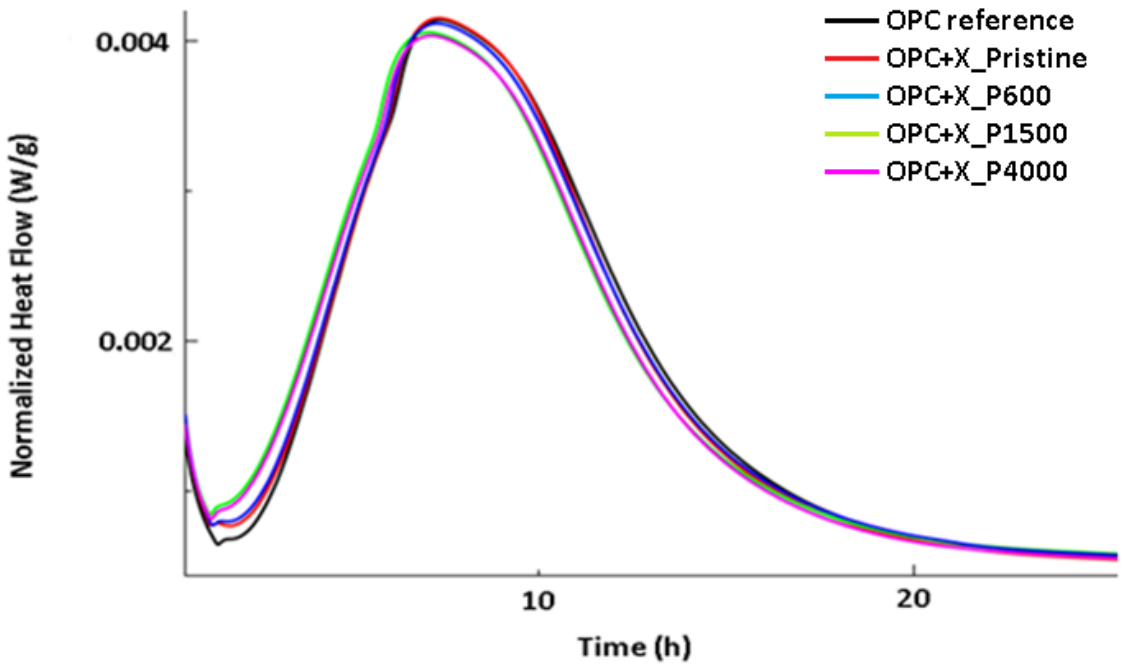

Figure V.17: Isothermal calorimetry of cement paste with xonotlite samples as additions obtained in continuous reactor. OPC cement paste reference (black curve), OPC with pristine xonotlite (red curve), OPC with xonotlite modified with PEG MW 600 (green curve), PEG MW 1500 (blue curve) and PEG MW 4000(pink curve).

Flexural and compressive tests of the cement specimens with the xonotlite sample additions were carried out after 8h and 24h of curing time (Figure V.18). After 8h it was observed that xonotlite with PEG MW600 and xonotlite with PEG MW4000 gave a slightly higher compressive resistance respect to the reference specimen. Nevertheless, no significant changes in compressive strength were observed after 8h of curing.

After 24h of curing time compressive strength are similar for every addition. In general, all xonotlite samples added to cement, increased compressive strength after 24h but this increase is lower depending on the PEG polymer of the modified xonotlite. PEG with higher molecular weight has a slightly more negative effect on compressive strength as it was observed for xonotlite samples prepared in subcritical batch reactor. No significant improvement was observed in flexural strength of cured pastes with pristine and modified xonotlite additions.

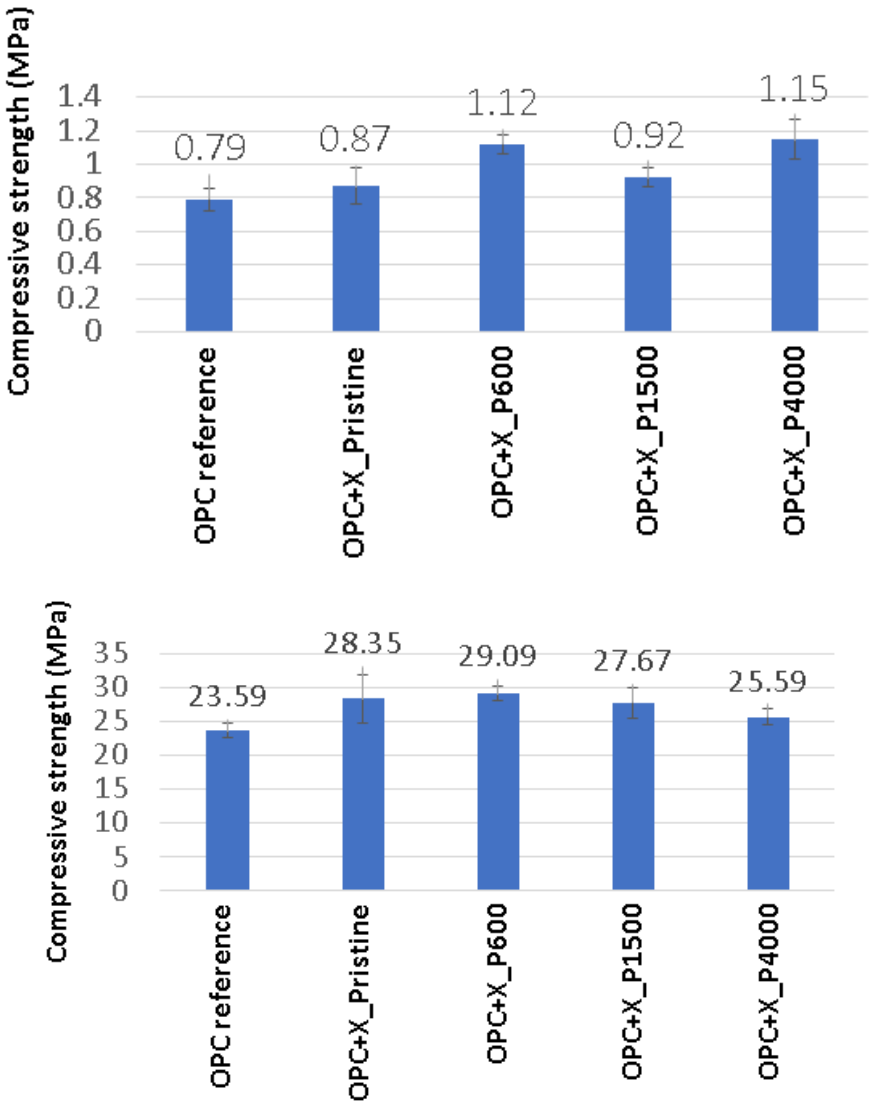

Figure V.18: Compressive strength of cement pastes with prepared xonotlite particles in continuous reactor. Samples tested after 8h (above) and 24h (below) of curing time.

Figure V.19 shows the viscosity measurement of cement pastes with tobermorite and tobermorite PEG MW 4000 as additions. On one hand cement paste with pristine tobermorite showed a viscosity increase as it was expected. On other hand, tobermorite modified with PEG MW 4000 significantly reduced the viscosity of the paste and it even gave a lower viscosity than the reference paste. This result is similar to the results obtained with the pastes that contain the different tobermorite samples synthesized in batch reactor. However, the T_P4000 sample obtained in continuous reactor showed a significant reduction of viscosity using a lower content of PEG in its composition than in the case of T_P4000 obtained in batch reactor.

Moreover, the addition of pristine tobermorite and T_P4000 synthesized in continuous reactor added to the cement paste accelerated the hydration as it can be seen in Figure V.20. The acceleration effect of tobermorite and tobermorite with PEG was very similar and PEG MW4000 had a negligible deceleration effect.

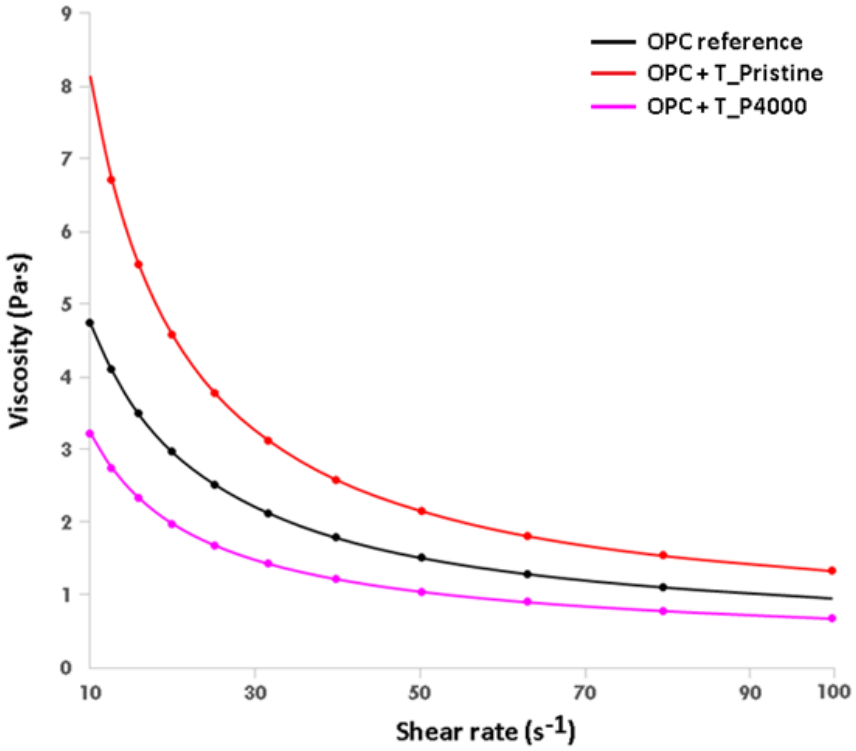

Figure IV.19: Viscosity versus shear rate curve of tobermorite samples obtained in continuous reactor. OPC cement paste reference (black curve), OPC with pristine tobermorite (red curve) and PEG MW 4000(pink curve).

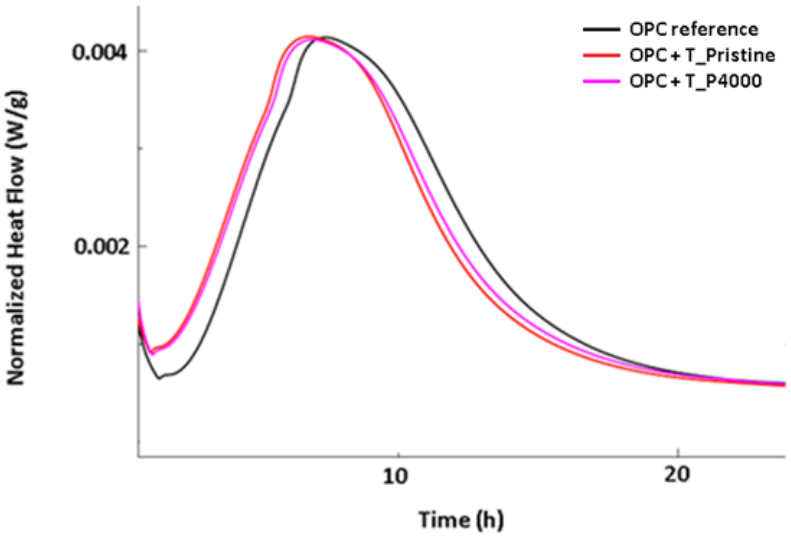

Figure V.20: Isothermal calorimetry of cement paste with tobermorite samples obtained in continuous reactor. OPC cement paste reference (black curve), OPC with pristine xonotlite (red curve) and PEG MW 4000(pink curve).

Compressive tests gave the same tendency after 8h and after 24h of curing time (Figure V.21). Pristine tobermorite and tobermorite with PEG MW 4000 showed a higher compressive strength compared to the reference paste. Nevertheless, the compressive strength was higher for specimens with pristine tobermorite than modified one as it was also observed for samples prepared in the subcritical batch reactor.

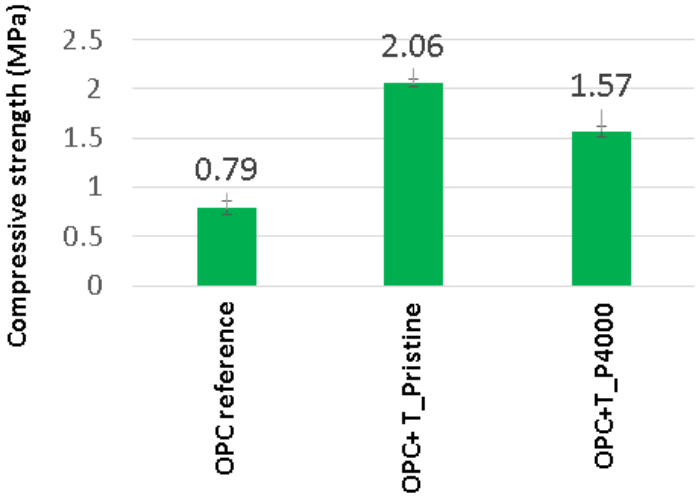

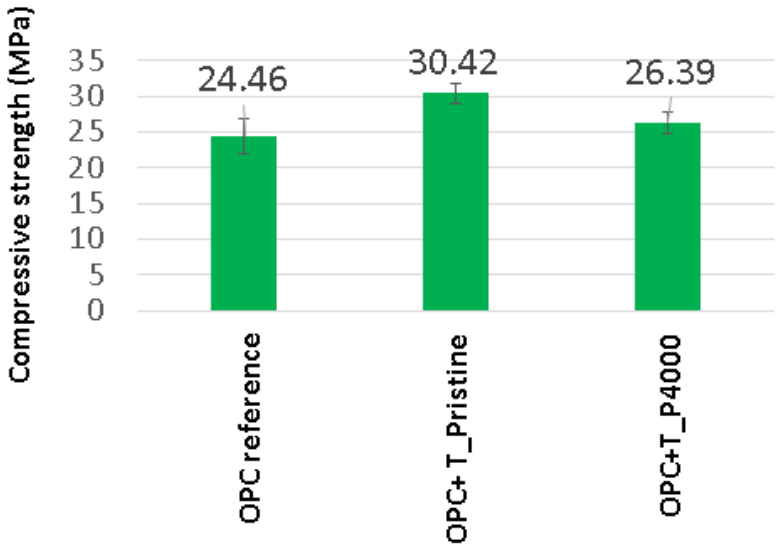

Figure V.21: Compressive strength of cement pastes with additions of synthesized tobermorite particles in continuous reactor. Samples tested after 8 hours (above) and 24 hours (below) of curing time.

In conclusion, advantages were found adding samples (xonotlite and tobermorite) prepared with PEG in continuous reactor to cement pastes. Although xonotlite additions did not significantly accelerate the cement hydration, samples modified with PEG improved the workability of the mixtures. On the other hand, tobermorite with PEG MW4000 demonstrated significant reduction of paste viscosity and showed an acceleration effect similar to additions of pristine tobermorite. These results could be a first step on designing new admixtures capable to accelerate the cement hydration without worsening its workability. Moreover, the high reduction of viscosity below the reference paste could indicate that these particles could be used as water reducers and accelerating admixtures at the same time.

V.6. References.

[1] E. John, J. D. Epping, D. Stephan, *Constr. Build. Mater., 228* (**2019**) 116723.

[2] M. Diez-Garcia, J. J. Gaitero, J. S.Dolado, C. Aymonier*, Angew. Chem.* (**2017**), 129, pp. 1–6.

[3] H. Wu, J. Yang, H. W. Ma, *Integr. Ferroelect. Int. J., 146:1,* (**2013**), pp. 144-153.

[4] X. Li and J. Chang, *Chem. Lett., 33, 11* (**2004**).

[5] K. Lin, J. Chang, G. Chen, M. Ruan, C. Ning, *J. Crystal Growth 300,2,* (**2007**) pp. 267–271.

[6] K. Luke and H. F. W. Taylor, *Cem. Concr. Res. Vol. II*, (**1981**), pp. 197-203.

[7] K. Luke and H. F. W. Taylor, *Cem. Concr. Res., Vol. 14*, (**1984**), pp. 657-662.

[8] T. F. Sevelsted and J. Skibsted. *Cem. Concr. Res.* 71 (**2015**) pp. 56–65.

[9] V. Musumeci, G. Goracci, P. Sanz Camacho, J. S. Dolado, C. Aymonier, *Chem. Eur. J., 27, 44*, (**2021**) pp. 11309-11318.

[10] N. S. Bell, S. Venigalla, P. M. Gill, J. H. Adair, *J. Am. Ceram. Soc., 79,* (**1996**) pp. 2175-2178.

[11] M. Monasterio, J. J. Gaitero, H. Manzano, J. S. Dolado, *Langmuir, 31,* (**2015**) pp. 4964-4972.

CHAPTER VI: GENERAL CONCLUSIONS.

This doctoral thesis focused on synthesizing and characterizing functionalized particles of crystalline xonotlite and tobermorite phases. This work tested the use of hydrothermal routes to obtain these phases in batch and continuous reactors, working at subcritical hydrothermal conditions and near supercritical hydrothermal conditions. Moreover, two different strategies were studied to guarantee a good dispersibility of these particles in cement suspensions. On one hand, these particles were obtained in presence of polyethylene glycol. This polymer was physiosorbed on particles surface to avoid the aggregation by steric hindrance. On the other hand, a first approach of covalent functionalization of xonotlite and tobermorite with zwitterionic molecules was studied. The idea of using sulfobetaine siloxane was to achieve particle dispersion by electro repulsive forces.

It is possible to obtain crystalline phases of calcium silicate hydrates, xonotlite and tobermorite, in the presence of polyethylene glycol polymers via subcritical hydrothermal route. No other byproducts were detected by XRD except traces of calcite from carbonation effect of calcium silicate hydrate phases. It is not clear if these traces are due to the presence of PEG or not. After washing and drying, it was demonstrated the presence of organic compounds (PEG) retained in xonotlite and tobermorite. The amount of PEG retained in xonotlite samples was higher than in tobermorite samples. Nevertheless, results of XRD and XPS suggested that the polymer interaction with the inorganic product is weak and is located on the surface.

According to the shift in Ca2p signals measured by XPS for xonotlite samples with PEG, it can be concluded that PEG polymer chains could be interacting with calcium species in the structure of xonotlite. However, this effect was not that significant in tobermorite samples prepared with polymer.

Following the ^{29}Si NMR and the calculated values of MCL (Mean Chain Length), a shortening effect of silicate chains is observed for xonotlite modified samples due to the presence of PEG during its synthesis. The higher the molecular weight of the PEG the shorter the silicate chain. There is not a direct correlation between coordination of calcium with PEG and the shortening effect in double silicate chains. However, it was

observed that PEG with higher molecular weight (PEG MW4000) present the shorter MCL values compared to other PEG with lower molecular weight (PEG MW600 and PEG MW1500). This shortening effect is manifested in the presence of silanol groups according to ^{1}H NMR. Moreover, the presence of PEG has an effect in how aluminum is introduced in double silicate chains for aluminum substituted tobermorite. This could be the cause of the changes observed in the stability of 11Å-tobermorite treated at 300°C for 24 hours (anomalous behavior).

Additions of xonotlite and tobermorite samples with PEG (1% wbc) obtained in batch reactor in cement paste increase the workability of the pastes respect to pastes with pristine particle additions.

The PEG from samples has a negative effect on cement hydration rate. However, this effect is lower than the acceleration effect caused by seed particles. Therefore, modified particles still work as seeds accelerating the hydration reaction. This acceleration increases the compressive strength values at early ages as well.

On the other hand, the synthesis of crystalline xonotlite and tobermorite particles in the presence of PEG at the supercritical conditions of water cannot be carried out without the partial degradation of PEG and carbonation of the inorganic compound.

The maximum temperature condition to eliminate the degradation of PEG and carbonation of xonotlite in continuous reactor was 325°C. This temperature condition is not enough to produce tobermorite crystals in continuous setup.

Analyzing the calculated MCL values from deconvoluted areas in ^{29}Si NMR, it was observed the same shortening effect in double silicate chains for xonotlite prepared with PEGs in continuous reactor. This tendency is also observed in the xonotlite compounds obtained in batch reactor, although the MCL values are longer in the case of compounds obtained in batch. Results from ^{29}Si NMR also showed traces of silica for pristine xonotlite and xonotlite with PEG MW1500. The silica could come from non-reacted silicon precursor solution or could indicate a malfunction in the calcium pump that should be reviewed for future works.

Results from rheology analysis showed significant reductions of viscosity in cement pastes mixed with xonotlite and tobermorite prepared in continuous setup with PEG. This means that particles prepared with this route (continuous reactor) and using PEG as surface modifier could be good candidates as seeds with water reducer properties.

Finally, the addition of SBS affects the synthesis of crystalline xonotlite and tobermorite. However, it is not clear how SBS is bound and to which compound. Samples prepared with a content of 1 mol of SBS per 4 mols of SiO_2 obtained a structure similar to xonotlite. The reaction is not finished after 4 hours and the structure according to XRD patterns, changes if the time of the reaction is increased to 8h. This could indicate that the reaction is still running and xonotlite is still reacting for longer periods. In the case of the synthesis of tobermorite particles with SBS, concentrations of 1 mol of SBS per 4 moles of SiO_2 generates only amorphous products, even increasing the time employed for the synthesis. In both cases, xonotlite like structure and tobermorite like structure presented amorphous silica as byproduct. SBS showed good stabilizing properties for X_SBS and T_SBS products in water according to z-potential measurements. Moreover, addition of xonotlite and tobermorite samples prepared with SBS to cement paste reduced its viscosity. Its addition, unlike particles modified with PEG polymer did not show a reduction of the acceleration effect of the cement hydration.

In conclusion, the synthesis of xonotlite and tobermorite (modified and unmodified ones) prepared in batch reactor gave larger particles and lower workability properties than in the case of the same particles synthesized in continuous reactor. However, in the case of xonotlite, samples prepared in batch showed a higher acceleration in cement hydration than xonotlite samples obtained in continuous according to the differences found in respect to the cement paste reference measured by isothermal calorimetry. It is necessary a more in-depth analysis to describe this effect, but it could be related a priori to the higher presence of silanol groups in samples prepared in batch reactor. If SBS and PEG are compared as workability enhancers, both showed reductions in viscosity compared to pristine samples. However, the use of PEG in general causes a more significant reduction in the accelerating effect of these xonotlite particles or particles with a high content of PEG.

APPENDIX

APPENDIX A.1. ^{29}Si NMR DECONVOLUTION PRISTINE XONOTLITE.

[06/01/2019 23:24 "" (2458489)]

Notes

Notes

X-Function fitPeaks

User Name FRANCISCO Time 06/01/2019 23:23:59

Parameters

	Value	Error
y0	-0,430621149634	22,842953392335
xc1	-98,744712559766	0,0096538443474451
w1	0.83300461004415061	0,029392331134488
A1	7898,0403226582	212,30137881647
xc2	-88,30529078678	0,016317715929342
w2	0.75746279706700836	0,044277527951786
A2	7631,8905296522	627,17541870733
xc3	-87,644413711577	0,015516219946578
w3	0.79457323411674063	0,040467669878414
A3	8963,1483776182	637,77231030376
xc4	-80,88414316093	0.14382659728386402
w4	1,4781172278801	0.45017757956285026
A4	1253,4687688007	301,12135435285

Statistics

Statistics	
DF	131
COD (R^2)	0.99096016123790565
ReducedChiSq	32530,667657182

APPENDIX A.2. ^{29}Si NMR DECONVOLUTION XONOTLITE WITH PEG MW600.

[06/01/2019 23:32 "" (2458489)]

Notes

Notes	
X-Function	fitPeaks
User Name	FRANCISCOTime 06/01/2019 23:32:25

Parameters

	Value	Error
y0	-0,148221065614	1,576925511836
xc1	-98,745980746855	0,0099707031771174
w1	0.93262505645491756	0,03011547663375
A1	8936,0826636313	217,89897922352
xc2	-88,319931445283	0,017403957964128
w2	0.76093305086554397	0,049249631212754
A2	7197,0575706451	708,54368333196
xc3	-87,632335812503	0,018035366075547
w3	0.9541512000697504	0,041158041355587
A3	11834,57681046	765,3226181203
xc4	-81,15699775257	0,073153798202654
w4	1,3625197379886	0.22325050566628168
A4	2151,317385956	270,53578595016

Statistics

Statistics	
DF	156
COD (R^2)	0.99128673279144708
ReducedChiSq	31645,164281667

APPENDIX A.3. ^{29}Si NMR DECONVOLUTION XONOTLITE WITH PEG MW1500.

```
[21/12/2018  18:26  ""  (2458473)]
      Notes
-------------------------------
                            Notes
-------------------------------
X-Function                        fitPeaks
          User  Name              FRANCISCOTime   21/12/2018
                18:26
                :29


      Parameters
-----------------------------------------------
                     Value                  Error
-----------------------------------------------
          y0       2616,6461438194       777,46641564933
         xc1        -98,62936795319    0,0076113113580872
          w1   0.95664739473979088     0,023994649036777
          A1        341893,62148282       6765,8522409433
         xc2       -88,311709137687     0,013139920911994
          w2   0.68988236285762405     0,041049356286447
          A2        227571,24019484       21511,142986151
         xc3       -87,657233826684     0,015281505058573
          w3        1,0347521935833     0,031323838392993
          A3        516556,31847968       24808,215066915
         xc4       -80,957389857307     0,079539200276929
          w4         1,952822624476   0.25892635481560788
          A4        95557,628773714       10518,038036466


      Statistics
--------------------------------
                           Statistics
--------------------------------
                  DF                    247
           COD  (R^2)    0.99213156951711468
ReducedChiSq                50025117,197257
```

APPENDIX A.4. ^{29}Si NMR DECONVOLUTION XONOTLITE WITH PEG MW4000.

[21/12/2018 21:05 "" (2458473)]

Input Data

	Input X Data Source	Input Y Data Source	Range
B	[Book1]exp30_29Si comas!A	[Book1]exp30_29Si comas!B	[1*:1024*]

Parameters

	Value	Error
y0	-17,9143766479	5,0365148870486
xc1	-98,712995198138	0,0072025680130313
w1	0.97778818283029367	0,020542366204581
A1	11442,259448885	171,29231503271
xc2	-88,311043062674	0,017188220514643
w2	1,0280199633831	0,033801204469714
A2	14811,948326985	898,49909891096
xc3	-87,643493691687	0,01407871233631
w3	0.8635898740076593	0,035375856245426
A3	11705,078857929	861,12862428037
xc4	-81,033191292121	0,052289667711063
w4	1,2273335822058	0.1497891037880158
A4	2217,018442166	193,30724541631

Statistics

	Statistics
DF	1011
COD (R^2)	0.98046567727199496
ReducedChiSq	23500,500417442

APPENDIX A.5. ^{1}H NMR DECONVOLUTION PRISTINE XONOTLITE.

[09/03/2019 09:34 "" (2458551)]

X-Function fitPeaks

User Name FRANCISCO

Time 09/03/2019 09:34:16

Parameters

	Value	Error
y0	-0,769127311171	6,1726121915673
xc1	5,0220320734326	0,037581367621664
w1	1,9185797451967	0,099437853756107
A1	4699,3882894631	512,30694455374
xc2	3,4767543494211	0,02902027535299
w2	2,233057710582	0.14379821277092339
A2	8170,4084115846	776,13311110047
xc3	2,0763390478871	9,7422477674063E-4
w3	0.41784562159909322	0,0029786215539006
A3	16198,754918159	176,62175460194
xc4	1,7774904853864	0,0011710969603322
w4	0.32385396192808741	0,0043985324329065
A4	7312,9470861044	148,46079862221
xc5	1,1259312351994	0,0032707157894843
w5	0.76223405031543368	0,015800369629519
A5	6739,1900599091	187,72626819307
xc6	-0,15051434165824	0.24650453094560559
w6	5,1908491531638	0.39117476981114785
A6	5069,3304157892	647,58833684113

Statistics

Statistics	
DF	451
COD (R^2)	0.99970595430035158
ReducedChiSq	4157,2939760542

APPENDIX A.6. ^{29}Si NMR DECONVOLUTION PRISTINE TOBERMORITE.

[1/6/2020 14:39 "/Graph4"
(2458854)]Data: A29SIMAS1_B
Model: PsdVoigt1Weighting: y w = 1/(data1_a)^2

Chi^2/DoF R^2

---------- 35710.90159
0.99091

Parameter	Value	Error
y0	0	0
xc1	-98.01377	0.04727
A1	3561.00554	196.56813
w1	1.50747	0.11363
mu1	0.5	0
xc2	-93.50828	0.08019
A2	2476.86707	210.71431
w2	1.73173	0.19733
mu2	0.5	0
xc3	-87.03903	0.01016
A3	16655.23236	225.64818
w3	1.46486	0.02436
mu3	0.5	0
xc4	-84.04656	0.04432
A4	7075.41615	391.85622
w4	2.01345	0.12582
mu4	0.5	0
xc5	-81.59418	0.08974
A5	2408.74291	319.67264
w5	1.51463	0.24982
mu5	0.5	0

APPENDIX A.7. ^{29}Si NMR DECONVOLUTION PRISTINE TOBERMORITE TREATED AT 300°C FOR 24 HOURS.

```
[15/06/2021  10:35  "/Folder1/NLSFwiz1"  (2459380)]
Data:
exp1730024h
_BModel:
PsdVoigt1
Weighting:
y               w  =  1/(book1_a)^2

Chi^2/DoF       R^2
------------------------------
---------- 9139.29411
               0.99123
----------------------------------------


Parameter       Value           Error
------------------------------------
 y0                    0           0
xc1            -98.30588     0.20119
 A1            154.91816    60.71734
 w1                0.562      0.3444
mu1                  0.5           0
xc2            -85.26153     0.03873
 A2          16604.05469   484.83432
 w2              3.46447     0.07603
mu2                  0.7           0
xc3            -82.50521     0.08016
 A3           3436.24337   944.44606
 w3              1.78814     0.24771
mu3                  0.8           0
xc4            -80.37507     1.35881
 A4            572.90486   634.66979
 w4              3.08503     2.79102
mu4                  0.1           0
```

APPENDIX A.8. ^{27}Al NMR DECONVOLUTION PRISTINE TOBERMORITE.

[12/06/2021 17:58 "/Graph1" (2459377)]

Data: exp17bis_B

Model: PsdVoigt1

Weighting:

y w = (data1_a)

```
Chi^2/DoF      R^2
----------------------------
15453.66339     0.99925
----------------------------------------

Parameter       Value           Error
------------------------------------
 y0                   0               0
xc1             56.80686        0.19274
 A1           114482.1526     3595.03684
 w1              14.20559        0.30559
mu1               0.44344        0.03047
xc2               63.7803        0.01165
 A2            79817.0845     3638.3922
 w2               5.19369        0.05515
mu2               0.08324        0.06003
```

APPENDIX A.9. ^{27}Al NMR DECONVOLUTION PRISTINE TOBERMORITE TREATED AT 300°C FOR 24 HOURS.

[15/06/2021 08:50 "/Graph1" (2459380)]

Data: exp1730024h_B

Model: PsdVoigt1

Weighting:

y w = 1/(data1_a)^2

```
Chi^2/DoF       R^2
----------------------------
313967.94985  0.99576
----------------------------------------

Parameter       Value           Error
------------------------------------
 y0                     0               0
xc1                    54               0
 A1            696398.7437    12724.79379
 w1               16.84273        0.38502
mu1                     1               0
xc2               64.04722        0.25324
 A2           145334.68331     7769.23835
 w2               11.72823        0.63794
mu2                    0.2               0
```

APPENDIX A.10. ^{1}H NMR DECONVOLUTION PRISTINE TOBERMORITE.

[14/06/2021 10:43 "/Folder1/Graph3" (2459379)]

Data: A1HMAS_B

Model: PsdVoigt1

Weighting:

y w = (book1_a)

Chi^2/DoF R^2

152.77841 0.99115

Parameter	Value	Error
y0	0	0
xc1	0.90142	0
A1	172.80555	1.61707
w1	0.22559	0.00231
mu1	1.07326	0.01005
xc2	2.01	0
A2	75.79132	8.90879
w2	1.43692	0.0439
mu2	0.14033	0.20428
xc3	3.43	0
A3	49.81772	3.2009
w3	0.49664	0.00808
mu3	0.2644	0.12774
xc4	4.91688	0.00807
A4	4036.95745	10.39575
w4	5.52366	0.01728
mu4	0.99943	0.00409

APPENDIX A.11. ^{1}H NMR DECONVOLUTION PRISTINE TOBERMORITE TREATED AT 300°C FOR 24 HOURS.

[14/06/2021 14:27 "/Graph2" (2459379)]

Data: exp1730024h_B

Model: PsdVoigt1

Weighting:

y w = 1/(data1_a)^2

Chi^2/DoF R^2

74248.25811 0.99822

Parameter	Value	Error
y0	-0.01282	17.69492
xc1	1.09435	0.0053
A1	19752.5164	486.4792
w1	0.76985	0.02238
mu1	1.42169	0.02971
xc2	2.02147	0.00787
A2	9455.38704	422.69829
w2	0.76985	0.03238
mu2	1	0
xc3	4.37988	0.0061
A3	129862.91817	861.48447
w3	3.34832	0.02206
mu3	0.95947	0.01203

APPENDIX A.12. ^{29}Si NMR DECONVOLUTION TOBERMORITE WITH PEG MW600.

	Value	Standard Error	t-Value	Prob>|t|	Dependency
y0	0	0	--	--	0
xc1	-98,18771	0,1055	-930,67204	1,58E-238	0,24983
A1	2625,16748	360,84612	7,27503	3,55E-11	0,55307
wG1	929,39433	--	--	--	--
wL1	1,31805	0,2789	4,72589	6,15E-06	0,61985
mu1	1	0	--	--	0
xc2	-93,42278	0,09809	-952,40668	9,24E-240	0,23322
A2	2905,3879	370,30042	7,84603	1,78E-12	0,56167
wG2	1850,64486	2,07E+07	8,96E-05	0,99993	--
wL2	1,3617	0,26552	5,12848	1,10E-06	0,6226
mu2	1	0	--	--	0
xc3	-86,99531	0,01954	-4452,55062	0	0,25927
A3	14277,7705	446,19586	31,99889	1,77E-61	0,70482
wG3	1538917,41	--	--	--	--
wL3	1,33144	0,05507	24,17554	1,48E-48	0,66049
mu3	1	0,00E+00	--	--	0
xc4	-84,14098	0,06045	-1391,85035	4,91E-260	0,32914
A4	5924,26777	647,58726	9,15E+00	1,53E-15	0,83827
wG4	5,13E+09	--	--	--	--
wL4	1,53649	0,20192	7,60957	6,20E-12	0,77447
mu4	1	0	--	--	0
xc5	-81,36302	0,12072	-674,00821	2,74E-221	0,32029
A5	3869,45124	613,39905	6,30821	4,63E-09	0,7819
wG5	1,42827	0	--	--	--
wL5	1,85781	0,38846	4,78247	4,86E-06	0,74721
mu5	1	0	--	--	0

Reduced Chi-Sqr	71360,5903
Adj. R-Square	0,96147

APPENDIX A.13. ^{29}Si NMR DECONVOLUTION TOBERMORITE WITH PEG MW1500.

	Value	Standard Error	t-Value	Prob>|t|	Dependency
y0	0	0	--	--	0
xc1	-97,29247	0,05831	-1668,60998	0	0,23393
A1	1085,25331	84,54683	12,83612	1,97E-28	0,60104
wG1	2215,99137	--	--	--	--
wL1	1,38407	0,15901	8,70453	8,11E-16	0,63013
mu1	1	0	--	--	0
xc2	-92,83933	0,05644	-1645,04995	0	0,16387
A2	1871,42735	1,02E+07	1,83E-04	0,99985	1
wG2	7090396,17	--	--	--	5,13E+09
wL2	1,89122	0,16758	11,28568	1,53E-23	0,63936
mu2	0,88983	4857,05909	1,83E-04	0,99985	1
xc3	-86,85013	0,01557	-5579,62561	0	0,44775
A3	6888,88452	177,25363	38,86456	1,02E-99	0,88203
wG3	73449,7102	3,18E+10	2,31E-06	1	--
wL3	1,79953	0,04382	41,06313	2,76E-104	0,73457
mu3	1	0	--	--	0
xc4	-84,28755	0,04661	-1808,3114	0	0,50497
A4	2867,54261	264,47319	10,84247	3,61E-22	0,94052
wG4	2,25E+09	3,78E+15	5,94E-07	1	--
wL4	2,01896	0,19699	10,24906	2,34E-20	0,89285
mu4	1	0	--	--	0
xc5	-81,70993	0,06757	-1209,19818	0	0,42455
A5	1180,18839	150,66164	7,83337	2,09E-13	0,86474
wG5	1,67463	0	--	--	--
wL5	1,4896	0,2272	6,55646	3,96E-10	0,80892
mu5	1	0	--	--	0

Reduced Chi-Sqr	6168,50348
Adj. R-Square	0,98152

APPENDIX A.14. ^{29}Si NMR DECONVOLUTION TOBERMORITE WITH PEG MW4000.

	Value	Standard Error	t-Value	Prob>|t|	Dependency
y0	0	0	--	--	0
xc1	-98,03499	0,04785	-2048,75139	0	0,27644
A1	884,59653	57,86861	1,53E+01	5,26E-36	0,55294
wG1	757,81015	--	--	--	--
wL1	1,22171	0,12462	9,80319	6,17E-19	0,6293
mu1	1	0	--	--	0
xc2	-93,30451	0,06123	-1523,75994	0	0,224
A2	799,86099	62,88441	12,71954	6,93E-28	0,56681
wG2	3713,01605	--	--	--	--
wL2	1,39858	0,16703	8,37E+00	7,78E-15	0,62171
mu2	1	0	--	--	0
	0	0	--	--	0
xc3	-87,0544	0,01375	-6331,37871	0	0,2841
A3	4489,72829	96,855	4,64E+01	1,36E-112	0,79016
wG3	6,79E+07	--	--	--	--
wL3	1,60711	0,04018	4,00E+01	1,87E-100	0,68513
mu3	1	0	--	--	0
xc4	-84,11469	0,04718	-1782,95746	0	0,41833
A4	1908,73529	158,65902	12,03042	1,00E-25	0,9053
wG4	8,98E+12	1,87E+14	4,81E-02	0,96171	--
wL4	1,94498	0,17553	11,08042	8,72E-23	0,83801
mu4	1	0	--	--	0
xc5	-81,51402	0,11469	-710,76119	0	0,42307
A5	641,3801	120,64862	5,3161	2,69E-07	0,85761
wG5	1,59986	0	--	--	--
wL5	1,68846	0,38406	4,40E+00	1,74E-05	0,80342
mu5	1	0	--	--	0
Reduced Chi-Sqr	3668,34323				
Adj. R-Square	0,97604				

APPENDIX A.15. ^{29}Si NMR DECONVOLUTION PRISTINE XONOTLITE SYNTHESIZED IN CONTINUOUS SETUP (325°C, 235bar and 9.9mL/min).

```
[25/05/2021  11:02

"/NLSFwiz1"  (2459359)]
Data:
A29Six5cnue
_BModel:
PsdVoigt1
Weighting:
y              w  =  (data1_a)

Chi^2/DoF      R^2
----------------------------
------------ 1322842.83902
0.99276
----------------------------------------


Parameter      Value          Error
----------------------------------------
  y0             0.70648          0
 xc1          -114.97048          0
  A1         422577.3363          0
  w1            17.78119          0
 mu1             1.19076          0
 xc2           -99.0982           0
  A2        178706.79348   440.094
                                 4
  w2              1.2212   0.00413
 mu2             0.84953          0


----------------------------------------
```

APPENDIX A.16. ^{29}Si NMR DECONVOLUTION XONOTLITE WITH PEG MW 600 SYNTHESIZED IN CONTINUOUS SETUP (325°C, 235bar and 9.9mL/min).

```
[25/05/2021  11:12  "/Graph2"
(2459359)]Data:
A29SiF16503_B
Model:  Lorentz
Equation:  y  =  y0  +  (2*A/PI)*(w/(4*(x-xc)^2  +
w^2))Weighting:
y              No  weighting


Chi^2/DoF      R^2
----------------------------
------------ 4226.68331
               0.98194
----------------------------------------


Parameter      Value          Error
----------------------------------------
   y0            -0.0949    0.06141
  xc1          -87.60074    0.00957
   w1            2.43242     0.0291
   A1          9764.4955    88.6304
                                   4
  xc2          -98.60084          0
   w2            2.47396          0
   A2         3830.15033          0
  xc3           -82.05223          0
   w3            5.38928          0
   A3         3381.92878          0


----------------------------------------
```

APPENDIX A.17. ^{29}Si NMR DECONVOLUTION XONOTLITE WITH PEG MW 1500 SYNTHESIZED IN CONTINUOUS SETUP (325°C, 235bar and 9.9mL/min).

[25/05/2021 11:56 "/Graph3" (2459359)]
Data:
A29Six5cP15
_BModel:
Lorentz
Equation: y = y0 + (2*A/PI)*(w/(4*(x-xc)^2 + w^2))Weighting:
y No weighting

Chi^2/DoF	R^2
----------	262.09904 0.9916

Parameter	Value	Error
y0	-0.4078	0
xc1	-112.46953	0.05254
w1	15.23217	0.16771
A1	3671.02479	29.71155
xc2	-99.01444	0.00432
w2	1.55664	0.01329
A2	1380.51467	9.07197
xc3	-88.06186	0.00257
w3	2.00007	0.01003
A3	3616.8281	18.92108
xc4	-83.66661	0.05182
w4	6.53935	0.13674
A4	1547.29745	31.18495

APPENDIX A.18. ^{29}Si NMR DECONVOLUTION XONOTLITE WITH PEG MW 4000 SYNTHESIZED IN CONTINUOUS SETUP (325°C, 235bar and 9.9mL/min).

[25/05/2021 12:03 "/Graph4"
(2459359)]Data:
A29SiF15502_B
Model: Lorentz
Equation: y = y0 + (2*A/PI)*(w/(4*(x-xc)^2 +
w^2))Weighting:
y No weighting

Chi^2/DoF	R^2
----------	846.21047
	0.96833

Parameter	Value	Error
y0	-0.14925	0
xc1	-87.41303	0.00973
w1	2.53911	0.02869
A1	3275.25845	27.17554
xc2	-98.28152	0.0308
w2	3.42258	0.08928
A2	1605.08237	29.88342

APPENDIX A.19. ^{29}Si NMR DECONVOLUTION PRISTINE TOBERMORITE SYNTHESIZED IN CONTINUOUS SETUP (400°C, 235bar and 6.5mL/min).

[15/09/2021 09:37 "/Graph1"
(2459472)]Data:
A29SiF16703_B
Model:
PsdVoigt1
Weighting:
y w = 1/(data1_a)^2

Chi^2/DoF R^2

--- 919.9184
0.99618

Parameter	Value	Error
y0	0	0
xc1	-97.6709	0.0611
A1	2624.27789	278.87586
w1	4.16474	0.1244
mu1	0.60282	0.0849
xc2	-92.74534	0
A2	1437.54797	755.12969
w2	4.66907	0.85657
mu2	0.74801	0.50763
xc3	-86.92903	0.01996
A3	11050.77426	839.05757
w3	3.79348	0.12438
mu3	1.22091	0.04011
xc4	-83.82394	0.02124
A4	2958.91933	679.52347
w4	2.63521	0.21039
mu4	1.01018	0.18223
xc5	-81.6552	0

APPENDIX A.20. ^{29}Si NMR DECONVOLUTION TOBERMORITE WITH PEG MW4000 SYNTHESIZED IN CONTINUOUS SETUP (400°C, 235bar and 6.5mL/min).

[15/09/2021 09:10 "/Graph2" (2459472)]Data:
A29SiF16704_B
Model:
PsdVoigt1
Weighting:
y w = 1/(data1_a)^2

Chi^2/DoF R^2

--- 171.72461
0.99161

Parameter	Value	Error
y0	0	0
xc1	-98.17941	0.05703
A1	181.99668	24.12819
w1	2.27127	0.16783
mu1	0.52936	0.29084
xc2	-91	0
A2	421.74395	54.31492
w2	3.58083	0.18308
mu2	0.59355	0.2416
xc3	-87.18417	0.0235
A3	2057.57132	123.5291 4
w3	3.10569	0.04623
mu3	0.61796	0.08486
xc4	-84.03965	0.02784
A4	1345.73605	152.1259 7
w4	2.9908	0.09868
mu4	0.476	0.16718

APPENDIX A.21. GAMS MODEL FOR TOBERMORITE STRUCTURE. SOLVE SUMMARY.

```
Variable  result;
Positive Variables     X, Y, Z, W;
Equations      obj, posresult, pos1, pos2, pos3, pos4,
Q21Al_Q31Alupper, Q21Al_Q31Allower, Q1_Q31Alupper, Q1_Q31Allower, Q1_Q3upper,
Q1_Q3lower, tot;

obj..result =e= ((2*X+4*Y+2*Z)/(4*W+2*Z)-0.319716);
posresult.. result=g=0;
pos1.. X =g= 0;
pos2.. Y =g= 0;
pos3.. Z =g= 0;
pos4.. W =g= 0;

//Boundary conditions//
Q21Al_Q31Alupper..(2*X+4*Y+2*Z)/(Z) =l= 5;
Q21Al_Q31Allower..  (2*X+4*Y+2*Z)/(Z) =g= 2.0;
Q1_Q31Alupper..    (2*X)/(Z) =l= 4.0;
Q1_Q31Allower..      (2*X)/(Z) =g= 1.0;
Q1_Q3upper..        X/W =l= 0.7;
Q1_Q3lower..         X/W =g= 0.2;

tot..               (X+Y+Z+W) =e= 1;

Model structuretober / all /;
X.l=0.1; Y.l=0; Z.l=0.2; W.l=0.1;
solve structuretober using nlp minimizing result;
```

```
 MODEL   structuretober      OBJECTIVE  result

     TYPE    NLP                 DIRECTION  MINIMIZE

     SOLVER  CONOPT              FROM LINE  26

**** SOLVER STATUS     1 Normal Completion

**** MODEL STATUS      2 Locally Optimal

**** OBJECTIVE VALUE                0.0000

 RESOURCE USAGE, LIMIT          0.063      1000.000

 ITERATION COUNT, LIMIT        17    2000000000

 EVALUATION ERRORS              0             0

CONOPT 3         26.1.0 rf2b37b9 Released Feb 02, 2019 WEI x86
64bit/MS Window  C O N O P T 3   version 3.17I. Copyright (C)   ARKI
Consulting and Development A/S

                    Bagsvaerdvej 246 A

                    DK-2880 Bagsvaerd, Denmark
```

```
 The model has 5 variables and 13 constraints
    with 28 Jacobian elements, 18 of which are nonlinear.
    The Hessian of the Lagrangian has 2 elements on the diagonal,
    5 elements below the diagonal, and 4 nonlinear variables.
                    Pre-triangular equations:   0
                    Post-triangular equations:  4
                    Definitional equations:     1
 ** Optimal solution. Reduced gradient less than tolerance.
 CONOPT time Total                              0.051 seconds
   of which: Function evaluations               0.000 =  0.0%
             1st Derivative evaluations         0.000 =  0.0%

                              LOWER     LEVEL     UPPER    MARGINAL

---- EQU obj                 -0.320    -0.320    -0.320      EPS
---- EQU posresult              .         .        +INF      1.000
---- EQU pos1                   .        0.160     +INF       .
---- EQU pos2                   .         .        +INF       .
---- EQU pos3                   .        0.285     +INF       .
---- EQU pos4                   .        0.554     +INF       .
---- EQU Q21Al_Q31~          -INF        3.125     5.000      .
---- EQU Q21Al_Q31~           2.000      3.125     +INF       .
---- EQU Q1_Q31Alu~           -INF       1.125     4.000      .
---- EQU Q1_Q31All~           1.000      1.125     +INF       EPS
---- EQU Q1_Q3upper           -INF       0.289     0.700      .
---- EQU Q1_Q3lower           0.200      0.289     +INF       .
---- EQU tot                  1.000      1.000     1.000      EPS

                              LOWER     LEVEL     UPPER    MARGINAL

---- VAR result               -INF         .       +INF          .
```

```
---- VAR X                           .     0.160      +INF          .

---- VAR Y                           .         .      +INF        EPS

---- VAR Z                           .     0.285      +INF          .

---- VAR W                           .     0.554      +INF          .

**** REPORT SUMMARY :

                             0     NONOPT

                             0 INFEASIBLE

                             0  UNBOUNDED

                             0     ERRORS

EXECUTION TIME       =        0.000 SECONDS      2 MB  26.1.0 rf2b37b9
WEX-WEI

USER: GAMS Development Corporation, USA              G871201/0000CA-
ANY

      Free Demo, +1 202-342-0180, support@gams.com, www.gams.com
DC0000
```

APPENDIX A.22. XRF OF PRISTINE XONOTLITE.

Universidad De Málaga SCAI
ES

7/6/2021 1:44:10PM
Calculated by UniQuant
Thermo Fisher Scientific

2021_00312_F1-69-071 (X-S) - NJOB.118

Analisis Semicuantitativo. Elementos trazas presentan altos valores de Est. Error.

9955360 Rh 60kV LiF200 LiF220 Ge111 AX03

Method	: X_UQ	Measure time	: 7/2/2021	4:32:43PM	
Kappa List	: AnySample	X-ray Path:	: Vacuum		
Shapes & ImpFc	: Bead	Film Type	: None		
Calculated as	: Oxides	Collimator Mask	: 2400 W		
Case Number	: 0 = All known	Viewed Diameter	=	29.00	mm
		Viewed Area	=	660.19	mm2
		Viewed Mass	=	5911.58	mg
Reporting Level	> 100 ppm and wt% > 2 Est.Err.	Sample Height	=	3.00	mm

Compound	Wt%	Est.Error	Element	Wt%	Est.Error
SiO2	48.32	0.25	Si	22.59	0.12
CaO	45.22	0.25	Ca	32.33	0.18
Na2O	0.385	0.035	Na	0.285	0.026
BaO	0.369	0.023	Ba	0.331	0.021
Cs2O	0.235	0.019	Cs	0.222	0.018
MgO	0.182	0.019	Mg	0.110	0.011
SO3	0.148	0.0074	Sx	0.0594	0.0030
I	0.103	0.012	I	0.103	0.012
As2O3	0.0555	0.015	As	0.0420	0.011
TeO2	0.0524	0.014	Te	0.0419	0.011
Cl	0.0387	0.0029	Cl	0.0387	0.0029
Fe2O3	0.0373	0.0019	Fe	0.0261	0.0013
K2O	0.0309	0.0015	K	0.0256	0.0013
PtO2	0.0139	0.0030	Pt	0.0120	0.0026
Au	0.0136	0.0027	Au	0.0136	0.0027
NiO	0.0133	0.0012	Ni	0.0105	0.0010
P2O5	0.0127	0.0029	Px	0.0056	0.0013
Ag2O	0.0126	0.0054	Ag	0.0118	0.0051
CuO	0.0112	0.0015	Cu	0.0090	0.0012

Known Concentration = 4.72 LOI D/S = 10.230 Fundente
Sum Weight% before normalization to 100% = 108.3 %
Total Weight% Oxygen = 38.99

APPENDIX A.23. XRF OF PRISTINE TOBERMORITE.

25/07/2019 13:30:33
Calculated by UniQuant
Thermo Fisher Scientific

UNIVERSIDAD DE MALAGA - ES

2019_00540 - EXP. 142 - NJOB.109

Análisis Semicuantitativo. Elementos trazas presentan altos valores de Est. Error.

ADXP Rh 60kV LiF200 PET AX03 LiF220		Measured on	: 24/07/2019 19:03:58
Method	: X UQ	X-ray Path:	: Vacuum
Kappa List	: AnySample	Film Type	: None
Shapes & ImpFc	: Bead	Collimator Mask	: 29 mm
Calculated as	: Oxides	Viewed Diameter	= 29,00 mm
Case Number	: 0 = All known	Viewed Area	= 660,52 mm2
		Viewed Mass	= 5985.00 mg
Reporting Level	> 100 ppm and wt% 2 Est.Err. >	Sample Height	= 3,00 mm

Compound	Wt%	Est.Error	Element	Wt%	Est.Error
SiO2	43,15	0,25	Si	20,17	0,12
CaO	36,32	0,24	Ca	25,97	0,17
Al2O3	4,57	0,10	Al	2,42	0,06
Na2O	0,115	0,022	Na	0,0855	0,016
Fe2O3	0,0566	0,0028	Fe	0,0396	0,0020
MgO	0,0382	0,013	Mg	0,0230	0,0081
Cl	0,0230	0,0028	Cl	0,0230	0,0028
TiO2	0,0183	0,0017	Ti	0,0110	0,0010
NiO	0,0151	0,0014	Ni	0,0119	0,0011

Known Concentration =15,67 LOI

D/S = 9.82 Fundente 0

Sum Weight% before normalization to 100% = 101,4 %

Total Weight% Oxygen = 35.56

APPENDIX A.24. RIETVELD QUANTIFICATION OF XONOTLITE AFTER 4 HOURS OF REACTION.

R-Values

Rexp : 2.86 Rwp : 8.51 Rp : 5.39 GOF : 2.98
Rexp`: 6.58 Rwp`: 19.59 Rp` : 18.04 DW : 0.27

Quantitative Analysis, Wt%

		Rietveld	Spiked	Original
	Amorphous content	0	49(14)	66(18)
1	*Corundum	49(13)	25.010	0.000
2	Calcite	4.1(11)	2.10(12)	2.79(16)
3	Xonotlite	30(8)	15.1(5)	20.1(6)
4	Wollastonite 2M	1.4(7)	0.7(3)	1.0(4)
5	Stishovite	5.4(15)	2.8(2)	3.7(3)
6	Dolomite	1.1(10)	0.6(5)	0.7(6)
7	Periclase	traces		
8	Brucite	0.4(4)	0.20(18)	0.3(2)
9	Coesite	2(2)	1.1(10)	1.4(13)
10	"Aphthitalite (Okada)"	5.8(16)	2.92(16)	3.9(2)

APPENDIX A.25. RIETVELD QUANTIFICATION OF XONOTLITE AFTER 8 HOURS OF REACTION.

R-Values

Rexp : 2.87 Rwp : 8.59 Rp : 5.51 GOF : 2.99
Rexp`: 6.37 Rwp`: 19.06 Rp` : 17.36 DW : 0.27

Quantitative Analysis, Wt%

		Rietveld	Spiked	Original
	Amorphous content	0	48(12)	64(16)
1	*Corundum	48(11)	25.040	0.000
2	Calcite	4.8(11)	2.49(13)	3.32(17)
3	Xonotlite	32(7)	16.5(5)	22.1(6)
4	Wollastonite 2M	1.5(5)	0.8(2)	1.1(3)
5	Stishovite	5.1(13)	2.7(2)	3.6(3)
6	Dolomite	0.9(9)	0.5(5)	0.6(6)
7	Periclase	traces		
8	Brucite	0.3(3)	0.17(17)	0.2(2)
9	Coesite	1.9(16)	1.0(8)	1.3(11)
10	"Aphthitalite (Okada)"	5.3(13)	2.75(15)	3.66(19)

APPENDIX A.26. RIETVELD QUANTIFICATION OF TOBERMORITE AFTER 4 HOURS REACTION.

R-Values

Rexp : 2.79 Rwp : 7.42 Rp : 4.71 GOF : 2.66
Rexp`: 7.97 Rwp`: 21.21 Rp` : 20.27 DW : 0.41

Quantitative Analysis, Wt%

			Rietveld	Spiked	Original
	Amorphous content		0	62(1)	82(2)
1	*Corundum		66(12)	25.010	0.000
2	Calcite		7.7(14)	2.96(15)	3.9(2)
3	Tobermorite		5.9(13)	2.2(3)	3.0(5)
4	Dolomite		6.7(13)	2.57(18)	3.4(2)
5	Periclase		traces		
6	Coesite		2.0(1)	0.8(1)	1.0(1)
7	Aphthitalite	(Okada)	1.0(4)	0.50(17)	1.0(2)
8	Aragonite		6.5(12)	2.47(14)	3.30(19)
9	Quartz		1.0(4)	0.39(13)	0.51(17)
10	Magnesite		2.9(7)	1.10(16)	1.5(2)

APPENDIX A.27. RIETVELD QUANTIFICATION OF TOBERMORITE AFTER 8 HOURS OF REACTION.

R-Values

Rexp : 2.77 Rwp : 7.13 Rp : 4.53 GOF : 2.57
Rexp`: 7.95 Rwp`: 20.45 Rp` : 19.54 DW : 0.40

Quantitative Analysis, Wt%

			Rietveld	Spiked	Original
	Amorphous content		0	60(1)	80(2)
1	*Corundum		63(11)	25.060	0.000
2	Calcite		12(2)	4.91(18)	6.6(2)
3	Tobermorite		6.3(15)	2.5(5)	3.3(6)
4	Dolomite		6.0(11)	2.38(17)	3.2(2)
5	Periclase		traces		
6	Coesite		2.0(6)	1.0(2)	1.0(3)
7	Aphthitalite	(Okada)	2.0(4)	0.70(17)	1.0(2)
8	Aragonite		4.8(10)	1.9(2)	2.5(3)
9	Quartz		1.3(4)	0.52(13)	0.70(17)
10	Magnesite		2.9(6)	1.17(12)	1.57(16)